UNIVERSITY OF ROME TOR VERGATA
ENGINEERING MACROAREA

PhD in Design, Manufacturing and Operations Engineering

XXXI Cicle

ANISOGRID COMPOSITE LATTICE SHELLS AND THEIR COMPOSITE BOLTED JOINTS: THEORETICAL AND NUMERICAL MODELING, STRUCTURAL ANALYSIS AND OPTIMIZATION

Valerio G. Belardi

Supervisor:
Prof. Francesco Vivio

Coordinator:
Prof. Pietro Salvini

Academic Year: 2017/2018

UNIVERSITÀ DI ROMA TOR VERGATA
MACROAREA DI INGEGNERIA

Dottorato di Ricerca in Ingegneria per la Progettazione e Produzione Industriale

XXXI Ciclo

ANISOGRID COMPOSITE LATTICE SHELLS ED I LORO COLLEGAMENTI BULLONATI IN COMPOSITO: MODELLAZIONE TEORICA E NUMERICA, ANALISI STRUTTURALE ED OTTIMIZZAZIONE

Valerio G. Belardi

Docente Guida:
Prof. Francesco Vivio

Coordinatore:
Prof. Pietro Salvini

Anno Accademico: 2017/2018

Ai miei Genitori
e ad Elisa

"There is nothing noble in being superior to your fellow man;
true nobility is being superior to your former self."
Ernest Hemingway

CONTENTS

LIST OF FIGURES

LIST OF TABLES

ABSTRACT

The present Thesis aims to define a new methodology for the optimal design of anisogrid composite lattice structures in the framework of aerospace and aeronautic industries, such as rocket interstages, payload adapters and fuselage segments along with the theoretical background complete development of accurate and computationally-light FE modeling techniques for the analysis of bolted joints utilized for the assembly of the anisogrid lattice shells in the overall structure where they are employed.

In particular, the outlined research activities received the financial support of Avio SpA through a PhD grant funding. In fact, Avio SpA is in charge of designing and manufacturing with anisogrid technology the Interstage 2/3 of Vega C, the new generation of European launcher developed by the Italian Space Agency and the European Space Agency.

In the field of anisogrid composite lattice structures optimization methods, this Thesis presents a comprehensive optimal design methodology which is capable of determining the minimum mass configuration of the lattice shell accounting for the contemporaneous action of different external load typologies and multiple stiffness constraints.

The outlined method makes use of a full FE parametric model of both the cylindrical and the conical configurations of the anisogrid structures which was fully coupled with an optimization technique based on the NSGA-II genetic algorithm. As a consequence, it is possible to overcome all the restrictions of the continuous approaches to the design related to the assessment of the buckling failure and the ones of the discrete approaches which correctly describe the structural behavior of the anisogrid lattice structure but that have been utilized with still limited optimization margins. Indeed, using the discrete approach to exactly evaluate the critical buckling load in the design analysis, regardless of the specific buckling failure mode, it is possible to realize a comprehensive analysis of the buckling failure of anisogrid lattice structures taking into account all possible buckling modes deriving from different load conditions, including those which cannot be adequately described by means of an analytical formulation, and thus reliably optimize the lattice shell.

Some numerical case studies related to actual industrial cases are proposed, multiple external loads and stiffness constraints applied simultaneously to the anisogrid lattice structures are considered in order to demonstrate the potentialities of this optimal design methodology.

Moreover, with reference to the bolted joints used in the final assembly of the anisogrid composite lattice structures, it is required the proper simulation of these connections since this aspect represents a critical issue for the structural integrity of the entire project. As a consequence, stemming from this specific problem and considering the wide and relevant employment of composite bolted joints in

the aeronautic and aerospace fields, an efficient and reliable design tool capable of returning accurate results in terms of junction stiffness, without making computationally heavier the global FE model, turns out to be a potential great benefit in this context. Thus, the theoretical framework that is the basis of an original FE modeling technique for composite bolted joints is presented.

This FE modeling technique is founded on the new definition of a Spot Joint Element representative of the structural behavior of a region surrounding the spot joint comprising the bolt and a circular portion of the connected plates. The enhanced version implements a stiffness matrix whose terms are obtained according to the analytical solution of the composite bolted joint theoretical reference model. The theoretical model consists in an annular plate, with rectilinear orthotropic material properties, featuring a rigid core at the inner radius and fully clamped conditions at the outer edge undergoing different external loads: (*i*) transversal load, (*ii*) in-plane load, (*iii*) in-plane bending moment and (*iv*) torsional moment.

The bolted joint element is realized through a suitable assembly of beam-type elements and, even if this FE tool features a reduced number of DOFs with respect to a complex 3D model, it preserves a substantial accuracy in the simulation of bolted joint connections.

The obtainment of the novel Spot Joint Element stiffness matrix required the analytical solution of the composite bolted joint theoretical reference model; in this regard, the main complication with respect to the previous version of this FE simulation tool is represented by the fact of considering rectilinear orthotropic material properties, that are intrinsically symmetric in a Cartesian coordinate system, for an annular plate, i.e. an axisymmetric geometry. This aspect introduces a circumferential variation of the composite annular plate bending stiffnesses and of the displacement components as a consequence. This makes it impossible the chance to obtain closed form solutions, as for the classical version of the Spot Joint Element where the theoretical reference model featured isotropic material properties.

Therefore, the constitutive equations of the rectilinear orthotropic circular plate are determined in the frame of the Classical Lamination Plate Theory and are further derived according to First-order Shear Deformation Plate Theory in order to make wider the range of applicability of the presented method. In particular, the circumferentially variable stiffness terms of this typologies of plates are outlined.

Initial efforts towards the analytical solution of the composite bolted joint theoretical reference model made use of vector approach: the governing equation was determined for thin-plates from the equilibrium and the compatibility equations of the laminate circular plate. Then, as regards the transversal load condition and considering the lack of closed form solutions, the governing equation was solved through the application of Galerkin method. Approximation functions compliant with the displacement constraints introduced by the joint theoretical model are derived and utilized in the application of Galerkin method.

Nevertheless, the solution method founded on the vector approach can hardly be enlarged to the other load conditions needed to characterize the new spot joint theoretical reference model. Indeed, Galerkin method necessitates of approximation functions that are compliant with both essential and natural boundary conditions of the problem and their search results demanding for load conditions more complicated than the transversal load one.

Consequently, the solution strategy was further improved exploiting the energy approach; a solution methodology based on the Ritz method along with the virtual displacements principle is outlined. The Ritz formulation of the problem is presented in general form and, subsequently, it is particularized for the four load conditions required by the theoretical reference model. Two symmetrical lay-ups commonly employed in literature regarding composite bolted joints are considered in

the results presentation.

Besides, the results concerning the transversal load condition and the in-plane bending moment load condition demonstrated the necessity of accounting for the composite plate shear deformability when dealing with higher values of the plate slenderness ratio, in order to extend and make more flexible the usage of both the analytical method and of the Spot Joint Element.

In the end, a first application of the composite bolted joint element, considering only the in-plane load condition, with the analytic solution embedded into the FE stiffness matrix of the new version of Spot Joint Element, is reported. The comparison between a complex 3D model and the presented FE modeling approach demonstrate the benefits achievable through the employment of this simulation technique in terms of reduced computational weight with no accuracy loss.

CHAPTER 1

INTRODUCTION

NOWADAYS composite material components represent a consolidated design opportunity for numerous industrial applications involving plates and shells, especially if the design demands to combine outstanding structural performances along with mass savings. In this context, the growing needs of lightweight and structural efficiency in aeronautic and aerospace industries brought to the development of a new design solution for grid structures: anisogrid composite lattice structures, which represent an effective technical solution for applications that require structural components characterized by high load-bearing and stiffness capabilities as well as a low mass amount. These features allow to obtain important advantages in terms of mass and cost reductions in reference to conventional aluminum components. The idea of grid structures realized with composite materials belong to Vasiliev et al. [1], initial studies on this topic took place in Russia during the early 80s with a research program that brought to the development of the first design and manufacturing methods. Successive papers about anisogrid composite lattice structures of the same authors shown progresses in this field [2, 3]: load-bearing parts such as rocket interstages, payload adapters and fuselage segments, characterized by high structural and mass efficiencies, were made by continuous filament winding which remains the most widespread fabrication technology. More recently, a new technology based on dry robotic winding of the lattice structure, followed by resin infusion under vacuum was demonstrated [4]. Additionally, this kind of structures are utilized in all the principal space programs, further studies took place in the USA, regarding both the structural behavior [5] and the manufacturing process [6] of composite grid-structures. The interest of the Japan Space Agency about this topic is likewise growing, aiming to the production of a future launchers generation [7, 8].

Launcher components such as rocket interstages, payload adapters and fairings have been realized making use of anisogrid structures and the possibility of employing them in the production of fuselage barrels is further being studied [9].

Anisogrid lattice structures can be found in the form of cylindrical or conical lattice shells, depending on the particular application. They are composed of a regular pattern of elementary lattice cells constructed by two systems of unidirectional composite ribs: two sets of helical ribs, inclined with respect to the meridian curve of the shell with the same angle but in opposite directions and hoop ribs. Geometrical schemes made of hexagonal or triangular cells are normally constructed through cells repetition alongside the meridian curve of shell and around its axis; in the first case, the hoop ribs divide equally the helical ribs segments spanning between adjacent intersection points; in the latter, the hoop ribs crosses the helical ribs in proximity of their intersection points. Furthermore,

in [10] the skin-added X-lattice composite structure is presented: this new design solution avoids the use of hoop ribs introducing an external thin skin, with fibers in the hoop direction, to increase the mechanical performance. The external skin contributes to prevent buckling modes characterized by local rotations of the helical ribs.

The particular choice of the elementary lattice cell type affects the strength and the stiffness of the anisogrid lattice structure. When needed, a skin, external or internal to the ribs and co-cured with them, without important structural characteristics but with a functional role is added to the lattice shell.

According to the design process, the goal is the identification of the optimal anisogrid composite lattice structure configuration, i.e. the layout with the lowest mass amount capable of fulfilling the set of constraint conditions which in general concern with static strength, buckling resistance and stiffness requirements. Different optimization methodologies can be found in literature, which concern with cylindrical and conical lattice shells and both typologies of cells. These methodologies can be divided in continuous approaches and discrete approaches. Many of these methods consider the anisogrid lattice structure as a continuum shell and the stiffness properties of the ribs are distributed over the medium surface of the equivalent shell applying smearing techniques [11, 12, 13, 14] meanwhile discrete approaches based on the finite element method are less common [15, 16].

The minimization of safety factors belongs to the former category of approaches and it was proposed by Vasiliev et al. for cylindrical [11] and conical shells [17]. It represents an analytical solution to the problem of constrained structural optimization of an axially compressed anisogrid composite lattice structure without an additional skin.

Totaro and Gürdal expanded this approach [12], including the axial stiffness requirement of the anisogrid lattice structure through a numerical optimization routine capable of parametrically exploring configurations with different number of helical ribs to find the solution which satisfies all constraints. Furthermore, a formulation of the local buckling coefficient which takes into account material and geometrical properties of the unidirectional ribs was provided for the triangular [18] and the hexagonal cell [19] permitting to better estimate the in-plane local buckling resistance. A similar numerical approach, but without constraints related to the stiffness of the lattice shell, was developed in [20].

Slinchenko and Verijenko homogenization modeling technique can give reliable stress resultants evaluations of the lattice structure, except in areas where loads and constraints are applied [13]. Similarly, Kidane et al. [21] developed an equivalent model smearing the stiffness properties of the ribs and summing them to the external skin ones.

An alternative smearing technique is the energy-based smeared stiffener model proposed by Buragohain and Velmurugan [22]; this last allows to evaluate differences in material features between ribs and nodal points where different ribs converge being reason of higher fiber volume fraction and mechanical properties. Following, global buckling critical load is evaluated and in [23] an optimal sizing procedure is outlined based on parametric analysis.

Failure maps of the cylindrical lattice structure are derived by Zheng et al. [14] revealing that the most dangerous failure mode for large-scale cylinders under axial compression is the global buckling. A numerical optimization method is then implemented to size the structure under strength and axial stiffness constraints.

In [24] Shi et al. came up to the analytical expressions of critical local and global buckling load under uniform external transverse pressure, through the application of the minimum potential energy principle, for advanced grid-stiffened conical shells making use of an equivalent stiffness model that accounts for the non-uniform grid disposition. The application of a hybrid genetic algorithm was

employed to maximize the critical load.

A closed-form solution for buckling of heterogeneous orthotropic truncated conical shells under external pressures is presented in [25]. The theoretical model is formulated taking into account the first-order shear deformation making use of the Donnell shell theory. Additionally, the Galerkin method is exploited to solve the partial differential equations of the problem. Results are validated by numerical applications and comparisons with results present in literature. The effect of temperature on buckling resistance of functionally graded material conical shells is investigated in [26]. The method is developed taking into account the Donnel shell theory, moreover non-linear temperature rise across the thickness is considered. the effect of transverse shear deformations and of geometric parameters on the buckling occurrence are investigated.

Grid-stiffened functionally graded cylindrical shells are investigated in [27]. The method is based on Reddy higher-order shear deformation theory and the buckling response under the coupled compressive and thermal loads were examined; buckling modes are derived taking into consideration the effects of: different grid patterns, FGMs properties, temperature fields and geometric parameters.

The work by Sobhaniaragh et al. [28] concerns the mechanical buckling behavior of continuously graded Carbon Nano-Tube (CNT)-reinforced shells stiffened by stringer and rings subjected to axial and lateral loads, that are modeled as Euler-Bernoulli beams, in the frame of the the third-order shear deformation theory. Moreover, the Generalized Differential Quadrature Method (GDQM) is employed to solve the stability equations. The effect of different geometrical and material parameters involved on the critical mechanical buckling is assessed by means of a parametric study.

An insight of the functionally graded cylindrical shells torsional buckling analysis is reported in [29], where size-dependent torsional buckling behavior is studied on the basis of modified couple stress theory using the shell model. The changes of material properties through the thickness is taken account with a power law distribution, the Von Kármán geometrical non-linearity is considered and the minimum potential energy principle is used to derive the governing equations.

Furthermore, the continuous approach was used for buckling analysis of anisogrid plates with clamped edges with various loading conditions [30, 31] and for the optimization of longitudinally compressed anisogrid lattice panels [32]. Moreover, the deformability of the anisogrid lattice structure can be analyzed exploiting the orthotropic shell theory supplied with the equivalent stiffness properties: in [33] an analytical formula to assess the axial displacement of anisogrid lattice cylindrical shells undergoing axial compression was obtained and in [34] the analytical expressions for flexural, torsional and axial global stiffness properties for anisogrid lattice conical shells are expressed.

Anyway, continuous approaches can be applied for the preliminary design of axially compressed anisogrid structures, meanwhile they cannot address the analysis of different or mixed loading conditions. In addition, the ribs-density level of the lattice shell has a significant influence on the results accuracy, i.e. an adequately dense system of ribs is required as prerequisite to apply these techniques. Moreover, the continuous approaches present the intrinsic limit of taking into consideration the onset of a limited number of critical buckling modes which can affect the integrity of the anisogrid structure, i.e. the global one, typical of the orthotropic shells, and the local one, which interests the helical ribs segments delimited by two consecutive intersection points. As described in [35], further buckling modes can occur, causing the structure to collapse for a critical buckling load lower than the one predicted by the continuous approach.

On the other hand, the purpose of discrete approaches is to consider the lattice shell accounting for its reticulated nature, i.e. the actual one, not including equivalent stiffness properties. Usually, the employed discretization is strictly connected with the finite element method and, typically, beam or 3D solid finite element models have been developed. Conversely, works based on smearing techniques

make use of finite element analysis only to provide a comparison to the theory or a refinement of the results previously obtained with the continuum models.

Buragohain and Velmurugan made use of finite element analysis in combination with twenty noded 3D layered brick elements to compare the outcomes of their smeared stiffener model [22] and of their experimental studies [36].

In the experimental study of Sorrentino et al., anisogrid cylinder was realized with filament winding; the numerical simulation of the curing process was performed through a 3D solid finite element model [37].

Morozov et al. carried out the first in-depth research works on anisogrid composite lattice structures based on the application of beam elements. Furthermore, an automated procedure to generate meshes was developed for both cylindrical [15] and conical [38] lattice shells. Different load cases were examined, showing the influence of structural parameters on the critical buckling load.

Lai et al. analysed six different elementary lattice cells, studying the influence of the inclination of helical ribs on the buckling failure for anisogrid cylindrical shells [16].

Nevertheless, 3D solid element models are highly computationally onerous and their application is restricted to the study of structures with a limited number of ribs or to the simulation of the manufacturing process. Otherwise, beam element modeling is more attractive and allows for the comprehension and the assessment of different crucial phenomena. As Morozov et al. [15] explain, the modeling of the anisogrid lattice structure as a three-dimensional frame is a more comprehensive and accurate design instrument giving the possibility to get a greater insight of instability behavior, highlighting buckling modes that smeared models are not able to provide.

Another optimization methodology was presented in [39] where Maes et al. developed a numerical optimization workflow exploiting shell elements meshes of a CAD model and a genetic algorithm.

The discrete approach was further utilized to study the buckling behavior of advanced grid stiffened carbon-fiber composite cylindrical shells with reinforced cutouts in [40]. The influence on buckling behavior of different cutout geometries in conjunction with diverse local grid reinforcements close to the cutout area were studied through non-linear buckling FE analyses. An optimal grid reinforcement configuration was found to increase buckling resistance under axial loading.

Even glass fibers are employed in the production of beam-like components, in particular in the civil engineering frame. As an example, in [41] the authors present a lattice model to determine the crack propagation in the web-flange junction of pultruded glass fiber reinforced polymer (GFRP) I-beams subject to web-flange delamination processes.

Ansari and Torabi [42] developed a numerical method in order to analyze the buckling and vibration behavior of axially-compressed functionally graded carbon nanotube-reinforced composite conical shells using the variational differential quadrature method. The extended rule of mixture is employed to define the material properties of the functionally graded conical shells that are supposed smoothly varying along the thickness direction. The discretized matrix form of the Hamilton principle is written for the problem in the framework of the first order shear deformation theory. Results are compared with the literature ones; it is found that the buckling and vibration characteristics of the functionally graded conical shells are influenced by the volume fraction and the distribution of CNTs, boundary conditions and various geometrical parameters.

The optimization of fiber-reinforced laminated truncated conical shells is described in [43], the target is represented by the maximization of the critical buckling load acting on the fiber orientations. The golden section method is the technique chosen to perform this study. Different parametric analyses were conducted to assess the dependence of the buckling resistance on the boundary conditions, geometrical features and cutout size.

According to nonlocal modeling of lattice structures, an analytical study concerning the bending problem of functionally graded nano-beams is presented in [44, 45] exploiting the nonlocal stress-driven fully nonlocal mode; exact solutions concerning the bending problem for the most usual loading conditions and external constraints are outlined. Additionally, with same nonlocal approach is investigated the torsional [46, 47, 48], the thermoelastic [49] and the vibrational [50] behaviors of nano-beams.

A numerical procedure for the optimization of anisogrid lattice structures is outlined in [39]; the methodology employs a FE software that is supplied with a CAD model of the structure and a genetic algorithm.

In this Thesis a full parametric FE model of anisogrid cylindrical and conical lattice shells was developed and combined with the genetic algorithm NSGA-II in an optimization workflow [35, 51]. The FE parametric procedure generates the model taking as input the geometrical variables of the lattice shell, making use of beam elements, that are furnished by the genetic algorithm that manages the analyses to reach the structural optimization of the lattice shell in conformity with structural and stiffness constraints.

Furthermore, one of the main issues linked to anisogrid technology is the connection of the composite lattice shells to the launcher rocket motors; in this perspective, the composite end-rings of the anisogrid structure are connected to aluminum flanges by means of bolted joints. In fact, in the specific field of anisogrid lattice structures and in general in the constructive practice, it is not uncommon to face the necessity of joining together different composite parts, or composite and metal parts, and in this regard bolted joints connections are a reliable and widespread technical solution which finds extensive applications in many fields [52, 53, 54, 55]. Moreover, the aspect of bolted joints design is not of secondary importance as it is likewise a crucial aspect for the safety and the structural integrity of the overall project. Hence, the proper simulation, by means of complex three-dimensional FE models, of these connections is highly significant as pointed out by the broad literature devoted to this subject [52, 53, 56, 57, 58, 59, 60, 61]; nevertheless, this kind of modeling badly affects both modeling and computational time.

Accordingly, one of the purposes of this Thesis is the definition of a custom Spot Joint Element representative of the structural behavior of a region surrounding the bolted joint, comprising the bolt and a circular portion of both the plates. The Spot Joint Element definition is in accordance with a finite element assembly originally developed for the analysis of spot welded joint for metal sheets or riveted joints [62]. The great benefits belonging to this simulation tool are represented by the heavily reduced number of DOFs involved in the FE analysis of the spot joint without any loss in the results accuracy. Consequently, this tool turns out to be particularly advantageous in the analysis of multi-jointed structures [63].

The theoretical formulation of this element is derived from the full analytical solution of the spot joint theoretical reference model. In the original formulation of the Spot Joint Element, the reference model is an annular plate with isotropic material properties featuring a rigid core (when a bolt connection is considered) applied to the inner radius and fully clamped conditions at the outer edge.

Therefore, this consolidated FE architecture can be further improved to encompass the FE analysis of composite bolted joints, considering a new theoretical reference model in which the annular plate is made of rectilinear orthotropic composite material. Its analytical solution is reported in the following [64, 65, 66, 67, 68] for the required load conditions: (*i*) transversal load, (*ii*) in-plane load, (*iii*) in-plane bending moment and (*iv*) torsional moment.

An initial attempt of transferring the analytical solution of the in-plane load condition into the

FE stiffness matrix of the novel composite bolted joint element is discussed in [69]; results, hereinafter reported, demonstrate the benefits achievable through the employment of this simulation technique in terms of reduced computational weight with no accuracy loss.

The composite circular plates are divided in two main groups according to their material properties which are definable as rectilinear orthotropic or circular orthotropic. In the first case the composite circular plate can be considered as if it were cut-out from a common rectangular composite laminate; it is made up of layers, differently orientated, with fibers arranged along rectilinear trajectories and the global stiffness properties of the composite circular plate depends on the circumferential coordinate as a consequence. On the other hand, for the case of circular orthotropic material properties, the layers composing the composite circular plate present fibers organized along the circumferential or the radial direction and the overall composite plate stiffness properties are axisymmetric. As previously outlined, the first category is the one that must be investigated in order to acquire the necessary theoretical background for the realization of a custom composite bolted joint finite element.

In literature, despite the wide and differentiated range of technical applications of rectilinear orthotropic circular plates, most of the published works are referred to circular orthotropic plates, and many of the available ones concerns sector plates.

As reported by Timoshenko and Woinowsky-Krieger [70], the first and preliminary approach to the analysis of rectilinear orthotropic circular plate is attributed to Lekhnitskii [71]. A simplified loading condition was solved, it consists in an elliptic plate, or circular plate as a particular case, clamped on the boundary and carrying a uniform transversal load; the solution procedure is based on the definition of a mid-surface deflection function, specific for the particular geometry and load, which verifies the governing equation of the problem.

Subsequently, the topic of composite circular plates has been further investigated according to different needs. Tang in [72] made use of Galerkin method to discuss the elastic stability of circular plates featuring rectilinear anisotropy subject to in-plane compressive forces along the external edge. A buckling mode characterized by axisymmetric deflection of the plate mid-surface is assumed in the solution method. Two cases of load application are considered: uniform in-plane compression of the plate mid-surface and unidirectional application of the compression force; both results show that, because of the initial assumption of rotationally symmetric deflection, the stiffnesses terms due to bending-twisting coupling do not influence the critical buckling load.

Elastic instability of polar orthotropic annular plates is investigated in [73], the authors provide a solution based on Green's function method and functional analysis in order to define buckled and post-buckled states of the composite plates taking into account different boundary conditions.

In [74], Fu and Waas analyzed the problem of polar and rectilinear orthotropic annular circular plate undergoing both internal or external pressure loading, without restriction to axisymmetric buckling modes, making use of the Rayleigh-Ritz method. In the polar orthotropic case the pre-stress distributions are exactly evaluated, meanwhile the rectilinear orthotropic pre-buckling stress state is approximated through Galerkin method and introducing the Airy stress function. It is demonstrated that the non-axisymmetric modes of buckling are often the critical ones.

Seifi et al. [75] dealt with symmetric buckling of cross-ply laminated annular thin-plates, buckling loads and mode shapes were derived exploiting the energy method and finite element analysis. The effects of thickness, boundary conditions, layers lay-up and ratios of outer to inner radius of the plate were investigated. It is found that the symmetric buckling assumption is not adequate when considering clamped boundary conditions.

Analogously, the buckling and vibration analysis of two-directional functionally graded moder-

ately thick circular plates is performed in [76]. The authors assess the effect of peripheral loading on the free axisymmetric vibrations along with the critical buckling load for different constraint conditions; the analyses are performed according to Mindlin plate theory obtaining numerical solutions of Hamilton energy principle.

The natural frequencies and mode shapes of a rectilinear orthotropic clamped circular plate are provided in [77] applying Galerkin method and in [78] making use of the least-squares interior collocation method.

Additionally, in [79], the asymmetric free vibration characteristics and thermoelastic stability of functionally graded circular plates was investigated making use of the finite element approach exploiting a three-noded shear flexible plate element; the material properties are considered graded along the thickness direction and temperature field is supposed to vary lengthwise the same direction. The influence on critical buckling load of geometric parameters, circumferential wave number and boundary conditions was assessed.

In addition, the dynamic analysis of symmetrically laminated composite and circular plates is provided in [80] taking into account the effect of fiber orientation on the natural frequencies, the approach is based on the Rayleigh-Ritz method.

The Ritz solution to the 3D free vibration analysis of thick annular functionally graded plates with piezoelectric layers is outlined in [81]. The displacement and the electrical potential fields are expressed through Chebyshev polynomials. The annular plates feature functionally graded mechanical properties which are supposed to vary along the thickness according to either exponent or power law distribution depending on the volume fraction of the constituents. The effect of geometrical parameters, mechanical and electrical properties on natural frequencies is analyzed determining that the higher the plate thickness to radius ratio, the higher the frequency parameters of piezoelectric annular plates.

In [82] the free vibration behavior of functionally graded sector plates was discussed resorting to three-dimensional theory of elasticity, general boundary conditions were considered. The material properties vary in both thickness and radial direction in accordance with two typologies of distribution; the displacement functions were approximated by means of 3D Fourier series and auxiliary functions. Numerical examples are reported to show the effect on the free vibration behavior of boundary conditions and material profiles.

Moreover, the work by Wang et al. [83] regards a unified solution method for the vibration analysis of functionally graded circular and annular plates and sectors; materials properties are graded in the thickness direction according to a four-parameter power-law. The unknown displacement components are formulated as an improved Fourier series and employing auxiliary functions in order to avoid discontinuities in the displacement field at the boundaries. General boundary conditions are taken into account exploiting the artificial spring boundary technique. The method is verified through numerical case-studies with plates featuring different shapes and boundary conditions.

Salehi and Sobhani published a work [84] concerning symmetrically laminated sector plate presenting rectilinear orthotropic characteristics, Mindlin plate theory was employed. Two typologies of displacement constraints were considered, in particular, simply supported and clamped edge, meanwhile the applied external load was a constant pressure. The system of equilibrium differential equations, in both linear and non-linear forms, of the plate were discretized through the application of the DR iterative method together with the finite difference discretization technique. Results were presented taking into account various angles of the sector, different slenderness ratios of the plate and lay-up configurations, the comparison with FE analyses shows a good agreement.

Another approach to non-linear static analysis of laminated sector plates is the one in [85] where

the generalized differential quadrature method is used for geometrically non-linear large deformation of laminated sector plates with any combination of clamped, simply supported and free edges and general laminate lay-ups. Von Kármán non-linearity is considered in conjunction with First-order Shear Deformation Plate Theory. Moreover, results concerning asymmetric lay-ups are presented.

Kadkhodayan et al. [86] analyzed square, circular and elliptical rectilinear orthotropic plates under the action of a uniform transversal load. The focus is on the combination of the DXDR dynamic relaxation method, that is employed to solve the finite-difference discretized governing plate equations in terms of Cartesian coordinates, and irregular schemes of rectilinear mesh.

Maleki and Tahani [87] studied the bending of sector plates in the frame of First-order Shear Deformation Plate Theory with different lay-ups and displacement boundary conditions. For the laminate circular plates, both polar and rectilinear orthotropy are considered and the circumferential variation of stiffness is taken into account for the latter case. Problem formulation is carried out in the cylindrical coordinate system then, governing equations and related boundary conditions are discretized with the generalized differential quadrature method.

Golmakani and Kadkhodayan [88] investigated the large deflection behaviors of stiffened annular functionally graded sector plates under mechanical and thermo-mechanical loadings subject to thermo-mechanical load and different boundary conditions. Mechanical and thermal material properties are considered varying continuously throughout the plate thickness. The nonlinear equilibrium equations were obtained according to the first-order shear deformation plate theory and Von Kármán relations for large deflection, whereas the solution method exploits a dynamic relaxation method combined with a finite difference discretization. Furthermore, the study is extended to ring-stiffened functionally graded circular plates [89].

The thermo-elastic behavior of functionally graded circular plates is also discussed [90]. Full Analytical solutions are provided for axisymmetric mechanical and thermal loads acting on the upper and lower surfaces of the plate.

The bending problem of composite circular plates featuring a square hole is treated in [91]. The bending moment distribution around square hole is obtained with a known mapping function in symmetric laminates undergoing different loading conditions.

The non-linear bending analysis, according to Von Kármán geometric non-linearity, of variable thickness two-directional functionally graded circular and annular sector plates resting on the nonlinear elastic foundation was investigated in [92]. The work is based on a higher-order shear deformation theory and the solution strategy makes use of the generalized differential quadrature and the Newton-Raphson methods to solve the equilibrium equations. These last ones were obtained by means of the principle of minimum total potential energy. Results are compared with those available in the open literature and a high degree of agreement was found.

Ref. [93] outlines the derivation of axisymmetric solutions for circular plates made up of functional graded material, featuring transverse isotropy, undergoing constant thermal loadings on the upper and lower faces. Numerical case studies are presented in order to show the effect of material heterogeneity and the piezoelectric effect on the plate behavior.

Similarly, Alibeigloo [94] discussed the thermoelastic behavior of functionally graded solid circular and annular plates containing piezoelectric layers by means of differential quadrature method subject to thermo-electro mechanical load. The analysis of results demonstrate that the radial displacement vary nonlinearly through the thickness direction in annular plates unlike solid circular plates.

Alipour in [95] presents an analytical study founded on three-dimensional theory of elasticity and layer-wise theory for bending and stress analysis of elastically restrained sandwich circular plates made up of functionally graded material layers. Arbitrary distributed normal and shear loads were

considered in the work.

As regards the structure of this Thesis, it is made up of two principal parts: the first one is related to the overall minimum mass design of anisogrid lattice structures for aerospace applications, in both cylindrical and conical configurations, in order to define an optimal design methodology for launcher interstages and payload adapters. In the second one, the focus is on the the analysis of composite bolted joints, such as the ones utilized to connect the interstage to the launcher motors, with aim of defining a custom FE modeling technique capable of simulating the joint with a high degree of accuracy and limited computational efforts. In the following, the topics discussed in the Thesis Chapters are reported.

In Chapter 2 a structural analysis and an optimization method for anisogrid composite lattice shell structures is proposed, considering cylindrical structures simultaneously subjected to different external loads and multiple stiffness constraints. A discrete approach is used to exactly estimate the critical buckling load of the anisogrid lattice structure, independently of the buckling failure mode. The method makes use of a full FE parametric modeling technique able to manage all the geometrical parameters of the anisogrid composite lattice structure. Then, an optimization procedure based on the genetic algorithm NSGA-II has been performed; it allows to analyze different alternatives in terms of geometrical variables, both continuous and discrete, driving the search towards the optimal solution in term of mass and conformity with all structural and stiffness constraints, aiming at the preliminary design of an actual structure. The practical usefulness and applicability of the proposed procedure to industrial cases was demonstrated through numerical examples where the anisogrid lattice structure was subjected to multiple external loads and stiffness constraints simultaneously applied.

Following, Chapter 3 expands what discussed in Chapter 2 dealing with a methodology for structural analysis and optimal design of conical anisogrid composite lattice shell structures subject to different external loads concurrently applied and multiple stiffness constraints. The critical buckling load of the anisogrid lattice conical structure is exactly assessed, independently of the buckling failure mode, by means of a discrete approach. The method makes use of a full FE parametric modeling technique able to manage all the geometrical parameters of the anisogrid composite lattice structure. Additionally, the genetic algorithm NSGA-II is employed to set up an optimization procedure which allows to analyze different sets of geometrical variables, both continuous and discrete, to reach the optimal solution in terms of mass amount and fulfilling of structural and stiffness requirements, aiming at the preliminary design of an actual structure. Numerical case-studies are outlined in order to demonstrate the practical usefulness and versatility of the proposed procedure to industrial cases where the anisogrid lattice conical structure undergoes multiple external loads and various stiffness constraints must be satisfied.

Chapter 4 outlines the definition of specific fixing equipment aimed to the experimental campaign on limited portions of the anisogrid structure, i.e. panels cut out from the entire lattice shell. This necessity arises since the relevant dimensions of the anisogrid lattice structures, in reference to the most widespread testing machines, make really demanding the execution of an experimental test on a complete lattice shell because of the high loads involved. On the other hand, the panel testing represents a valid alternative capable of returning meaningful results, useful to drive the overall design. Furthermore, it is shown that, for interstage application, aluminum flanges are employed to connect the anisogrid end rings and the motors by means of bolted joints.

In Chapter 5 the rectilinear orthotropic composite plates are introduced from a continuum mechanics standpoint. These plates have been scarcely investigated taking into account the increasing use of composite materials in structural applications in the last years. This kind of plates are

laminates with axisymmetric geometry and they are made up of unidirectionally reinforced layers with different orientations; composite lay-ups commonly employed for spot junctions are considered. Loading them, the resulting displacement field is not independent from the circumferential coordinate even for axisymmetric load conditions, unlike the case of isotropic circular plate. Nevertheless, the quasi-isotropic stacking sequence makes still possible, in some cases, to introduce the hypothesis of axisymmetry for the mid-surface deflection under transversal load, disregarding the circumferential variation of the vertical displacement connected to the variable bending stiffness. Then, the constitutive equations for this specific family of plates were obtained finding the stress resultants-strains relations in the global cylindrical coordinate system. An original approach is presented combining these expressions, along with the equilibrium equations, to derive the governing equation of the problem in the frame of Kirchhoff-Love hypothesis of the Classical Lamination Plate Theory. Furthermore, the constitutive equations for rectilinear orthotropic composite circular plates are also derived in the frame of First-order Shear Deformation Plate Theory.

Chapter 6 outlines a novel solution method for bending analysis of rectilinear orthotropic composite circular plates subject to transversal load which makes use of Galerkin method to solve the governing third order differential equation in terms of mid-surface deflection, introducing appropriate polynomial approximation functions compliant with the boundary conditions. This study represents the first step for the definition of a Spot Joint Element for spot junctions, such as bolts, rivets or generic pins, applied to a composite plate. In this order of ideas, displacement constraints involving clamped outer radius and rigid core at the inner radius, deriving from the theoretical reference model of Spot Joint Element, are taken into account. The expressions of the approximation functions are derived from constraints conditions and depicted in a general formulation. The characterization of this model allows to define the stiffness matrix terms of a custom composite bolted joint finite element. Results of the original proposed method for different typologies of composite laminate plates are presented and compared to those obtained by means of FEA performed with a refined reference model, demonstrating a good agreement.

Chapter 7 expands the theoretical investigation of the previous Chapters presenting an analytical procedure for the analysis of elastic behavior of rectilinear orthotropic composite circular plates subjected to orthogonal loads, in-plane loads, in-plane bending moment and torque moment. The displacement components are determined, according to a novel approach, applying Ritz method to the virtual displacements principle for the load conditions treated in this work. The energy approach allows for the analysis of loading conditions more complex than the transversal load one which can hardly be studied by means of Galerkin method. Additionally, displacement constraints deriving from the theoretical reference model of Spot Joint Element are considered. The employment of these specific boundary conditions required the derivation of suitable approximation functions, here reported in parametric form. Analytical results obtained by using the proposed procedure precisely match numerical results obtained by using refined FE models, for different aspect ratios of the plate and different laminate symmetrical lay-ups.

Chapter 8 deals with the application of Ritz method previously presented to the principle of virtual works written in the frame of First-order Shear Deformation Plate Theory with the scope of reducing the percentage variation obtained for the transversal and in-plane bending moment load conditions. The outcomes demonstrate that it is possible to strongly reduce the variation with respect to the FE analyses results to very limited values.

Chapter 9 Based on an analytical solution of the theoretical reference model of the composite bolted joint undergoing in-plane loads, a modeling technique for this kind of demountable connections is presented. The novel composite bolted joint element substitutes a region of the original model,

comprising the bolt and the peripheral area, with a set of radially arranged beams: the cross-section properties are opportunely tailored in order to establish a stiffness equivalence between the theoretical reference model and the presented finite element through the resolution of a system of algebraic equations. The in-plane load condition is considered in this work because of its prevalence in comparison with other ones in many practical applications as the double lap shear joint. Numerical case studies are provided to validate the novel composite bolted joint element comparing FE models of circular plates, featuring a quasi-isotropic lay-up, with an internal rigid core or with the presented FE tool.

CHAPTER 2

STRUCTURAL ANALYSIS AND OPTIMIZATION OF ANISOGRID COMPOSITE LATTICE CYLINDRICAL SHELLS

This Chapter outlines a novel optimal design method for anisogrid composite lattice cylindrical shells, the aim of the presented methodology is making use of the discrete approach to accurately evaluate the critical buckling load in the design analysis, irrespective of the particular failure mode, giving a complete and exhaustive description of the buckling failure of anisogrid lattice structures, capturing all possible buckling modes connected to a particular load condition including those that cannot be properly described through an analytical formulation and thus reliably optimize the lattice shell [35].

The method makes use of a full FE parametric modeling technique able to manage all the geometrical parameters of the anisogrid composite lattice structure. Then an optimization procedure based on the nondominated sorting genetic algorithm II (NSGA-II) [96] has been performed; it allows to analyze different alternatives in terms of geometrical variables, both continuous and discrete, driving the search towards the optimal solution in term of mass and conformity with all structural and stiffness constraints, aiming at the preliminary design of an actual structure.

In this way, it is possible to overcome the limits proper of the continuous approaches concerning the assessment of the buckling failure (the numerical examples in §2.4 are devoted to this purpose) and those of the discrete approaches which accurately describe the structural behavior of the anisogrid lattice structure but that have been exploited with limited margins of optimization, not completely taking advantage of all their possible benefits. In fact, discrete models have not been fully coupled with an optimization technique yet and the studies conducted with these techniques have presented results showing the influence on mass amount and mechanical behavior of a single parameter variation while the others are kept fixed. Differently, the combination of parametric modeling and a genetic algorithm allows to make simultaneous changes of all variables intended to reach the optimum.

Furthermore, the only load case treated by the continuous approaches is the axial compression and neither the discrete approaches have been employed to optimize the anisogrid lattice structure

undergoing a mixed loading condition. On the other hand, the proposed procedure provides the structural optimization when different types of loads are concurrently applied and when multiple stiffness constraints are considered. Indeed, the widely required condition on axial stiffness can be added to other ones, e.g. bending stiffness.

The practical usefulness and applicability of the proposed procedure to industrial cases was demonstrated through numerical examples where the anisogrid lattice structure was subjected to multiple external loads and stiffness constraints simultaneously applied.

2.1 FE parametric modeling

A FE parametric modeling technique was developed in order to optimize anisogrid composite lattice cylindrical shells, the presence of the skin was not considered in this work. The developed parametric procedure is needed to explore different design solutions for an anisogrid lattice structure with assigned material properties, height L and diameter D (Fig. 2.1).

Anisogrid lattice structures present helical and hoop ribs mutually interlaced in the overlapping zones, their intersections determine a specific and repetitive geometrical scheme that can be considered the basic unity of the lattice shell, the elementary lattice cell, that is repeated along the height and the diameter of the lattice shell.

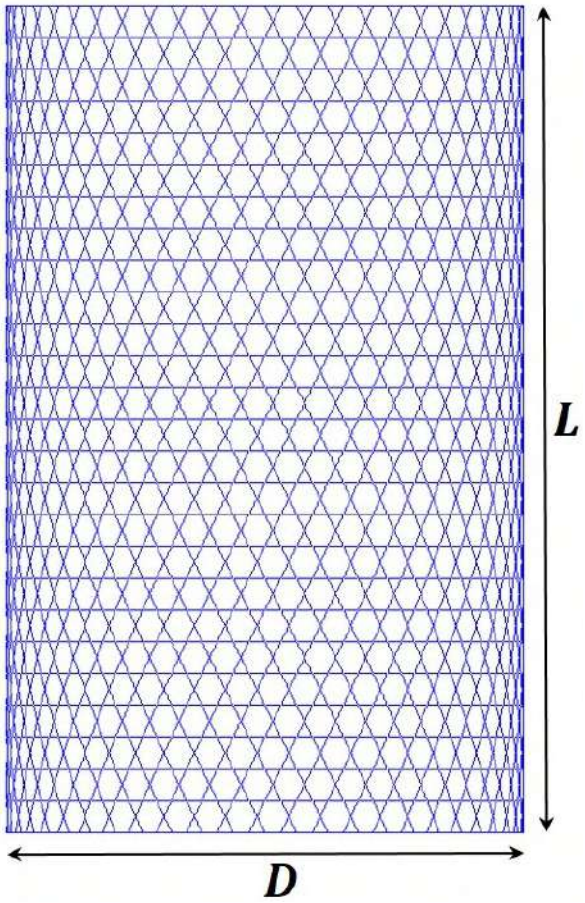

Figure 2.1: Cylindrical anisogrid lattice structure composed of hexagonal elementary lattice cells.

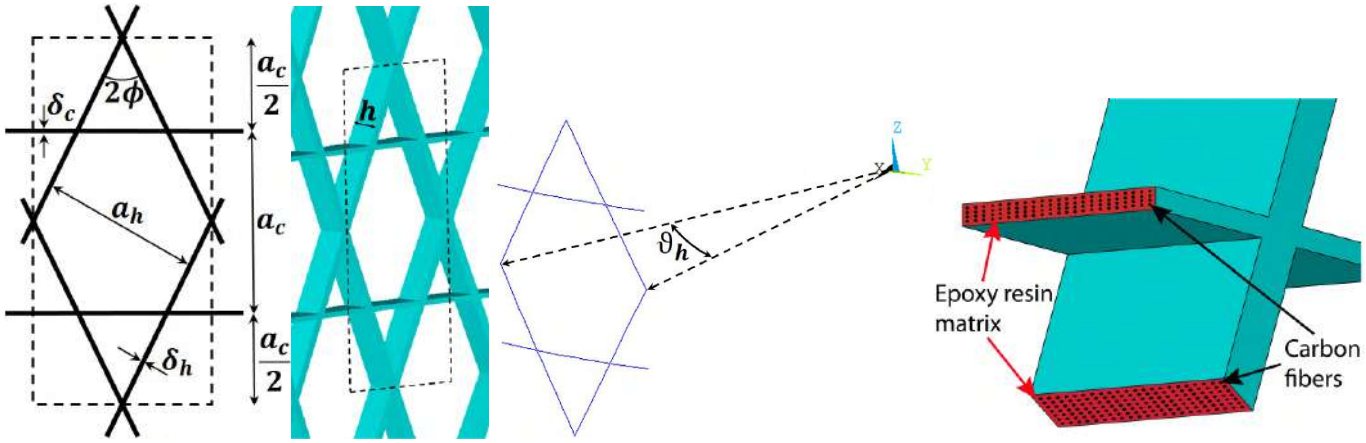

(a) (b) (c) (d)

Figure 2.2: Geometry of hexagonal elementary lattice cell: (a) 2D and (b) 3D view. (c) Angle ϑ_h between two consecutive helical ribs intersection points and (d) carbon fiber disposition inside the ribs.

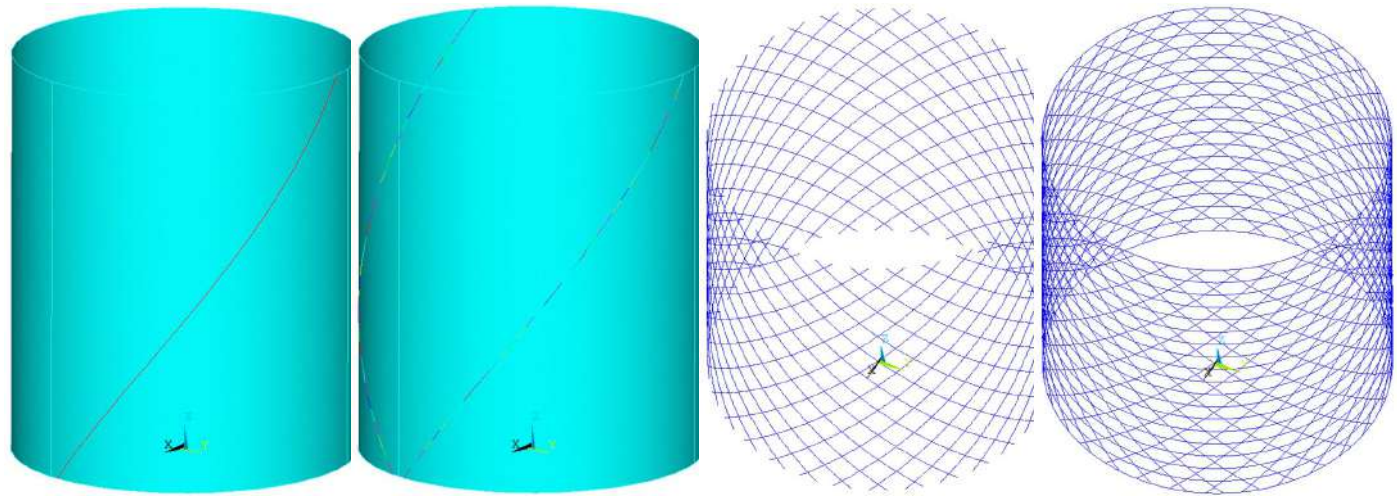

(a) (b) (c) (d)

Figure 2.3: (a) Geodetic curve on cylindrical surface defining the helical ribs mid-line; (b) the two geodetic curves, one for every sense of winding, after cutting; (c) mesh of helical ribs; (d) complete mesh of anisogrid lattice structure.

The parametric procedure allows to realize FE meshes of anisogrid lattice cylindrical structures composed of hexagonal elementary lattice cells (Fig. 2.2a): in this case hoop ribs cross halfway the helical ribs segments. Furthermore, the parametric procedure can be easily extended to the case of triangular elementary lattice cells where the hoop ribs pass through the overlapping areas between helical ribs, Fig. 2.5.

The unidirectional composite ribs (Fig. 2.2d) are usually made of epoxy matrix and carbon fiber directed as the ribs.

The parametric procedure is based on five variables, three of them are continuous variables (Figs. 2.2a and 2.2b) and are needed to define the cross-section dimensions of the two kinds of ribs: the radial thickness h and the widths of helical and hoop ribs, δ_h and δ_c respectively. In addition, two discrete variables, constituted by positive and integer numbers, are employed: the number of helical ribs with the same slope n_h and the number of cells N arranged alongside the axis of the lattice shell. This choice of geometrical variables has two strong effects on the design of the anisogrid lattice structure: firstly, the anisogrid lattice structure is manufacturable, as it consists of a finite amount of ribs and elementary lattice cells placed along its height, the second one regards the inclination angle of helical ribs ϕ that is converted from an optimal fixed value to an outcome parameter which is a function of the two discrete variables, which is an indispensable condition to verify any stiffness constraints.

The other geometrical parameters required to completely define a particular configuration of an anisogrid lattice structure can be extrapolated from the discrete variables: the angle between two consecutive helical ribs intersection points, Fig. 2.2c:

$$\vartheta_h = \frac{2\pi}{n_h} \tag{2.1}$$

and the distance between hoop ribs:

$$a_c = \frac{L}{2N} \tag{2.2}$$

which is necessary to evaluate the height of an elementary lattice cell that is $2a_c$. Furthermore, the inclination angle of the helical ribs can be extrapolated from the discrete variables:

$$\phi = tan^{-1}\left(\frac{\pi DN}{Ln_h}\right) \tag{2.3}$$

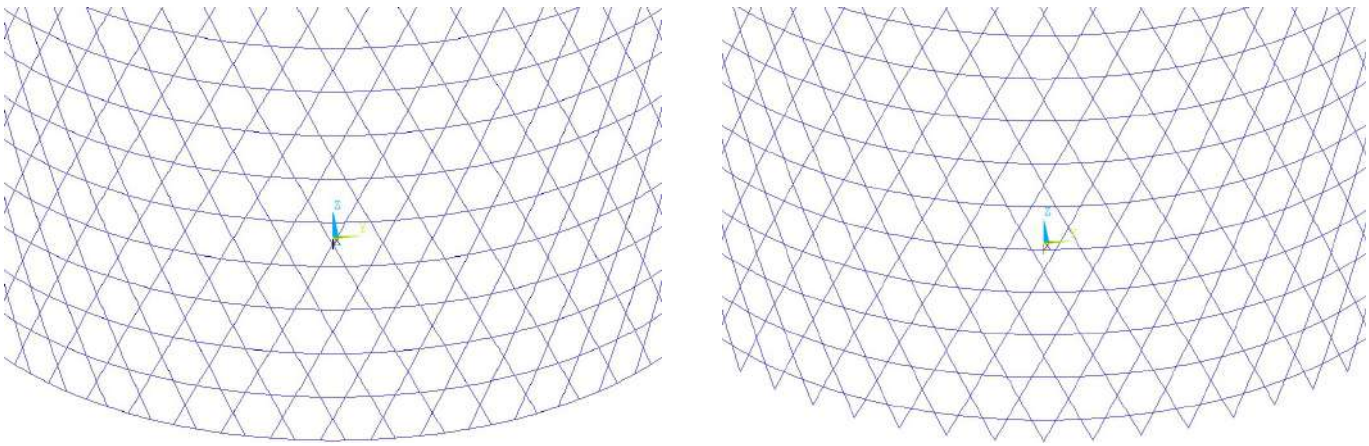

(a) (b)

Figure 2.4: Configurations of anisogrid lattice structure consisting of hexagonal elementary lattice cells delimited by: (a) extremal hoop ribs and (b) overlapping areas between helical ribs.

Beforehand, to start the mesh generation, the first operation carried out by the FE modeler is the analytical characterization of the helical ribs mid-line. In particular, it is a geodetic curve lying on a

Table 2.1: Coordinates of the points P_1 and P_2 utilized to determine the constants C_1 and C_2.

Layout	$\mathbf{P_1}$		$\mathbf{P_2}$	
	$\mathbf{z_1}$	$\vartheta_\mathbf{1}$	$\mathbf{z_2}$	$\vartheta_\mathbf{2}$
Hexagonal Cell – Extremal Hoop Ribs	0	$\frac{\vartheta_h}{4}$	$\frac{a_c}{2}$	$\frac{\vartheta_h}{2}$
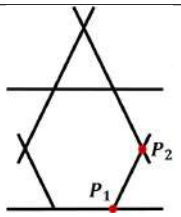				
Hexagonal Cell – No Extremal Hoop Ribs	0	0	$\frac{a_c}{2}$	$\frac{\vartheta_h}{4}$
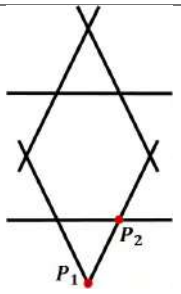				
Triangular Cell	0	0	a_c	$\frac{\vartheta_h}{2}$
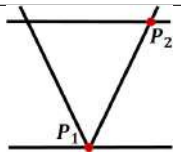				

cylindrical surface, i.e. an helix curve as shown in Fig. 2.3a. Making use of a cylindrical coordinate system (r, ϑ, z) with the origin at the bottom of the lattice structure and the z axis coincident with its axis of symmetry, the analytical expression of the helical ribs mid-line is:

$$\vartheta(z) = C_1 z + C_2 \tag{2.4}$$

This expression must be univocally defined, for the specific anisogrid lattice structure with the prescribed geometrical variables, through the identification of the coefficients C_1 and C_2 present in the equation. Taking into account two geometrical points $P_1(z_1, \vartheta_1)$ and $P_2(z_2, \vartheta_2)$ that belong to the curve, with known coordinates univocally determined by the geometric variables previously established, the coefficients becomes:

$$C_1 = \frac{\vartheta_2 - \vartheta_1}{z_2 - z_1} \qquad\qquad C_2 = \vartheta_1 - z_1 \frac{\vartheta_2 - \vartheta_1}{z_2 - z_1} \tag{2.5}$$

Once the equation of the helical ribs mid-line has been determined, the procedure codified in the finite element software traces two geodetic curves, one for every verse of winding on the cylindrical surface. Afterwards, the two geodetic curves are cut to find the positions of the intersection points between two helical ribs and between an helical rib and an hoop rib, the result is shown in Fig. 2.3b. This is necessary to force the successive generation of elements nodes in correspondence of

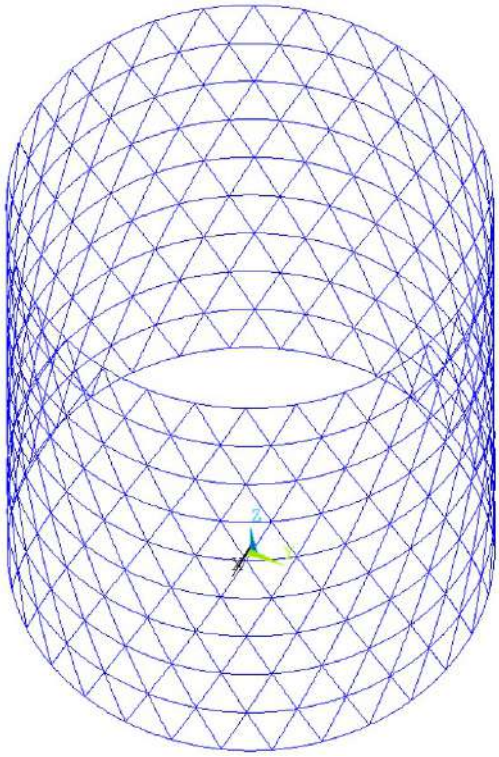

Figure 2.5: Mesh of anisogrid lattice structure with triangular cells.

these geometrical points. This operation is carried out by means of a series of cuts executed with a geometrical plane orthogonal to the axis of the lattice shell. The geometrical plane is initially located at the vertical coordinate $z = a_c/2$ and after every cut it is moved ahead, along the z axis, of a quantity $a_c/2$ until the cut sequence is completed.

The curves obtained cutting the two geodetic curves are copied n_h times around the axis of the lattice structure with an angular step of ϑ_h. All these lines are meshed with two noded beam element, having six degrees of freedom per node (Fig. 2.3c). To conveniently reproduce the twist proper of the helical rib cross-section alongside its mid-line, the beam element coordinate system is adjusted making use of the orientation node that is positioned on the axis of the anisogrid lattice structure. In this way, the width of the helical rib cross-section remains perpendicular to the radius of the shell along the length of helical rib mid-line.

After that, a set of n_c circumferences is drawn in the positions of hoop ribs: the first one is realized at $z = 0$, the others have a shift of a_c from the previous one in the z direction. Each circumference is composed of circular segments with angular extension equal to ϑ_h so that they can be enclosed between two geometrical points of intersection with helical ribs previously determined. Following, the curves constituent the hoop ribs are meshed completing the anisogrid lattice structure mesh as reported in (Fig. 2.3d).

Subsequently, the FE modeler computes the mass of the lattice shell evaluating the contributions of the helical ribs:

$$M_h = 2n_h \frac{L}{cos\phi} h \delta_h \rho_h \tag{2.6}$$

and the one related to the hoop ribs:

$$M_c = n_c \pi D h \delta_c \rho_c \tag{2.7}$$

ρ_h and ρ_c are the mass densities of helical and hoop ribs, respectively. The number of hoop ribs n_c depends on the number of elementary lattice cells alongside the axis of the anisogrid structure: $n_c = 2N + 1$. The total mass is obtained summing up the two expressions:

$$M = M_h + M_c \tag{2.8}$$

Moreover, it should be noted that the particular choice of the two geometrical points P_1 and P_2, whose coordinates are outlined in Table 2.1, permits to realize two different structure layouts with hexagonal elementary lattice cells: the one described up to now, delimited by extremal hoop ribs helpful to consider the presence of the end rings in Fig. 2.4a, and the one which ends with the overlapping areas between helical ribs, Fig. 2.4b. For the second layout, the first circumference necessary to generate the hoop ribs is positioned at $z = a_c/2$, meanwhile their number is $n_c = 2N$.

The parametric modeling technique employed offers the opportunity of easily realizing anisogrid lattice structures composed of triangular elementary lattice cells (Fig. 2.5). The coordinates of the geometrical points P_1 and P_2 for this arrangement is illustrated in the third row of Table 2.1, the distance between two consecutive hoop ribs becomes: $a_c = L/N$ and for this configuration the number of hoop ribs is $n_c = 2N + 1$.

2.2 Structural optimization using the NSGA-II

The design strategy for structural optimization makes use of an automatic process based on the coupling of the FE parametric procedure and the computationally fast genetic algorithm NSGA-II [96], an elitist nondominated sorting-based multi-objective genetic algorithm implemented in many optimization commercial software packages. The NSGA-II requires no training and allows to deal with constrained multi-objective optimization problems involving discrete and continuous variables. For this work it is used to reach a single objective, i.e. mass minimization.

The NSGA-II provides the optimal solution ensuring the validity of a fixed number of conditions formulated as inequalities, i.e. constraints, which must be verified to accept a particular sample as a feasible solution which contributes to the attainment of the optimum. The constraints employed for the optimization of anisogrid lattice structures state:

- Material compressive strength

$$\sigma_{MIN} \leq \sigma_0;$$

- Buckling resistance

$$\lambda_1 \geq 1;$$

- Minimum level of stiffnesses

$$S_i \geq S_i^{MIN}.$$

The first imposed condition concerns the material failure and it involves only the helical ribs, stating that their maximum compressive stress σ_{MIN} must not exceed material compressive strength

σ_0. Indeed, the axial force agent on the anisogrid lattice structure is responsible of a compression stress state for helical ribs and a general traction stress state for hoop ribs. Being the material strength larger in traction than in compression, and the stress level reached by helical ribs higher than the hoop ribs one, this last is not taken into account. Moreover, manufacturing imperfections could be reason of an elliptical cross-section of the lattice shell and consequently decrease the critical buckling load; the general tension stress state of hoop ribs neutralizes this problem recovering the circular shape for the lattice shell cross-section. Hence, no knock-down factor for the critical buckling load due to geometrical imprecisions is needed in designing anisogrid lattice structures [1].

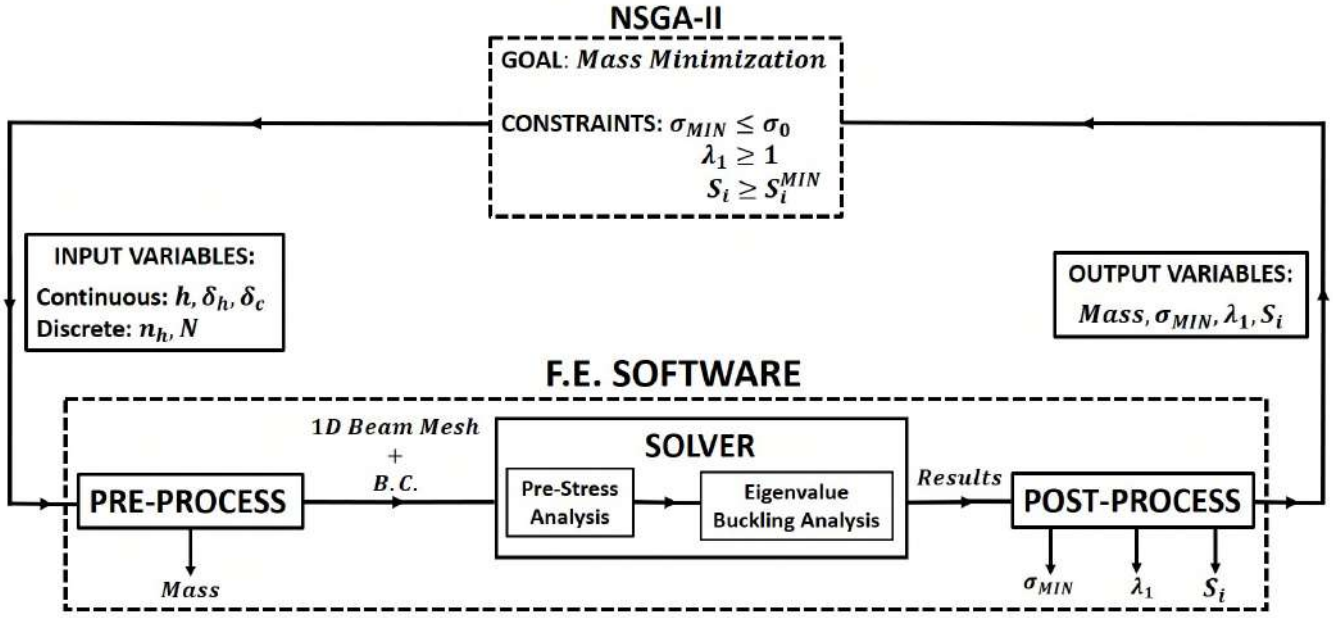

Figure 2.6: Logical workflow of the optimization procedure based on the finite element method coupled with the genetic algorithm NSGA-II.

To complete the requisites on structural strength, the capability of preventing buckling occurrence must be added to the conditions prescribed to the optimization algorithm. The analytical approaches offer a buckling strength prevision affected by the intrinsic limit deriving from supposing only two modes as responsible of buckling failure. Indeed, these methods consider the structure as if it could only behave in two different and extremely distinct ways: as a continuum shell whose buckling response can be treated with orthotropic shell relationships or as a three-dimensional frame, which can undergo local instability. In many cases, actually, the anisogrid lattice structure does not exhibit a well defined mechanical behavior ascribable to an orthotropic shell or to a beam framework. More frequently, it is a composition of them and the lattice structure shows buckling failure modes that are connected with its dual nature and that are characterized by the presence of lobes distributions along and around the axis of the shell. Besides, equations developed with smearing techniques to evaluate the critical buckling load are not capable to capture these types of collapse. Therefore, sometimes the correlated optimization methodologies overestimate the buckling resistance, giving as output geometrical dimensions for the lattice shell unable to fulfill the structural requirements and that consequently do not represent a reliable design solution. Hence, the re-examination of the project is needed and it could produce an exaggerated mass addition.

To overcome these limits, the discrete approaches are needed to get the correct estimation of the buckling resistance and the instability requirement must be formulated regardless of the particular buckling failure mode. In the proposed procedure, this is achieved making use of a constraint which imposes that the first eigenvalue λ_1 computed through finite element analysis must be at least unitary. In this way, the condition on buckling strength is expressed in the most general manner encompassing all possible modes, including the local and global ones and those without a simplified theoretical formulation.

The proposed optimization methodology is highly general and further constraints concerning structural stiffness can be settled. Taking as an example the design of a rocket interstage, it must possess a controlled flexibility in order to be compliant with the guide systems of the launcher. Subsequently, some minimum level of stiffnesses parameters could be demanded to the output design. The genetic algorithm affords this requirement similarly to the others, i.e. the values are deduced by the finite element analysis and supplied to the NSGA-II which compares it with the reference values.

An extension range must be defined for the five variables, imposing their minimum and maximum values. The combination of all allowable values defines the design space where the NSGA-II operates. In this phase, some requisites regarding the manufacturing process can be introduced, such as those about ribs width which is a multiple of the fiber one.

To start the optimization process, a design of experiments (DOE) is needed. A DOE produces an initial population of samples whose purpose is providing an assessment of the structural response of the anisogrid lattice structure to the genetic algorithm, and consequently starting the automatic generation of samples. In this regard, the most widespread exploration of the design space is important to guarantee the identification of the optimal design. The Uniform Latin-Hypercube DOE [97] has been used in order to obtain an initial population characterized by a uniform and random distribution of the samples in the design space.

The procedure utilized to optimize the design of the anisogrid lattice structure follows the logical workflow shown in Fig. 2.6. During the computing loops, the genetic algorithm NSGA-II supplies the finite element software with a set of geometrical variables written in a file which acts as input for the finite element software. Once input variables have been defined, the procedure calls for a batch file needed to manage the finite element analysis. Its pre-processor constructs the mesh of the anisogrid lattice structure according to the sequence of operations previously described and computes its mass M. In the subsequent step, boundary conditions are introduced in the model: the bottom end is fixed; nodes of the upper extremal hoop rib are connected through a set of rigid links (shown in Table 2.2) to the one present in its geometrical center, free from displacement constraints, where external loads are applied.

Then, finite element eigenvalue buckling analysis is carried out identifying the output variables that must be furnished to the NSGA-II to check the conformity with constraints. The anisogrid lattice structure mass M, the highest compressive stress σ_{MIN}, the first eigenvalue λ_1 and stiffness values S_i are recorded in an output file and acquired by the genetic algorithm, closing the loop. With this information, it deduces the set of input variables for the following iteration. The process goes on until all the samples have been analyzed.

Finally, the design which satisfies all the constraints conditions with the lowest mass is the optimal solution.

Table 2.2: The four load cases and their loading conditions and stiffness constraints.

Load Case 1 (LC1)	**Load Case 2 (LC2)**	**Load Case 3 (LC3)**	**Load Case 4 (LC4)**
Loading Conditions			
Axial Compression	Axial Compression Transverse Bending Force	Axial Compression Bending Moment	Axial Compression Torque Moment
Stiffness Constraints			
Axial Stiffness	Axial Stiffness Transverse Bending Stiffness	Axial Stiffness Bending Stiffness	Axial Stiffness Torsional Stiffness
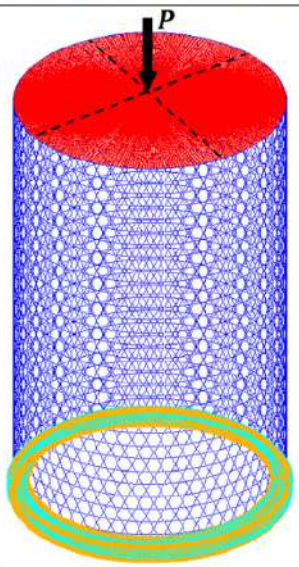	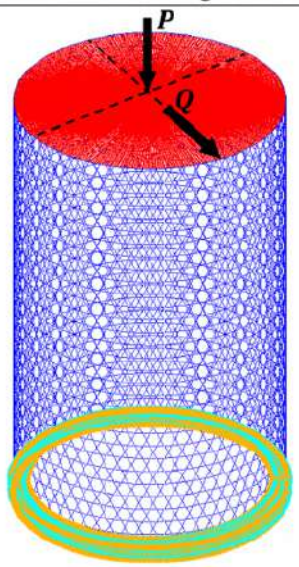	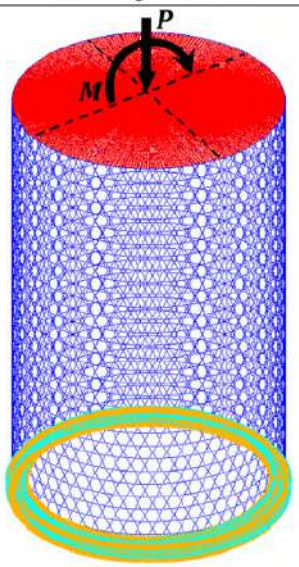	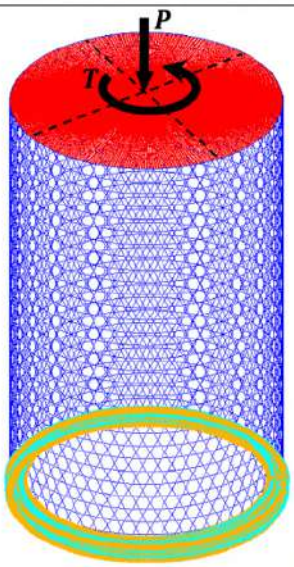

2.3 Numerical results

The optimal solutions for the design of anisogrid lattice structures subjected to different load typologies and multiple stiffness requirements are here considered. These examples are presented with the aim to validate the effectiveness and the accuracy of the proposed optimal design method and the broad potentialities of the NSGA-II, in particular when various external loads act simultaneously on the lattice shell.

The starting case-study involves a loading condition of axial compression and, in addition, a minimum axial stiffness must be assured. Nevertheless, operating conditions can consist of a mixed set of loads, so the subsequent case-studies are obtained taking into account the presence of further loads and stiffness constraints. One load condition and stiffness constraint at a time will be considered and superimposed to the first load case and then, the anisogrid lattice structure accordingly sized. Overall, four load cases were analyzed, represented in Table 2.2.

Object of the analyses considered in the load cases hereinafter presented is a cylindrical anisogrid lattice structure consisting of hexagonal elementary lattice cells with extremal hoop ribs, diameter $D = 4$ m and height $L = 7$ m. The lattice shell material employed in the following analyses is carbon-epoxy, it is the same for both helical and hoop ribs and its properties are: Young modulus $E = 100$ GPa, compressive strength $\sigma_0 = 450$ MPa and mass density $\rho = 1,500$ Kg/m^3. Material

properties are strongly dependent on the manufacturing process and so, for simulation purposes, the ribs were modeled with isotropic material; the Young Modulus considered is that evaluated along the ribs trajectories, usually deduced with experimental tests on specimens cut out from the global structure.

Aiming at a high level of generality, a wide design space was utilized to perform the analyses of the following case-studies. The minimum and maximum values of the geometrical variables used in the FE parametric modeling procedure are listed in Table 2.3; the design space consists of all their possible combinations.

Table 2.3: Range variation of problem variables defining the design space.

	h [mm]	δ_h [mm]	δ_c [mm]	n_h	N
MIN Value	13.00	2.30	2.30	65	20
MAX Value	35.00	18.00	18.00	140	50

Table 2.4: Geometric parameters and finite element analysis results of the anisogrid lattice structure designed for the four load cases considered.

	U.o.M.	Load Case 1	Load Case 2	Load Case 3	Load Case 4
M	[Kg]	563.15	705.07	642.19	677.10
h	[mm]	26.66	30.78	30.25	27.18
δ_h	[mm]	6.70	11.24	8.02	6.92
δ_c	[mm]	2.33	2.30	3.04	2.32
ϕ	[°m]	25.25	23.65	24.39	28.31
n_h	[−]	118	82	99	130
N	[−]	31	20	25	39
σ_{MIN}	[MPa]	288.38	289.15	319.87	370.12
λ_1	[−]	1.00	1.03	1.01	1.01
u_z^{MAX}	[mm]	29.72	22.62	24.80	29.72
S_A	[MN/m]	370.12	486.30	443.55	370.12
u_x^{MAX}	[mm]		16.66		
S_{TB}	[MN/m]		30.00		
rot_y^{MAX}	[rad]			$3.39 \cdot 10^{-3}$	
S_B	[MNm/rad]			884.96	
rot_z^{MAX}	[rad]				$5.42 \cdot 10^{-3}$
S_T	[MNm/rad]				553.51

2.3.1 Compression axial load and axial stiffness constraint (LC1)

The anisogrid lattice structure with dimensions and material properties earlier assigned must be designed to withstand the axial load $P = 11$ MN with a further requirement: it has to guarantee a minimum axial stiffness $S_A = 370$ MN/m. This parameter is evaluated through the ratio between the applied load P and the maximum axial displacement in the z direction u_z^{MAX}.

The minimum mass design which concurrently satisfies the structural conditions on the maximum compressive stress, buckling resistance and restricted axial deformability was determined through the application of the FE parametric modeling technique and the genetic algorithm; results concerning the geometric variables and the structural performances can be found in Table 2.4.

This case-study is useful for the explanation of the physical meaning of the discrete variables. In fact, the anisogrid lattice structure can be considered as a series of N circular-springs coaxial with the lattice shell and disposed along its axis, a reduction of this variable contributes to raise its axial stiffness; on the other hand, an increase of this parameter is responsible of a higher flexibility. Besides, the number of helical ribs n_h has a direct influence on the stiffness of a single individual circular-spring.

The limiting conditions for this design, which drove the sizing of the lattice shell, turned out to be the buckling and stiffness constraints, that are strictly verified. Unlike, the safety factor concerning the other failure mode connected to helical ribs compressive strength is about 1.56.

The collapse of the lattice shell is due to a buckling failure mode, reported in Fig. 2.7, characterized by the presence of 10 vertical series of lobes and each one consists of 10 lobes. Their amplitude is more accentuated in the central zone of the anisogrid lattice structure meanwhile it decreases moving towards the extremal hoop ribs because of the clamping effect due to the boundary conditions and to the set of rigid links.

2.3.2 Transverse bending force and transverse bending stiffness constraint (LC2)

In this case-study, the basic compression load case beforehand discussed is expanded through the application of a transverse bending force $Q = 0.5$ MN (along the x-axis of the model) to the upper extremal end of the lattice shell. Likewise, a second stiffness constraint is further imposed demanding a minimum transverse bending stiffness $S_{TB} = 30$ MN/m; it is defined as the ratio of the transverse bending force and the maximum displacement alongside its direction of application, i.e. u_x^{MAX}.

Table 2.4 lists the results of the optimization performed with the NSGA-II. The presence of the double external load and stiffness conditions increased the mass of 25.19% with respect to the previous case-study involving only axial compression force and axial stiffness constraint.

Concerning to ribs cross-section dimensions, the thickness h and helical ribs width δ_h are greater than those of the preceding sizing, while hoop ribs width δ_c is practically unchanged. Both discrete variables n_h and N are reduced to assure the validity of the required minimum values of stiffness.

Once again, the constraint on compressive strength resistance is amply fulfilled, indeed the associated safety factor is 1.56 as for the previous load case. Similarly, the axial stiffness S_A is 31.43% higher than the minimum value. Conversely, the constraints on buckling failure mode and transverse bending stiffness resulted being the most stringent for the sizing.

The buckling failure mode of this load case, as shown in Fig. 2.8, makes the structure to buckle more locally, in a confined region, if compared with the previous one. The instability interests the area where the compressive stress state of the helical ribs due to the transverse bending force and axial compression are superimposed.

2.3.3 Bending moment and bending stiffness constraint (LC3)

The anisogrid lattice structure undergoes the action of the axial compression force and of the bending moment $M = 3$ MNm applied to the top of the lattice shell (along the y-axis of the model). Additionally, the stiffness constraint concerning axial stiffness was considered along with a constraint on bending stiffness, a minimum value of $S_B = 875$ MNm/rad was requested. This last stiffness value is evaluated through the ratio of the bending moment and the consequent angle of rotation rot_y^{MAX} experienced by the upper cross-section of the lattice shell.

The application of the optimization methodology produced the outputs reported in Table 2.4. The mass of the lattice shell increased of 14.03% with respect to the baseline configuration of the first load case. Both discrete variables decreased and contextually the cross-sections of the two kinds of ribs present increased dimensions.

The condition on buckling failure was again a driver for the sizing of the anisogrid structure, as λ_1 is very close to the unity; likewise, the value obtained for S_B strictly respects the condition for this parameter. The axial stiffness S_A is the 19.88% greater than the limit value. Once again the compressive strength of helical ribs is not a critical condition being the safety factor for the failure mode induced by the compressive stress 1.41.

The buckling failure of the anisogrid lattice structure took place in the half where the bending moment causes a compression stress state of the helical ribs. The buckling mode, as shown in Fig. 2.9, is characterized by 3 main vertical series of lobes composed of 9 lobes. The lobes of the central strip have a bigger amplitude whit respect the other two and it progressively decreases towards the extremal hoop ribs.

2.3.4 Torque moment and torsional stiffness constraint (LC4)

This load case was set up adding a torque moment $T = 3$ MNm (along the z-axis of the model) to the simple compression load condition; in addition, a torsional stiffness constraint must be verified as well as the axial one. The torsional stiffness S_T is computed dividing the torque moment T by the rotation rot_z^{MAX} of the upper extremal end about the axis of the lattice shell. A minimum torsional stiffness $S_T = 550$ MNm/rad is required.

The application of the NSGA-II allowed to find out the optimal design parameters reported in Table 2.4.

This case-study requires a mass increase of 20.22% in reference to the configuration of the initial load case. Moreover, the number of helical ribs n_h and of elementary lattice cells alongside the meridian curve of the shell N are higher. In addition, the cross-section dimensions of helical and hoop ribs are almost unchanged.

The superposition of the torque moment and the axial force produced an intensification of the maximum compressive axial stress of helical ribs σ_{MIN}; anyway, it does not reach the compressive strength in fact, the safety factors for this failure mode is 1.41. Contrariwise, the two constraints regarding axial and torsional stiffness and the one about buckling strength of the anisogrid lattice structure are very close to their limit value.

Because of the mixed loading condition here examined, the anisogrid lattice structure buckles according to a buckling failure mode which exhibits 14 oblique stretched lobes alternatively oriented inward and outward with respect to the lattice shell curvature (Fig. 2.10).

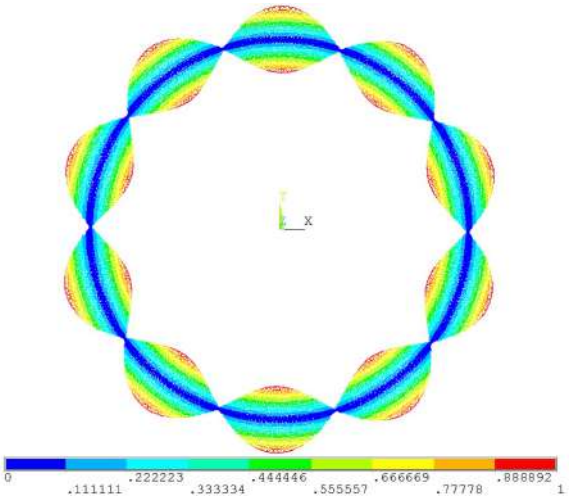

(a)

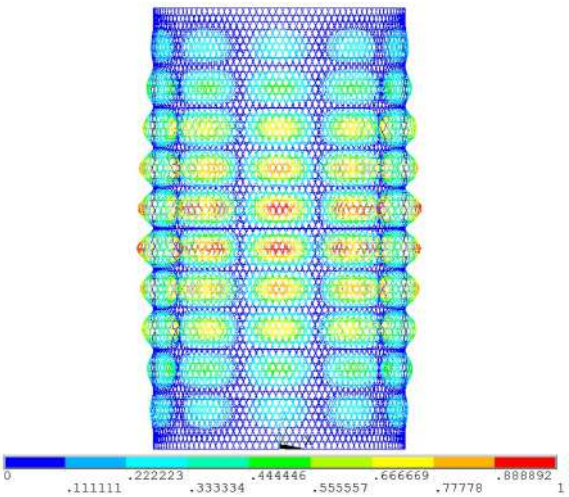

(b)

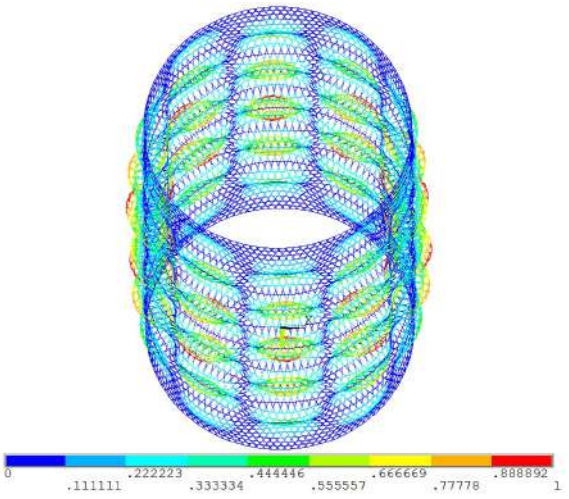

(c)

Figure 2.7: Buckling failure mode under the action of axial compression (LC1), $\lambda_1 = 1.00$.

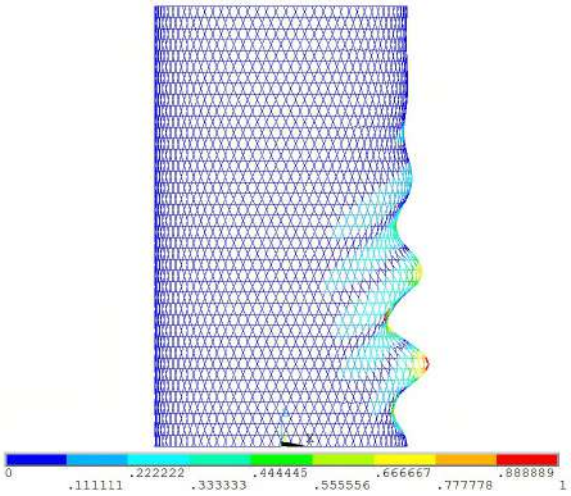

(a)

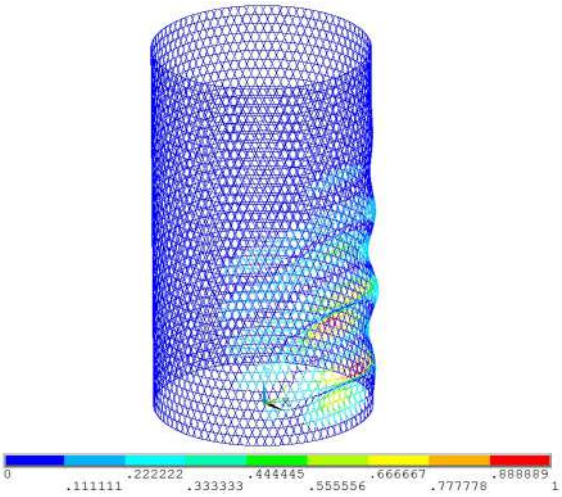

(b)

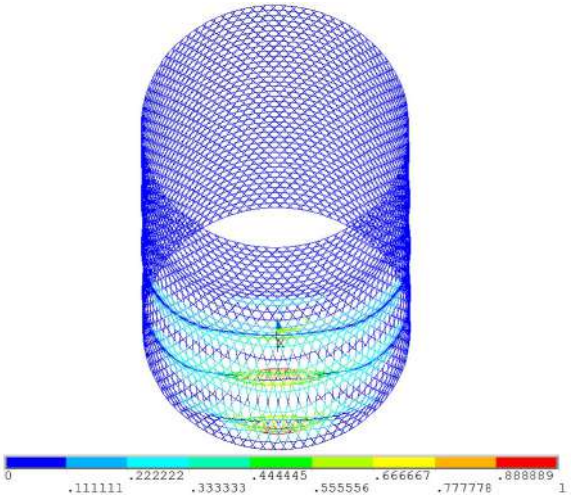

(c)

Figure 2.8: Buckling failure mode under the action of axial compression and transverse bending forces (LC2), $\lambda_1 = 1.03$.

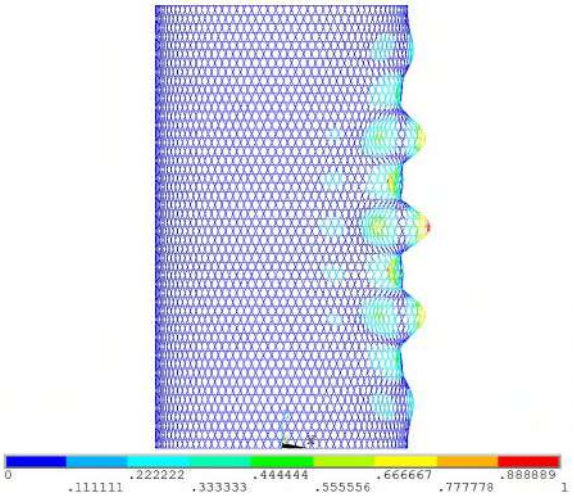

(a)

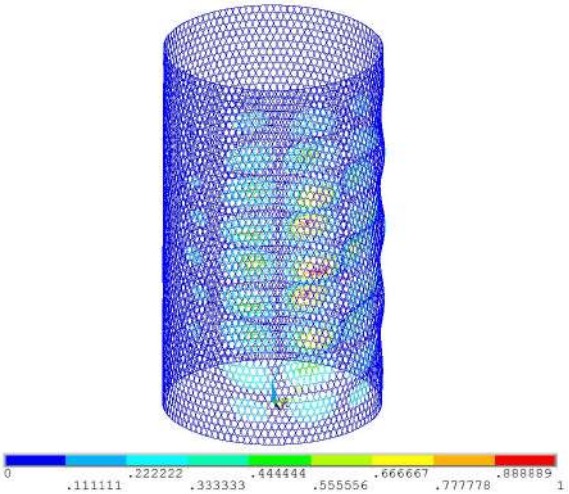

(b)

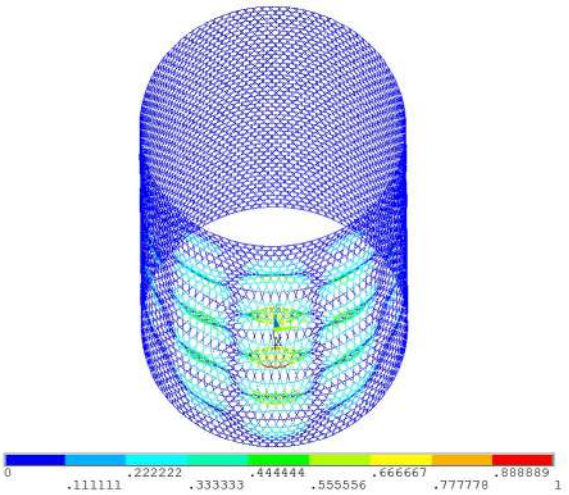

(c)

Figure 2.9: Buckling failure mode under the action of axial compression force and bending moment (LC3), $\lambda_1 = 1.01$.

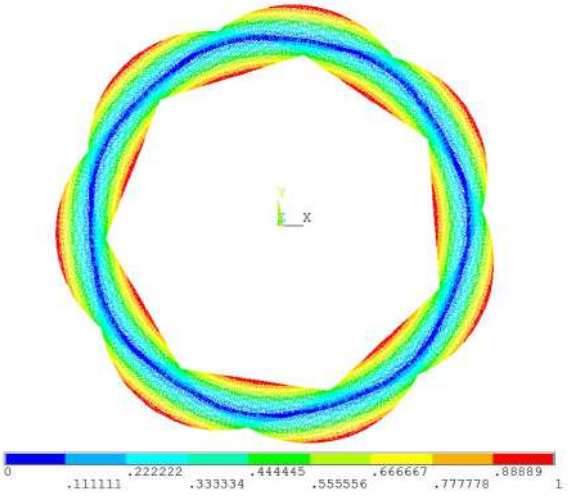

(a)

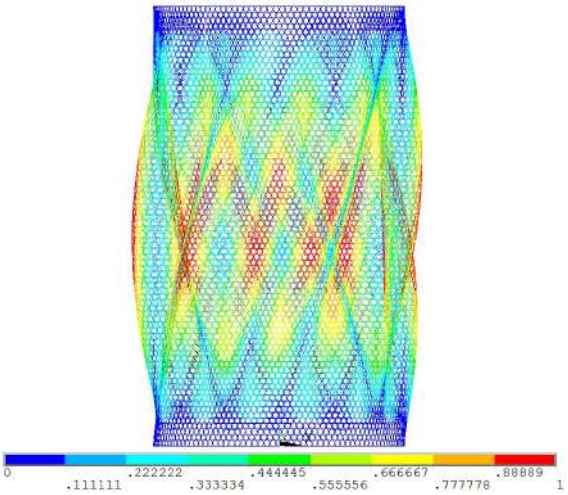

(b)

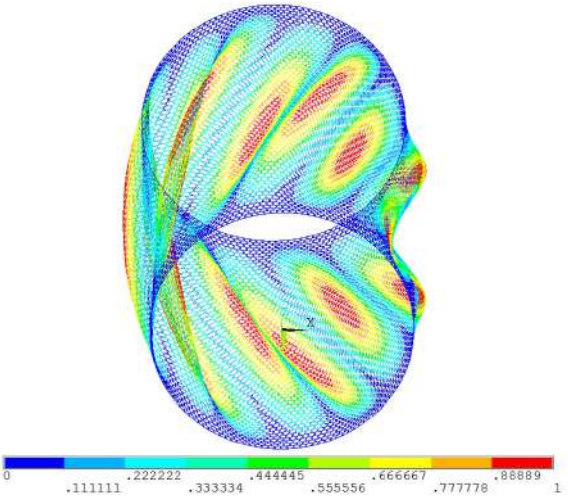

(c)

Figure 2.10: Buckling failure mode under the action of axial compression force and torque moment (LC4), $\lambda_1 = 1.01$.

2.4 Comparison between continuous and discrete approaches

The methodology of optimization based on the FE parametric modeling technique in conjunction with the genetic algorithm NSGA-II offers some advantages in respect of the continuous approaches. One of them concerns the capability of providing optimal design solutions for anisogrid lattice structures operating in conditions where different types of load act simultaneously; moreover, any stiffness requirements can be imposed to the lattice shell.

Besides, the continuous approaches present the possibility of inexactly evaluating the critical buckling load of anisogrid lattice structures because the arising of some buckling failure modes is not taken into account by these methods. This can be avoided making use of the proposed method of optimization. In order to further deepen the latter aspect, the numerical results of a sizing problem executed with both methods are presented. The most common optimization technique based on a continuous approach was chosen for this purpose: the minimization of safety factors [11].

The minimization of safety factors is an analytical procedure applicable to anisogrid lattice structures subjected to load cases involving exclusively axial compression, without stiffness requirements, to identify the minimum mass configuration. Global buckling conditions are analyzed considering a continuum shell with equivalent smeared orthotropic stiffness properties.

Because of these features of the analytical method, the anisogrid lattice structure with dimensions and material properties reported in §2.3 is investigated considering only the axial compression load $P = 11$ MN without additional stiffness constraints.

Furthermore, the minimization of safety factors considers three constraint conditions which address compressive strength of helical ribs and resistance to two buckling conditions: global buckling of the shell as a continuum media and in-plane local buckling of helical ribs segments enclosed by two subsequent nodal points, investigated with Euler formula for columns. This analytical method makes use of four variables: (I) the radial thickness h, (II) the angle that the helical ribs form with the meridian curve of the shell ϕ and two dimensionless values: (III) $\bar{\delta}_h$ and (IV) $\bar{\delta}_c$. The dimensionless variables represent the ratio of helical ribs width δ_h over their spacing a_h and the ratio of hoop ribs width δ_c over their spacing a_c, respectively. The values of the mass M of the optimal configuration and its geometrical variables obtained with this method are listed in Table 2.5.

Table 2.5: Design of the anisogrid lattice structure under axial compression with the minimization of safety factors.

M [Kg]	h [mm]	$\bar{\delta}_h$ [−]	$\bar{\delta}_c$ [−]	ϕ [°]
518.9	24.10	0.0653	0.0326	26.57

Table 2.6: Geometric parameters and finite element analysis results of the anisogrid lattice structure configurations designed under axial compression with the minimization of safety factors.

Conf.	M [Kg]	a_c [mm]	δ_h [mm]	δ_c [mm]	ϕ [°]	n_h	N	σ_{MIN} [MPa]	λ_1
(I)	519.62	134.6	7.86	4.39	26.65	93	26	349.07	0.81
(II)	519.73	112.9	6.59	3.69	26.63	111	31	348.76	0.86
(III)	519.89	97.2	5.68	3.17	26.61	129	36	348.13	0.89

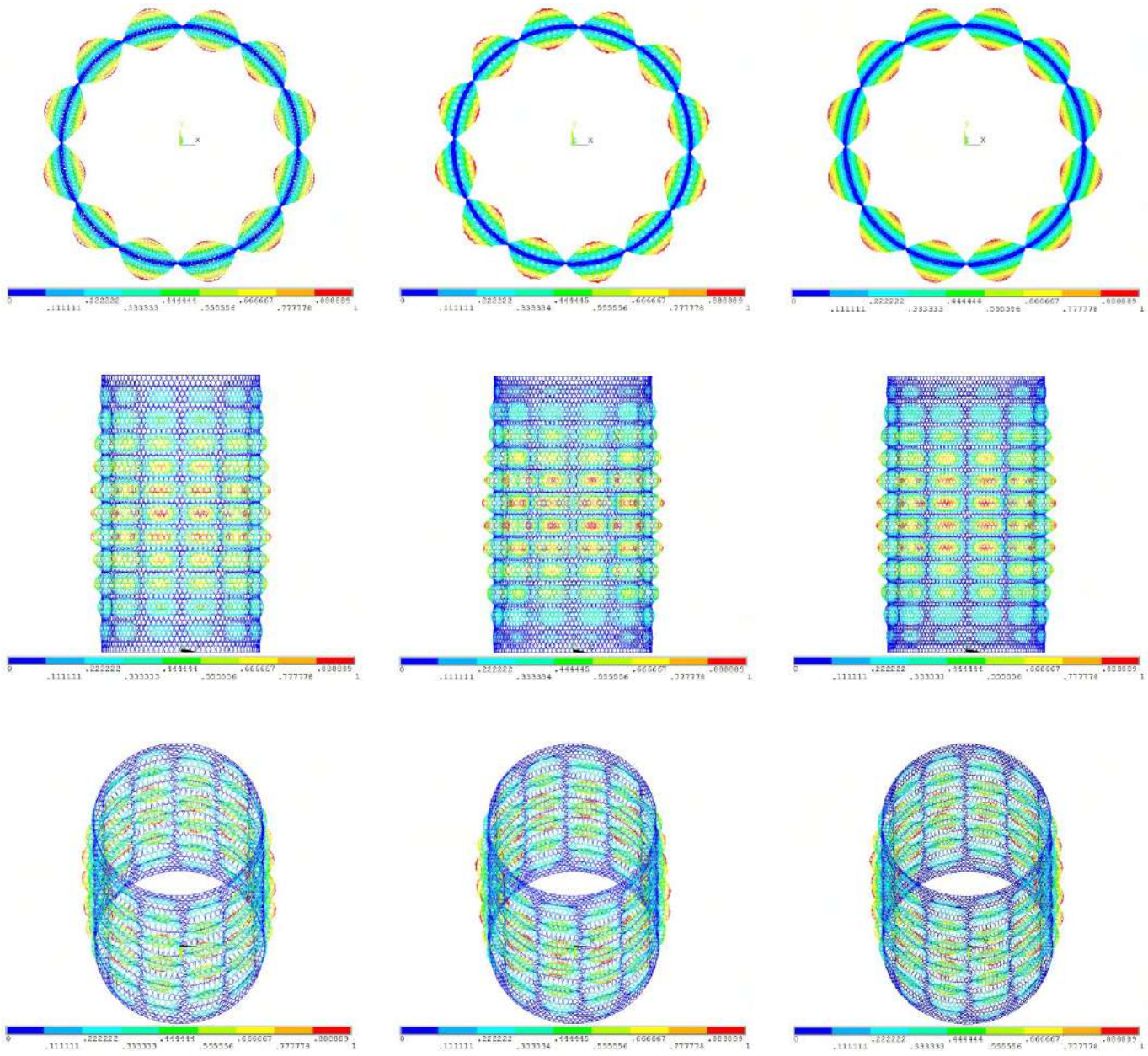

(I) (II) (III)

Figure 2.11: Buckling failure modes under axial compression of the three anisogrid lattice structure configurations designed with minimization of safety factors. (I) $\lambda_1 = 0.81$, (II) $\lambda_1 = 0.86$, (III) $\lambda_1 = 0.89$.

Table 2.7: Geometric parameters and FEA results of the anisogrid lattice structure designed under axial compression with FE parametric modeling and the NSGA-II.

M [Kg]	h [mm]	δ_h [mm]	δ_c [mm]	ϕ [°]	n_h	N	σ_{MIN} [MPa]	λ_1
525.00	26.12	4.91	3.37	31.93	121	42	417.16	1.00

Owing to the dimensionless variables, it is theoretically possible to find a set of structurally equivalent solutions with different spacings and subsequently diverse number of ribs. Then, the spacing between hoop ribs a_c and helical ribs a_h have to be established to complete the set of geometrical variables and so identify the widths of the ribs. Anyway, the two spacings are not independent, in fact $a_h = 2a_c \sin\phi$, thus it is sufficient to define one of them. In addition, the possible solutions are limited by the technological requirement of realizing an integer number of ribs.

Among the feasible configurations of the lattice shell, three of them were selected to perform the comparison with the results obtained applying the technique of optimization presented in this paper. The configurations were identified establishing a particular value of hoop ribs spacing a_c and consequently of helical ribs spacing a_h; following, the widths of the ribs cross-section were computed and are listed in Table 2.6.

Finite element models of the three chosen configurations were generated by means of the FE parametric modeling technique and the corresponding values of mass M and angle ϕ can be found in Table 2.6. The slight differences of these values with respect to the analytical ones in Table 2.5 are due to the necessary rounding of the variables and because the minimization of safety factors considers a configuration of the lattice shell delimited by the overlapping areas between helical ribs, whereas the finite element models were realized choosing the layout with extremal hoop ribs. Anyway, these differences do not influence considerably the structural behavior of the anisogrid lattice structure.

Afterwards, the three identified configurations were verified through finite element analyses (results are reported in Table 2.6) showing that the anisogrid lattice structure dimensioned with the minimization of safety factors does not resist to the applied compression load. Indeed, the lattice shells obtained from the minimization of safety factors undergoes buckling failure as their first eigenvalues λ_1, evaluated with finite element analyses, do not reach the unity.

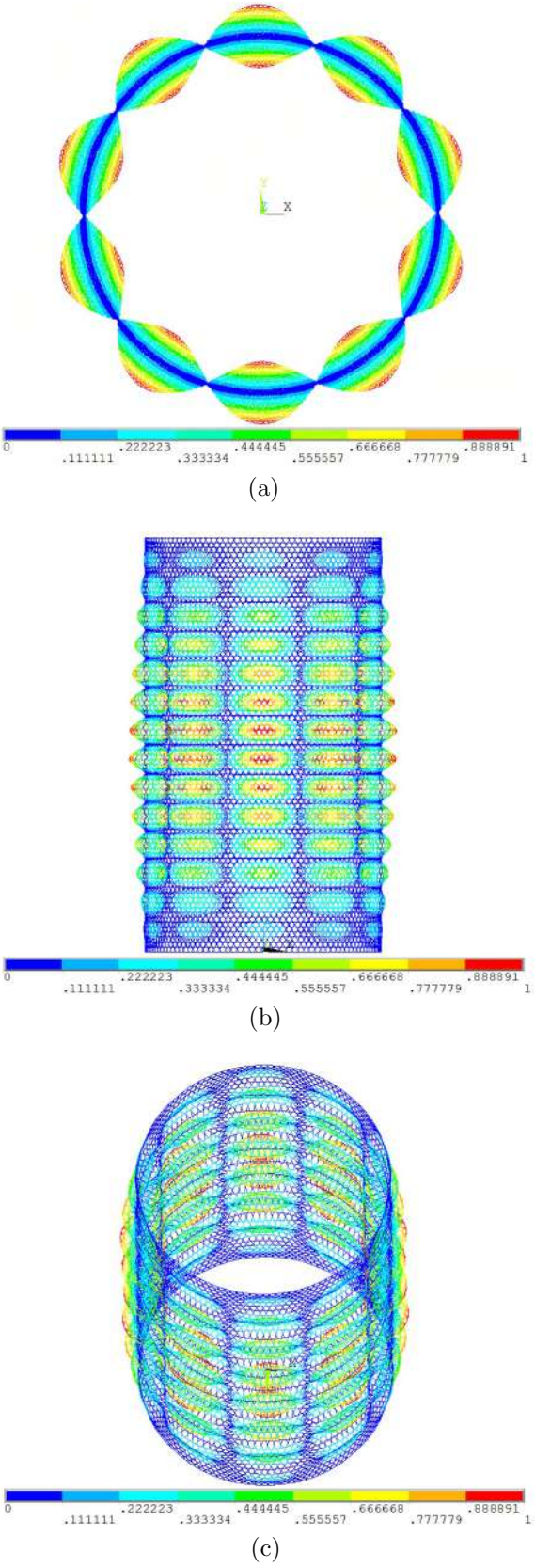

(a) (b) (c)

Figure 2.12: Buckling failure mode under axial compression of the anisogrid lattice structure designed with the FE parametric modeling and NSGA-II, $\lambda_1 = 1.00$.

The load-bearing capacity, expressed as critical buckling load, demonstrates an increase with the number of helical ribs n_h passing from the first to the third configuration. Nevertheless, the best load-bearing capacity belongs to the third configuration that buckles for an applied load of about 9.82 MN, i.e. the 10.7% under the value imposed for the design. The reason for the missed fulfillment of the instability constraint is that the buckling failure experienced by the three configurations of anisogrid lattice structure takes place by way of a mode not included in the buckling constraints of the minimization of safety factors, as shown in Fig. 2.11. For example, the third configuration presents a buckling failure mode featured by 12 series of lobes located around the lattice shell axis and each row consists of 12 lobes arranged in parallel with the lattice shell axis and their amplitude decreases moving towards the extremal hoop ribs.

The design procedure here presented was further applied to size the anisogrid lattice structure described in the previous Section without considering stiffness constraints. The lattice shell was optimized reaching a configuration with mass $M = 525.0$ Kg that satisfies the structural constraints, included the one regarding the buckling resistance. The geometrical variables of this configuration are reported in Table 2.7. The sizing was dominated by the buckling constraint, in fact the first eigenvalue λ_1 approaches the unity; instead, the safety factor for the compressive stress failure mode is 1.08. The buckling failure mode, reported in Fig. 2.12, exhibits 10 vertical series of lobes distributed on the circumference, every series is composed of 14 lobes.

Moreover, as additional comparison with the continuous approach, it should be noted that the inclination angle ϕ of the optimum identified by the genetic algorithm differs from the theoretical optimal solution being bigger than that value.

The benefits of an optimization routine with the capability of recognizing all the possible buckling modes that can occur and accordingly sizing the anisogrid lattice structure are relevant. The design solution that it provides does not call for successive adjustments of the lattice structure connected to an overrated failure resistance, this permits to find the true optimal configuration.

CHAPTER 3

DESIGN, ANALYSIS AND OPTIMIZATION OF ANISOGRID COMPOSITE LATTICE CONICAL SHELLS

The present Chapter aims to expand the methodology presented in Chapter 2 encompassing the anisogrid lattice conical shells to get a comprehensive design methodology capable of giving precise insights of the buckling behavior for every loading condition and facing all the requirements concerning the design of these structures [51]. The proposed procedure uses a complete parametric modeling of the conical configuration of the structure that has been completely coupled with an optimization technique based on the NSGA-II genetic algorithm. In this way it is possible to overcome all the limitations of the continuous approaches concerning the assessment of the buckling failure and those of the discrete approaches which accurately describe the structural behavior of the anisogrid lattice structure but that have been exploited with still limited optimization margins. Using the discrete approach to accurately evaluate the critical buckling load in the design analysis, irrespective of the particular failure mode, it is possible to perform a complete and exhaustive description of the buckling failure of anisogrid lattice structures, considering all possible buckling modes, connected to different load conditions, including those that cannot be properly described through an analytical formulation and thus reliably optimize the lattice shell.

A structural optimization procedure which takes into account the simultaneous application of different load typologies and introducing multiple stiffness constraints has been defined; the consolidated condition on axial stiffness can be added to bending and torsional stiffnesses.

The proposed procedure has been applied to some numerical examples related to actual industrial cases, considering multiple external loads and stiffness constraints applied simultaneously to the anisogrid lattice conical structure.

3.1 Parametric modeling technique

An efficient and adaptable FE parametric modeling technique for anisogrid lattice conical structures was developed in order to feed the structural response of the lattice shell to the genetic algorithm NSGA-II, setting up an optimization workflow based on the interaction between ANSYS FE software and the NSGA-II. The FE parametric model is realized with two-noded beam element having six degrees of freedom per node.

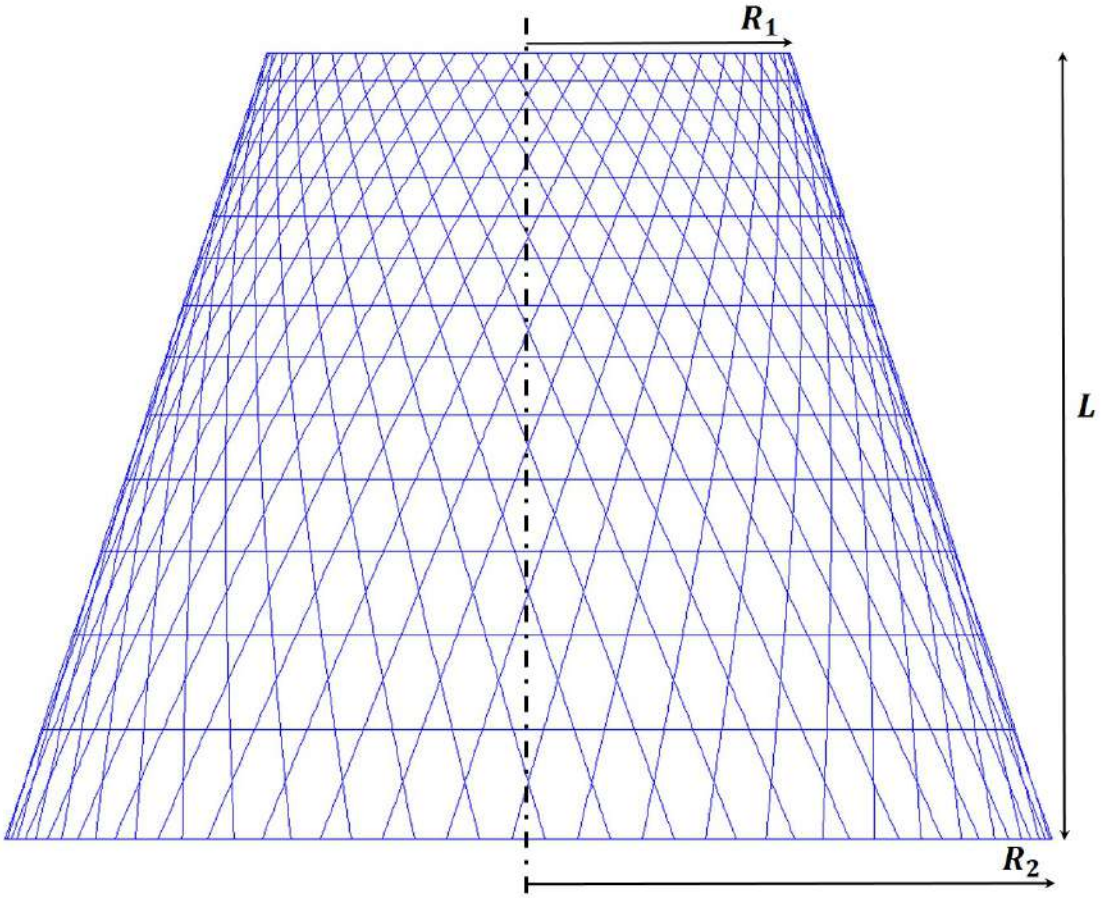

Figure 3.1: Anisogrid lattice conical structure composed of hexagonal elementary lattice cells.

For a generic design problem involving anisogrid lattice conical shells (Fig. 3.1), the global geometrical dimensions of the conical structure are defined, i.e. the smaller and the larger radii, R_1 and R_2 respectively, and the height L in conjunction with the material properties of the ribs. On the contrary, the design objective is the definition of the helical and hoop ribs arrangement, i.e. the number of ribs, as well as their cross-section dimensions.

For this purpose, five geometrical variables are used in the parametric characterization of the lattice conical shell to completely define the FE model geometry. In particular, two of them are discrete variables represented by positive and integer numbers:

- n_h the number of helical ribs with the same sense of winding;
- n_c the number of hoop ribs.

In addition, three continuous variables are needed to define the rectangular cross-section dimensions of the two typologies of ribs (Fig. 3.2a):

- h the radial thickness;
- δ_h the helical ribs width;
- δ_c the hoop ribs width.

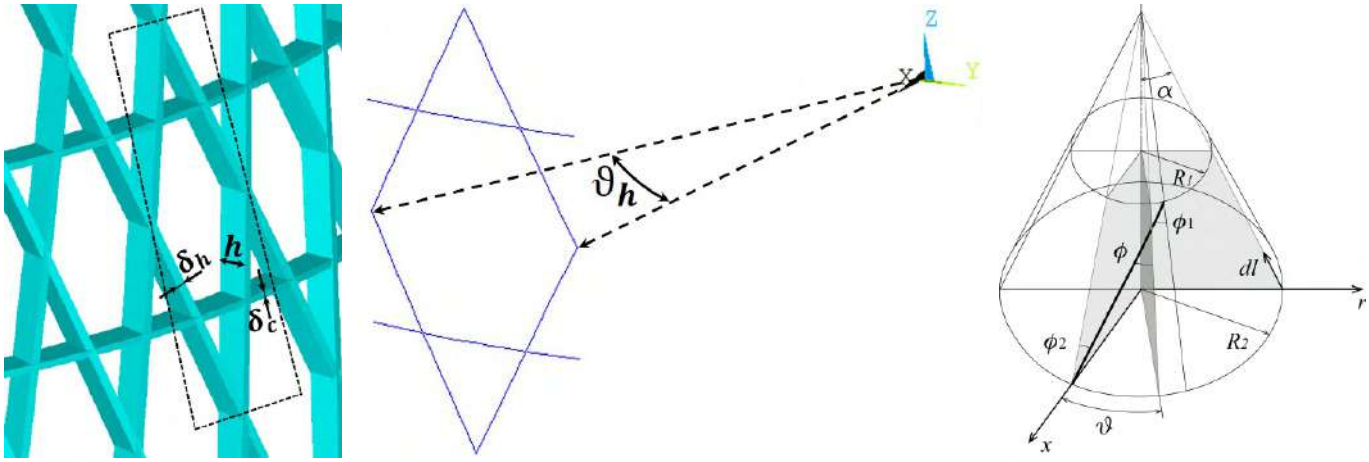

(a) (b) (c)

Figure 3.2: (a) Geometry of hexagonal elementary lattice cell. (b) Angle ϑ_h between two consecutive helical ribs intersection points. (c) Geometrical variables of the lattice conical shell.

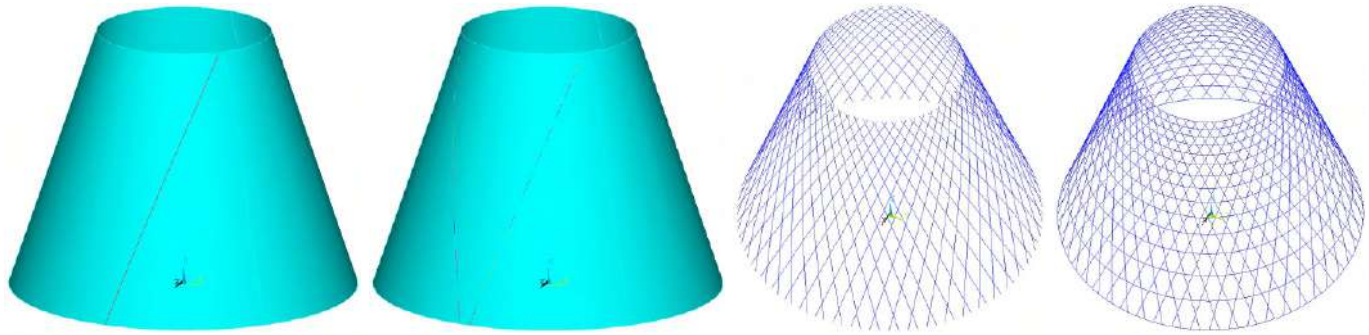

(a) (b) (c) (d)

Figure 3.3: (a) Geodetic curve on conical surface defining the helical ribs mid-line; (b) the two geodetic curves, one for every sense of winding, after cutting; (c) mesh of helical ribs; (d) complete mesh of anisogrid lattice conical structure.

During the manufacturing process, the helical ribs are realized by placing the carbon fibers along geodetic trajectories on the conical surface of the lattice shell. Consequently, the first operation carried out by the FE modeler is the analytical characterization of the helical ribs mid-line that is a geodetic curve lying on a conical surface. The equation of the geodetic curve is characterized by the specific values assigned to the geometrical variables and implemented in the FE procedure.

For the anisogrid conical structures the angle between the helical ribs and the meridian curve of the conical surface changes continuously along the helical rib mid-line. As a consequence, the elementary lattice cell does not preserve its dimensions and geometrical proportions across the structure. This makes more complex its analytical description with respect to the cylindrical case [35]. The analytical expression describing the helical rib mid-line (Fig. 3.3a) in the cylindrical coordinate system with origin at the larger end of the lattice conical shell, on the axis of symmetry, can be derived considering three geometrical relationships [98]:

$$\frac{r d\vartheta}{dl} = \tan\phi(r) \tag{3.1}$$

$$\frac{dr}{dl} = \sin\alpha \tag{3.2}$$

$$r\sin\phi(r) = C_0 \tag{3.3}$$

where, as also reported in Fig. 3.2c, r represents the generic cone radius evaluated in a plane orthogonal to the axis of the structure, ϑ is the latitude angle evaluated with respect to a reference meridian plane, $\phi(r)$ is the angle between the helical ribs mid-line and the meridian curve of the conical surface at a generic radius r, α is the cone semi-opening angle and l is a coordinate along the meridian curve. Note that Eq. (3.3) is the Clairaut Equation which is valid for a geodetic curve lying on a surface of revolution.

Taking into account Eqs. (3.1-3.3), a differential equation that relates the latitude angle ϑ and the generic radius r can be determined. This relation must be integrated to get the final expression of the helical rib mid-line:

$$\int_{\vartheta_0}^{\vartheta} d\vartheta = -\int_{R_2}^{r} \frac{C_0}{r^2\sqrt{1-\frac{C_0}{r^2}}}\frac{dr}{\sin\alpha} \tag{3.4}$$

In Eq. (3.4) ϑ_0 is the initial shift that is responsible of the anisogrid conical structure layout; in fact, the configuration with extremal hoop ribs is characterized by $\vartheta_0 = \vartheta_h/4$, where ϑ_h is the angle between two consecutive helical ribs intersection points (Fig. 3.2b), meanwhile the arrangement delimited by the overlapping areas between helical ribs has a null initial shift ϑ_0; R_2 is the larger radius of the lattice conical shell.

The final expression of the geodetic curve on conical surface, obtained integrating Eq. (3.4), and expressing the conical radius r as a function of the angle ϑ is:

$$r(\vartheta) = C_0\sqrt{\frac{2}{1+\sin\left(2\sin\alpha(\vartheta-\vartheta_0)+\arcsin\left(\frac{2C_0^2-R_2^2}{R_2^2}\right)\right)}} \tag{3.5}$$

The constant C_0 in Eq. (3.5) must be computed according to the overall geometry and the specific couple of discrete variables. In particular, it can be evaluated through Eq. (3.3) at the smaller or larger radius of the lattice conical shell where both the radius r and the inclination angle ϕ are known. The expressions for the angles between the helical rib and the meridian curve ϕ_1 and ϕ_2, at the smaller and at the larger diameter were derived by Vasiliev et al. in [20]:

$$\phi_1 = \tan^{-1}\left(\frac{R_2\sin\gamma}{R_2\cos\gamma - R_1}\right) \tag{3.6}$$

$$\phi_2 = \phi_1 - \gamma \tag{3.7}$$

where $\gamma = \pi \sin \alpha \frac{n_c - 1}{n_h}$.

Once Eq. (3.5) has been particularized for the specific anisogrid conical structure under design, the FE parametric procedure draws two helical rib mid-line, one for every sense of winding on the conical surface, realizing a set of geometrical points which are then interpolated by means of spline curves. The next operation requires the execution of a series of cuts, performed with geometrical planes orthogonal to the lattice structure axis, needed to manage the mesh generation; this operation provides nodes in correspondence of the intersection points between two helical ribs and between a helical rib and a hoop rib (Fig. 3.3b).

Afterwards, the proper cross-section features are assigned to the lines obtained cutting the two helical ribs mid-line and copied n_h times around the lattice shell axis (Fig. 3.3c). Additionally, the characteristic twist of the helical rib's cross-section alongside its mid-line is achieved acting on the the beam element's third node that regulates its coordinate system orientation with respect to the the global one.

To complete the FE model, n_c circumferences are drawn in correspondence to the hoop ribs position, each one composed of circular segments that can be enclosed between two geometrical points of intersection with helical ribs determined with the cut series. Following, the FE procedure meshes the hoop ribs curves completing the anisogrid lattice conical structure mesh as reported in Fig. 3.3d. When the model generation phase is complete the overall mass M can be easily evaluated.

3.2 Optimization workflow based on NSGA-II genetic algorithm

The proposed design methodology consists in an automatic workflow capable of determining the optimal structural configuration, ensuring the validity of a fixed number of requirements, of anisogrid lattice conical structures exploiting an FE software equipped with the aforementioned FE parametric procedure. FE analyses are executed in conjunction with the NSGA-II genetic algorithm [99], also available in many optimization commercial software packages. In particular, NSGA-II is an elitist nondominated sorting-based genetic algorithm and no training is necessary for its application. This algorithm is suitable to manage with constrained single or multi-objective optimization problems involving discrete and continuous variables. Hereinafter, it is employed for single-objective analyses requiring mass minimization and the verification of structural and stiffness constraints.

Any sample analyzed by the FE software must fulfill four constraints whose validity is checked by the NSGA-II to be accepted as a possible solution; the constraints are expressed as the following inequalities:

- (I) Material compressive strength

$$\sigma_{MIN} \leq \sigma_0^C;$$

- (II) Material tensile strength

$$\sigma_{MAX} \leq \sigma_0^T;$$

- (III) Buckling resistance

$$\lambda_1 \geq 1;$$

- (IV) Minimum level of stiffnesses

$$S_i \geq S_i^{MIN}.$$

According to the constraints (I) and (II), they deal with the static strength of the anisogrid lattice conical structure, i.e. the action of external loads must not provoke the ribs material failure. Specifically, these conditions state that the highest compressive and tensile stresses, σ_{MIN} and σ_{MAX} respectively, must not exceed the material compressive and traction strengths (σ_0^C and σ_0^T). The stress criterion utilized to verify the ribs static strength is the maximum stress criterion because it deals with mono-directionally reinforced material [1]. The stresses σ_{MIN} and σ_{MAX} are given by the combined action of the axial and bending stresses and they are evaluated alongside the ribs trajectories, i.e. along the axis of the beam elements which constitute the lattice structure. The stress evaluation is performed not taking into account local effects connected to constraint and load conditions. On the contrary, the analytical approaches neglect the material failure caused by the tensile stress state and exclusively admit the compressive stress as responsible of the static failure [1, 12].

Additionally, in general, the anisogrid structures mainly undergo compression loads that are responsible of a compression stress state in the helical ribs, meanwhile the hoop ribs are subjected to a traction stress state. The traction stress state acting in the hoop ribs considerably prevents the occurrence of the buckling failure since it contributes to preserve the original circular cross-section of the structure, being reason of the substantial buckling strength featured by the anisogrid structures.

In order to assure the structural strength, the resistance to the buckling onset is further considered by means of the constraint (III). In particular, the requirement is formulated stating that the first eigenvalue λ_1 obtained by finite element eigenvalue buckling analysis must be greater or equal to one. Consequently, exploiting the discrete approach, the formulation of this constraint is achieved regardless a specific buckling failure mode, i.e. it is as generic as possible, since it embraces all buckling modes that the anisogrid lattice structure can experience.

This specific expression of the buckling resistance constraint overcomes the limits of the buckling strength prediction capability proper of the analytical approaches, which account for a limit set of possible critical buckling modes as responsible of the structure failure. This hypothesis affects the prediction of the critical buckling load and consequently the integrity of the overall structure, as outlined in [35]. In fact, on the one hand the analytical approaches analyze the anisogrid lattice structure as a continuum media through the introduction of equivalent smeared stiffness properties, i.e. it is supposed to behave as an orthotropic shell which undergoes global buckling failure. Likewise, the overall structure is considered as a three-dimensional frame which can fail because of local instability. However, the anisogrid lattice structure frequently undergoes buckling modes other than those expected by the analytical approaches; these modes are associated with its dual features that are a combination of the shell and beam-framework ones. As a consequence, this simplified estimation of the buckling failure may result in overestimated assessment of the critical buckling load and subsequently provide a design of the structure that miss the conformity with the buckling resistance requirement.

Furthermore, the optimization workflow can also manage functional constraints, which do not concern the structural integrity, such as those related to stiffness requirements. Indeed, anisogrid

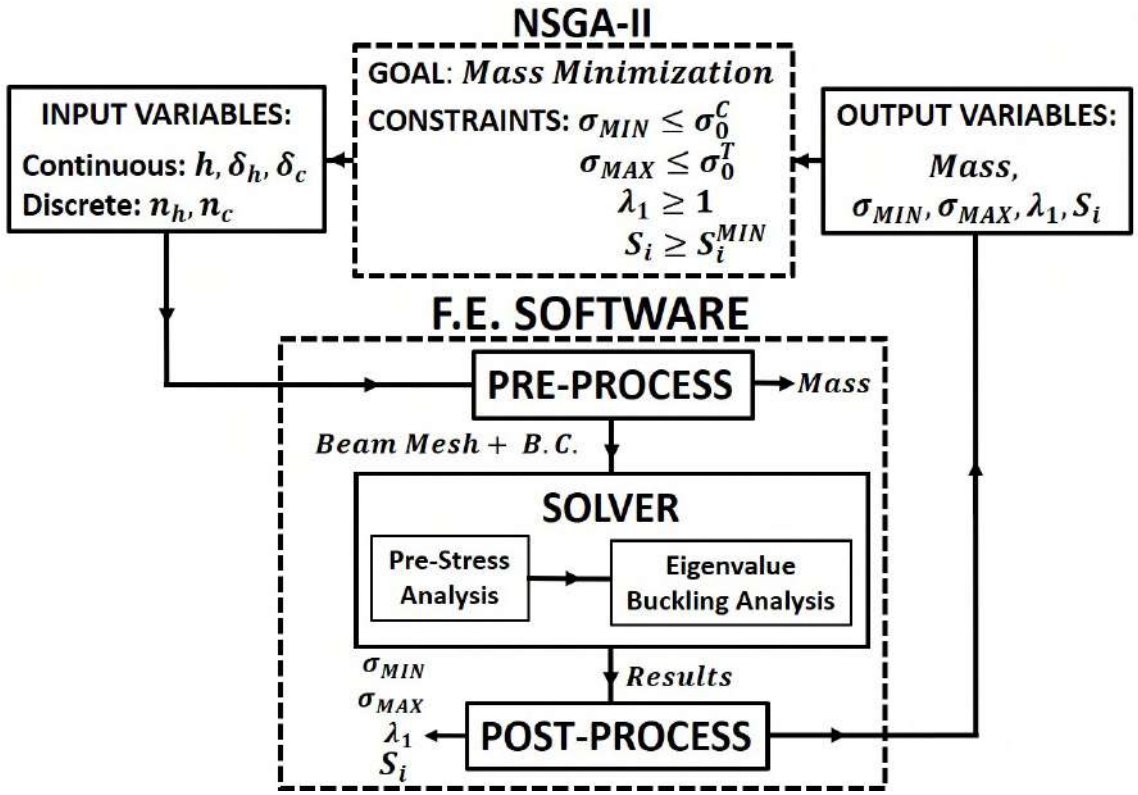

Figure 3.4: Logical workflow of the optimization procedure based on the finite element method coupled with the genetic algorithm NSGA-II.

lattice structure must commonly feature controlled levels of stiffness, especially when it is a crucial part of a particular application.

The optimal solution identified by the NSGA-II is determined within the design space that is defined through the imposition of minimum and maximum values of the five variables needed to completely define a configuration of the anisogrid lattice structure.

Moreover, the genetic algorithm is supplied with a design of experiments (DOE): the algorithm analyzes an initial population of samples, selected in the design space, to estimate the structural behavior of the anisogrid lattice structure and start the automatic process of samples generation aimed at the search of the optimum. The initial population of samples is determined by means of the Uniform Latin-Hypercube DOE technique [97] that furnishes a uniform and random distribution of samples in the design space.

Fig. 3.4 outlines the logical workflow employed for the optimization process of anisogrid lattice structures, that is iteratively repeated during the overall analysis. At the beginning of every computing loop, the genetic algorithm NSGA-II defines a set of geometrical variables that is transmitted to the finite element code by means of an input file. Then, the FE software executes the analysis: the pre-processor generates the FE model according to the procedure described in §3.1 and evaluates the mass M of the structure. Then, the bottom hoop rib of the FE model is clamped and a set of rigid links (shown in Table 3.1), connecting the nodes belonging to the upper extremal hoop rib to the one present in its geometrical center, where external loads are applied, is realized.

The successive step consists in the finite element eigenvalue buckling analysis and the output

variables, i.e. anisogrid lattice structure mass M, highest compressive stress σ_{MIN}, highest tensile stress σ_{MAX}, first eigenvalue λ_1 and stiffness values S_i, are reported in an output file. Afterwards, the computing loop is closed providing the output file to the genetic algorithm. The NSGA-II verifies the fulfillment of the constraints and identifies the set of input variables for the next iteration; the optimization process ends when the predefined number of samples to be analyzed has been reached. The configuration of anisogrid lattice structure featuring the lowest mass amount and satisfying all the required constraints is the optimal solution.

Table 3.1: The four load cases and their loading conditions and stiffness constraints.

Load Case 1 (LC1)	**Load Case 2 (LC2)**	**Load Case 3 (LC3)**	**Load Case 4 (LC4)**
Loading Conditions			
Axial Compression	Axial Compression Transverse Bending Force	Axial Compression Bending Moment	Axial Compression Torque Moment
Stiffness Constraints			
Axial Stiffness	Axial Stiffness Transverse Bending Stiffness	Axial Stiffness Bending Stiffness	Axial Stiffness Torsional Stiffness
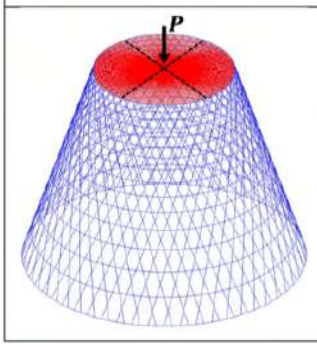	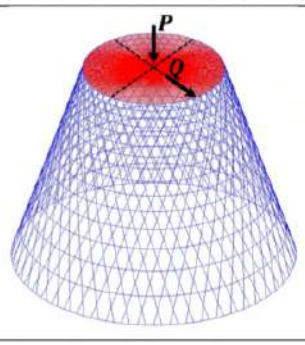	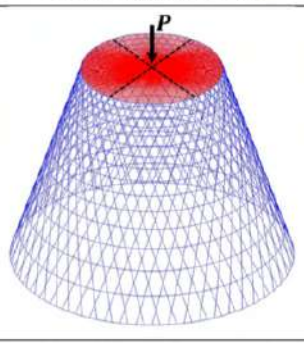	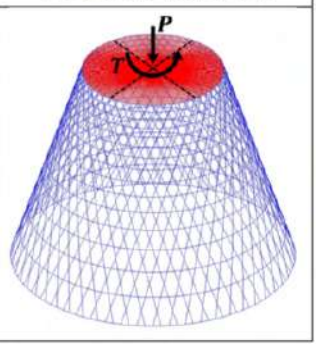

3.3 Results

The results hereinafter presented regard optimization analyses of an anisogrid lattice conical structure featuring hexagonal elementary lattice cells and delimited by extremal hoop ribs. The geometrical characteristics are: small radius $R_1 = 0.5$ m, large radius $R_2 = 1$ m and height $L = 1.5$ m. The unidirectional composite ribs are made of epoxy matrix and carbon fiber directed as the ribs, the composite material properties are: Young modulus $E = 100$ GPa, compressive strength $\sigma_0^C = 450$ MPa, tensile strength $\sigma_0^T = 600$ MPa and mass density $\rho = 1,500$ Kg/m^3. Furthermore, being the material properties highly dependent on the manufacturing process, the ribs were modeled with isotropic material for simulation purposes. As remarked in [15, 38], the use of isotropic constitutive law is an acceptable approximation. ribs Young Modulus is that evaluated along the ribs trajectories, which can be determined by means of experimental tests on specimens extracted from the overall structure.

The present Section reports some case-studies in order to exhibit the efficiency and the accuracy of the optimal design methodology here presented. The numerical examples involve the optimal

design of anisogrid lattice conical structures in operating conditions, i.e. experiencing, simultaneously, different load typologies and stiffness constraints. The four load cases analyzed are listed and graphically represented in in Table 3.1. The first one concerns the action of an axial compression load and, in addition, a requirement on the axial stiffness must be satisfied. Next, the subsequent case-studies are defined superimposing one load condition and stiffness constraint at a time to the first load case.

The analyses are performed in a broad design space to prove the effectiveness and the capabilities of the genetic algorithm NSGA-II. The design space is obtained fixing the minimum and maximum values of the geometrical variables that are listed in Table 3.2.

Table 3.2: Range variation of problem variables defining the design space.

	h [mm]	δ_h [mm]	δ_c [mm]	n_h [−]	n_c [−]
MIN	7.00	2.30	2.30	15	5
MAX	25.00	17.00	17.00	65	30

Table 3.3: Geometric parameters and finite element analysis results of the anisogrid lattice conical structure designed for the four load cases considered.

	U.o.M.	Load Case 1	Load Case 2	Load Case 3	Load Case 4
M	[Kg]	42.54	49.35	58.75	58.34
h	[mm]	18.95	20.18	18.94	22.56
δ_h	[mm]	6.22	8.71	15.92	15.12
δ_c	[mm]	4.86	3.10	3.37	3.75
n_h	[−]	55	48	36	31
n_c	[−]	16	15	10	9
σ_{MIN}	[MPa]	373.84	449.98	423.05	449.96
σ_{MAX}	[MPa]	205.03	426.17	548.00	428.31
λ_1	[−]	1.00	1.03	1.16	1.16
u_z^{MAX}	[mm]	6.12	5.17	3.81	3.93
S_A	[MN/m]	572.05	676.65	917.89	890.93
u_x^{MAX}	[mm]		4.94		
S_{TB}	[MN/m]		101.31		
rot_y^{MAX}	[rad]			$3.85 \cdot 10^{-3}$	
S_B	[MNm/rad]			130.03	
rot_z^{MAX}	[rad]				$1.39 \cdot 10^{-2}$
S_T	[MNm/rad]				72.02

3.3.1 Compression axial load and axial stiffness constraint (LC1)

This load case requires the design of an anisogrid lattice conical structure, with the dimensions and the material properties previously assigned, to sustain the axial compressive load $P = 3.5$ MN. Additionally, the design must present a minimum axial stiffness $S_A = 550$ MN/m, intended as the ratio between the external load P and the maximum axial displacement in the z direction u_z^{MAX} experienced by the upper hoop rib of the lattice shell. The loading values represent typical design target in aerospace applications.

The application of the optimization methodology, which exploits the FE parametric modeling technique and the genetic algorithm NSGA-II, determined a minimum mass design satisfying the structural and the stiffness constraints. The optimal design characteristics in terms of geometric variables and structural performance are reported in Table 3.3.

The most heavy requirements for the sizing resulted to be the buckling and the stiffness ones: the first eigenvalue reached the unity and the axial stiffness of the lattice shell is slightly higher than the required value, whereas the failure modes related to the ribs static strength were not critical for the design; indeed the safety factor for the compressive strength is 1.20 and the one for the tensile strength is 2.93.

The anisogrid lattice shell fails because of a buckling failure mode which presents 8 lobes alternatively oriented inward and outward with respect to the lattice shell curvature (Fig. 3.5). The lobes are located in the lower portion of the lattice shell, above the larger extremal hoop rib. Moreover, a second series of circularly disposed lobes, featuring a less pronounced amplitude, is present over the principal one.

3.3.2 Transverse bending force and transverse bending stiffness constraint (LC2)

The present case-study is set up adding a transverse bending force $Q = 0.5$ MN to the compression load condition earlier analyzed; the transverse bending force acts along the x axis of the model and is applied to the upper extremal end of the lattice shell. Additionally, a transverse bending stiffness constraint must be satisfied as well as the axial one, a minimum value of $S_{TB} = 100$ MN/m is requested. This last stiffness value is computed through the ratio of the transverse bending force Q and the maximum displacement alongside its direction of application, i.e. u_x^{MAX}.

The optimization analysis performed by means of the NSGA-II allowed to find out the design parameters reported in Table 3.3. The action of the two external loads, along with the second stiffness requirement, asked for a mass increase of 16.01%.

According to ribs cross-section dimensions, the thickness h and helical ribs width δ_h are greater than those of the preceding sizing, meanwhile hoop ribs width δ_c is decreased. Moreover, the number of helical ribs n_h is reduced and the number of hoop ribs n_c is almost unchanged.

Three constraints turned out to be a driver for the sizing of the anisogrid structure: once again the buckling failure one, since λ_1 is very close to the unity, the maximum compressive stress σ_{MIN} nearly reached its threshold value and, similarly, the transverse bending stiffness S_{TB} is very close to the minimum required value. Contrariwise, the other conditions were not stringent: the safety factor for the tensile strength is 1.41 (it is higher than the previous load case) and the axial stiffness S_A is 23.03 % higher than the minimum value.

The buckling failure mode of the anisogrid lattice structure is shown in Fig. 3.6; the collapse of the lattice shell takes place in the central zone of the structure, where the compression stress state provoked by the axial force is superimposed to the one due to the transverse bending force Q.

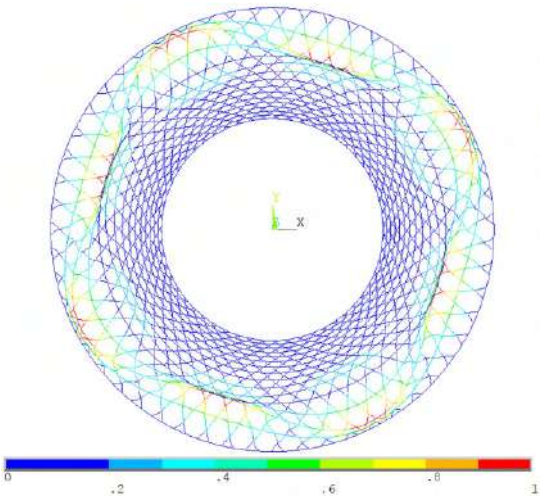

(a)

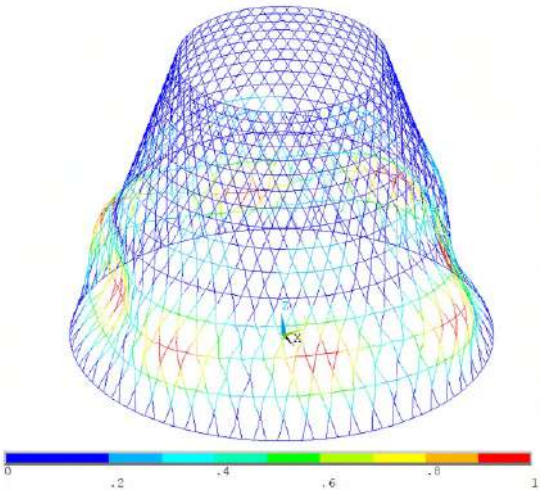

(b)

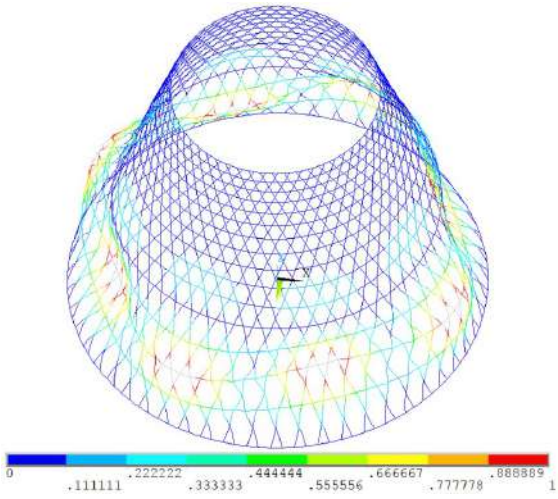

(c)

Figure 3.5: Buckling failure mode for axial compression load case (LC1), $\lambda_1 = 1.00$.

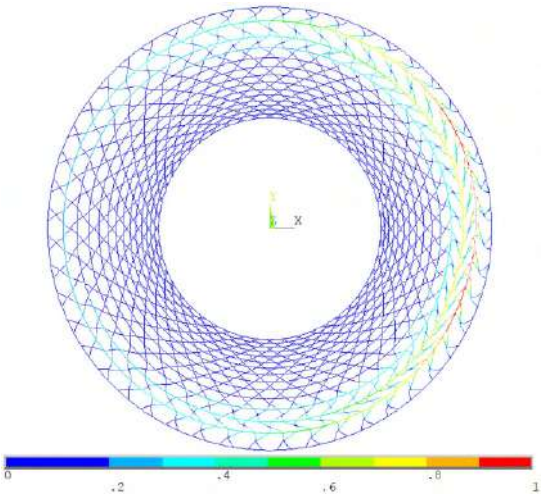

(a)

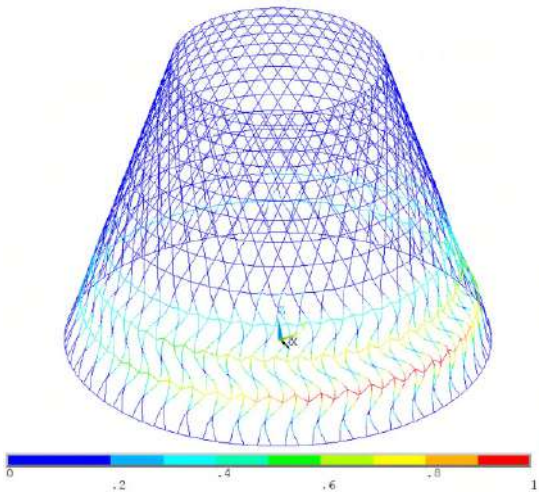

(b)

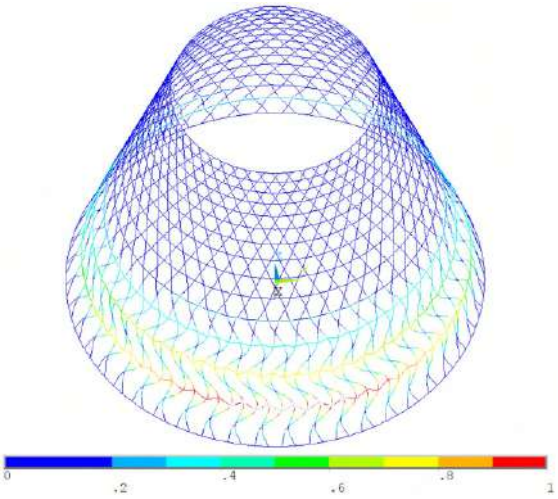

(c)

Figure 3.6: Buckling failure mode for load case (LC2) with combination of axial compression and transverse bending forces , $\lambda_1 = 1.03$.

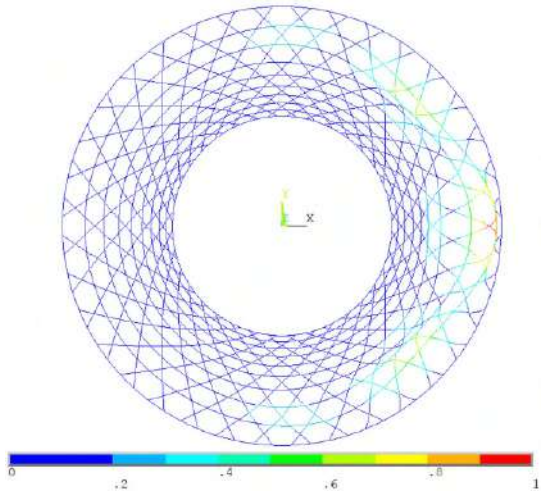

(a)

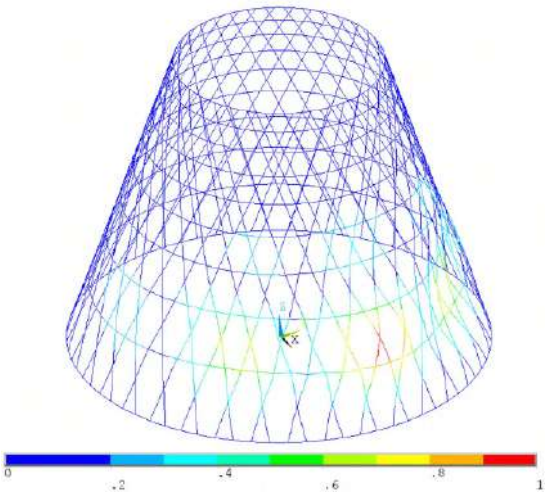

(b)

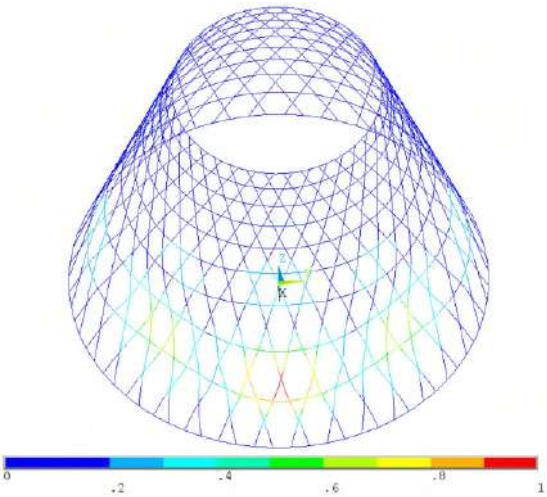

(c)

Figure 3.7: Buckling failure mode for load case (LC3) with combination of axial compression and bending moment, $\lambda_1 = 1.16$.

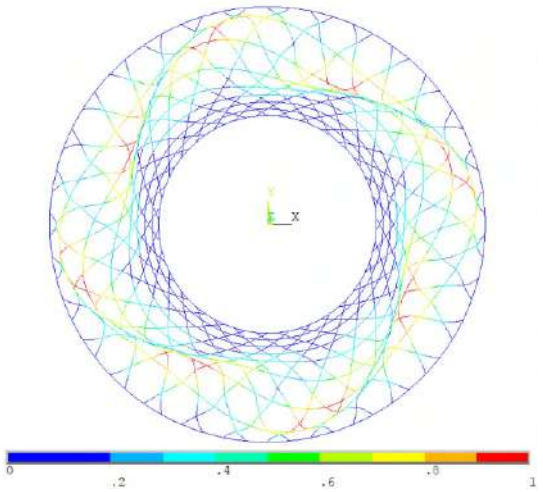

(a)

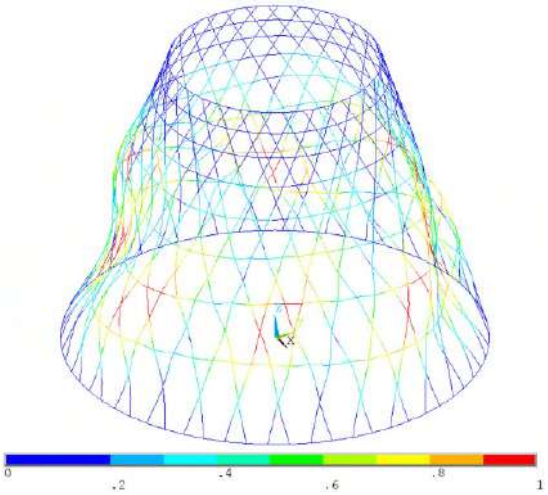

(b)

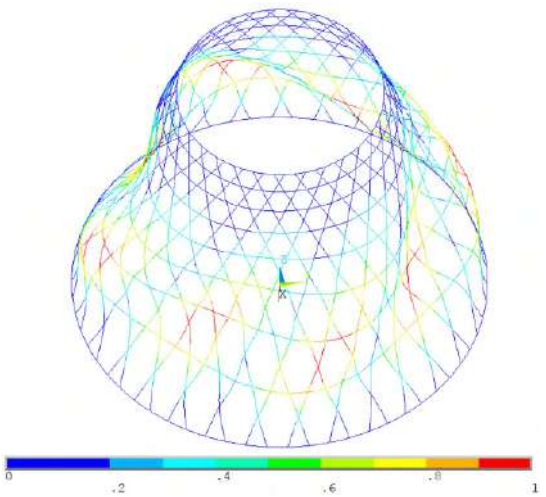

(c)

Figure 3.8: Buckling failure mode for load case (LC4) with combination of axial compression and torque moment, $\lambda_1 = 1.16$.

In particular, the instability causes the rotation of both helical and hoop ribs in the tangential plane and it does not induce any radial displacement. Anyway, the buckling occurrence is circumscribed to a region close to the larger diameter, as for the previous load case.

3.3.3 Bending moment and bending stiffness constraint (LC3)

In this case-study, the bending moment $M = 0.5$ MNm is applied to the top of the lattice shell, along the y axis of the model, to enlarge the basic compression load case beforehand discussed. Likewise, a second stiffness constraint is further imposed demanding a minimum bending stiffness $S_B = 130$ MNm/rad; it is defined as ratio of the bending moment and the resulting angle of rotation rot_y^{MAX} undergone by the upper cross-section of the anisogrid lattice structure.

Table 3.3 presents the outcomes of the optimization performed with the proposed procedure. Compared to the first case-study involving only axial compression force and axial stiffness constraint, the presence of the double external load and stiffness constraints increases the mass by 38.11%. Furthermore, the value of the thickness h did not considerably change, helical ribs width δ_h is greater than the one of the first sizing, while hoop ribs width δ_c is reduced; both discrete variables are decreased.

The most strictly verified constraint condition is the bending stiffness one, indeed the optimal lattice shell features a value correlated to this property just over the minimum. The other requirements are more amply fulfilled: the compressive strength presents a safety factor of 1.06, the tensile strength a safety factor of 1.09 and the axial stiffness is abundantly greater than the imposed minimum value. The buckling failure is not critical for this sizing being the first eigenvalue λ_1=1.16.

Because of the mixed loading condition, the buckling failure occurs in the half of the anisogrid lattice conical structure where the bending moment establishes a compression stress state of the helical ribs, as shown in Fig. 3.7. The buckling mode is characterized by three lobes: one of them directed outward, with respect to the lattice shell curvature, and two inward.

3.3.4 Torque moment and torsional stiffness constraint (LC4)

The anisogrid lattice structure undergoes the action of the axial compression force and of the torque moment $T = 1$ MNm along the z axis of the model. Moreover, the stiffness constraint concerning axial stiffness was considered together with a requirement on torsional stiffness: a requested minimum value of $S_T = 70$ MNm/rad was defined. The torsional stiffness is evaluated dividing the torque moment T by the rotation rot_z^{MAX} of the upper extremal end about the axis of the lattice shell.

The results of the optimization process are reported in Table 3.3. The mass of the lattice shell increases of 37.14 % with respect to the baseline configuration of the first load case. Concerning to ribs cross-section dimensions: the thickness h and helical ribs width δ_h are greater than those of the simple compression load case, while hoop ribs width δ_c decreased; besides, both discrete variables n_h and N are reduced.

The maximum compressive stress σ_{MIN} experienced an intensification by reason of the superposition of the axial force and the torque moment, so that it approaches the strength limit. Conversely, the tensile strength is not stringent for this design being the safety factor for this failure mode 1.40; similarly, the first eigenvalue is λ_1=1.16. Once again, the axial stiffness constraint is largely verified.

The combined action of the axial and the torsional loads makes the anisogrid lattice conical structure to buckle according to a buckling failure mode, reported in Fig. 3.8, characterized by 8

oblique stretched lobes alternatively oriented inward and outward with respect to the lattice shell curvature.

3.4 Comparison between continuous and discrete approaches

The proposed optimization methodology, founded on the FE parametric modeling technique and the genetic algorithm NSGA-II, was compared with a widely employed continuous approach is hereinafter reported, in order to show its benefits with respect to the continuous approaches. The most common optimization technique, based on a continuous approach, was chosen for this purpose: the minimization of safety factors [98], which represents an analytical procedure devoted to the optimal design of conical anisogrid lattice structures. This methodology can be only employed for the axial compression load case, without stiffness requirements, to identify the minimum mass configuration. Furthermore, the minimization of safety factors considers three constraint conditions which address compressive strength of helical ribs and resistance to two buckling conditions: global buckling of the shell as a continuum media and in-plane local buckling of helical ribs segments enclosed by two subsequent nodal points. A comparative study between the two optimal design methods was already set up in [35] in case of cylindrical lattice structures.

Because of these features of the analytical method, the conical anisogrid lattice structure with dimensions and material properties reported in §3.3 is investigated considering only the axial compression load $P = 3.5$ MN without additional stiffness constraints.

The minimization of safety factors makes use of dimensionless variables for the design of the conical anisogrid lattice structure. As a consequence, a set of structurally equivalent solutions with different number of ribs is theoretically determined: three of them were selected to execute the comparative study with the outcomes of the optimization methodology presented in this paper.

Subsequently, FE models of the three chosen configurations were generated by means of the FE parametric modeling technique and they were verified through finite element analyses (geometrical characteristics and results are reported in Table 3.4) showing that the conical anisogrid lattice structure dimensioned with the minimization of safety factors does not resist to the applied compression load: the conical lattice shells obtained from the minimization of safety factors undergoes buckling failure as their first eigenvalues λ_1, evaluated with finite element analyses, do not reach the unity. In addition, even the requirements concerning the static strength of the ribs turn out to be unfulfilled, since the values σ_{MIN} and σ_{MAX} determined through FE analyses overcome the static strengths in compression and traction, respectively. This behavior can be explained considering that the FE analysis can take into account the effect of the combined traction and bending stress, meanwhile the analytical model evaluates exclusively the effect of axial stress.

As regards the load-bearing capacity, expressed as critical buckling load, it does not demonstrate a particular correlation with the number of helical or hoop ribs. Nevertheless, the best load-bearing

Table 3.4: Geometric parameters and finite element analysis results of the conical anisogrid lattice structure configurations designed under axial compression with the minimization of safety factors.

Conf.	M [Kg]	h [mm]	δ_h [mm]	δ_c [mm]	ϕ_2 [°]	n_h [−]	n_c [−]	σ_{MIN} [MPa]	σ_{MAX} [MPa]	λ_1
(I)	34.58	16.37	9.02	4.40	19.75	35	15	590.43	615.55	0.71
(II)	34.70	16.32	6.61	3.32	19.60	48	20	583.44	583.09	0.72
(III)	34.78	16.29	5.22	2.66	19.51	61	25	559.07	564.37	0.67

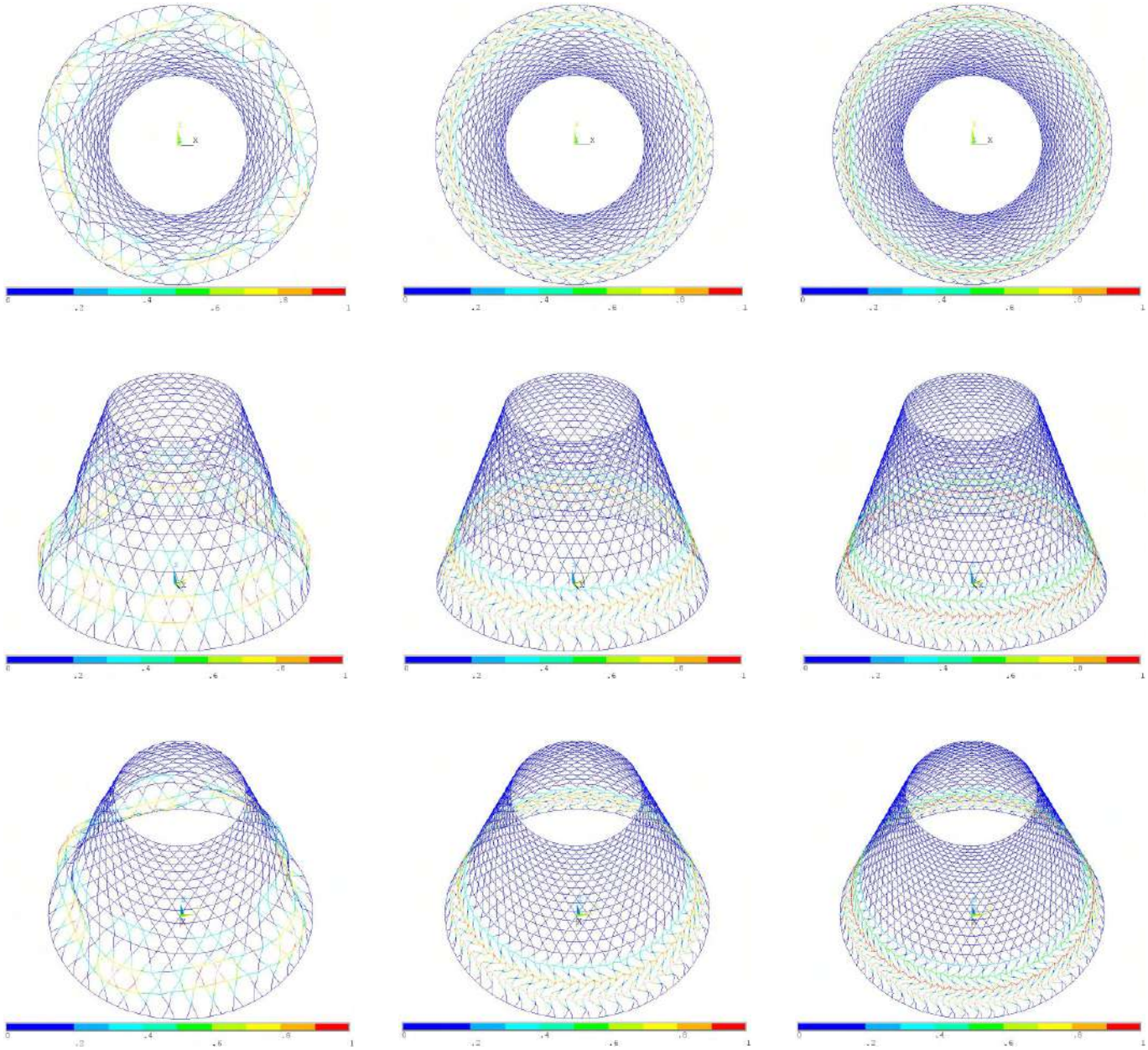

(I) (II) (III)

Figure 3.9: Buckling failure modes under axial compression of the three conical anisogrid lattice structure configurations designed with minimization of safety factors. (I) $\lambda_1 = 0.71$, (II) $\lambda_1 = 0.72$, (III) $\lambda_1 = 0.67$.

Table 3.5: Geometric parameters and finite element analysis results of the conical anisogrid lattice structure designed under axial compression with FE parametric modeling and the NSGA-II.

M [Kg]	h [mm]	δ_h [mm]	δ_c [mm]	ϕ_2 [°]	n_h [−]	n_c [−]	σ_{MIN} [MPa]	σ_{MAX} [MPa]	λ_1
39.87	16.35	7.19	2.89	17.64	55	20	449.86	495.86	1.00

capacity belongs to the configuration (II) that buckles for an applied load of about 2.51 MN, i.e. the 28.3% under the value imposed by the design requirement.

Furthermore, as shown in Fig. 3.9, the configuration (I) presents a buckling failure mode featured by a main series of 8 lobes located around the lattice shell, in the area close to larger diameter of the structure; whereas the configurations (II) and (III) buckle according to a mode consisting in the lateral deflection of both helical and hoop ribs in the tangential plane.

Additionally, the optimization procedure based on FE parametric modeling was employed to size the conical anisogrid lattice structure described in §3.3 without considering stiffness constraints. The optimum configuration of the conical lattice shell features a mass $M = 39.87$ Kg that satisfies the structural constraints. The geometrical variables of this configuration and its analysis outcomes are reported in Table 3.5.

The optimal design was driven by both the buckling constraint, the first eigenvalue λ_1 reaches the unity, and by the compressive static strength since the safety factor for this failure mode is 1. Conversely, the safety factor for the traction stress failure mode is 1.21. The buckling failure mode, reported in Fig. 3.10, exhibits the lateral deflection of the helical and hoop ribs in the lower area of the conical anisogrid lattice structure, above the largest cross-section, without any radial displacement.

Furthermore, as additional comparison with the continuous approach, it should be noted that the inclination angle ϕ_2 of the optimum identified by the genetic algorithm differs from the theoretical optimal solution being smaller than that value; on the other hand, the radial thickness h is very similar and the number of hoop ribs n_c is the same of the mostly buckling resistant configuration designed with the minimization of safety factors. The benefits of an optimization routine with the capability of recognizing all the possible buckling modes that can occur, of accurately assessing the stress acting in the ribs and of accordingly sizing the conical anisogrid lattice structure,

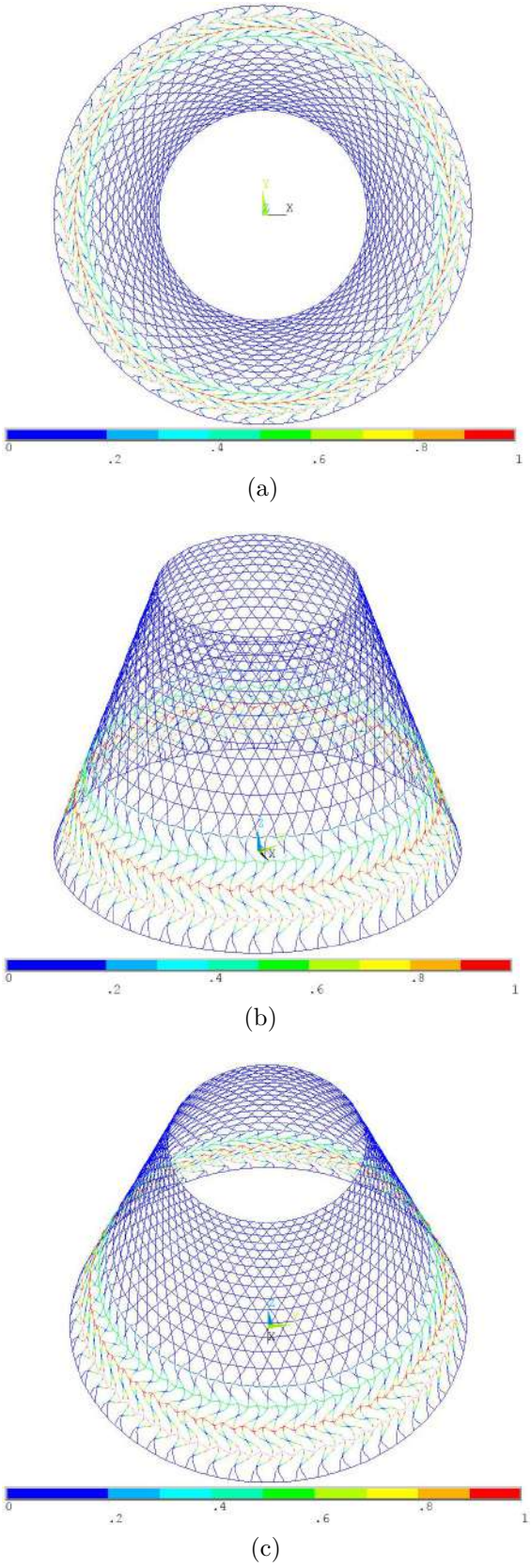

(a)

(b)

(c)

Figure 3.10: Buckling failure mode under axial compression of the conical anisogrid lattice structure designed with the FE parametric modeling and NSGA-II, $\lambda_1 = 1.00$.

are relevant. The design solution that it provides does not call for successive adjustments of the conical lattice structure connected to an overrated failure resistance, this permits to find the true optimal configuration.

CHAPTER 4

DEFINITION OF EQUIPMENT FOR EXPERIMENTAL TESTS

The relevant dimensions of the anisogrid lattice structures, in reference to the most widespread testing machines, make really demanding the execution of an experimental test on a complete lattice shell because of the high loads involved. This aspect represents a further issue to be considered in the sizing and testing of an anisogrid structure. Subsequently, the set up of an experimental campaign on limited portions of the anisogrid structure, i.e. panels cut out from the entire lattice shell, represents a valid alternative capable of returning meaningful results, useful to drive the overall design. Moreover, a description of the experimental results cannot be provided in this Thesis because of their industrial relevance.

Considering the structural design of a conical anisogrid lattice structure for interstage application, the project presents the necessity of joining the lattice shell to the launcher rocket motors; in this perspective, aluminum flanges connected to the anisogrid end rings and the motors by means of bolted joints can be employed as shown in Fig. 4.1. In particular, the aluminum flanges consist in aluminum rings that grab the composite end-rings of the anisogrid structure. The flanges are realized in two components: as regards the flange for the larger diameter, for example, the principal part of the flange is inserted in the anisogrid structure and the second part of the flange, composed of eight angular sectors, is mounted to enclose the composite end-ring between the two components of the flange. Bolted joints are utilized to fasten the flanges and the composite end-rings together; i.e. considering that the bolts connect three elements of different material, double-lap hybrid bolted joints are determined.

Consequently, in this order of ideas, conical anisogrid lattice panels can be extracted from a complete manufactured lattice shell to be tested. In particular, it can be particularly relevant to set up a experimental campaign for the following category of panels:

- **Short panels**; the short panels are cut out from the overall structure in areas adjacent to the lattice shell lower and upper end rings, including both a part of anisogrid structures and a part of aluminum flanges, in order to obtain an assessment of the structure behavior in the area neighboring the bolted joints; the CAD model of the resulting lower and upper short models are shown in Fig. 4.2(a) and Fig. 4.2(b), respectively.

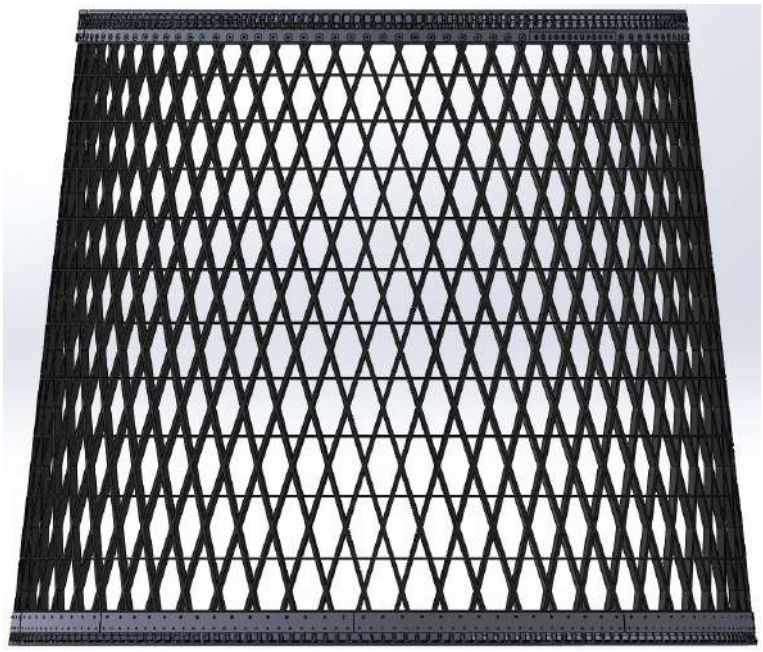

(a)

(b)

Figure 4.1: (a) Front view and (b) prospective view of conical anisogrid lattice structure with aluminum flanges.

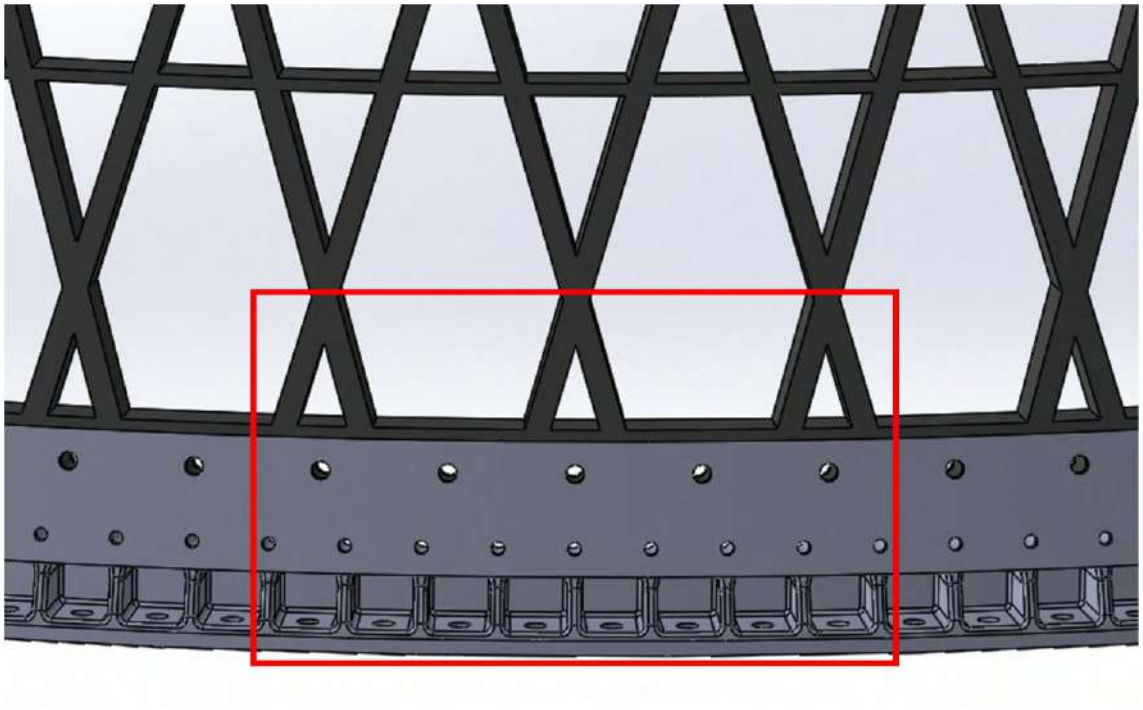

(a)

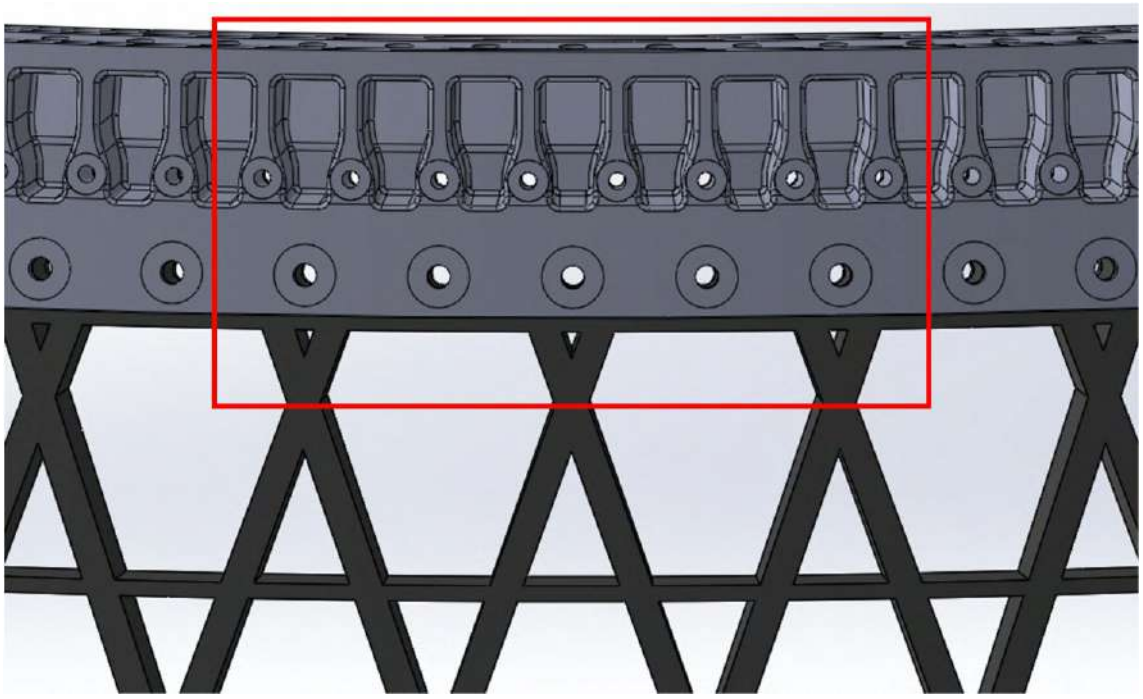

(b)

Figure 4.2: (a) Lower short panel and (b) upper short panel cut out from the conical lattice structure and the aluminum flanges.

- **Large panels**; on the other hand, it is likewise an important issue to execute tests on large panels (Fig. 4.3) comprising a significant height and angular portion of the anisogrid structure so as to achieve a reliable estimation of the global structure resistance along with an evaluation of the manufacturing process quality.

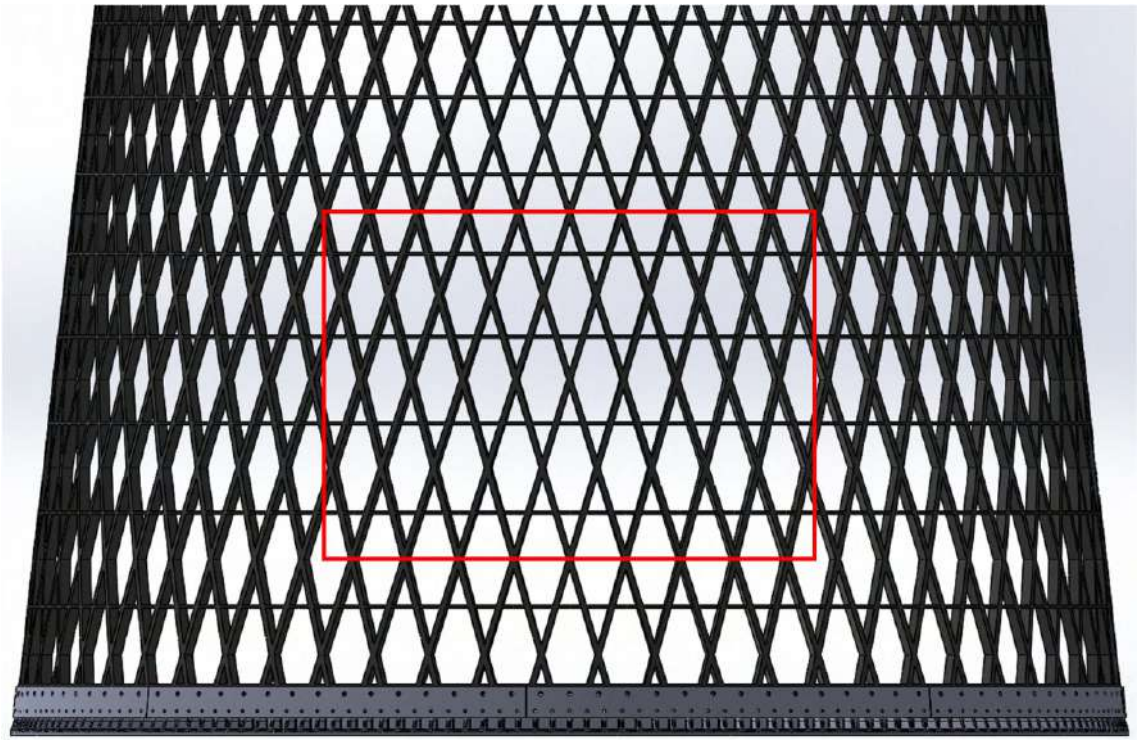

Figure 4.3: Large panel cut out from the conical anisogrid lattice structure.

Moreover, if the panel is inclined with respect to the axis of the structure of the cone semi-opening angle, during the application of the testing compression force, bending effects are induced on the panel so that the results of the experimental tests are altered. Thus, specific fixing equipment to mount the panels in the testing machine must be realized with the aim of annulling the slope proper of the conical lattice shell. In this way the panel can be tested through the application of pure membrane compression force, excluding the action of bending moments. The fixing equipment must not alter the experimental test results, thus they must feature a higher stiffness with respect to the one of the anisogrid panels and the aluminum flanges. This issue is solved through the employment of steel fixing equipment that are more stiffer of both the composite material and the aluminum.

4.1 Fixing equipment for short panels

Aiming to exclude bending moments acting on the short panels during the experimental campaign, obtaining the execution of pure compression tests in both the short and large configurations, a suitable fixing equipment fulfilling the function of interface with the testing machine must be designed. In fact, the portion of the flanges where the composite end-rings are placed presents the same slope of the cone semi-opening angle in order to allow the assembly between the flanges and the composite end-rings, as outlined in Fig. 4.4.

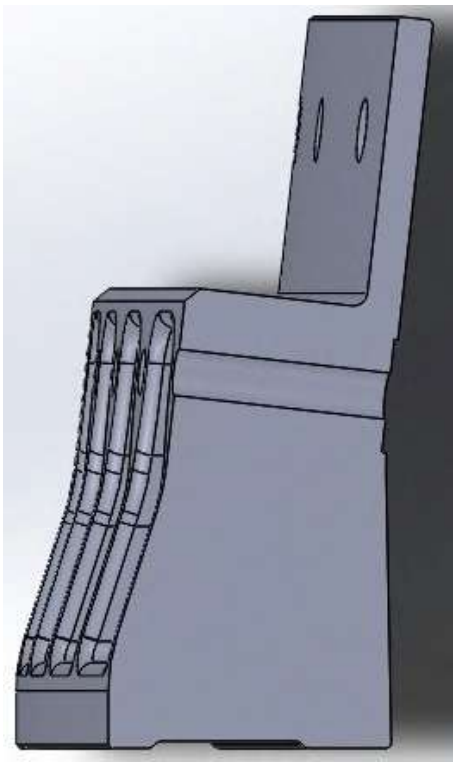

Figure 4.4: Section view of the lower aluminum flange.

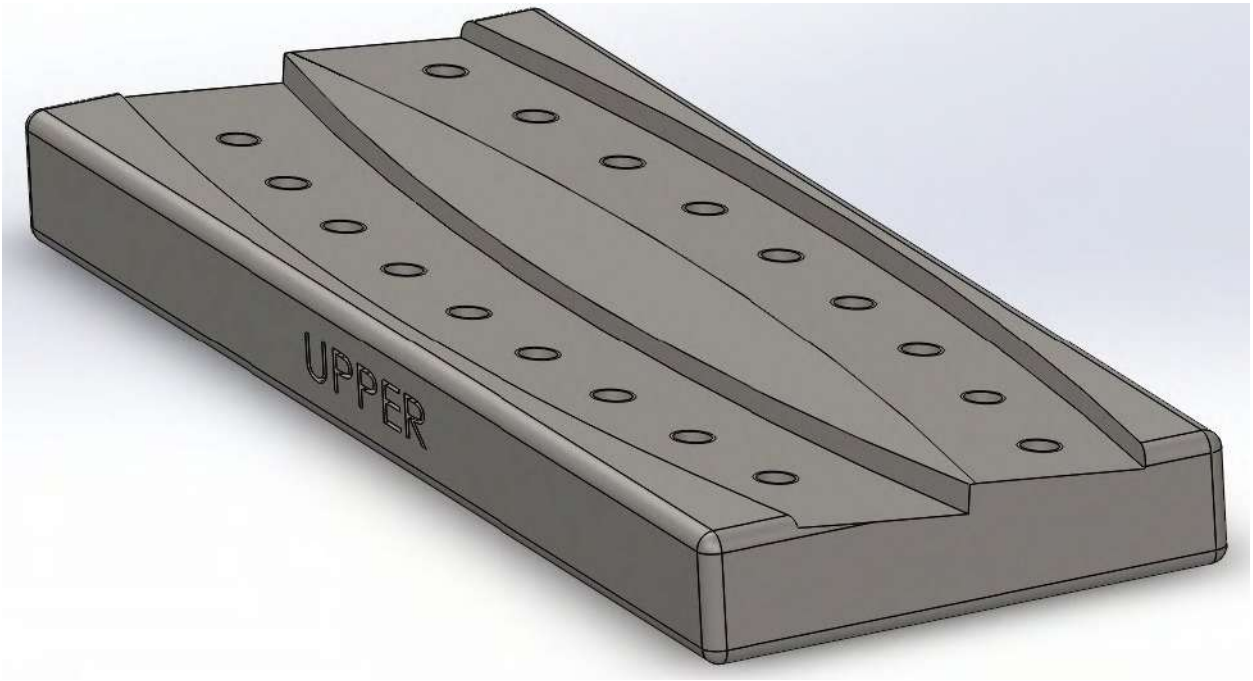

Figure 4.5: CAD model of the fixing equipment for the short panels compression test featuring the grooves for both the lower and upper configurations.

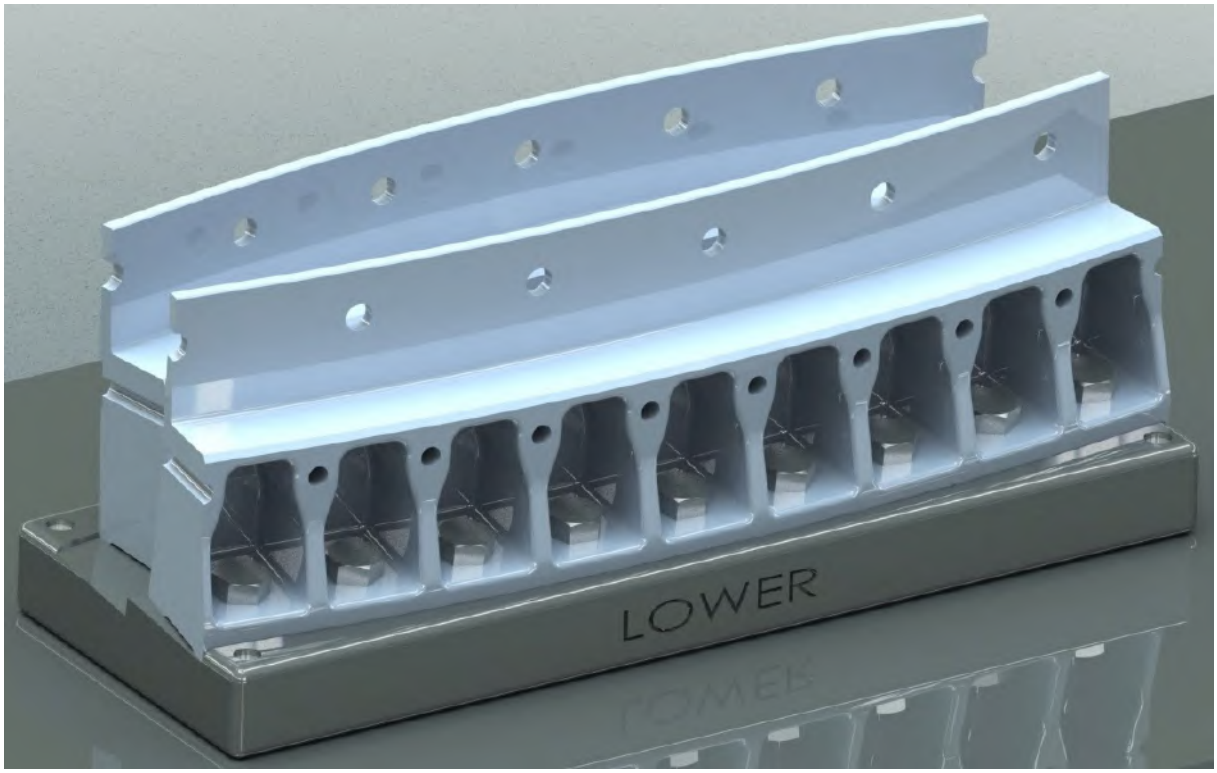

(a)

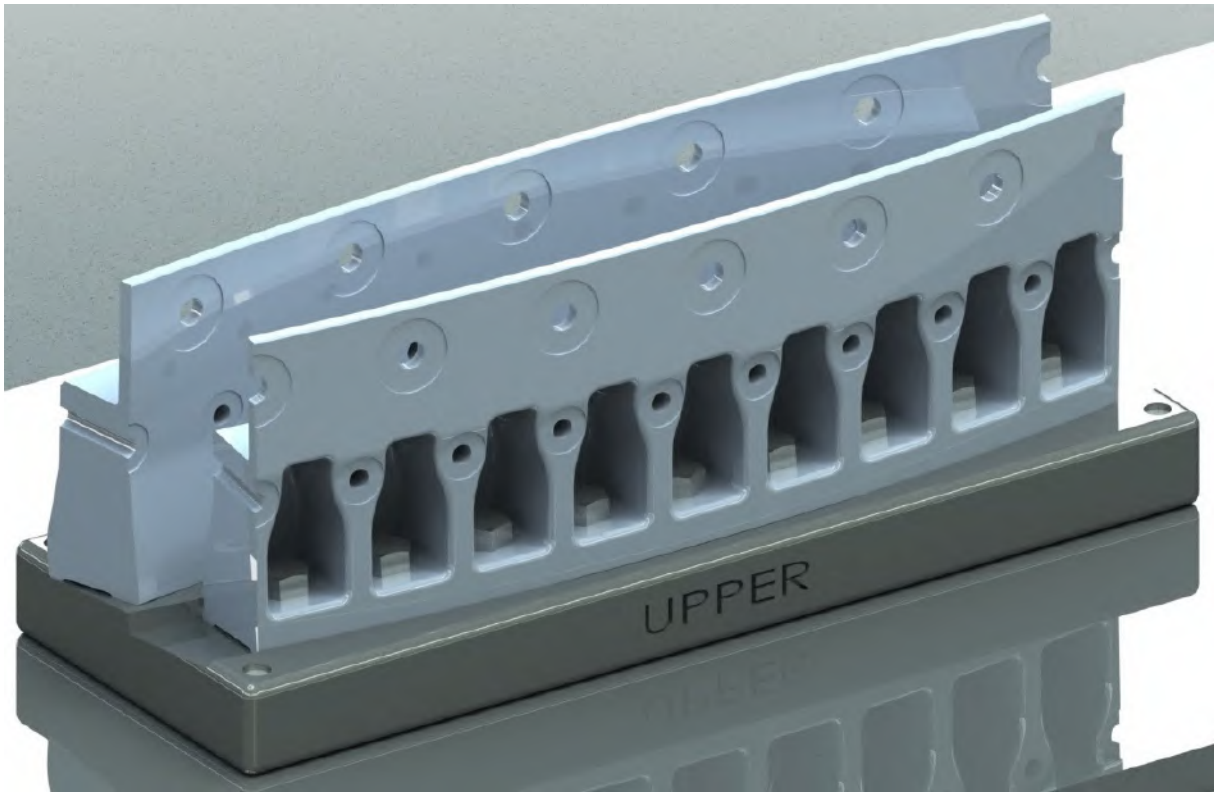

(b)

Figure 4.6: Rendering of the fixing equipment for short panels and of the lower (a) and upper (b) flanges.

The proposed design to preserve the cost-effectiveness and practical usefulness in the realization of the fixing equipment regards a single equipment for both the panel configurations. It is provided with two properly designed grooves, in which the lower and the upper short panels are hold during the tests, so that they can undergo an in-axis external load, without the occurrence of bending moments that can alter the failure mode and therefore nullify the benefits of the experimental tests.

Furthermore, the fixing equipment is realized by milling a steel bulk in order to obtain the grooves for the fastening of the two configurations of short panel. The CAD model of the fixing equipment previously described is reported in Fig. 4.5, whereas Fig. 4.6 shows the rendering of the aluminum flanges of the lower and upper panels assembled on the fixing equipment.

4.2 Fixing equipment for large panels

As previously described, the large panels are cut out from the conical anisogrid lattice structure in an area not adjacent to the aluminum flanges and they are tested exploiting specific fixing equipment, Fig. 4.7. Large panels feature bigger size with respect to short panels since their objective is the assessment of the anisogrid structure mechanical resistance, whereas the short panels scope is the evaluation of the interaction with the aluminum flanges.

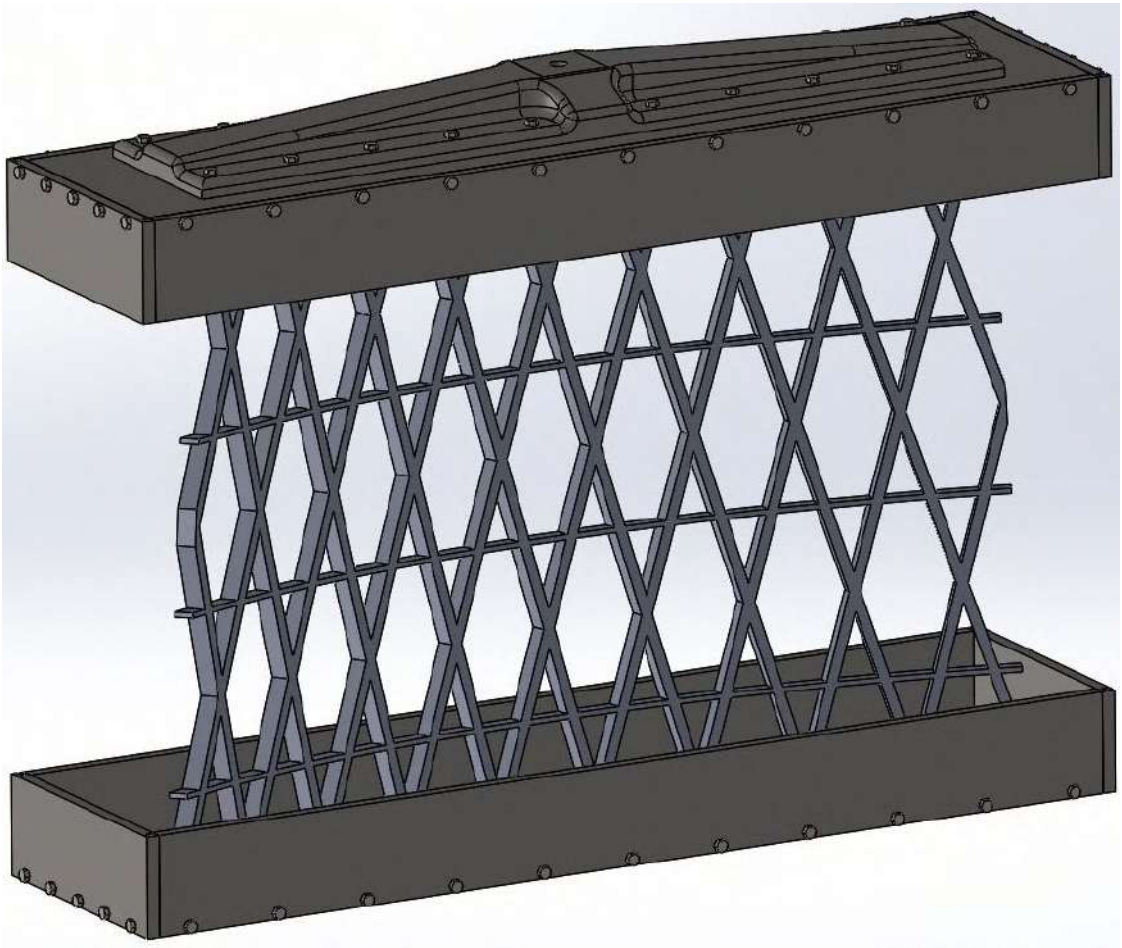

Figure 4.7: CAD model of large panel and relative fixing equipment.

Besides, the testing of large panels is needed to avoid compression tests of the entire conical anisogrid lattice structure and, as a consequence, the necessity of analyzing a wide and significant portion of lattice shell arises. Even in this case the problematic of excluding bending effects is present and more relevant as the larger dimension of the panels can be responsible of higher eccentricity of the external load and, consequently, of unwanted bending moments on the panels which alter the failure mode. In this case, the problematic is avoided through the couples of cuts needed to realize the large panels: the first two cuts are geometrically realized by means of two meridian planes; the second couple of cuts is executed perpendicularly with respect to the meridian line of the conical anisogrid lattice structure. These last cuts allow to regain the semi-opening angle of the large panel when it is positioned along the vertical direction.

Additionally, properly designed fixing equipment must be realized so that the direction of the external load passes through the center of gravity of the large panel. The fixing equipment consists in two concave supports where the large panels are inserted, Fig. 4.8; then, the supports are filled up with resin capable of polymerize at ambient temperature. The upper concave support presents an interface specific for the load cell of the testing machine.

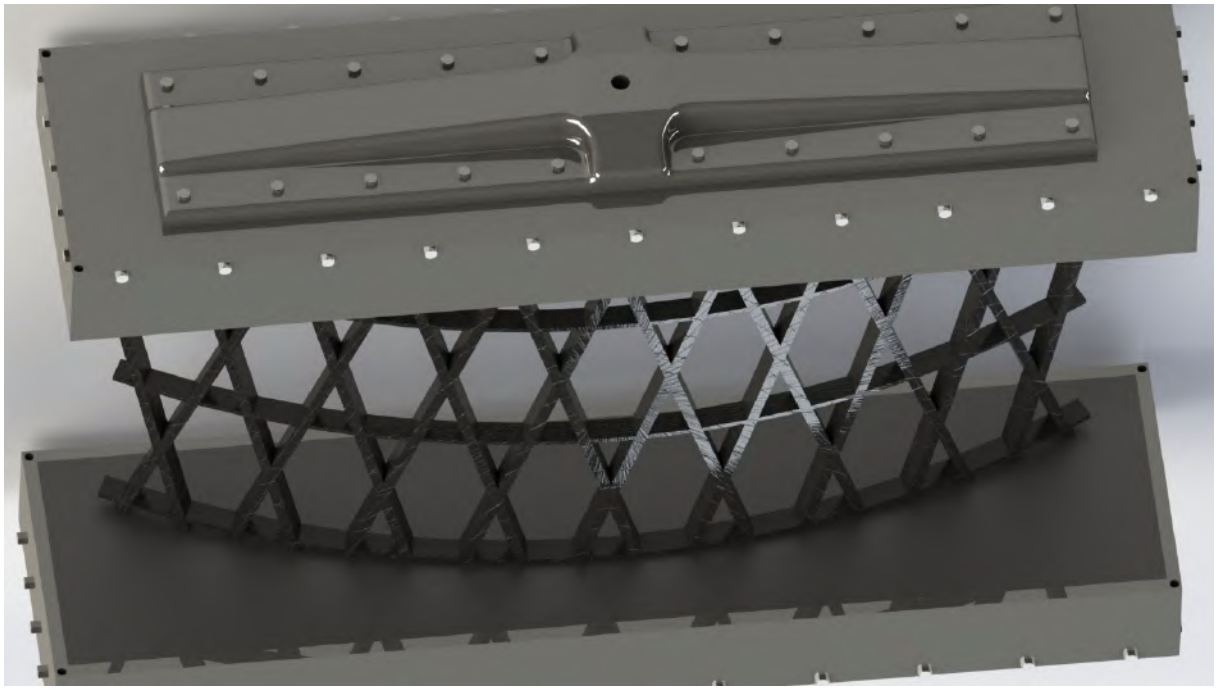

Figure 4.8: Rendering of large panel and relative fixing equipment.

CHAPTER 5

RECTILINEAR ORTHOTROPIC COMPOSITE CIRCULAR PLATES – CONSTITUTIVE EQUATIONS

One of the objectives of this Thesis is the obtainment of a reliable, low-computationally demanding, custom Spot Joint Element capable of accurately simulating the structural behavior of a region surrounding the bolted joint, comprising the bolt and a circular portion of both the plates.

The Spot Joint Element was initially presented in Ref. [62]: it is a finite element assembly devoted to the analysis of spot welded joint for metal sheets or riveted joints. The heavily reduced number of DOFs needed to perform the FE analysis of the spot joint - with no penalization in results accuracy - makes the architecture of this simulation tool very interesting even for the FE analysis of composite bolted joints, especially in case of multi-jointed structures. The theoretical formulation of this element is derived from the full analytical solution of the spot joint theoretical reference model. According to the original formulation of the Spot Joint Element, the theoretical reference model consists in an isotropic annular plate, clamped at the outer radius, characterized by a rigid core (when a bolt connection is considered) applied to the inner radius.

Preliminarily, the obtainment of the updated Spot Joint Element aimed to the accurate modeling composite and hybrid composite-metal bolted joints implies a mandatory preparatory phase which regards the characterization of its stiffness matrix terms. Therefore, the analytical study of the composite bolted joint theoretical model turns out to be necessary; this theoretical model consists in an annular plate realized in rectilinear orthotropic composite material with clamped outer radius and a central rigid core that must be solved under the action of various load typologies. The presence of rectilinear orthotropic material properties represents one of the most challenging issues to deal with in order to analytically solve the theoretical reference model; contrariwise, the current Spot Joint Element is based on an isotropic annular plate theoretical model and it features the capabilities of simulating of metal sheet spot joints with high accuracy.

With reference to the material properties, the composite plates of interest for the theoretical definition of a custom composite bolted joint finite element are the rectilinear orthotropic ones which are made up of layers disposed, as stated by the stacking sequence, alongside rectilinear paths; i.e. they are portions of rectangular plates. This characteristic produces overall stiffness properties that are variable with the circumferential coordinate.

In this regard, the developed theoretical background for rectilinear orthotropic composite circular plates is presented in this Chapter. Firstly, the governing equation is determined in the frame of the Classical Plate Theory (CPT), i.e. for thin-plates, from the equilibrium and the constitutive equations of the laminate circular plate. Then, the derivation of constitutive equations of rectilinear orthotropic composite plates is outlined taking into account the shear deformability in the frame of First-order Shear Deformation Plate Theory (FSDT).

5.1 Constitutive equations – Classical Laminate Plate Theory

A rectilinear orthotropic composite circular plate is a circular portion of a laminate composite rectangular plate. The major peculiarity of this class of plates consists in the fact that the rectilinear orthotropic material has a unique set of principal directions, meanwhile the plate geometry is axisymmetric. These features make the bending analysis of rectilinear orthotropic composite plates a bidimensional problem as the bending stiffnesses of the composite plate are dependent on the angular coordinate θ.

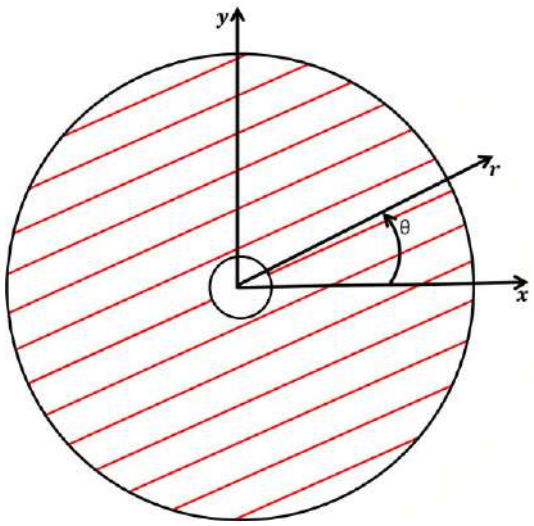

Figure 5.1: Fiber-reinforced rectilinear orthotropic layer.

The stress-strain relations written in the global Cartesian coordinate system (x, y, z) for a generic k^{th} rectilinear orthotropic layer belonging to a laminate annular plate, Fig. 5.1, and limited to in plane stress and strain conditions, are [100]:

$$\left\{\begin{array}{c}\sigma_x\\ \sigma_y\\ \tau_{xy}\end{array}\right\}_k = \left[\overline{Q}\right]_k \left\{\begin{array}{c}\varepsilon_x\\ \varepsilon_y\\ \gamma_{xy}\end{array}\right\}_k = \left[\begin{array}{ccc}\overline{Q}_{11} & \overline{Q}_{12} & \overline{Q}_{16}\\ \overline{Q}_{12} & \overline{Q}_{22} & \overline{Q}_{26}\\ \overline{Q}_{16} & \overline{Q}_{26} & \overline{Q}_{66}\end{array}\right]_k \left\{\begin{array}{c}\varepsilon_x\\ \varepsilon_y\\ \gamma_{xy}\end{array}\right\}_k \tag{5.1}$$

with $\left[\overline{Q}\right]_k$ the transformed reduced stiffness matrix of the layer. The global Cartesian coordinate system does not coincide with the principal material coordinate system for a finite rotation around the $z-$axis that is common for the two reference systems.

The expressions for stresses and the strains of the rectilinear orthotropic layer in the cylindrical coordinate system (r, θ, z) are obtainable applying the rotation matrix to the stress and strains vectors in (5.1):

$$\begin{Bmatrix} \sigma_r \\ \sigma_\theta \\ \tau_{r\theta} \end{Bmatrix}_k = \big[T(\theta)\big] \begin{Bmatrix} \sigma_x \\ \sigma_y \\ \tau_{xy} \end{Bmatrix}_k \qquad \begin{Bmatrix} \varepsilon_r \\ \varepsilon_\theta \\ \gamma_{r\theta} \end{Bmatrix}_k = \big[T(\theta)\big]^{-T} \begin{Bmatrix} \varepsilon_x \\ \varepsilon_y \\ \gamma_{xy} \end{Bmatrix}_k \tag{5.2}$$

The coordinate system transformation matrix has the form:

$$\big[T(\theta)\big] = \begin{bmatrix} c^2 & s^2 & 2cs \\ s^2 & c^2 & -2cs \\ -cs & cs & c^2 - s^2 \end{bmatrix} \tag{5.3}$$

where: $c = \cos(\theta)$, $s = \sin(\theta)$ and θ is the angle evaluated from the x-axis of the Cartesian coordinate system to the r-axis of the cylindrical coordinate system.

Moreover, the combination of the layer stress-strain relation in the Cartesian coordinate system (5.1) and the equations for the coordinates transformations (5.2), returns the stress-strain relation for the k^{th} layer in the cylindrical coordinate system:

$$\begin{Bmatrix} \sigma_r \\ \sigma_\theta \\ \tau_{r\theta} \end{Bmatrix}_k = \big[\overline{Q}(\theta)\big]_k \begin{Bmatrix} \varepsilon_r \\ \varepsilon_\theta \\ \gamma_{r\theta} \end{Bmatrix}_k = \begin{bmatrix} \overline{Q}_{11}(\theta) & \overline{Q}_{12}(\theta) & \overline{Q}_{16}(\theta) \\ \overline{Q}_{12}(\theta) & \overline{Q}_{22}(\theta) & \overline{Q}_{26}(\theta) \\ \overline{Q}_{16}(\theta) & \overline{Q}_{26}(\theta) & \overline{Q}_{66}(\theta) \end{bmatrix}_k \begin{Bmatrix} \varepsilon_r \\ \varepsilon_\theta \\ \gamma_{r\theta} \end{Bmatrix}_k \tag{5.4}$$

in which:

$$\big[\overline{Q}(\theta)\big]_k = \big[T(\theta)\big]\,\big[\overline{Q}\big]_k\,\big[T(\theta)\big]^T \tag{5.5}$$

is the transformed reduced stiffness matrix in the cylindrical coordinate system and its terms are:

$$\begin{aligned}
\overline{Q}_{11}^{(k)}(\theta) &= \overline{Q}_{11}^{(k)}c^4 + \Big(\overline{Q}_{12}^{(k)} + 2\overline{Q}_{66}^{(k)}\Big)2c^2s^2 + \Big(\overline{Q}_{16}^{(k)}c^2 + \overline{Q}_{26}^{(k)}s^2\Big)4cs + \overline{Q}_{22}^{(k)}s^4 \\
\overline{Q}_{12}^{(k)}(\theta) &= \overline{Q}_{12}^{(k)} + \Big[\overline{Q}_{11}^{(k)} + \overline{Q}_{22}^{(k)} - 2\Big(\overline{Q}_{12}^{(k)} + 2\overline{Q}_{66}^{(k)}\Big)\Big]c^2s^2 + \Big[\Big(\overline{Q}_{26}^{(k)} - \overline{Q}_{16}^{(k)}\Big)c^2 + \Big(\overline{Q}_{16}^{(k)} - \overline{Q}_{26}^{(k)}\Big)s^2\Big]2cs \\
\overline{Q}_{16}^{(k)}(\theta) &= \Big[\Big(\overline{Q}_{12}^{(k)} - \overline{Q}_{11}^{(k)} + 2\overline{Q}_{66}^{(k)}\Big)c^2 + \Big(\overline{Q}_{22}^{(k)} - \overline{Q}_{12}^{(k)} - 2\overline{Q}_{66}^{(k)}\Big)s^2\Big]cs + \overline{Q}_{16}^{(k)}c^2\Big(1 - 4s^2\Big) + \overline{Q}_{26}^{(k)}s^2\Big(4c^2 - 1\Big) \\
\overline{Q}_{22}^{(k)}(\theta) &= \overline{Q}_{22}^{(k)}c^4 + \Big(\overline{Q}_{12}^{(k)} + 2\overline{Q}_{66}^{(k)}\Big)2c^2s^2 - \Big(\overline{Q}_{16}^{(k)}s^2 + \overline{Q}_{26}^{(k)}c^2\Big)4cs + \overline{Q}_{11}^{(k)}s^4 \\
\overline{Q}_{26}^{(k)}(\theta) &= \Big[\Big(\overline{Q}_{22}^{(k)} - \overline{Q}_{12}^{(k)} - 2\overline{Q}_{66}^{(k)}\Big)c^2 + \Big(\overline{Q}_{12}^{(k)} - \overline{Q}_{11}^{(k)} + 2\overline{Q}_{66}^{(k)}\Big)s^2\Big]cs + \overline{Q}_{26}^{(k)}c^2\Big(1 - 4s^2\Big) + \overline{Q}_{16}^{(k)}s^2\Big(4c^2 - 1\Big) \\
\overline{Q}_{66}^{(k)}(\theta) &= \overline{Q}_{66}^{(k)} + \Big(\overline{Q}_{11}^{(k)} + \overline{Q}_{22}^{(k)} - 2\Big(\overline{Q}_{12}^{(k)} + 2\overline{Q}_{66}^{(k)}\Big)\Big)c^2s^2 + \Big(\overline{Q}_{26}^{(k)} - \overline{Q}_{16}^{(k)}\Big)\Big(c^2 - s^2\Big)2cs
\end{aligned} \tag{5.6}$$

The terms composing the reduced stiffness matrix in the cylindrical coordinate system $\big[\overline{Q}(\theta)\big]_k$ of the k^{th} rectilinear orthotropic layer are no more constants as the layer exhibits a different elastic response depending on the angular coordinate θ.

The stress vector of the overall rectilinear orthotropic composite circular plate can be obtained introducing one of the Classical Lamination Plate Theory hypotheses according to which, to be part of the same laminate, the layers are perfectly bonded together - no relative slip between the layers is admissible [100]. As a consequence, the displacement and strain fields are continuous along the plate thickness; this implies that the homologous stress terms of all the N layers, that make up the rectilinear orthotropic composite circular plate, can be summed up to obtain the comprehensive laminate stresses:

$$\begin{Bmatrix} \sigma_r \\ \\ \sigma_\theta \\ \\ \tau_{r\theta} \end{Bmatrix} = \sum_{k=1}^{N} \begin{Bmatrix} \sigma_r \\ \\ \sigma_\theta \\ \\ \tau_{r\theta} \end{Bmatrix}_k = \sum_{k=1}^{N} \left[\overline{Q}(\theta)\right]_k \begin{Bmatrix} \varepsilon_r \\ \\ \varepsilon_\theta \\ \\ \gamma_{r\theta} \end{Bmatrix} = \left[\overline{Q}(\theta)\right] \begin{Bmatrix} \varepsilon_r \\ \\ \varepsilon_\theta \\ \\ \gamma_{r\theta} \end{Bmatrix} \tag{5.7}$$

where a single term of the laminate reduced stiffness matrix is $\overline{Q}_{ij}(\theta) = \sum_{k=1}^{N} \overline{Q}_{ij}^{(k)}(\theta)$.

By virtue of the Kirchhoff-Love hypotheses of the Classical Plate Theory, the displacements along the coordinate directions r, θ and z of a thin-plate are respectively:

$$\begin{aligned} u_r(r,\theta,z) &= u(r,\theta) - z\frac{\partial w}{\partial r} \\ u_\theta(r,\theta,z) &= v(r,\theta) - z\frac{1}{r}\frac{\partial w}{\partial \theta} \\ u_z(r,\theta,z) &= w(r,\theta) \end{aligned} \tag{5.8}$$

where u, v and w denote the plate mid-surface ($z = 0$) radial, circumferential and deflection displacements.

Subsequently, the strains associated with this displacement field are:

$$\begin{aligned} \varepsilon_r &= \frac{\partial u_r}{\partial r} \\ \varepsilon_\theta &= \frac{u_r}{r} + \frac{1}{r}\frac{\partial u_\theta}{\partial \theta} \\ \gamma_{r\theta} &= \frac{1}{r}\frac{\partial u_r}{\partial \theta} + \frac{\partial u_\theta}{\partial r} - \frac{u_\theta}{r} \end{aligned} \tag{5.9}$$

being each strain composed of two contributions, the first one represents the mid-surface strains and the latter connected to mid-surface curvatures:

$$\begin{Bmatrix} \varepsilon_r \\ \\ \varepsilon_\theta \\ \\ \gamma_{r\theta} \end{Bmatrix} = \begin{Bmatrix} \varepsilon_r^0 \\ \\ \varepsilon_\theta^0 \\ \\ \gamma_{r\theta}^0 \end{Bmatrix} + z \begin{Bmatrix} \kappa_r \\ \\ \kappa_\theta \\ \\ \kappa_{r\theta} \end{Bmatrix} \tag{5.10}$$

Then, each strain and curvature in (5.10) term can be written as a function of the mid-surface displacements:

$$\begin{aligned} \varepsilon_r^0 &= \frac{\partial u}{\partial r} & \kappa_r &= -\frac{\partial^2 w}{\partial^2 r} \\ \varepsilon_\theta^0 &= \frac{u}{r} + \frac{1}{r}\frac{\partial v}{\partial \theta} & \kappa_\theta &= -\frac{1}{r}\left(\frac{\partial w}{\partial r} + \frac{1}{r}\frac{\partial^2 w}{\partial^2 \theta}\right) \\ \gamma_{r\theta}^0 &= \frac{1}{r}\frac{\partial u}{\partial \theta} + \frac{\partial v}{\partial r} - \frac{v}{r} & \kappa_{r\theta} &= -2\frac{\partial^2}{\partial r \partial \theta}\frac{w}{r} \end{aligned} \tag{5.11}$$

Furthermore, the stress resultants per unit width can be obtained through the elemental forces and moments integration over the N-layers in the laminate thickness t. The resulting in-plane forces are:

$$\begin{Bmatrix} N_r \\ N_\theta \\ N_{r\theta} \end{Bmatrix} = \int_{-t/2}^{t/2} \begin{Bmatrix} \sigma_r \\ \sigma_\theta \\ \tau_{r\theta} \end{Bmatrix} dz = \big[A(\theta)\big] \begin{Bmatrix} \varepsilon_r^0 \\ \varepsilon_\theta^0 \\ \gamma_{r\theta}^0 \end{Bmatrix} + \big[B(\theta)\big] \begin{Bmatrix} \kappa_r \\ \kappa_\theta \\ \kappa_{r\theta} \end{Bmatrix} \tag{5.12}$$

meanwhile the resulting bending moments and the torque moment are given by:

$$\begin{Bmatrix} M_r \\ M_\theta \\ M_{r\theta} \end{Bmatrix} = \int_{-t/2}^{t/2} \begin{Bmatrix} \sigma_r \\ \sigma_\theta \\ \tau_{r\theta} \end{Bmatrix} z dz = \big[B(\theta)\big] \begin{Bmatrix} \varepsilon_r^0 \\ \varepsilon_\theta^0 \\ \gamma_{r\theta}^0 \end{Bmatrix} + \big[D(\theta)\big] \begin{Bmatrix} \kappa_r \\ \kappa_\theta \\ \kappa_{r\theta} \end{Bmatrix} \tag{5.13}$$

The θ-dependent stiffness coefficients present in these expressions are:

$$\begin{aligned} A_{ij}(\theta) &= \sum_{k=1}^{N} \overline{Q}_{ij}^{(k)}(\theta)(z_k - z_{k-1}) \\ B_{ij}(\theta) &= \frac{1}{2}\sum_{k=1}^{N} \overline{Q}_{ij}^{(k)}(\theta)(z_k^2 - z_{k-1}^2) \\ D_{ij}(\theta) &= \frac{1}{3}\sum_{k=1}^{N} \overline{Q}_{ij}^{(k)}(\theta)(z_k^3 - z_{k-1}^3) \end{aligned} \tag{5.14}$$

where $A_{ij}(\theta)$ are the extensional stiffnesses, $B_{ij}(\theta)$ the bending-extension coupling stiffnesses and $D_{ij}(\theta)$ the bending stiffnesses for a rectilinear orthotropic composite circular plate expressed in the cylindrical coordinate system. In addition, z_k and z_{k-1} are the oriented distances to the bottom and the top, respectively, of the k^{th} layer.

5.2 Derivation of the governing equation

The governing equation for bending of rectilinear orthotropic composite circular thin-plates was derived in the frame of the Classical Lamination Plate Theory which encompasses the Kirchhoff-Love hypotheses. The transversal load condition involves the application of a force P acting on the plate axis. The only stress resultants that must be considered in writing the equilibrium equations

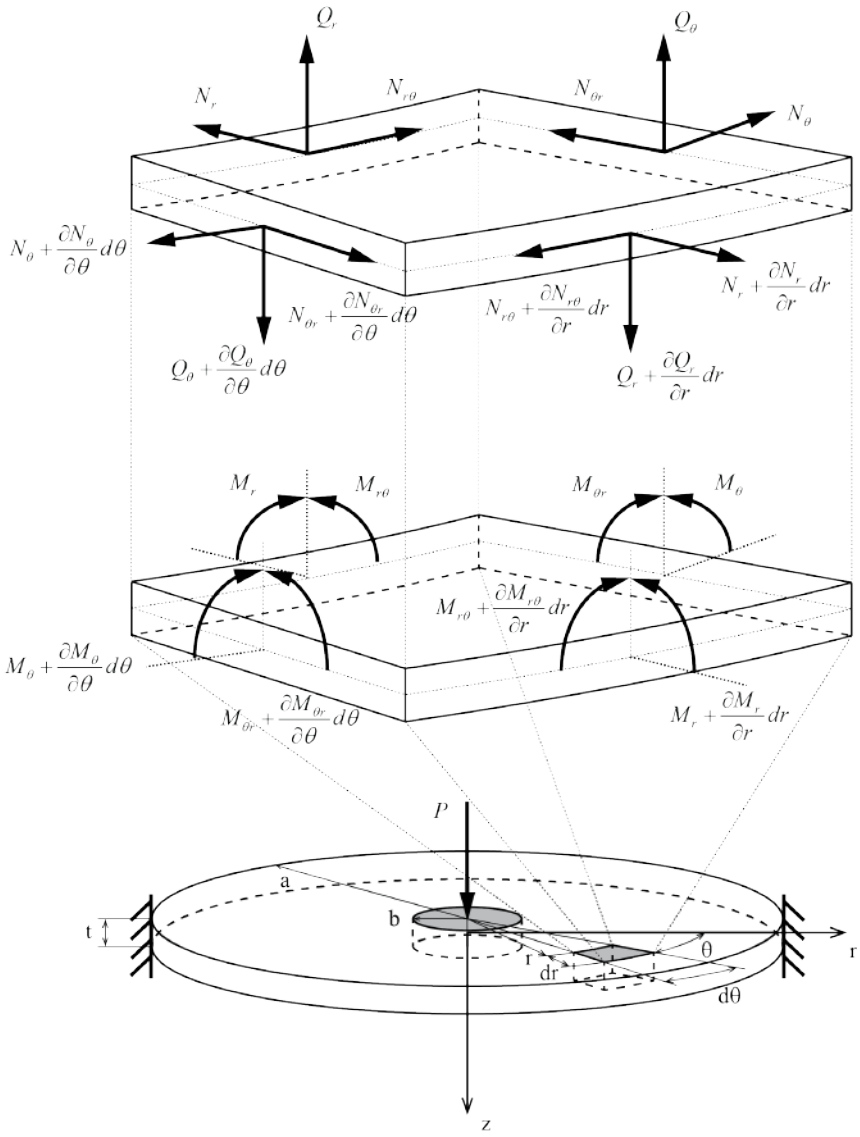

Figure 5.2: Stress resultants acting on a plate element.

are the radial and the circumferential bending moments M_r and M_θ, the torque moment $M_{r\theta}$ and the shear forces Q_r and Q_θ, Fig. 5.2. In fact, being valid the thin-plate assumption, the application of a load transversal to the plate mid-surface does not produce any membrane-shell coupling effect and consequently no mid-surface strains. Moreover, considering a laminate thin-plate with a lay-up symmetrical respect to the mid-plane, the bending-extension coupling stiffnesses $B_{ij}(\theta)$ are all null and therefore the curvature variations does not produce any in-plane stress resultant. As a consequence, the bending and torque moments in (5.13), must be rewritten with the only curvature contributes:

$$\begin{aligned} M_r &= D_{11}(\theta)\kappa_r + D_{12}(\theta)\kappa_\theta + D_{16}(\theta)\kappa_{r\theta} \\ M_\theta &= D_{12}(\theta)\kappa_r + D_{22}(\theta)\kappa_\theta + D_{26}(\theta)\kappa_{r\theta} \\ M_{r\theta} &= D_{16}(\theta)\kappa_r + D_{26}(\theta)\kappa_\theta + D_{66}(\theta)\kappa_{r\theta} \end{aligned} \tag{5.15}$$

Furthermore, the only unknown displacement component of the composite annular plate is the mid-surface deflection $w(r,\theta)$ as its radial u and circumferential v displacements are not present.

The three equilibrium equations that must be considered are:

- Equilibrium of forces along the z-axis

$$\frac{Q_r}{r} + \frac{\partial Q_r}{\partial r} + \frac{1}{r}\frac{\partial Q_\theta}{\partial \theta} + q = 0 \tag{5.16}$$

- Equilibrium of moments about the r-axis

$$\frac{2}{r}M_{r\theta} + \frac{\partial M_{r\theta}}{\partial r} + \frac{1}{r}\frac{\partial M_\theta}{\partial \theta} - Q_\theta = 0 \tag{5.17}$$

- Equilibrium of moments about the θ-axis

$$\frac{M_r - M_\theta}{r} + \frac{\partial M_r}{\partial r} + \frac{1}{r}\frac{\partial M_{r\theta}}{\partial \theta} - Q_r = 0 \tag{5.18}$$

Afterwards, the general equilibrium equation, which encompasses bending moments, torque moment and shear forces is obtained as a composition of the three equilibrium equations. Specifically, substituting the circumferential shear force Q_θ from (5.17) into (5.16) and, after that, the radial shear force Q_r from (5.16) into (5.18), the resulting general equilibrium equation is:

$$M_r - M_\theta + 3\frac{\partial M_{r\theta}}{\partial \theta} + \frac{\partial^2 M_\theta}{\partial \theta^2} + r\left[\frac{\partial M_r}{\partial r} + \frac{\partial^2 M_{r\theta}}{\partial r \partial \theta} + r\left(\frac{\partial Q_r}{\partial r} + q(r,\theta)\right)\right] = 0 \tag{5.19}$$

The unknown component of displacement $w(r,\theta)$ can be shown explicitly in the general equilibrium equation by replacing the bending moments and the torque moment with their expression in (5.15) and the curvatures in (5.11) to come up to the following partial derivative equation:

$$\begin{aligned}
&\frac{\partial^3 w}{\partial r^3}\left(D_{11}(\theta) + \frac{dD_{16}(\theta)}{d\theta}\right) + D_{16}(\theta)\frac{\partial^4 w}{\partial r^3 \partial \theta} + \frac{1}{r^2}\frac{\partial^3 w}{\partial r \partial \theta^2}\left(D_{12}(\theta) + D_{22}(\theta) + 2D_{66}(\theta) + 5\frac{dD_{26}(\theta)}{d\theta}\right) + \\
&+\frac{1}{r}\frac{\partial^3 w}{\partial r^2 \partial \theta}\left(5D_{16}(\theta) + D_{26}(\theta) + 2\left(\frac{dD_{12}(\theta)}{d\theta} + \frac{dD_{66}(\theta)}{d\theta}\right)\right) + \frac{2}{r^2}\frac{\partial^2 w}{\partial r \partial \theta}\left(-D_{16}(\theta) + \frac{dD_{22}(\theta)}{d\theta} + \frac{dD_{66}(\theta)}{d\theta} + \frac{d^2 D_{26}(\theta)}{d\theta^2}\right) + \\
&+\frac{1}{r}\frac{\partial^2 w}{\partial r^2}\left(D_{11}(\theta) + 3\frac{dD_{16}(\theta)}{d\theta} + \frac{dD_{26}(\theta)}{d\theta} + \frac{d^2 D_{12}(\theta)}{d\theta^2}\right) + 3\frac{D_{26}(\theta)}{r^2}\frac{\partial^4 w}{\partial r \partial \theta^3} + \frac{1}{r}\frac{\partial^4 w}{\partial r^2 \partial \theta^2}\left(D_{12}(\theta) + 2D_{66}(\theta)\right) + \\
&+\frac{1}{r^2}\frac{\partial w}{\partial r}\left(-D_{22}(\theta) + 2\frac{dD_{26}(\theta)}{d\theta} + \frac{d^2 D_{22}(\theta)}{d\theta^2}\right) + \frac{2}{r^3}\frac{\partial w}{\partial \theta}\left(D_{16}(\theta) + D_{26}(\theta) - \frac{dD_{66}(\theta)}{d\theta} - \frac{d^2 D_{26}(\theta)}{d\theta^2}\right) + \\
&-\frac{1}{r^3}\frac{\partial^2 w}{\partial \theta^2}\left(D_{12}(\theta) + D_{22}(\theta) + 2D_{66}(\theta) + 3\frac{dD_{26}(\theta)}{d\theta} - \frac{d^2 D_{22}(\theta)}{d\theta^2}\right) + \frac{1}{r^3}\frac{\partial^3 w}{\partial \theta^3}\left(2\frac{dD_{22}(\theta)}{d\theta} - D_{26}(\theta)\right) + \frac{D_{22}(\theta)}{r^3}\frac{\partial^4 w}{\partial \theta^4} + \\
&-r\left(\frac{\partial Q_r}{\partial r} + q(r,\theta)\right) = 0
\end{aligned} \tag{5.20}$$

Equation (5.20), that is a third order partial derivative equation in the unknown mid-surface deflection $w(r,\theta)$, is the governing equation of the problem here approached.

5.3 Governing equation – Axisymmetric case

A quasi-isotropic stacking sequence, symmetric respect to the plate mid-surface, was taken into account in this Section. The transversal loading condition was realized through the application of a unitary force P acting on the plate axis, alongside the z-axis of the cylindrical coordinate system and with the same verse, orthogonally with respect to the mid-surface of the rectilinear orthotropic composite circular plate. The derivation of the governing equation for bending of rectilinear orthotropic laminate circular plates is performed within the framework of Classical Lamination Plate Theory and, as a consequence, Kirchhoff-Love hypotheses are considered to outline the plate behavior [64].

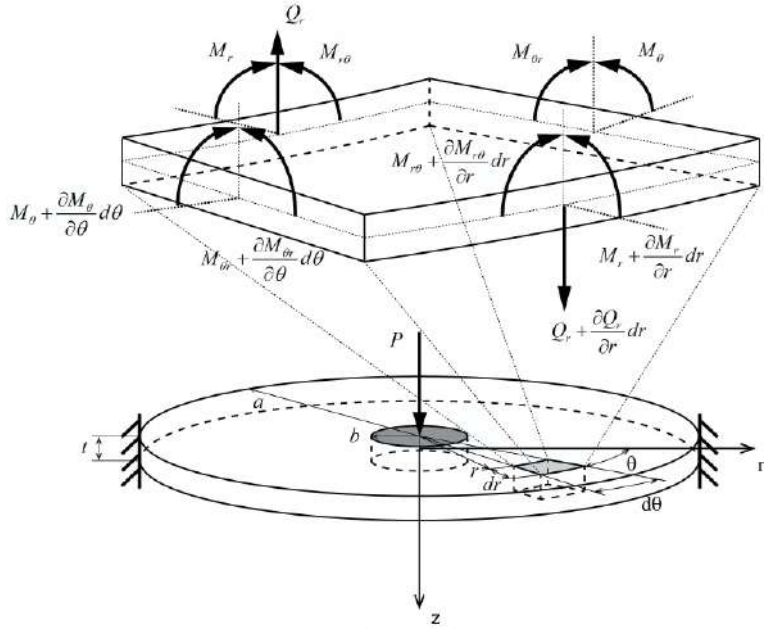

Figure 5.3: Stress resultants acting on a plate element (up) and theoretical reference model (down).

According to these assumptions and to the quasi-isotropic stacking sequence considered, the mid-surface deflection w and the radial and circumferential bending moments M_r and M_θ are assumed to depend only on the radial coordinate r; furthermore, the torque moment $M_{r\theta}$ vanishes. The stress resultants that must be considered in writing the equilibrium equations are the radial and the circumferential bending moments M_r and M_θ, and the shear force Q_r (Fig. 5.3).

In addition, no in-plane stress resultants act on the plate because no membrane-shell coupling effects are considered and consequently no mid-surface strains that induce in-plane stress resultants are present. Moreover, being the quasi-isotropic stacking sequence symmetrical respect to the plate mid-surface, the bending-extension coupling stiffnesses matrix $\left[B(\theta)\right]$ is null and therefore no in-plane stress resultants are produced by the curvature variations.

The only non-null moments, the radial and the circumferential bending moments M_r and M_θ in (5.13), assume the form, considering Eqs. (5.14):

$$\begin{Bmatrix} M_r \\ M_\theta \end{Bmatrix} = \begin{bmatrix} D_{11}(\theta) & D_{12}(\theta) \\ D_{12}(\theta) & D_{22}(\theta) \end{bmatrix} \begin{Bmatrix} \kappa_r \\ \kappa_\theta \end{Bmatrix} \tag{5.21}$$

Furthermore, the only unknown displacement component of the composite annular plate is the mid-surface deflection $w(r)$ as its radial u and circumferential v displacements are not present.

In the end, combining the equilibrium of forces along the z-axis and the equilibrium of moments about the θ-axis, the resulting general equilibrium equation can be found:

$$M_r - M_\theta + r\left[\frac{\partial M_r}{\partial r} + r\left(\frac{\partial Q_r}{\partial r} + q(r)\right)\right] = 0 \tag{5.22}$$

The analytical expression of the governing equation can be identified replacing the bending moments with their expression in (5.21) and the curvatures in (5.10):

$$\frac{\partial^3 w}{\partial r^3} D_{11}(\theta) + \frac{1}{r}\frac{\partial^2 w}{\partial r^2}\left(D_{11}(\theta) + \frac{d^2 D_{12}(\theta)}{d\theta^2}\right) + \frac{1}{r^2}\frac{\partial w}{\partial r}\left(-D_{22}(\theta) + \frac{d^2 D_{22}(\theta)}{d\theta^2}\right) - r\left(\frac{\partial Q_r}{\partial r} + q(r)\right) = 0 \tag{5.23}$$

This is a third order differential equation where the unknown displacement component $w(r)$ compares explicitly.

5.4 Constitutive equations – First-order Shear Deformation Plate Theory

A circular portion extracted from a rectangular laminate composite plate features, despite the axysimmetric geometry, a unique set of material properties principal directions and, as a consequence, its elastic response turns out to be dependent on the angular coordinate θ. This behavior arises because of the particular fibers arrangement present within the layers that make up the laminate. In fact, the fibers of every layer are disposed longwise straight trajectories and form a specific angle with respect to the x-axis of the Cartesian coordinate system, Fig. 5.2, according to the plate stacking sequence. As a consequence of the circumferentially variable bending stiffnesses, the bending analysis of this class of circular plates involves the solution of a bidimensional problem in order to determine the displacement field produced by the action of transversal or bending loads.

Nevertheless, it is suitable to conduct the elastic analysis of rectilinear orthotropic composite circular plates in the cylindrical coordinate system (r, θ, z). Therefore, it is necessary to derive stresses and strains relations in cylindrical coordinates for a generic k^{th} rectilinear orthotropic layer belonging to a laminate annular plate; these expressions can be obtained by means of the application of the rotation matrix $\big[T(\theta)\big]$ to the stress and strains vectors expressed in Cartesian coordinates (x, y, z):

$$\begin{Bmatrix} \sigma_r \\ \sigma_\theta \\ \tau_{\theta z} \\ \tau_{rz} \\ \tau_{r\theta} \end{Bmatrix}_k = \big[T(\theta)\big] \begin{Bmatrix} \sigma_x \\ \sigma_y \\ \tau_{yz} \\ \tau_{xz} \\ \tau_{xy} \end{Bmatrix}_k \qquad \begin{Bmatrix} \varepsilon_r \\ \varepsilon_\theta \\ \gamma_{\theta z} \\ \gamma_{rz} \\ \gamma_{r\theta} \end{Bmatrix}_k = \big[T(\theta)\big]^{-T} \begin{Bmatrix} \varepsilon_x \\ \varepsilon_y \\ \gamma_{yz} \\ \gamma_{xz} \\ \gamma_{xy} \end{Bmatrix}_k \tag{5.24}$$

Besides, the coordinate system transformation matrix is structured as:

$$\left[T(\theta)\right] = \begin{bmatrix} c^2 & s^2 & 0 & 0 & 2cs \\ s^2 & c^2 & 0 & 0 & -2cs \\ 0 & 0 & c & -s & 0 \\ 0 & 0 & s & c & 0 \\ -cs & cs & 0 & 0 & c^2 - s^2 \end{bmatrix} \tag{5.25}$$

being: $c = \cos(\theta)$, $s = \sin(\theta)$ and θ the angle evaluated from the x-axis of the Cartesian coordinate system to the r-axis of the cylindrical coordinate system, Fig. 5.2.

In addition, the stress-strain relations written in the global Cartesian coordinate system for a generic k^{th} rectilinear orthotropic layer belonging to a laminate annular plate, and utilized to obtain the analogous Eq. (5.24) in cylindrical coordinates, are:

$$\begin{Bmatrix} \sigma_x \\ \sigma_y \\ \tau_{yz} \\ \tau_{xz} \\ \tau_{xy} \end{Bmatrix}_k = \left[\overline{Q}\right]_k \begin{Bmatrix} \varepsilon_x \\ \varepsilon_y \\ \gamma_{yz} \\ \gamma_{xz} \\ \gamma_{xy} \end{Bmatrix}_k \tag{5.26}$$

in which $\left[\overline{Q}\right]_k$ indicates the transformed reduced stiffness matrix of the k^{th} layer which is derived considering that the global Cartesian coordinate system and the principal material coordinate system differ for a finite rotation around the $z-$axis, which is common for the two reference systems.

Consequently, the stress-strain relations for the k^{th} layer in the cylindrical coordinate system are returned through the substitution of the layer stress-strain relations in the Cartesian coordinate system (5.26) in the equations for the coordinates transformations (5.24):

$$\begin{Bmatrix} \sigma_r \\ \sigma_\theta \\ \tau_{\theta z} \\ \tau_{rz} \\ \tau_{r\theta} \end{Bmatrix}_k = \left[\overline{Q}(\theta)\right]_k \begin{Bmatrix} \varepsilon_r \\ \varepsilon_\theta \\ \gamma_{\theta z} \\ \gamma_{rz} \\ \gamma_{r\theta} \end{Bmatrix}_k \tag{5.27}$$

where the transformed reduced stiffness matrix in cylindrical coordinates $\left[\overline{Q}(\theta)\right]_k$ is:

$$\left[\overline{Q}(\theta)\right]_k = \begin{bmatrix} \overline{Q}_{11}(\theta) & \overline{Q}_{12}(\theta) & 0 & 0 & \overline{Q}_{16}(\theta) \\ \overline{Q}_{12}(\theta) & \overline{Q}_{22}(\theta) & 0 & 0 & \overline{Q}_{26}(\theta) \\ 0 & 0 & \overline{Q}_{44}(\theta) & \overline{Q}_{45}(\theta) & 0 \\ 0 & 0 & \overline{Q}_{45}(\theta) & \overline{Q}_{55}(\theta) & 0 \\ \overline{Q}_{16}(\theta) & \overline{Q}_{26}(\theta) & 0 & 0 & \overline{Q}_{66}(\theta) \end{bmatrix}_k \tag{5.28}$$

It is obtained by means of the matrix product:

$$\left[\overline{Q}(\theta)\right]_k = \left[T(\theta)\right]\left[\overline{Q}\right]_k\left[T(\theta)\right]^T \tag{5.29}$$

The angular dependent terms of the matrix are:

$$\begin{aligned}
\overline{Q}_{11}^{(k)}(\theta) &= \overline{Q}_{11}^{(k)}c^4 + \left(\overline{Q}_{12}^{(k)} + 2\overline{Q}_{66}^{(k)}\right)2c^2s^2 + \left(\overline{Q}_{16}^{(k)}c^2 + \overline{Q}_{26}^{(k)}s^2\right)4cs + \overline{Q}_{22}^{(k)}s^4 \\
\overline{Q}_{12}^{(k)}(\theta) &= \overline{Q}_{12}^{(k)} + \left[\overline{Q}_{11}^{(k)} + \overline{Q}_{22}^{(k)} - 2\left(\overline{Q}_{12}^{(k)} + 2\overline{Q}_{66}^{(k)}\right)\right]c^2s^2 + \left[\left(\overline{Q}_{26}^{(k)} - \overline{Q}_{16}^{(k)}\right)c^2 + \left(\overline{Q}_{16}^{(k)} - \overline{Q}_{26}^{(k)}\right)s^2\right]2cs \\
\overline{Q}_{16}^{(k)}(\theta) &= \left[\left(\overline{Q}_{12}^{(k)} - \overline{Q}_{11}^{(k)} + 2\overline{Q}_{66}^{(k)}\right)c^2 + \left(\overline{Q}_{22}^{(k)} - \overline{Q}_{12}^{(k)} - 2\overline{Q}_{66}^{(k)}\right)s^2\right]cs + \overline{Q}_{16}^{(k)}c^2\left(1 - 4s^2\right) + \overline{Q}_{26}^{(k)}s^2\left(4c^2 - 1\right) \\
\overline{Q}_{22}^{(k)}(\theta) &= \overline{Q}_{22}^{(k)}c^4 + \left(\overline{Q}_{12}^{(k)} + 2\overline{Q}_{66}^{(k)}\right)2c^2s^2 - \left(\overline{Q}_{16}^{(k)}s^2 + \overline{Q}_{26}^{(k)}c^2\right)4cs + \overline{Q}_{11}^{(k)}s^4 \\
\overline{Q}_{26}^{(k)}(\theta) &= \left[\left(\overline{Q}_{22}^{(k)} - \overline{Q}_{12}^{(k)} - 2\overline{Q}_{66}^{(k)}\right)c^2 + \left(\overline{Q}_{12}^{(k)} - \overline{Q}_{11}^{(k)} + 2\overline{Q}_{66}^{(k)}\right)s^2\right]cs + \overline{Q}_{26}^{(k)}c^2\left(1 - 4s^2\right) + \overline{Q}_{16}^{(k)}s^2\left(4c^2 - 1\right) \\
\overline{Q}_{44}^{(k)}(\theta) &= \overline{Q}_{44}^{(k)}c^2 - \overline{Q}_{45}^{(k)}2cs + \overline{Q}_{55}^{(k)}s^2 \\
\overline{Q}_{45}^{(k)}(\theta) &= \left(\overline{Q}_{44}^{(k)} - \overline{Q}_{55}^{(k)}\right)cs + \overline{Q}_{45}^{(k)}\left(c^2 - s^2\right) \\
\overline{Q}_{55}^{(k)}(\theta) &= \overline{Q}_{55}^{(k)}c^2 + \overline{Q}_{45}^{(k)}2cs + \overline{Q}_{44}^{(k)}s^2 \\
\overline{Q}_{66}^{(k)}(\theta) &= \overline{Q}_{66}^{(k)} + \left(\overline{Q}_{11}^{(k)} + \overline{Q}_{22}^{(k)} - 2\left(\overline{Q}_{12}^{(k)} + 2\overline{Q}_{66}^{(k)}\right)\right)c^2s^2 + \left(\overline{Q}_{26}^{(k)} - \overline{Q}_{16}^{(k)}\right)\left(c^2 - s^2\right)2cs
\end{aligned} \tag{5.30}$$

The terms composing the reduced stiffness matrix in the cylindrical coordinate system $\left[\overline{Q}(\theta)\right]_k$ of the k^{th} rectilinear orthotropic layer are no more constants as the layer exhibits a different elastic response depending on the angular coordinate θ.

Moreover, a condition of perfect adhesion between the layers comprising the rectilinear orthotropic composite circular plate can be supposed, owing to one of the fundamental assumption encompassed in the Classical Lamination Plate Theory [100]. This aspect entails the displacements and strains are continuous functions alongside the plate thickness direction z and, subsequently, the comprehensive stresses of the rectilinear orthotropic composite circular plate can be derived adding up the homologous stress terms of the N layers over the thickness:

$$\begin{Bmatrix} \sigma_r \\ \sigma_\theta \\ \tau_{\theta z} \\ \tau_{rz} \\ \tau_{r\theta} \end{Bmatrix} = \sum_{k=1}^{N} \begin{Bmatrix} \sigma_r \\ \sigma_\theta \\ \tau_{\theta z} \\ \tau_{rz} \\ \tau_{r\theta} \end{Bmatrix}_k = \sum_{k=1}^{N} \left[\overline{Q}(\theta)\right]_k \begin{Bmatrix} \varepsilon_r \\ \varepsilon_\theta \\ \gamma_{\theta z} \\ \gamma_{rz} \\ \gamma_{r\theta} \end{Bmatrix} = \left[\overline{Q}(\theta)\right] \begin{Bmatrix} \varepsilon_r \\ \varepsilon_\theta \\ \gamma_{\theta z} \\ \gamma_{rz} \\ \gamma_{r\theta} \end{Bmatrix} \tag{5.31}$$

in which a generic term of the laminate reduced stiffness matrix in the cylindrical coordinate system is:

$$\overline{Q}_{ij}(\theta) = \sum_{k=1}^{N} \overline{Q}_{ij}^{(k)}(\theta) \tag{5.32}$$

As regards the kinematic assumptions, the FSDT relieves one of the basic hypotheses proper of the CPT; indeed, the normals to the plate mid-surface are no more presumed to remain perpendicular to the mid-surface when the laminate undergoes a deformation. This behavior is attained adding a constant state of transverse shear strains alongside the laminate thickness to the strain field. However, the assumptions of plane-stress state and inextensible normals are preserved; as a consequence, the mid-surface deflection w is constant in reference to the thickness coordinate z [101].

Therefore, according to Reissner-Mindlin assumptions, the FSDT state the components of the displacement field along the coordinate directions r, θ and z are:

$$\begin{aligned} u_r(r,\theta,z) &= u(r,\theta) + z\ \phi_r(r,\theta) \\ u_\theta(r,\theta,z) &= v(r,\theta) + z\ \phi_\theta(r,\theta) \\ u_z(r,\theta,z) &= w(r,\theta) \end{aligned} \tag{5.33}$$

where u, v and w denote the plate mid-surface ($z = 0$) radial, circumferential and deflection displacements respectively; whereas ϕ_r and ϕ_θ indicate the rotations of the normal to the plate mid-surface about the circumferential and radial directions.

Additionally, the strains expressed in cylindrical coordinates and related to the displacement components in (5.33) are:

$$\begin{aligned} \varepsilon_r &= \frac{\partial u_r}{\partial r} \\ \varepsilon_\theta &= \frac{u_r}{r} + \frac{1}{r}\frac{\partial u_\theta}{\partial \theta} \\ \gamma_{\theta z} &= \frac{\partial u_\theta}{\partial z} + \frac{1}{r}\frac{\partial u_z}{\partial \theta} \\ \gamma_{rz} &= \frac{\partial u_r}{\partial z} + \frac{\partial u_z}{\partial r} \\ \gamma_{r\theta} &= \frac{1}{r}\frac{\partial u_r}{\partial \theta} + \frac{\partial u_\theta}{\partial r} - \frac{u_\theta}{r} \end{aligned} \tag{5.34}$$

being each strain composed of two contributions, the first one represents the mid-surface strains and the latter connected to mid-surface curvatures:

$$\begin{Bmatrix} \varepsilon_r \\ \varepsilon_\theta \\ \gamma_{\theta z} \\ \gamma_{rz} \\ \gamma_{r\theta} \end{Bmatrix} = \begin{Bmatrix} \varepsilon_r^0 \\ \varepsilon_\theta^0 \\ \gamma_{\theta z}^0 \\ \gamma_{rz}^0 \\ \gamma_{r\theta}^0 \end{Bmatrix} + z \begin{Bmatrix} \kappa_r \\ \kappa_\theta \\ 0 \\ 0 \\ \kappa_{r\theta} \end{Bmatrix} \tag{5.35}$$

Then, each strain and curvature term in (5.35) can be written as a function of the mid-surface displacements:

$$\begin{aligned} \varepsilon_r^0 &= \frac{\partial u}{\partial r} & \kappa_r &= \frac{\partial \phi_r}{\partial r} \\ \varepsilon_\theta^0 &= \frac{u}{r} + \frac{1}{r}\frac{\partial v}{\partial \theta} & \kappa_\theta &= \frac{\phi_r}{r} + \frac{1}{r}\frac{\partial \phi_\theta}{\partial \theta} \\ \gamma_{\theta z}^0 &= \phi_\theta + \frac{1}{r}\frac{\partial w}{\partial \theta} & & \\ \gamma_{rz}^0 &= \phi_r + \frac{\partial w}{\partial r} & & \\ \gamma_{r\theta}^0 &= \frac{1}{r}\frac{\partial u}{\partial \theta} + \frac{\partial v}{\partial r} - \frac{v}{r} & \kappa_{r\theta} &= \frac{1}{r}\frac{\partial \phi_r}{\partial \theta} + \frac{\partial \phi_\theta}{\partial r} - \frac{\phi_\theta}{r} \end{aligned} \tag{5.36}$$

In the end, the strain field features in-plane components of strain which linearly depend on the coordinate z and overall amounts of the transverse shear strains that do not vary alongside the composite annular plate thickness.

Furthermore, the integration of the elemental forces and moments over the N-layers in the laminate thickness t returns the stress resultants per unit width:

- In-plane forces

$$\begin{Bmatrix} N_r \\ N_\theta \\ N_{r\theta} \end{Bmatrix} = \int_{-t/2}^{t/2} \begin{Bmatrix} \sigma_r \\ \sigma_\theta \\ \tau_{r\theta} \end{Bmatrix} dz = \begin{bmatrix} A_{11}(\theta) & A_{12}(\theta) & A_{16}(\theta) \\ A_{12}(\theta) & A_{22}(\theta) & A_{26}(\theta) \\ A_{16}(\theta) & A_{26}(\theta) & A_{66}(\theta) \end{bmatrix} \begin{Bmatrix} \varepsilon_r^0 \\ \varepsilon_\theta^0 \\ \gamma_{r\theta}^0 \end{Bmatrix} + \begin{bmatrix} B_{11}(\theta) & B_{12}(\theta) & B_{16}(\theta) \\ B_{12}(\theta) & B_{22}(\theta) & B_{26}(\theta) \\ B_{16}(\theta) & B_{26}(\theta) & B_{66}(\theta) \end{bmatrix} \begin{Bmatrix} \kappa_r \\ \kappa_\theta \\ \kappa_{r\theta} \end{Bmatrix} \tag{5.37}$$

- Shear forces

$$\begin{Bmatrix} Q_\theta \\ Q_r \end{Bmatrix} = K_s \int_{-t/2}^{t/2} \begin{Bmatrix} \tau_{\theta z} \\ \tau_{rz} \end{Bmatrix} dz = K_s \begin{bmatrix} A_{44}(\theta) & A_{45}(\theta) \\ A_{45}(\theta) & A_{55}(\theta) \end{bmatrix} \begin{Bmatrix} \gamma_{\theta z}^0 \\ \gamma_{rz}^0 \end{Bmatrix} \tag{5.38}$$

- Bending and torque moments

$$\begin{Bmatrix} M_r \\ M_\theta \\ M_{r\theta} \end{Bmatrix} = \int_{-t/2}^{t/2} \begin{Bmatrix} \sigma_r \\ \sigma_\theta \\ \tau_{r\theta} \end{Bmatrix} z dz = \begin{bmatrix} B_{11}(\theta) & B_{12}(\theta) & B_{16}(\theta) \\ B_{12}(\theta) & B_{22}(\theta) & B_{26}(\theta) \\ B_{16}(\theta) & B_{26}(\theta) & B_{66}(\theta) \end{bmatrix} \begin{Bmatrix} \varepsilon_r^0 \\ \varepsilon_\theta^0 \\ \gamma_{r\theta}^0 \end{Bmatrix} + \begin{bmatrix} D_{11}(\theta) & D_{12}(\theta) & D_{16}(\theta) \\ D_{12}(\theta) & D_{22}(\theta) & D_{26}(\theta) \\ D_{16}(\theta) & D_{26}(\theta) & D_{66}(\theta) \end{bmatrix} \begin{Bmatrix} \kappa_r \\ \kappa_\theta \\ \kappa_{r\theta} \end{Bmatrix} \tag{5.39}$$

The coefficient $K_s = \frac{5}{6}$ present in Eq. (5.38) is the shear correction factor needed to adjust the approximation introduced by the FSDT kinematic hypotheses which introduces a constant, over the thickness, distribution of shear stress which instead is of higher order.

Regarding the stiffness matrices proper of the expressions of stress resultants (5.37-5.39), the stiffness coefficients dependent on the angular coordinate θ are defined as:

$$\begin{aligned} A_{ij}(\theta) &= \sum_{k=1}^{N} \overline{Q}_{ij}^{(k)}(\theta)(z_k - z_{k-1}) \\ B_{ij}(\theta) &= \frac{1}{2} \sum_{k=1}^{N} \overline{Q}_{ij}^{(k)}(\theta)(z_k^2 - z_{k-1}^2) \\ D_{ij}(\theta) &= \frac{1}{3} \sum_{k=1}^{N} \overline{Q}_{ij}^{(k)}(\theta)(z_k^3 - z_{k-1}^3) \end{aligned} \tag{5.40}$$

where: $A_{ij}(\theta)$ are the extensional stiffnesses, $B_{ij}(\theta)$ the bending-extension coupling stiffnesses and $D_{ij}(\theta)$ the bending stiffnesses for a rectilinear orthotropic composite circular plate expressed in the cylindrical coordinate system. In addition, z_k and z_{k-1} are the oriented distances to the bottom and the top, respectively, of the k^{th} layer.

CHAPTER 6

BENDING ANALYSIS WITH GALERKIN METHOD OF RECTILINEAR ORTHOTROPIC COMPOSITE CIRCULAR PLATES SUBJECT TO TRANSVERSAL LOAD

This Chapter concerns the application of Galerkin method to the governing equation of a rectilinear orthotropic composite circular plate experiencing transversal load, which is derived in Chapter 5, as a first step towards the definition of the FE stiffness matrix of the composite bolted joint.

The main complication with respect to previous works about the topic of spot joint simulation, is represented by the fact of considering rectilinear orthotropic material properties, that are intrinsically symmetric in a Cartesian coordinate system, for an annular plate, i.e. an axisymmetric geometry. This aspect introduces a circumferential variation of the composite annular plate bending stiffnesses and of the displacement components as a consequence. This makes it impossible the chance to obtain closed form solutions, as for the isotropic case, and consequently required the application of Galerkin method.

Approximation functions compliant with the displacement constraints, introduced by the joint theoretical model proposed by [62], are derived and utilized in the application of Galerkin method. Moreover, the dependence of the mid-surface deflection on the circumferential coordinate is further taken into account, improving the solution presented in [64] where the mid-surface deflection circumferential variation is neglected.

With the present approach it is possible to reproduce, with a semi-analytical procedure, the stiffness behavior of a rectilinear orthotropic annular plate as never done before [65]. Moreover, the presented procedure considers clamping constraints at the outer radius and relative clamping at the inner radius, whose application is not resolved in any other researches in literature. It represents an original approach which is the basis for the definition of the FE stiffness matrix of the composite bolted joint.

Results are presented, in comparison with the outcomes of FE analyses, for two kinds of laminate

lay-ups: quasi-isotropic (QI) and zero-dominated (0D). These lay-ups were selected from literature about the topic of composite bolted joints FE structural analysis [53, 58, 59, 52, 60, 54, 102, 103]. It is found that the lay-up influences the dependence of the mid-surface deflection on the angular coordinate.

6.1 Application of Galerkin method

The Galerkin weighted residual method [104] is applied to the governing equation (5.20) in which a functional L acting on the mid-surface transversal displacement $w(r, \theta)$ can be identified. It is defined in the analytical integration region of the rectilinear orthotropic composite annular plate Ω as:

$$L(w) - f = 0 \qquad \text{in } \Omega \tag{6.1}$$

where L is a linear differential operator and f is a known term determined by the radial shear force Q_r and the distributed load $q(r, \theta)$. Additionally, equation (6.1) must be solved keeping in mind both essential and natural boundary conditions that are formulated on the boundary of the integration region Ω.

The Galerkin method states each unknown displacement component s to be written as a finite linear combination of approximation functions:

$$s \approx S_N = \varphi_0 + \sum_{j=1}^{N} c_j \ \varphi_j \tag{6.2}$$

In this expression, as required by the weighted residual methods, the terms φ_j are approximation functions that must be a continuous, linearly independent and complete set of functions fulfilling the homogeneous form of both essential and natural boundary conditions. On the other hand, φ_0 is the approximation function needed to satisfy the non-homogeneous boundary conditions if any is required, whereas c_j are unknown coefficients that serve as weights for the N approximation functions.

As previously outlined, the final objective of the work is providing a reference model for the simulation of a composite bolted joint. The reference model appropriate to the scope is represented by a composite annular plate with rectilinear orthotropy, restrained with fully clamped conditions at the outer radius along with a rigid core at the inner radius. Consequently, the approximation functions must be compliant with following boundary conditions which follow from the applied set of displacement constraints:

$$\begin{aligned} &(I)\ w(a, \theta) = 0; \qquad && (II)\ \frac{\partial w(a, \theta)}{\partial r} = 0; \\ &(III)\ \frac{\partial w(b, \theta)}{\partial r} = 0; \\ &(IV)\ w(b, \theta) = const \ \ \forall \theta \Rightarrow \ \frac{\partial w(b, \theta)}{\partial \theta} = 0. \end{aligned} \tag{6.3}$$

Conditions (I) and (II) state null deflection and rotation in radial plane along the outer edge of the composite annular plate, the (III) imposes null rotation in radial plane at the inner radius and the

(IV) prescribes constant deflection at the inner edge, i.e. not variable with circumferential coordinate θ.

The deflection surface of the rectilinear orthotropic composite circular plate presents no axisymmetry because of the bending stiffness variability along the circumferential direction; in fact, the laminate deflection surface presents a trigonometric dependence on the angular coordinate θ. To keep this aspect into account, the approximate form of the mid-surface deflection $W_N(r,\theta)$ is considered as the superimposition of a medium and constant (in reference to θ) component of vertical displacement to which a perturbation contribution is added. Equation (6.2) can be written in terms of approximation functions as:

$$w(r,\theta) \approx W_N(r,\theta) = \overline{W}_M(r) + \widetilde{W}_N(r,\theta) = \sum_{j=1}^{M} c_j \ \varphi_j(r) + \sum_{j=M+1}^{N} c_j \ \varphi_j(r,\theta) \tag{6.4}$$

in this expression $\overline{W}_M$ and $\widetilde{W}_N$ denote the approximate forms of the medium component of mid-surface deflection and of its fluctuation determined by material properties variation, respectively; φ_0 is null as all the boundary conditions are homogeneous.

The approximation functions utilized are polynomials and their search is distinct for what concern $\overline{W}_M(r)$ and $\widetilde{W}_N(r,\theta)$. Indeed, the medium component of transversal displacement depends only on the radial coordinate r and subsequently the (IV) boundary condition is automatically verified, meanwhile the other three are respected by a polynomial series. Then, the medium component of transversal displacement is expressed as:

$$\overline{W}_M(r) = \sum_{j=1}^{M} c_j \ \left((r-a)^{j+2} - \frac{j+2}{j+1}(b-a)(r-a)^{j+1} \right) \tag{6.5}$$

in which the lowest degree term capable of satisfying the boundary conditions is a cubic polynomial.

According to the circumferentially variable approximate mid-surface deflection component $\widetilde{W}_N(r,\theta)$, the approximation functions $\varphi_j(r,\theta)$ are expressed through the product of two functions, so this contribution to the approximate mid-surface deflection is:

$$\widetilde{W}_N(r,\theta) = \sum_{j=M+1}^{N} c_j \ f_j(r) \ g(\theta) \tag{6.6}$$

where $f_j(r)$ is a function that depends only on the radial coordinate r and is needed to verify the boundary conditions (6.3); whereas the function $g(\theta)$ introduces the deflection variability with the circumferential coordinate θ. In particular, in order to fulfill the boundary condition (IV) providing a uniform transversal displacement at the inner radius, the function $f_j(r)$ must vanish at the radius b despite the actual displacement experimented by the composite annular plate is other than zero. This aspect emphasizes the role played by the contribution $\widetilde{W}_N(r,\theta)$ to the mid-surface deflection, i.e. to provide an estimation of its fluctuation connected to the circumferentially variable bending stiffness. Even in this case, a polynomial function was chosen to characterize $f_j(r)$ whereas $g(\theta)$ is a trigonometric function depending on the lay-up of the composite annular plate. Specifically, the following forms of $g(\theta)$ were determined for the two symmetrical lay-ups here considered:

- QI lay-up

$$g(\theta) = \sin\left(2\theta + \frac{\pi}{4}\right) \tag{6.7}$$

- 0D lay-up

$$g(\theta) = \cos\left(2\theta - \frac{\pi}{8}\right) \tag{6.8}$$

The weight coefficients c_j can be found by means of a linear system where the N algebraic equations state the annulment of the weighted residual form of the governing equation (5.20):

$$\sum_{j=1}^{N} G_{ij}\ c_j - F_i = 0, \qquad i = 1, 2, \ldots, N \tag{6.9}$$

in which:

$$\begin{aligned} G_{ij} &= \int_b^a \int_{-\pi}^{\pi} \varphi_i\ L(\varphi_j)\ d\theta\ r dr \\ F_i &= \int_b^a \int_{-\pi}^{\pi} \varphi_i\ f\ d\theta\ r dr \end{aligned} \tag{6.10}$$

As required by Galerkin method, the weight functions coincide with the approximation functions.

In the realization of the case studies, presented in the following, 7 terms of the series $W_N(r,\theta)$ were taken into account. Specifically, a 6 terms series $\overline{W}_M(r)$ was employed, i.e. polynomial terms from the third to the eighth degree; meanwhile, a one term series $\widetilde{W}_N(r,\theta)$ was used:

$$\widetilde{W}_7(r,\theta) = c_7(r-a)^2(r-b)^2 g(\theta) \tag{6.11}$$

being $f_7(r)$ a fourth degree polynomial which fulfills the boundary conditions (6.3).

6.2 Results

In the following case-studies, some numerical applications of the presented method are reported and compared with the outcomes of finite element analyses, performed with refined FE models featuring 4 noded layered shell finite elements with 6 DOFs per node. The proposed method was employed for the solution of QI and 0D composite annular plates with different geometrical characteristics. These kinds of lay-up are commonly used to realize composite plates to be connected with bolted joints, [52, 56, 58, 59, 60]. In particular, the employed lay-ups (Table 6.1) and the unidirectional fiber-reinforced layer stiffness properties (Table 6.2) are reported in [56]; the layer thickness is $t_{lay} = 0.13$ mm.

Table 6.1: Lay-ups used in the numerical examples.

QI lay-up	0D lay-up
$[45/0/-45/90]_{5s}$	$[(45/0_2/-45/90)_3/45/0_2/-45/0]_s$

The composite annular plates hereinafter analyzed to verify the proposed method reliability are transversally loaded; the external transversal loads acting on the annular plates consist in a unitary force P (see Fig. 5.2) applied to the plate axis, along the z-axis of the cylindrical coordinate system and with the same verse; meanwhile the distributed load $q(r,\theta)$ is null.

Table 6.2: Unidirectional fiber-reinforced layer stiffness properties.

E_{11} [GPa]	E_{22} [GPa]	E_{33} [GPa]	G_{12} [GPa]	G_{13} [GPa]	G_{23} [GPa]	$\nu_{12}[-]$	$\nu_{13}[-]$	$\nu_{23}[-]$
140	10	10	5.2	5.2	3.9	0.3	0.3	0.5

Table 6.3: Mid-surface deflection percentage error, evaluated at $\rho = \beta$, between Galerkin method and FEA results for both lay-ups.

QI lay-up				0D lay-up			
$\frac{t}{a}$	$\Delta_{\beta_1}[\%]$	Δ_{β_2} [%]	Δ_{β_3} [%]	$\frac{t}{a}$	$\Delta_{\beta_1}[\%]$	Δ_{β_2} [%]	Δ_{β_3} [%]
0.02	0.36	0.42	−1.05	0.02	0.34	0.34	−0.92
0.03	−0.76	−0.67	−1.48	0.03	−1.01	−0.72	−1.53
0.04	−3.47	−3.18	−3.48	0.04	−3.96	−1.66	−2.52
0.05	−6.13	−6.31	−6.53	0.05	−7.03	−6.19	−6.72

The comparisons for both QI and 0D laminates were realized with a fixed value of the plate thickness ($t = 5.2$ mm). On the contrary, different slenderness ratios between the thickness t and the external radius a are considered to estimate the validity range of the thin-plate hypothesis in the frame of the Classical Plate Theory.

For both lay-ups and every slenderness ratio, numerical results are presented in terms of dimensionless deflection that is the ratio between the mid-surface deflection $w(r, 0)$ and its value at the inner edge $w(\beta, 0)$ obtained with FE analysis, being the shape ratio $\beta = \frac{b}{a}$. These diagrams show the dimensionless deflection variation along the dimensionless radius $\rho = \frac{r}{a}$, at the angular coordinate $\theta = 0$ rad.

Analogously, the circumferential variation is shown plotting against the dimensionless angle $\overline{\theta} = \frac{\theta}{\pi}$, the dimensionless form of the mid-surface deflection obtained through the ratio between $w(\rho, \overline{\theta})$ and the value at the inner radius $w(\beta, \overline{\theta})$ obtained with FE analysis.

Furthermore, for any given slenderness ratio, three different values of the shape ratio β are investigated to assess its influence on the annular composite plate deformation. The β values here considered are: $\beta_1 = 0.05$, $\beta_2 = 0.1$ and $\beta_3 = 0.2$.

The comparisons reported in Fig. 6.1 and 6.2, showing the mid-surface deflection on the dimensionless radial coordinate for the QI and the 0D lay-ups, indicate a good agreement between the outcomes obtained with the proposed method and the FE analysis ones. In addition, Table 6.3 outlines the percentage error evaluated at the inner radius $\rho = \beta$ between the results of the presented method and the FE ones for both the lay-ups. According to the shape parameter β, it should be noted that this parameter has fundamentally no effect on the accuracy of the presented method; indeed, the percentage error for a fixed slenderness ratio does not undergo a significant modification passing from β_1 to β_3, especially for lower slenderness ratios $\frac{t}{a}$.

Moreover, considering the effect of the slenderness ratio variability on the accuracy of the results provided by the proposed method is helpful to define the limits of validity of the method. As evidenced by the diagrams, the higher the slenderness ratio, the higher the plate shear deformability which causes a bigger deflection at the inner edge of the composite annular plate and non-null slope at the same radius; this effect is clearer for the curves with slenderness ratio $\frac{t}{a} = 0.04$ and 0.05.

The shear deformability influence is not considered in the presented method since the considered theoretical framework is based on the Classical Plate Theory; therefore the percentage error grows with the slenderness ratio for a fixed shape ratio β.

When $\frac{t}{a} = 0.04$ or 0.05, it is possible to remark an inversion of the trend of the error in respect to β. In fact, especially in case of 0D lay-up, the error is higher for β_1. This can be attributed again to shear effects neglecting. In fact, having a more concentrated load distribution on plate along with higher $\frac{t}{a}$ values emphasizes local shear deformations.

The circumferential variation of the mid-surface deflection is outlined in Fig. 6.3 and 6.4, for the QI and the 0D lay-ups respectively, for different values of the dimensionless radius ρ. In this case, the variation with the angular coordinate is reproduced accurately and the accordance between the proposed method and the finite element method is confirmed. The angular variability of the mid-surface deflection is more noticeable for $\rho = 0.4$ and 0.6, whereas for $\rho = 0.2$ and 0.8 the clamping effect of the constraints confines its fluctuation. Anyway, the 0D lay-up features a more pronounced dependence on the angular coordinate: the variation of mid-surface deflection for these types of composite annular plate reaches the 10%; on the other hand, the considered laminates with QI lay-up show a maximum fluctuation, for fixed ρ, of the 5%.

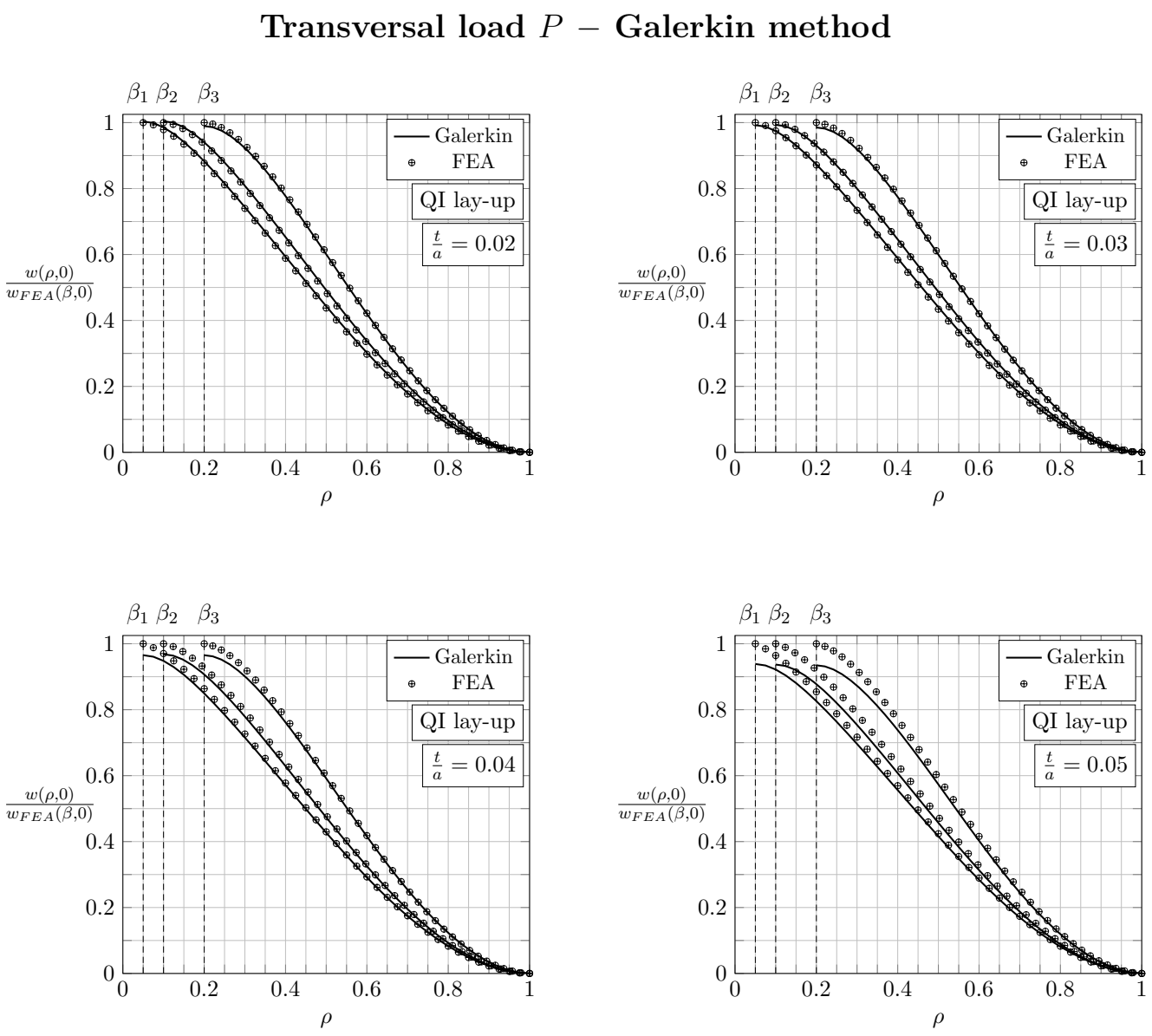

Figure 6.1: Variation of the dimensionless mid-surface deflection along the dimensionless radius ρ, evaluated at $\theta = 0$ rad for different ratios $\frac{t}{a}$ and for $\beta_1 = 0.05$, $\beta_2 = 0.1$ and $\beta_3 = 0.2$ with quasi-isotropic lay-up.

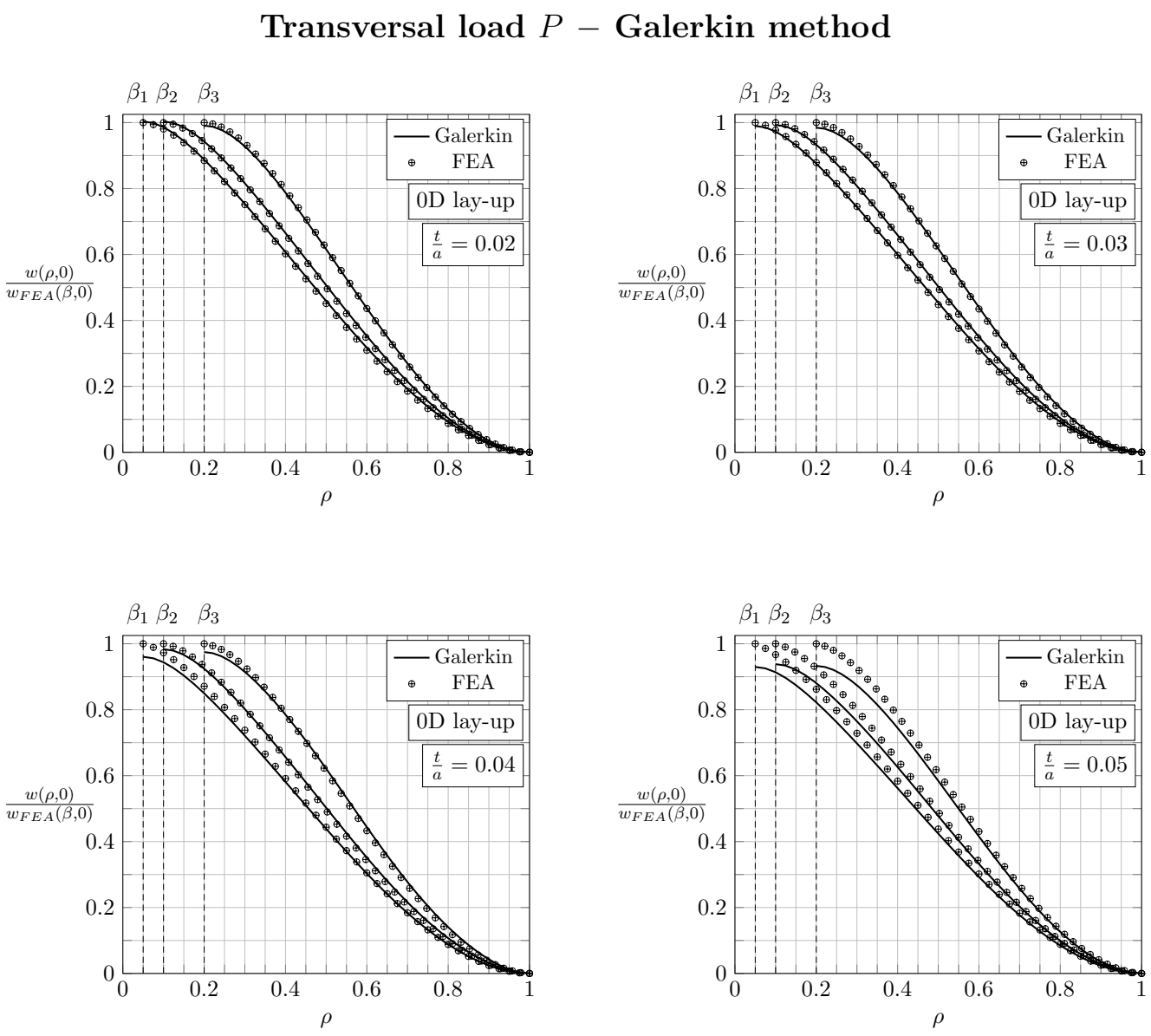

Figure 6.2: Variation of the dimensionless mid-surface deflection along the dimensionless radius ρ, evaluated at $\theta = 0$ rad for different ratios $\frac{t}{a}$ and for $\beta_1 = 0.05$, $\beta_2 = 0.1$ and $\beta_3 = 0.2$ with zero-dominated lay-up.

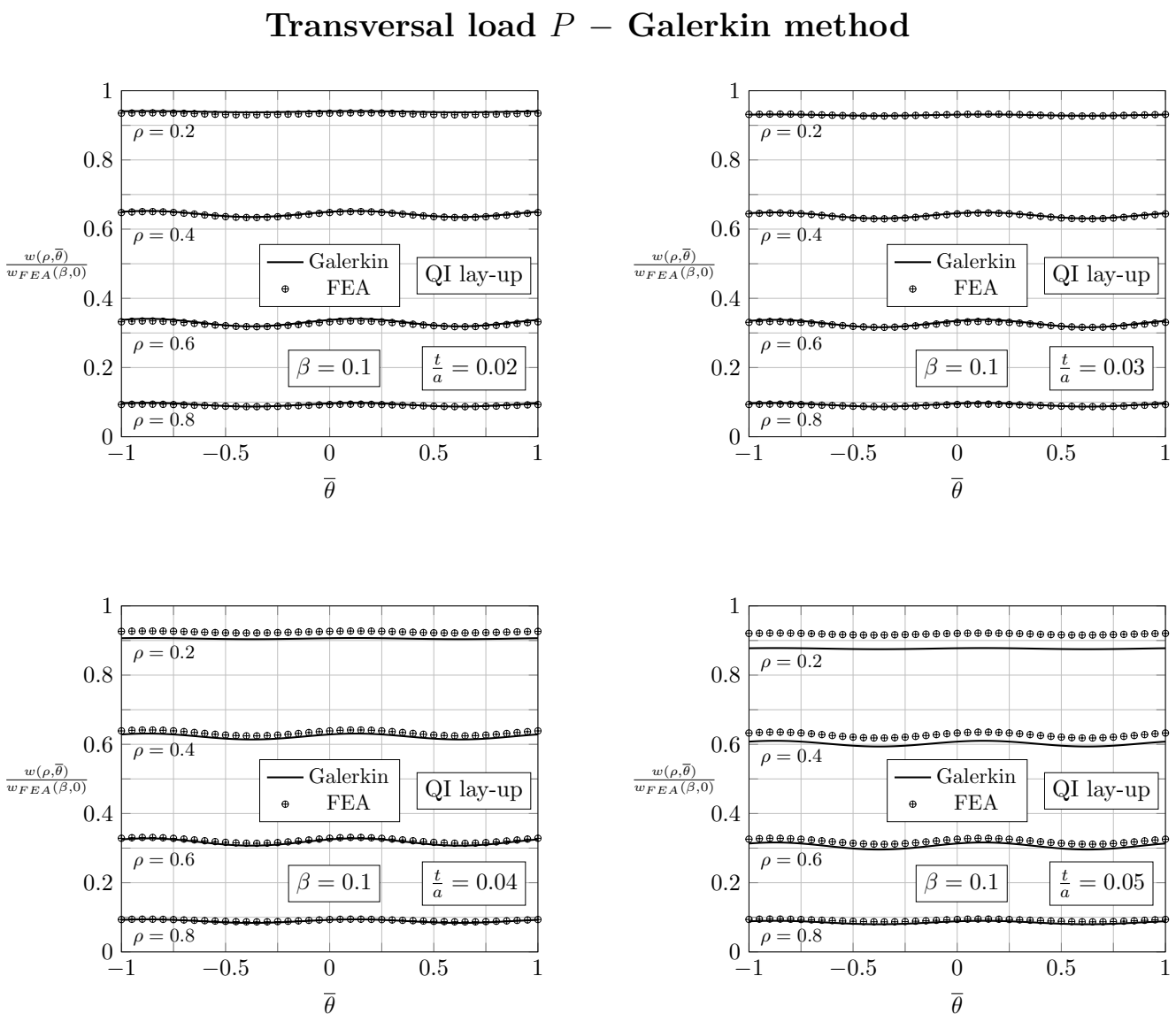

Figure 6.3: Circumferential variation along the dimensionless radial coordinate $\overline{\theta}$ of the dimensionless mid-surface deflection, evaluated for different ratios $\frac{t}{a}$ and for $\beta = 0.1$ at $\rho = 0.2$, 0.4, 0.6 and 0.8 with quasi-isotropic lay-up.

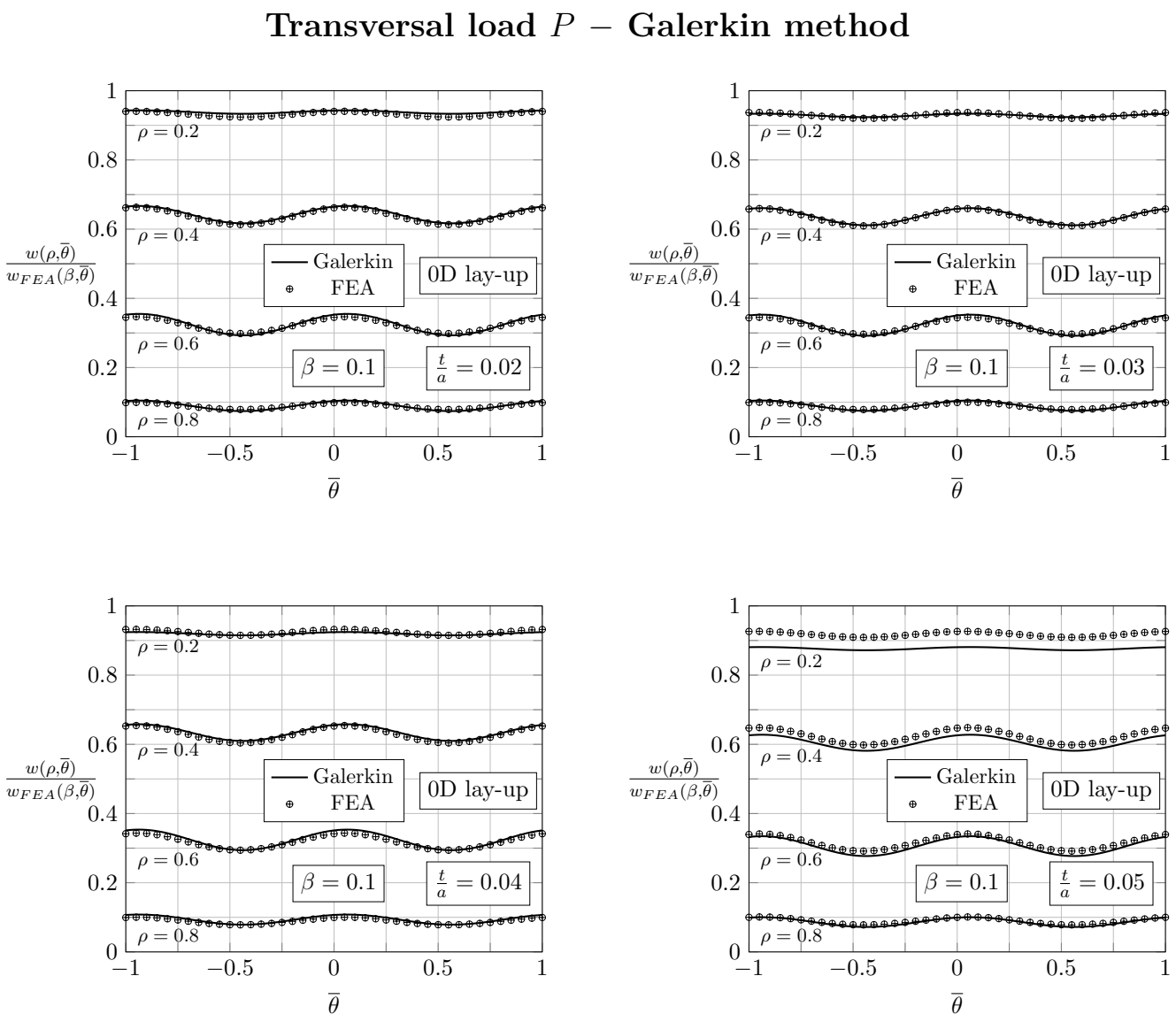

Figure 6.4: Circumferential variation along the dimensionless radial coordinate $\overline{\theta}$ of the dimensionless mid-surface deflection, evaluated for different ratios $\frac{t}{a}$ and for $\beta = 0.1$ at $\rho = 0.2$, 0.4, 0.6 and 0.8 with zero-dominated lay-up.

6.3 Results - Axisymmetric case

The results obtained by means of Galerkin method, applied to the governing equation in axisymmetric form(5.23) previously defined, are presented in comparison with corresponding FE analyses ones, performed with refined FE models featuring 4 noded layered shell finite elements with 6 DOFs per node. The loading condition acting on the theoretical reference model was reproduced setting a fully clamping constraint to the nodes at the outer radius, whereas the rigid inner core was realized connecting the nodes at the inner edge with a radial set of rigid beams to node present at the plate geometrical center where the external transversal load P is applied.

Quasi-isotropic composite annular plates were considered for the case-study and different geometrical features were tested. The quasi-isotropic stacking sequence hereinafter considered is $[45/0/\text{-}45/90]_{5s}$.

The loading condition considered consists in a force P applied to the plate axis, with unitary intensity, acting along the axis and transversally with respect to the plate mid-surface; the distributed load $q(r)$ is not present.

The rectilinear orthotropic composite annular plates analyzed are realized with 40 layers, each layer has thickness $t_{lay} = 0.13$ mm; consequently, the plate thickness results $t = 5.2$ mm.

In the order of ideas of evaluating the reliability and an applicability range of developed Galerkin approach to the transversally loaded rectilinear orthotropic composite annular plate, different slenderness ratios between the thickness t and the external radius a are studied.

Numerical results are reported in dimensionless form. The dimensionless deflection, evaluated as the ratio between mid-surface deflection $w(r)$ and its value at the inner edge $w(\beta)$ taken from FEA, with $\beta = \frac{b}{a}$, is reported in Fig. 6.5 against the dimensionless radius $\rho = \frac{r}{a}$.

Additionally, the inner hole radius effect on the mid-surface deflection is assessed providing results for different values of the β parameter for a fixed slenderness ratio. The β values investigated are: $\beta_1 = 0.05$, $\beta_2 = 0.1$, $\beta_3 = 0.2$.

The results in Fig. 6.5 outline the dimensionless mid-surface deflection as a function of the dimensionless radial coordinate; it can be highlighted that the approximation functions are adequate to satisfy the boundary conditions. Moreover, the outcomes provided by Galerkin method and those obtained through the FE analyses presents a high level of matching, indicating that the presented method represents a reliable instrument for the analysis of rectilinear orthotropic composite plates.

Furthermore, it should be noted that the accuracy of the results is not significantly affected by β value for all the slenderness ratios analyzed even if the percentage error at the inner radius grows with this parameter, as shown in Table 6.4.

About the validity range of the proposed procedure, at the increasing of slenderness ratio the plate shear deformability becomes not negligible. As a result, the diagrams show a bigger misfit between the two mid-surface deflection curves for higher slenderness ratios; this shows the limit of applicability of this approach based on the Classical Plate Theory.

Table 6.4: Mid-surface deflection percentage error, evaluated at $\rho = \beta$, between Galerkin method and FEA results.

$\frac{t}{a}$	$\Delta_{\beta_1}[\%]$	$\Delta_{\beta_2}[\%]$	$\Delta_{\beta_3}[\%]$
0.02	1.88	0.43	0.98
0.03	1.94	3.24	2.35
0.04	4.06	3.03	4.20
0.05	6.30	6.45	7.57

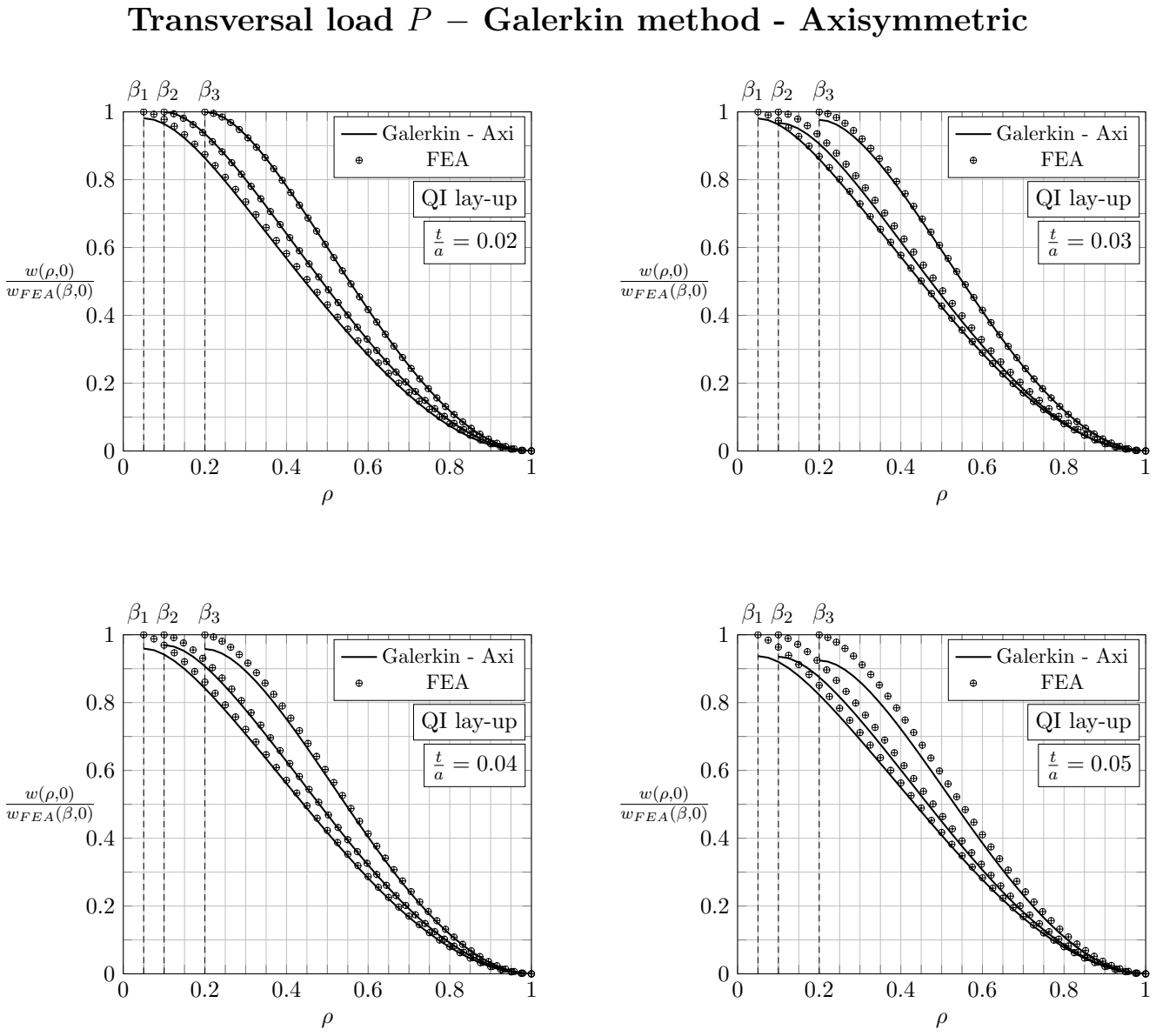

Figure 6.5: Variation of the dimensionless mid-surface deflection along the dimensionless radius for different ratios $\frac{t}{a}$ and for $\beta_1 = 0.05$, $\beta_2 = 0.1$ and $\beta_3 = 0.2$ - Axisymmetric results.

CHAPTER 7

ELASTIC ANALYSIS OF RECTILINEAR ORTHOTROPIC COMPOSITE CIRCULAR PLATES USING RITZ METHOD

In the previous Chapter a first approach to the solution of the spot joint element theoretical reference model for composite bolted joints was provided. A solution methodology which exploits Galerkin method is applied to the originally determined governing equation of the rectilinear orthotropic composite circular plate undergoing only orthogonal loads.

Anyway, this solution method based on the vector approach can hardly be enlarged to the other load conditions needed to characterize the new spot joint theoretical reference model. Indeed, Galerkin method necessitates of approximation functions that are compliant with both essential and natural boundary conditions of the problem and their search results demanding for load conditions more complicated than the transversal load one. The analytical procedure proposed in the present Chapter overcomes these limits through the adoption of the energy approach.

Considering the theoretical reference model of the composite bolted joint, i.e. a composite annular plate clamped at the outer radius and featuring a rigid inner core, the introduction of rectilinear orthotropic material properties, that are intrinsically symmetric in a Cartesian coordinate system, applied to an annular plate, i.e. an axisymmetric geometry, imply a circumferential variation of the in-plane and bending stiffnesses of the composite annular plate and displacement components. Therefore, unlike previous studies about the topic of Spot Joint Element in full axisymmetric hypotheses (i.e. considering plates made with isotropic and homogeneous material), this aspect makes it impossible to obtain closed form solutions.

Consequently, the method here presented is based on the Ritz method along with the virtual displacements principle. The Ritz formulation of the problem is presented in general form and, subsequently, it is particularized for the load conditions involved in the composite bolted joint theoretical reference model, Fig. 7.1, [66, 67]:

- **Transversal load** P applied to the plate axis, i.e. along the z-axis of the cylindrical coordinate system;
- **In-plane load** T acting on the rigid nugget and along the x-axis of the global Cartesian coordinate system;
- **In-plane bending moment** M applied along the x-axis of the global Cartesian coordinate system;
- **Torsional moment** M_T acting orthogonally to the plate mid-surface, along the z-axis of the cylindrical coordinate system.

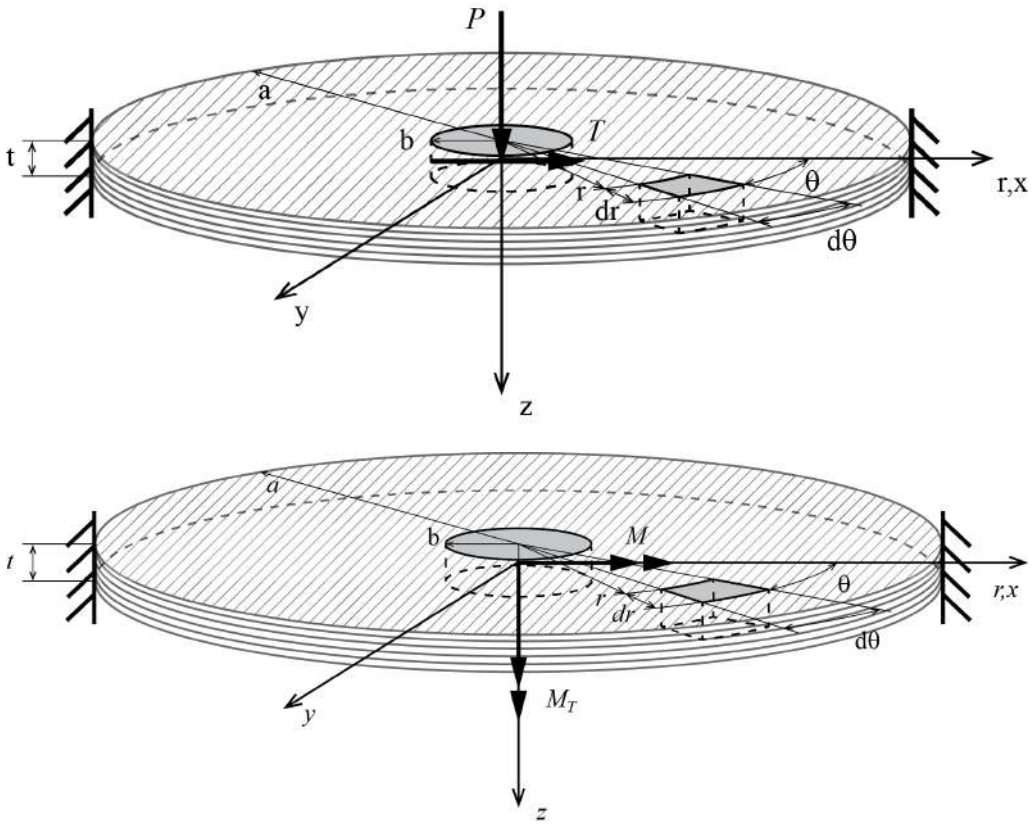

Figure 7.1: Theoretical reference model of composite bolted joint undergoing the four load conditions needed to define the Spot Joint Elemenr stiffness matrix.

As a consequence, these solutions these solutions complete the development of the enhanced Spot Joint Element stiffness matrix.

Furthermore, the derivation of appropriate approximation functions, compliant with the displacement constraints defined by the spot joint theoretical reference model previously outlined, is discussed. Then, the approximation functions are employed in the solution procedure based on Ritz method; in the specific case of transversal load condition the dependence of composite annular plate mid-surface transversal displacement on the angular coordinate is characterized for the two kinds of lay-up considered in the §7.2.

In addition, the effect of the aspect ratio of the composite circular plate on the results for both load conditions is investigated. Different slenderness ratios of the plates are further considered for the transversal and the in-plane bending moment load condition.

Results showing the dependence of displacement components on both radial and circumferential coordinates are compared with results of FE analyses performed with a refined reference model, and the agreement between the results is excellent. Two symmetrical lay-ups commonly employed in literature regarding composite bolted joints (see Refs. [52, 57, 58, 59, 60]) are considered in the Results Section: the quasi-isotropic (QI) and the zero-dominated (0D) ones.

7.1 Application of Ritz method to the principle of virtual works

The Ritz method must be applied in conjunction with an energy principle that accounts for the natural boundary conditions of the problem [104]. The principle of virtual displacements was chosen to the scope:

$$\delta W = \delta W_I + \delta W_E = 0 \tag{7.1}$$

where δW_I and δW_E are, respectively, the internal and the external virtual works. The general expressions of both the internal and the external virtual works for rectilinear orthotropic composite circular plates are:

$$\begin{aligned}\delta W_I = \int_\Omega \sigma_{ij}\ \delta\varepsilon_{ij}\ d\Omega &= \int_\Omega \Big(\sigma_r\ \delta\varepsilon_r + \sigma_\theta\ \delta\varepsilon_\theta + \tau_{r\theta}\ \delta\gamma_{r\theta}\Big)\ d\Omega \\ &= \int_b^a \int_{-\pi}^{\pi} \left[N_r \frac{\partial \delta u}{\partial r} + N_\theta\left(\frac{\delta u}{r} + \frac{1}{r}\frac{\partial \delta v}{\partial \theta}\right) + N_{r\theta}\left(\frac{1}{r}\frac{\partial \delta u}{\partial \theta} + \frac{\partial \delta v}{\partial r}\right) + \right. \\ &\left. - M_r \frac{\partial^2 \delta w}{\partial r^2} - M_\theta \frac{1}{r}\left(\frac{\partial \delta w}{\partial r} + \frac{1}{r}\frac{\partial^2 \delta w}{\partial^2 \theta}\right) - 2M_{r\theta}\frac{\partial^2}{\partial r \partial \theta}\frac{\delta w}{r}\right]\ d\theta\ r dr\end{aligned} \tag{7.2}$$

$$\delta W_E = -\left(\int_\Omega \mathbf{f}\cdot\delta\mathbf{u}\ d\Omega + \int_{\Gamma_\sigma} \mathbf{T}\cdot\delta\mathbf{u}\ d\Gamma\right) \tag{7.3}$$

in which the symbol δ is employed to indicate virtual displacements and strains, Ω is the analytical integration region defining the rectilinear orthotropic composite circular plate, $\mathbf{f}$ denotes the body forces per unit volume, $\mathbf{T}$ the surface tractions per unit area acting on the external boundary portion Γ_σ.

Furthermore, the Ritz method requires each unknown displacement component s to be written as a finite linear combination of approximation functions:

$$s \approx S_N = \varphi_0 + \sum_{j=1}^{N} c_j\ \varphi_j \tag{7.4}$$

in this expression, c_j are unknown coefficients that serve as weights for the N approximation functions φ_j and φ_0 is the approximation function needed to satisfy the non-homogeneous essential boundary conditions if any is required. The approximation functions are required to be a continuous, linear

independent and complete set of functions fulfilling the homogeneous form of the essential boundary conditions.

After the selection of the approximation functions and the substitution of the Eq. (7.4) in the Eq. (7.1), the principle of virtual displacements depends only on the N unknown coefficients and its validity must be assured for every admissible virtual displacement obtained with the δc_i coefficients:

$$\delta W(S_N) = \sum_{i=1}^{N} \frac{\partial W}{\partial c_i} \delta c_i = 0 \quad \forall \delta c_i \quad \Rightarrow \quad \frac{\partial W}{\partial c_i} = 0 \tag{7.5}$$

The validity of Eq. (7.5) requires the solution of a linear system of N algebraic equations to find the N unknown coefficients:

$$\sum_{j=1}^{N} R_{ij}\ c_j - F_i = 0, \qquad i = 1, 2, \ldots, N \tag{7.6}$$

in which the coefficient matrix terms R_{ij} are dependent to the approximation functions, material properties and plate geometry, meanwhile the known terms F_i depend on the external loads.

Afterwards, the algebraic equations system (7.6) is specialized for the different load conditions considered in this work. They consist in an annular plate featuring a rigid core at the inner edge and a fully clamped constraint at the outer one made up of composite material with rectilinear orthotropic properties subject to transversal or in-plane loads.

7.1.1 Transversal load condition

The transversal load condition involves the application of external loads orthogonally with respect to the mid-surface of the plate, such as distributed forces per unit-length acting at the outer or at the inner plate edge, Q_a and Q_b respectively, or a distributed load $q(r, \theta)$. Furthermore, for this specific load condition, the radial u and the circumferential v displacement components of the composite annular plate are null and the only displacement component that must be determined is the mid-surface deflection $w(r, \theta)$. Therefore the general expression of the external virtual work for the transversal load condition is:

$$\delta W_E = -\int_{-\pi}^{\pi} \Big(b\ Q_b\ \delta w(b, \theta) - a\ Q_a\ \delta w(a, \theta) \Big)\ d\theta\ - \int_b^a \int_{-\pi}^{\pi} q(r, \theta)\ \delta w(r, \theta)\ d\theta\ r dr \tag{7.7}$$

Indeed, taking into account a symmetrical lay-up with respect to the composite plate mid-surface, the bending-extension coupling stiffness terms $B_{ij}(\theta)$ are all null and subsequently no in-plane displacements are induced by the plate bending. Additionally, the application of a load transversal to the plate mid-surface does not produce any membrane-shell coupling effect since the thin-plate assumption is considered, consequently the are no components of displacement acting in the plate mid-surface.

Besides, for the same reasons, all the in-plane stress resultants are null and the bending and torque moments in (5.13) depend only on the curvatures:

$$\begin{aligned} M_r &= D_{11}(\theta)\kappa_r + D_{12}(\theta)\kappa_\theta + D_{16}(\theta)\kappa_{r\theta} \\ M_\theta &= D_{12}(\theta)\kappa_r + D_{22}(\theta)\kappa_\theta + D_{26}(\theta)\kappa_{r\theta} \\ M_{r\theta} &= D_{16}(\theta)\kappa_r + D_{26}(\theta)\kappa_\theta + D_{66}(\theta)\kappa_{r\theta} \end{aligned} \tag{7.8}$$

The boundary conditions deriving from the theoretical reference model of composite bolted joint for a transversally loaded composite annular plate are:

- Outer edge of the plate: $r = a$

$$\begin{aligned} &(I)\ w(a,\theta) = 0 \\ &(II)\ \frac{\partial w(a,\theta)}{\partial r} = 0 \\ &(III)\ \frac{1}{a}\frac{\partial w(a,\theta)}{\partial \theta} = 0 \end{aligned} \tag{7.9}$$

- Inner edge of the plate: $r = b$

$$\begin{aligned} &(IV)\ w(b,\theta) = const\ \ \forall\theta \Rightarrow\ \frac{\partial w(b,\theta)}{\partial \theta} = 0 \\ &(V)\ \frac{\partial w(b,\theta)}{\partial r} = 0 \\ &(VI)\ \frac{1}{b}\frac{\partial w(b,\theta)}{\partial \theta} = 0 \end{aligned} \tag{7.10}$$

Null deflection at the outer radius, null rotations around the circumferential and the radial directions at the same radius of the plate are addressed by conditions (I), (II) and (III) respectively. Moreover, condition (IV) imposes constant deflection at the inner radius in reference to the angular coordinate θ, whereas conditions (V) and (VI) state null rotations around the circumferential and the radial directions at the inner edge.

Owing to the circumferentially variable bending stiffnesses, the rectilinear orthotropic composite circular plate mid-surface deflection is not axisymmetric and depends on the angular coordinate θ according to a trigonometric function. As a consequence, the approximate form of the transversal displacement $W_N(r,\theta)$ is expressed as the sum of two contributions: the first one represents the medium component of the transversal deflection, independent of θ coordinate; the second one is representative of the angular perturbation induced on the medium component of displacement by the not-axisymmetry of the material properties. The approximate form of the mid-surface deflection is:

$$w(r,\theta) \approx W_N(r,\theta) = \overline{W}_M(r) + \widetilde{W}_N(r,\theta) = \sum_{j=1}^{M} c_j\ \varphi_j(r)\ +\ \sum_{j=M+1}^{N} c_j\ \varphi_j(r,\theta) \tag{7.11}$$

In Eq. (7.11) the first series $\overline{W}_M(r)$ represents the medium and axisymmetric component of mid-surface deflection, the latter $\widetilde{W}_N(r,\theta)$ is the angular perturbation needed to take into account the variable bending stiffnesses. Being all the boundary conditions homogeneous, φ_0 is null.

The series representing the medium component of mid-surface deflection $\overline{W}_M(r)$ automatically fulfills the (III), (IV) and (VI) boundary conditions being exclusively function of the radial coordinate r. The other boundary conditions are verified by a polynomial series, starting from the cubic term, that is:

$$\overline{W}_M(r) = \sum_{j=1}^{M} c_j\ \left((r-a)^{j+2} - \frac{j+2}{j+1}(b-a)(r-a)^{j+1}\right) \tag{7.12}$$

On the other hand, the approximation functions $\varphi_j(r,\theta)$ for the angular perturbation mid-surface deflection component $\widetilde{W}_N(r,\theta)$ are defined as the product of a function $f_j(r)$, that only depends on the radial coordinate r, and a function $g(\theta)$ which in turn is function of the only angular coordinate θ:

$$\widetilde{W}_N(r,\theta) = \sum_{j=M+1}^{N} c_j \; f_j(r) \; g(\theta) \tag{7.13}$$

Specifically, the purpose of the function $f_j(r)$ is the fulfillment of the boundary conditions (7.9) and (7.10); consequently, to respect the boundary condition (IV) which prescribes a uniform transversal displacement at the inner edge of the annular plate, it must vanish at the inner radius b, even if the actual displacement of the composite annular plate at the inner edge is not null. This characteristic underlines the task carried out by the contribution $\widetilde{W}_N(r,\theta)$: it represents the circumferential fluctuation of the composite annular plate mid-surface deflection own to the θ-dependent bending stiffnesses. In addition, this structure of mid-surface deflection component $\widetilde{W}_N(r,\theta)$ further fulfills the (III) and (VI) of boundary conditions (7.9) and (7.10).

Furthermore, the function $g(\theta)$ is a trigonometric function needed to take into account the circumferential variation of the mid-surface deflection in question and it assumes a specific form according to the lay-up of the composite annular plate. The two symmetrical lay-ups analyzed in the subsequent Section feature the following forms of the trigonometric function $g(\theta)$:

- QI lay-up

$$g(\theta) = \sin\left(2\theta + \frac{\pi}{4}\right) \tag{7.14}$$

- 0D lay-up

$$g(\theta) = \cos\left(2\theta - \frac{\pi}{8}\right) \tag{7.15}$$

The case studies discussed in §7.2 make use of a series $W_N(r,\theta)$ composed of 10 terms. In particular, a 9 terms series $\overline{W}_M(r)$, with polynomial terms from the third to the eleventh degree, was utilized together with a one term series $\widetilde{W}_N(r,\theta)$. A polynomial function was used for the function $f_{10}(r)$ that appears in this last series term, it has the following form:

$$\widetilde{W}_{10}(r,\theta) = c_{10}(r-a)^2(r-b)^2 g(\theta) \tag{7.16}$$

For what concerns the determination of the scalar coefficients c_j, the substitution of the approximate form of transversal displacement outlined in (7.11) in the principle of virtual displacements (7.5) returns a linear system of the type (7.6) whose matrix coefficients terms are:

$$R_{ij} = \int_b^a \int_{-\pi}^{\pi} \left\{\Phi_i\right\}^T \left[D(\theta)\right] \left\{\Phi_j\right\} \; d\theta \; r dr \tag{7.17}$$

in which:

$$\left\{\Phi_{i,j}\right\} = \begin{Bmatrix} \frac{\partial \varphi_{i,j}^2}{\partial r^2} \\ \frac{1}{r}\left(\frac{\partial \varphi_{i,j}}{\partial r} + \frac{1}{r}\frac{\partial \varphi_{i,j}^2}{\partial \theta^2}\right) \\ 2\frac{\partial \varphi_{i,j}^2}{\partial r \partial \theta} \end{Bmatrix} \tag{7.18}$$

Additionally, according to the expression of the external virtual work in (7.7), the known terms in the general case where different kinds of load act on the annular plate are:

$$F_i = \int_{-\pi}^{\pi} \Big(b\ Q_b\ \varphi_i(b,\theta) - a\ Q_a\ \varphi_i(a,\theta) \Big)\ d\theta\ + \int_b^a \int_{-\pi}^{\pi} q(r,\theta)\ \varphi_i(r,\theta)\ d\theta\ r dr \tag{7.19}$$

In order to solve a load condition aimed to the definition of a custom composite bolted joint finite element stiffness matrix, the transversal load of interest is represented by a force P applied to the annular plate axis, in correspondence of the rigid core, directed as the z-axis of cylindrical coordinate system. Then, a distributed force per unit-length acting at the inner edge of the plate $Q_b = \frac{P}{2\pi b}$ is considered.

7.1.2 In-plane load condition

The load condition described below considers the rectilinear orthotropic composite annular plate subject to a load T, applied in correspondence of the symmetry axis, acting on its mid-surface along the x-axis of the global Cartesian coordinate system. Accordingly, the external virtual work turns out to be:

$$\delta W_E = -\left(\frac{T}{2} \delta u(b,0) - \frac{T}{2} \delta u(b,\pi) \right) \tag{7.20}$$

This expression was obtained keeping in mind that the application point of the in-plane load T does not belong to the annular plate integration domain Ω, so the external load was considered split in two contributions, acting along its direction, and applied at the inner radius b of the composite annular plate.

The stress resultants developed by this load condition on the composite annular plate are in-plane forces exclusively dependent on the mid-surface strains:

$$\begin{aligned} N_r &= A_{11}(\theta)\varepsilon_r^0 + A_{12}(\theta)\varepsilon_\theta^0 + A_{16}(\theta)\gamma_{r\theta}^0 \\ N_\theta &= A_{12}(\theta)\varepsilon_r^0 + A_{22}(\theta)\varepsilon_\theta^0 + A_{26}(\theta)\gamma_{r\theta}^0 \\ N_{r\theta} &= A_{16}(\theta)\varepsilon_r^0 + A_{26}(\theta)\varepsilon_\theta^0 + A_{66}(\theta)\gamma_{r\theta}^0 \end{aligned} \tag{7.21}$$

In fact, as previously outlined, the composite annular plate is considered to have an uncoupled bending-extension behavior because of the theoretical background that is founded on the Classical Plate Theory which regards thin-plates and owing to the symmetric lay-up that makes to vanish the $\big[B(\theta)\big]$ stiffness matrix. As a result of these hypotheses, the action of the in-plane load T does not produce any moment stress resultant as well as no mid-surface transversal displacement w. Thus, the unknown displacement components to be determined are those along the radial and the circumferential direction, u and v respectively.

According to the theoretical reference model of composite bolted joints, the constraints imposed to the radial u and the circumferential v displacement components are:

- Outer edge of the plate: $r = a$

$$\begin{gathered} (i)\ u(a,\theta) = 0 \\ \\ (ii)\ v(a,\theta) = 0 \end{gathered} \tag{7.22}$$

- Inner edge of the plate: $r = b$

$$(iii)\ u(b,0) = -v\left(b, \frac{\pi}{2}\right) \tag{7.23}$$

these boundary conditions considers the effects of the clamping conditions (i and ii) and of the central rigid core at the inner edge of the plate (iii).

The approximate forms of the in-plane displacement components u and v are:

$$\begin{aligned} u(r,\theta) &\approx U_N(r,\theta) = c_0\ \varphi_0(r,\theta) + \sum_{j=1}^{N} c_j\ \varphi_j(r,\theta) \\ v(r,\theta) &\approx V_M(r,\theta) = k_0\ \psi_0(r,\theta) + \sum_{l=1}^{M} k_l\ \psi_l(r,\theta) \end{aligned} \tag{7.24}$$

The employment of the φ_0 and ψ_0 approximation functions is related to the fact that at the inner radius the radial and the circumferential displacement components are other than zero but not known a priori.

Furthermore, the substitution of the approximated displacement components (7.24) in the (iii) boundary condition is helpful to characterize them:

$$c_0\ \varphi_0(b,0) + \sum_{j=1}^{N} c_j\ \varphi_j(b,0) + \ \ + \ k_0\ \psi_0\left(b, \frac{\pi}{2}\right) + \sum_{l=1}^{M} k_l\ \psi_l\left(b, \frac{\pi}{2}\right) = 0 \tag{7.25}$$

Primarily, the terms of the series featuring the approximation functions φ_j and ψ_l cannot be equal and opposite: in that case the trends of the radial u and circumferential v displacement components would result the same meanwhile they are distinct; therefore, in order to verify Eq. (7.25), they must necessarily vanish at the inner edge of the composite annular plate. Conversely, the terms with the approximation functions φ_0 and ψ_0 must be equal and opposite, so it is assumed that the scalar coefficients $c_0 = k_0$ and that the approximation functions $\varphi_0(b,0)$ and $\psi_0\left(b, \frac{\pi}{2}\right)$ are equal and opposite.

These necessities regarding the fulfillment of the the boundary conditions (7.22) and (7.23) are satisfied by a structure of the approximation functions which consists in the product of two functions: the first one exclusively depending on the radial coordinate r, equal for both the approximation functions $\varphi_{0,j}(r,\theta)$ and $\psi_{0,l}(r,\theta)$, and the second one that is a trigonometric function. Then, the approximation functions here considered are:

$$\begin{aligned} \varphi_{0,j}(r,\theta) &= p_{0,j}(r)\cos(\theta) \\ \psi_{0,l}(r,\theta) &= p_{0,l}(r)\Big(-\sin(\theta)\Big) \end{aligned} \tag{7.26}$$

Moreover, the choice of the cosinusoidal function for the approximation functions $\varphi_{0,j}$ is justified by the necessity of achieving a radial displacement that is maximum along the direction of the external load T and null along the orthogonal direction; analogously, the circumferential displacement must result null at the angular coordinate $\theta = 0$ and maximum in amplitude for $\theta = \frac{\pi}{2}$.

The results hereinafter presented in §7.2 are obtained with 7 terms for each of the series $U_N(r,\theta)$ and $V_M(r,\theta)$ representing the discretized forms of the radial and the circumferential displacement components respectively. The functions $p(r)$ cannot be expressed through a general form, so the functions from $p_0(r)$ to $p_6(r)$ employed in the numerical examples are listed in the Appendix A.

The application of Ritz method to the principle of virtual displacements in (7.5) for the in-plane load condition returns the following system of algebraic equations that must be solved to determine the weight coefficients of the approximation functions:

$$\left[\begin{array}{c|c|c} R_{00}^{1x1} & R_{0j}^{1xN} & R_{0l}^{1xM} \\ \hline R_{i0}^{Nx1} & R_{ij}^{NxN} & R_{il}^{NxM} \\ \hline R_{k0}^{Mx1} & R_{kj}^{MxN} & R_{kl}^{MxM} \end{array}\right] \begin{Bmatrix} c_0 \\ \vdots \\ c_j \\ \vdots \\ k_l \\ \vdots \end{Bmatrix} = \begin{Bmatrix} F_0 \\ \vdots \\ 0 \\ \vdots \\ 0 \\ \vdots \end{Bmatrix} \tag{7.27}$$

keeping in mind that the scalar coefficients c_0 and k_0 are equal. Furthermore, in the coefficient matrix of the system of algebraic equations (7.27), different submatrices can be identified whose elements are:

$$R_{00} = \int_b^a \int_{-\pi}^{\pi} \left\{\Upsilon_0\right\}^T \left[A(\theta)\right] \left\{\Upsilon_0\right\} \, d\theta \, r dr \tag{7.28a}$$

$$R_{0j} = \int_b^a \int_{-\pi}^{\pi} \left\{\Upsilon_0\right\}^T \left[A(\theta)\right] \left\{\Phi_j\right\} \, d\theta \, r dr \tag{7.28b}$$

$$R_{0l} = \int_b^a \int_{-\pi}^{\pi} \left\{\Upsilon_0\right\}^T \left[A_1(\theta)\right] \left\{\Psi_l\right\} \, d\theta \, r dr \tag{7.28c}$$

$$R_{i0} = \int_b^a \int_{-\pi}^{\pi} \left\{\Phi_i\right\}^T \left[A(\theta)\right] \left\{\Upsilon_0\right\} \, d\theta \, r dr \tag{7.28d}$$

$$R_{ij} = \int_b^a \int_{-\pi}^{\pi} \left\{\Phi_i\right\}^T \left[A(\theta)\right] \left\{\Phi_j\right\} \, d\theta \, r dr \tag{7.28e}$$

$$R_{il} = \int_b^a \int_{-\pi}^{\pi} \left\{\Phi_i\right\}^T \left[A_1(\theta)\right] \left\{\Psi_l\right\} \, d\theta \, r dr \tag{7.28f}$$

$$R_{k0} = \int_b^a \int_{-\pi}^{\pi} \left\{\Psi_k\right\}^T \left[A_1(\theta)\right]^T \left\{\Upsilon_0\right\} \, d\theta \, r dr \tag{7.28g}$$

$$R_{kj} = \int_b^a \int_{-\pi}^{\pi} \left\{\Psi_k\right\}^T \left[A_1(\theta)\right]^T \left\{\Phi_j\right\} \, d\theta \, r dr \tag{7.28h}$$

$$R_{kl} = \int_b^a \int_{-\pi}^{\pi} \left\{\Psi_k\right\}^T \left[A_2(\theta)\right] \left\{\Psi_l\right\} \, d\theta \, r dr \tag{7.28i}$$

(7.28j)

where:

$$\{\Upsilon_0\} = \begin{Bmatrix} \frac{\partial \varphi_0}{\partial r} \\ \frac{\varphi_0}{r} + \frac{1}{r}\frac{\partial \psi_0}{\partial \theta} \\ \frac{1}{r}\frac{\partial \varphi_0}{\partial \theta} + \frac{\partial \psi_0}{\partial r} - \frac{\psi_0}{r} \end{Bmatrix} \qquad \{\Phi_{i,j}\} = \begin{Bmatrix} \frac{\partial \varphi_{i,j}}{\partial r} \\ \frac{\varphi_{i,j}}{r} \\ \frac{1}{r}\frac{\partial \varphi_{i,j}}{\partial \theta} \end{Bmatrix} \qquad \{\Psi_{k,l}\} = \begin{Bmatrix} \frac{1}{r}\frac{\partial \psi_{k,l}}{\partial \theta} \\ \frac{\partial \psi_{k,l}}{\partial r} - \frac{\psi_{k,l}}{r} \end{Bmatrix} \tag{7.29}$$

$$[A_1(\theta)] = \begin{bmatrix} A_{12}(\theta) & A_{16}(\theta) \\ A_{22}(\theta) & A_{26}(\theta) \\ A_{26}(\theta) & A_{66}(\theta) \end{bmatrix} \qquad [A_2(\theta)] = \begin{bmatrix} A_{22}(\theta) & A_{26}(\theta) \\ A_{26}(\theta) & A_{66}(\theta) \end{bmatrix} \tag{7.30}$$

The non null element of the known terms vector is due to the external virtual work that the in-plane load T accomplishes on the virtual displacement at the inner edge which is determined by the approximation function φ_0, the only one that does not vanish at the internal radius b. It has the form:

$$F_0 = \frac{T}{2}\varphi_0(b,0) - \frac{T}{2}\varphi_0(b,\pi) \tag{7.31}$$

where, as previously discussed, in order to apply the external load T on the integration domain Ω of the annular plate, it was halved into two forces acting at the inner edge and in correspondence of the angular coordinates $\theta = 0$ and $\theta = \pi$, i.e. alongside the direction of the load T.

7.1.3 In-plane bending moment

The load condition hereinafter discussed regards the rectilinear orthotropic composite annular plate undergoing an in-plane bending moment M acting on its mid-surface along the x-axis of the global Cartesian coordinate system. As a consequence, the external virtual work is:

$$\delta W_E = -\left(\frac{M}{2}\frac{1}{b}\frac{\partial \delta w(b,0)}{\partial \theta} - \frac{M}{2}\frac{1}{b}\frac{\partial \delta w(b,\pi)}{\partial \theta} \right) \tag{7.32}$$

It should be noted that the application point of the in-plane bending moment M does not belong to the annular plate integration domain Ω, so the external load was considered halved in two contributions, acting along its direction, and applied at the inner radius b of the composite annular plate and at the angular coordinates $\theta = 0$ and $\theta = \pi$.

The solution of the composite annular plate subject to this load condition involves exclusively the determination of the mid-surface deflection $w(r,\theta)$, being the radial u and the circumferential v displacement components null. Indeed, taking into account a symmetrical lay-up with respect to the composite plate mid-surface, the bending-extension coupling stiffness terms $B_{ij}(\theta)$ are all null and subsequently no in-plane displacements are induced by the plate bending. Additionally, the application of an in-plane bending moment does not produce any membrane-shell coupling effect since the thin-plate assumption is considered, consequently the are no components of displacement acting in the plate mid-surface.

Accordingly, the in-plane stress resultants vanish and the bending and torque moments in (5.13)

are only functions of the curvatures being the mid-surface strains null:

$$\begin{aligned} M_r &= D_{11}(\theta)\kappa_r + D_{12}(\theta)\kappa_\theta + D_{16}(\theta)\kappa_{r\theta} \\ M_\theta &= D_{12}(\theta)\kappa_r + D_{22}(\theta)\kappa_\theta + D_{26}(\theta)\kappa_{r\theta} \\ M_{r\theta} &= D_{16}(\theta)\kappa_r + D_{26}(\theta)\kappa_\theta + D_{66}(\theta)\kappa_{r\theta} \end{aligned} \tag{7.33}$$

The theoretical reference model of composite bolted joint for a composite annular plate undergoing an in-plane bending moment imposes the following boundary conditions:

- Outer edge of the plate: $r = a$

$$\begin{gathered} (I)\ w(a,\theta) = 0 \\ (II)\ \frac{\partial w(a,\theta)}{\partial r} = 0 \\ (III)\ \frac{1}{a}\frac{\partial w(a,\theta)}{\partial \theta} = 0 \end{gathered} \tag{7.34}$$

- Inner edge of the plate: $r = b$

$$(IV)\ \frac{\partial w(b,\theta)}{\partial r} = \frac{w(b,\theta)}{b} \tag{7.35}$$

The boundary condition (I) states null deflection at the outer edge of the composite annular plate, whereas boundary conditions (II) and (III) impose null rotations around the circumferential and the radial direction, respectively. Then, owing to the rigid core, condition (IV) addresses that the rotation around the circumferential direction evaluated at the inner radius must be equal to the ratio between the deflection, at the same radial coordinate, and the inner radius.

According to the load condition and the material properties, the mid-surface deflection of the rectilinear orthotropic composite circular plate turns out to be not-axisymmetric, so the approximate form of the transversal displacement $W_N(r,\theta)$ features approximation functions $\varphi_j(r,\theta)$ that are defined as the product of a function $f_j(r)$, that only depends on the radial coordinate r, and a function $g(\theta)$ which in turn is function of the only angular coordinate θ:

$$w(r,\theta) \approx W_N(r,\theta) = \sum_{j=1}^{N} c_j\ \varphi_j(r,\theta) = \sum_{j=1}^{N} c_j\ f_j(r)g(\theta) \tag{7.36}$$

In particular, the purpose of the function $f_j(r)$ is the fulfillment of the boundary conditions (7.34) and (7.35); moreover, the function $g(\theta)$ is a trigonometric function needed to take into account the dependence on the angular coordinate θ of the mid-surface deflection caused by the in-plane bending moment which, considering the specific disposition of the external load, results being of sinusoidal type.

The results hereinafter presented in §7.2 are obtained with 10 terms of the series $W_N(r,\theta)$ representing the discretized form of the mid-surface transversal displacement. The functions $f(r)$ cannot

be expressed through a general form, so the functions from $f_1(r)$ to $f_{10}(r)$ employed in the numerical examples are listed in the Appendix B.

A linear system of the type (7.6) to determine the scalar coefficients c_j is defined through the substitution of the approximate form of transversal displacement, expressed in (7.36), in the principle of virtual displacements (7.5). The matrix coefficients features terms of the type:

$$R_{ij} = \int_b^a \int_{-\pi}^{\pi} \left\{\Phi_i\right\}^T \left[D(\theta)\right] \left\{\Phi_j\right\} \; d\theta \; r dr \tag{7.37}$$

where:

$$\left\{\Phi_{i,j}\right\} = \begin{Bmatrix} \frac{\partial \varphi_{i,j}^2}{\partial r^2} \\ \frac{1}{r}\left(\frac{\partial \varphi_{i,j}}{\partial r} + \frac{1}{r}\frac{\partial \varphi_{i,j}^2}{\partial \theta^2}\right) \\ 2\frac{\partial \varphi_{i,j}^2}{\partial r \partial \theta} \end{Bmatrix} \tag{7.38}$$

Moreover, as can be deduced from the the external virtual work outlined in Eq. (7.32), the known terms of the linear system for the in-plane bending moment load condition are:

$$F_i = \frac{M}{2}\frac{1}{b}\frac{\partial \varphi_i(b,0)}{\partial \theta} - \frac{M}{2}\frac{1}{b}\frac{\partial \varphi_i(b,\pi)}{\partial \theta} \tag{7.39}$$

where, in order to transfer the in-plane bending moment M on the integration domain Ω of the annular plate, it was split into two bending moments acting at the inner radius and in correspondence of the angular coordinates $\theta = 0$ and $\theta = \pi$, i.e. alongside the direction of the external load M.

7.1.4 Torsional moment

The present load condition involves the action of a torsional moment M_T in correspondence of the symmetry axis of the rectilinear orthotropic composite annular plate, directed as the z-axis of the cylindrical coordinate system, and applied to the rigid core.

In addition, since the rigid core does not belong to the integration domain Ω where the annular plate is defined, a statically equivalent couple of parallel and self-balanced forces P_T acting at the inner edge of the plate and at the angular coordinates $\theta = 0$ and $\theta = \pi$ is analyzed instead of the torsional moment T; the external virtual work turns out to be:

$$\delta W_E = -\Big(P_T \delta v(b,0) + P_T \delta v(b,\pi)\Big) \tag{7.40}$$

The stress resultants developed by this load condition on the composite annular plate are in-plane forces exclusively dependent on the mid-surface strains:

$$\begin{aligned} N_r &= A_{11}(\theta)\varepsilon_r^0 + A_{12}(\theta)\varepsilon_\theta^0 + A_{16}(\theta)\gamma_{r\theta}^0 \\ N_\theta &= A_{12}(\theta)\varepsilon_r^0 + A_{22}(\theta)\varepsilon_\theta^0 + A_{26}(\theta)\gamma_{r\theta}^0 \\ N_{r\theta} &= A_{16}(\theta)\varepsilon_r^0 + A_{26}(\theta)\varepsilon_\theta^0 + A_{66}(\theta)\gamma_{r\theta}^0 \end{aligned} \tag{7.41}$$

In fact, as previously outlined, the composite annular plate is considered to have an uncoupled bending-extension behavior because of the theoretical background that is founded on the Classical Plate Theory which regards thin-plates and owing to the symmetric lay-up that makes to vanish

the $\left[B(\theta)\right]$ stiffness matrix. As a result of these hypotheses, the action of the torsional moment M_T does not produce any moment stress resultant as well as no mid-surface transversal displacement w. Moreover, the only displacement component to be determined is the one along the circumferential direction v as the radial displacement u is not induced by the external load.

According to the theoretical reference model of composite bolted joints, the constraints imposed to the circumferential v displacement components are:

- Outer edge of the plate: $r = a$

$$(i)\ v(a,\theta) = 0 \tag{7.42}$$

- Inner edge of the plate: $r = b$

$$(ii)\ \frac{\partial v(b,\theta)}{\partial \theta} = 0 \tag{7.43}$$

The condition (i), deriving from the clamped conditions at the outer radius, states null circumferential displacement at this radius coordinate; furthermore, the condition (ii) prescribes constant circumferential displacement, in reference to the angular coordinate θ, at the inner radius because of the internal rigid core.

Owing to the circumferentially variable bending stiffnesses, the rectilinear orthotropic composite circular plate circumferential displacement is not axisymmetric and depends on the angular coordinate θ according to a trigonometric function. As a consequence, its approximate form $V_M(r,\theta)$ is expressed as the summation of two contributions: the first one represents the medium component of the circumferential displacement, not function of the angular coordinate θ; the second one is representative of the angular perturbation induced on the medium component of displacement by the not-axisymmetry of the material properties. The approximate form of the circumferential displacement is:

$$v(r,\theta) \approx V_M(r,\theta) = \overline{V}_N(r) + \widetilde{V}_M(r,\theta) = \sum_{l=1}^{N} k_l\ \psi_l(r) + \sum_{l=N+1}^{M} k_l\ \psi_l(r,\theta) \tag{7.44}$$

The first series $\overline{V}_N$ is the medium and axisymmetric component of circumferential displacement, the latter $\widetilde{V}_M$ represents the angular perturbation needed to take into account the variable bending stiffnesses. Additionally, no ψ_0 term is required being all the boundary conditions homogeneous.

The series representing the medium component of circumferential displacement $\overline{V}_N(r)$ automatically fulfills the (ii) boundary condition being exclusively function of the radial coordinate r.

Otherwise, the approximation functions $\psi_l(r,\theta)$ for the angular perturbation circumferential displacement component $\widetilde{V}_M(r,\theta)$ are obtained through the product of a function $h_l(r)$, only dependent on the radial coordinate r, and a function $g(\theta)$ which in turn is function of the only angular coordinate θ:

$$\widetilde{V}_M(r,\theta) = \sum_{l=N+1}^{M} k_l\ h_l(r)\ g(\theta) \tag{7.45}$$

The function $h_l(r)$ is needed to respect the boundary conditions (7.42) and (7.43); therefore, to fulfill the requirement of uniform circumferential displacement at the inner edge of the annular plate, prescribed by the boundary condition (ii), it must result null at the inner radius b, despite the displacement undergone by the composite annular plate at the inner edge is other than zero. This aspect clarifies that the contribution $\widetilde{V}_M(r,\theta)$ provides an assessment of the angular fluctuation of

the composite annular plate mid-surface circumferential displacement caused by the θ-dependent bending stiffnesses.

Besides, $g(\theta)$ is a trigonometric function, needed to account for the angular variation of the mid-surface circumferential displacement, whose specific form depends on the lay-up of the composite annular plate. The two symmetrical lay-ups afterwards analyzed in the next Section are characterized by the following forms of the trigonometric function $g(\theta)$:

- QI lay-up

$$g(\theta) = \sin\big(4\theta\big) \tag{7.46}$$

- 0D lay-up

$$g(\theta) = \cos\big(2\theta\big) \tag{7.47}$$

The case studies discussed in §7.2 make use of a series $V_M(r,\theta)$ composed of 10 terms. In particular, a 9 terms series $\overline{V}_N(r)$ was utilized, its terms cannot be expressed through a general form and are listed in the Appendix C; together with a one term series $\widetilde{V}_M(r,\theta)$. A polynomial function was used for the function $h_{10}(r)$ that appears in this last series term, it has the following form:

$$\widetilde{V}_{10}(r,\theta) = k_{10}(r-a)(r-b)g(\theta) \tag{7.48}$$

For what concerns the determination of the scalar coefficients k_l, the substitution of the approximate form of transversal displacement outlined in (7.36) in the principle of virtual displacements (7.5) returns a linear system of the type (7.6) whose matrix coefficients terms are:

$$R_{kl} = \int_b^a \int_{-\pi}^{\pi} \big\{\Psi_k\big\}^T \big[A^{2x2}(\theta)\big] \big\{\Psi_l\big\} \; d\theta \; r dr \tag{7.49}$$

in which:

$$\big\{\Psi_{k,l}\big\} = \begin{Bmatrix} \frac{1}{r}\frac{\partial \psi_{k,l}}{\partial \theta} \\ \frac{\partial \psi_{k,l}}{\partial r} - \frac{\psi_{k,l}}{r} \end{Bmatrix} \tag{7.50}$$

and:

$$\big[A^{2x2}(\theta)\big] = \begin{bmatrix} A_{22}(\theta) & A_{26}(\theta) \\ A_{26}(\theta) & A_{66}(\theta) \end{bmatrix} \tag{7.51}$$

Additionally, according to the expression of the external virtual work in (7.40), the known terms pf the linear system (7.6) are:

$$F_k = P_T \psi_k(b,0) + P_T \psi_k(b,\pi) \tag{7.52}$$

As previously outlined, the torsional moment M_T was transfered to the integration domain Ω through a statically equivalent couple of parallel forces $P_T = \frac{M_T}{2b}$ applied at the inner radius of the annular plate.

7.2 Results

This Section concerns the application of the proposed analytical formulation based on Ritz method to some case studies reproducing the reference model of spot joint element; as previously described, they are referred to annular plates clamped on the outer radius and featuring an internal rigid core. Load conditions are those whose solution procedure is set up in the previous Section: (i) transversal load P applied to the plate axis, i.e. along the z-axis of the cylindrical coordinate system; (ii) in-plane load T acting on rigid nugget and along the x-axis of the global Cartesian coordinate system; (iii) in-plane bending moment M applied along the x-axis of the global Cartesian coordinate system and (iv) torsional moment M_T acting orthogonally to the plate mid-surface, in correspondence of its axisymmetry axis, i.e. along the z-axis of the cylindrical coordinate system.

Results from all proposed case studies are then compared with those obtained by means of refined linear FE models. The FE models were made using layered shell featuring 4 nodes with 6 DOFs per node.

The application examples are carried out making use of rectilinear orthotropic composite annular plates made up of widely employed lay-ups for applications concerning composite bolted joints, i.e. QI and 0D lay-ups as reported in [52, 57, 58, 59, 60]. Specifically, the two lay-ups are taken from reference [57] and they are outlined in Table 6.1; likewise, the unidirectional fiber-reinforced layer stiffness properties are reported Table 6.2. The layers thickness is $t_{lay} = 0.13$ mm.

All the numerical tests were executed with a fixed value of the overall composite annular plate thickness $t = 5.2$ mm. Besides, the impact on results accuracy of composite annular plates geometrical characteristics was investigated. In particular, as regards the transversal load condition, four different slenderness ratios between the plate thickness t and its outer radius a were examined: 0.02, 0.03, 0.04 and 0.05. This study is needed to assess if the plate shear deformability affects the results furnished by the proposed method, being founded on the Classical Plate Theory. Additionally, six different plate aspect ratios $\beta = \frac{b}{a}$ obtained trough the ratio between the inner and the outer radii of the plate, were analyzed for both the load conditions: $\beta_0 = 0.05$, $\beta_1 = 0.1$, $\beta_2 = 0.2$, $\beta_3 = 0.3$, $\beta_4 = 0.4$ and $\beta_5 = 0.5$.

The comparisons between results of the proposed analytical method (named Ritz in the Figures) and FE analyses are presented in the diagrams in dimensionless form, showing the distribution of the displacement components along both radial and circumferential coordinates.

7.2.1 Transversal load P

Figs. 7.2 and 7.3 show curves of the dimensionless mid-surface deflection as function of the dimensionless radius $\rho = \frac{r}{a}$, at the angular coordinate $\theta = 0$, for the QI and the 0D lay-ups, respectively. Dimensionless quantities are based on the mid-surface deflection at the inner edge $w(\beta, 0)$ obtained with FE analyses.

Table 7.1 reports the percentage variations Δ_β, evaluated at the inner radius $\rho = \beta$, between the results of the analytical method and the FE ones for both QI and 0D lay-ups. The percentage difference grows constantly passing from the β_1 to β_5; as a result, it can be concluded that, for both lay-ups, a greater accuracy of the results is obtainable with smaller values of the aspect ratio β. Anyway, under the threshold value $\beta = 0.1$ the percentage difference starts growing again; indeed, for every value of slenderness ratio $\frac{t}{a}$ the percentage difference evaluated for β_0 is higher than the one for β_1.

Furthermore, a validity range of the proposed solution method, that is founded on a theoretical

background referred to thin-plates, can be set analyzing the effect of the slenderness ratio on the results accuracy. In fact, an increasing slenderness ratio provokes a bigger deflection at the composite annular plate inner edge along with non-null slope at the same radius because of the higher plate shear deformability that is not taken into account by the Classical Plate Theory; effect that is clearly visible for slenderness ratios $\frac{t}{a} = 0.04$ and 0.05. Additionally, as evidenced by Table 7.1, the percentage difference steadily grows with the slenderness ratio $\frac{t}{a}$ for a fixed aspect ratio β. As regards the influence of the lay-up, it should be noted that the results concerning the 0D lay-up, even maintaining a very acceptable accordance with those of the FE analyses, turn out to be characterized of slightly greater percentage difference with respect to the QI lay-up ones.

Similarly, Figs. 7.4 and 7.5 report for both the QI and 0D lay-ups, for all the considered slenderness ratios $\frac{t}{a}$, and for an aspect ratio $\beta = 0.1$, the variation of dimensionless mid-surface deflection along the dimensionless angle $\overline{\theta} = \frac{\theta}{\pi}$. Again, dimensionless quantities are based on the mid-surface deflection at the inner edge $w(\beta, 0)$ obtained with FE analyses. Moreover, any of these diagrams outline the circumferential variation of the mid-surface deflection at five values of the dimensionless radius: ρ=(β, 0.25, 0.40, 0.60, 0.80). Even in this case, the agreement between the results of the proposed analytical method and those obtained by FEA is confirmed.

In particular, the mid-surface deflection for $\rho = 0.40$ and 0.60 features a more notable fluctuation with the angular coordinate, meanwhile it is less evident for $\rho = \beta$, 0.25 and 0.80 because the constrains acting on the internal and external radii tend to limit its circumferential variability. It should be noted that the mid-surface deflection for $\rho = \beta$ turns out to be not dependent on the angular coordinate θ: this confirms the capability of chosen approximation functions of fulfilling the (IV) of boundary conditions (7.10).

According to the lay-up influence, the composite annular plates featuring QI lay-up present a maximum circumferential variation of the mid-surface deflection, for a given value of ρ, of 5%; instead, the laminates with 0D lay-up are characterized by a circumferential variation of mid-surface deflection of the order of 10%. Hence, the composite annular plates with 0D lay-up more strongly depends on the angular coordinate θ.

7.2.2 In-plane load T

Even for the in-plane load condition, results are reported in dimensionless form, considering different quantities for radial and tangential displacement curves, respectively: values of radial displacement $u(\beta, 0)$ and tangential displacement $v(\beta, \frac{\pi}{2})$, both evaluated by means of FEA.

Fig. 7.6 summarizes results regarding the variation of in-plane displacement components along the radial coordinate ρ (at $\theta = 0$ rad for the radial one and at $\theta = \frac{\pi}{2}$ rad for the circumferential one), for both lay-ups and for the slenderness ratio $\frac{t}{a} = 0.02$. Six values of the aspect ratio β, (i.e. 0.05, 0.1, 0.2, 0.3, 0.4 and 0.5) are considered. The percentage difference Δ_β between the analytical method and FE results, evaluated at the inner edge of the composite plate, for both the in-plane displacement components, are listed in Table 7.2; note that at the inner radius the maximum values of radial and circumferential displacement are $u(\beta, 0)$=$v(\beta, \frac{\pi}{2})$. The in-plane displacement components for the QI lay-up show a correspondence very close with the FE counterpart; in fact, whatever it is the value of the aspect ratio β − the difference between the curves obtained by means of Ritz solution method and FE analyses is essentially null for both the radial and the circumferential displacements. As regards the results for 0D lay-up, the differences in term circumferential displacement conserve the same not dependent behavior with respect to the aspect ratio β. However, a double trend can be recognized in the outcomes of the proposed analytical method, in term of radial displacement component: in the

zones close to the internal rigid core and to the outer radius constraint no variability with the shape factor is noticeable, meanwhile in the intermediate portion of the composite annular plate the higher the aspect ratio β, the higher the accordance of Ritz method outcomes with the FE results. This is due to the layer orientation, whose aperiodicity is not perfectly interpreted by the Ritz function.

In Fig. 7.7 the dimensionless radial and circumferential displacement components are presented in function of the dimensionless angular coordinate $\overline{\theta} = \frac{\theta}{\pi}$ for composite annular plates featuring both QI and 0D lay-ups. Results are related to shape factor $\beta = 0.1$ and different specific values of the dimensionless radius: ρ=(β, 0.20, 0.40, 0.60 and 0.80).

Results for the in-plane displacement components of composite annular plates with the two lay-ups exhibit good accuracy when compared with the curves provided by FE analyses. The approximation functions employed in the Ritz solution method reproduce exactly the circumferential variation of the in-plane displacement components alongside all the radial coordinate spanning from the inner to the external edge of the composite annular plates.

Table 7.1: Mid-surface deflection percentage variation $\Delta_{\beta_i}[\%]$, evaluated at $\rho = \beta$ for various values β_i, between analytical method and FEA for both lay-ups.

QI lay-up						
$\frac{t}{a}$	$\Delta_{\beta_0}[\%]$	$\Delta_{\beta_1}[\%]$	$\Delta_{\beta_2}[\%]$	$\Delta_{\beta_3}[\%]$	$\Delta_{\beta_4}[\%]$	$\Delta_{\beta_5}[\%]$
0.02	1.61	0.79	1.32	1.53	1.95	2.70
0.03	3.20	2.87	2.91	3.40	4.31	5.89
0.04	5.74	4.94	5.09	5.91	7.44	10.02
0.05	8.20	7.55	7.71	8.94	11.16	14.83

0D lay-up						
$\frac{t}{a}$	$\Delta_{\beta_0}[\%]$	$\Delta_{\beta_1}[\%]$	$\Delta_{\beta_2}[\%]$	$\Delta_{\beta_3}[\%]$	$\Delta_{\beta_4}[\%]$	$\Delta_{\beta_5}[\%]$
0.02	1.73	1.43	1.49	1.62	2.04	2.79
0.03	3.48	2.99	3.06	3.54	4.46	6.07
0.04	5.85	5.19	5.27	6.10	7.65	10.30
0.05	8.45	7.69	7.95	9.36	11.45	15.19

Table 7.2: Radial and circumferential displacement components percentage variation $\Delta_{\beta_i}[\%]$ evaluated at $\rho = \beta$ for various values β_i, $\theta = 0$ rad and $\theta = \frac{\pi}{2}$ rad respectively, between analytical method and FEA for both lay-ups.

Lay-up	$\Delta_{\beta_0}[\%]$	$\Delta_{\beta_1}[\%]$	$\Delta_{\beta_2}[\%]$	$\Delta_{\beta_3}[\%]$	$\Delta_{\beta_4}[\%]$	$\Delta_{\beta_5}[\%]$
QI	0.22	0.07	0.04	0.03	0.03	0.02
0D	1.27	0.86	0.52	0.31	0.20	0.19

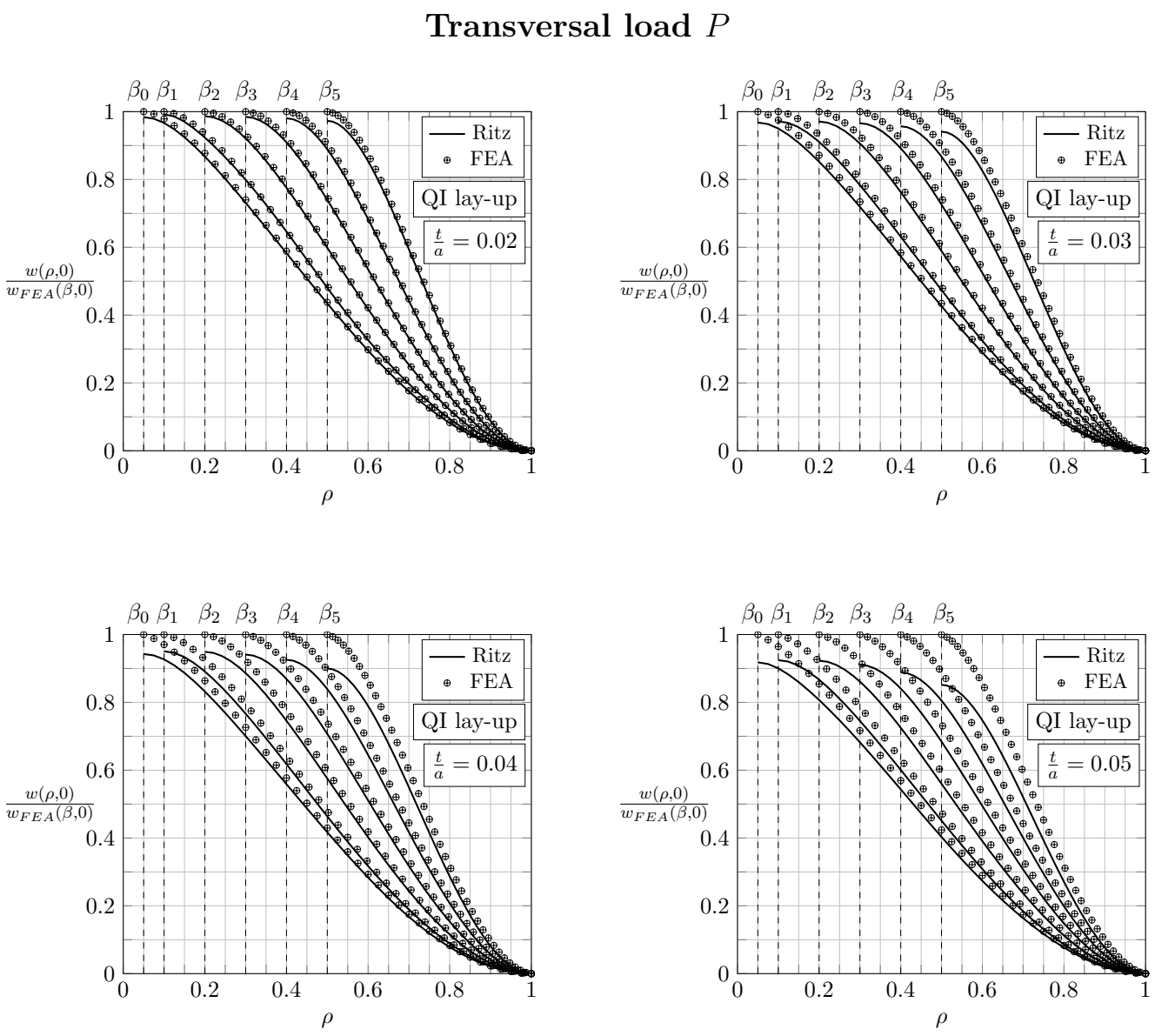

Figure 7.2: Curves of dimensionless mid-surface deflection as function of ρ, evaluated at $\theta = 0$ rad for different ratios $\frac{t}{a}$ and for $\beta_0 = 0.05$, $\beta_1 = 0.1$, $\beta_2 = 0.2$, $\beta_3 = 0.3$, $\beta_4 = 0.4$ and $\beta_5 = 0.5$ - quasi-isotropic lay-up.

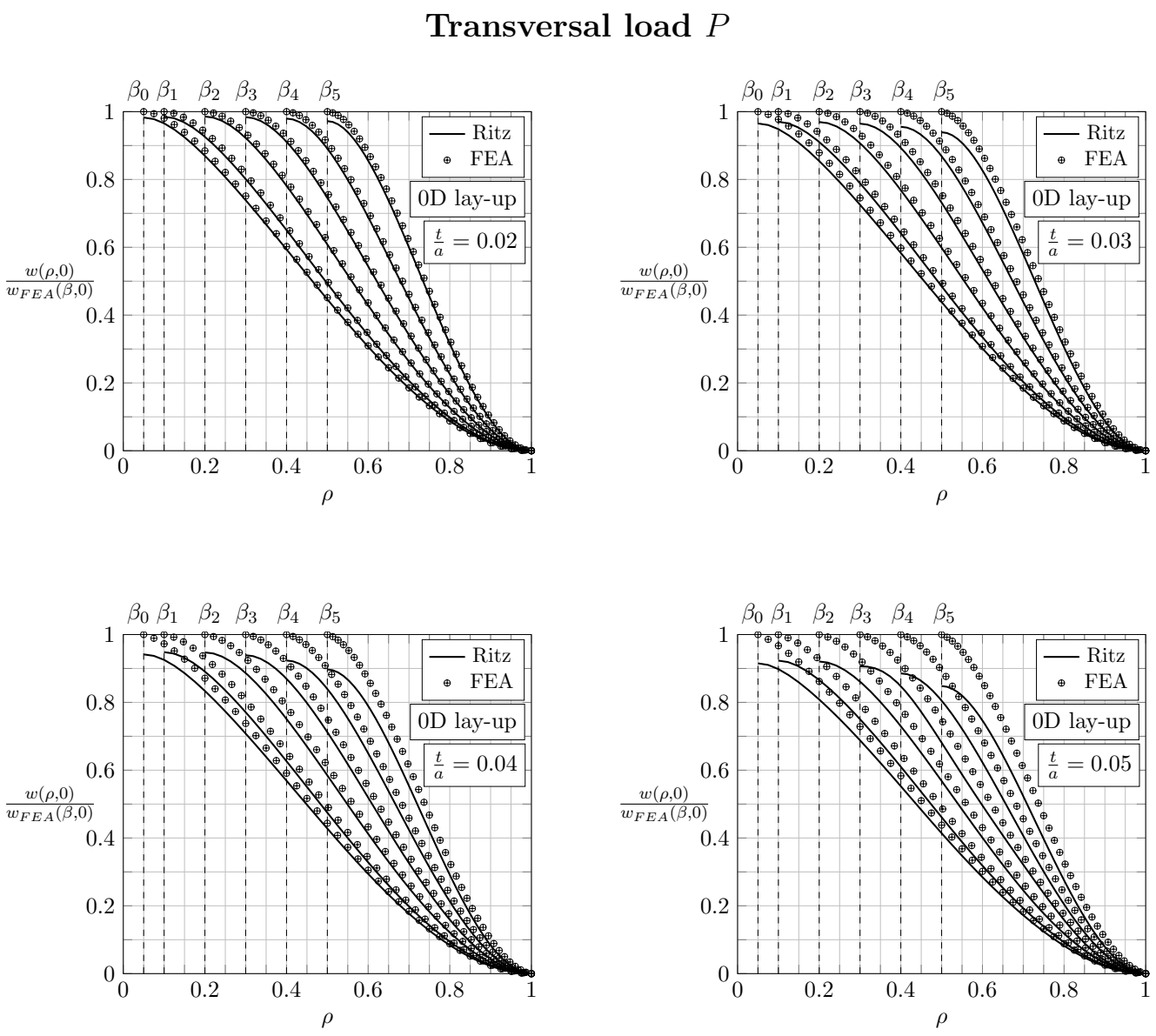

Figure 7.3: Curves of dimensionless mid-surface deflection as function of ρ, evaluated at $\theta = 0$ rad for different ratios $\frac{t}{a}$ and for $\beta_0 = 0.05$, $\beta_1 = 0.1$, $\beta_2 = 0.2$, $\beta_3 = 0.3$, $\beta_4 = 0.4$ and $\beta_5 = 0.5$ - zero-dominated lay-up.

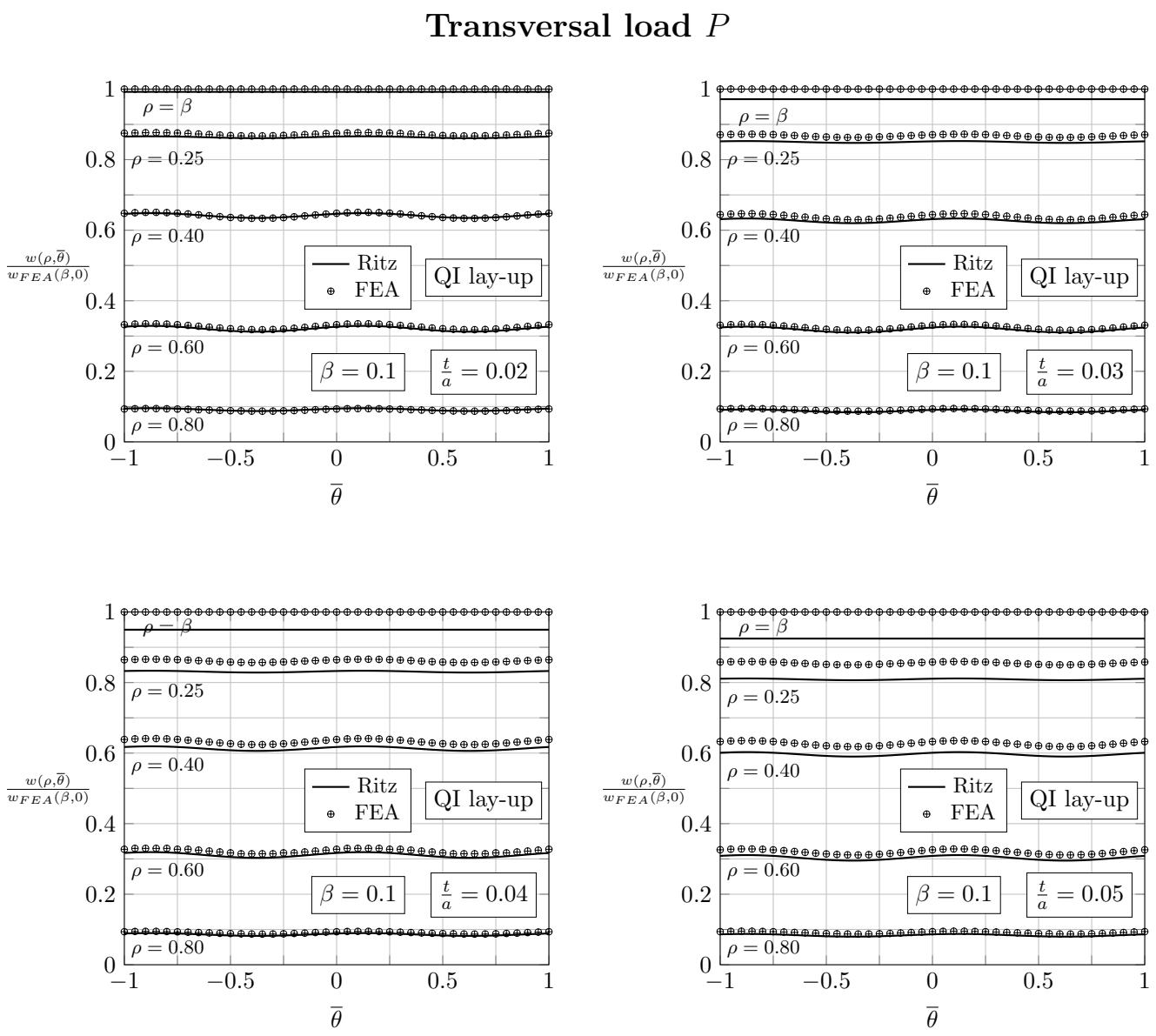

Figure 7.4: Curves of dimensionless mid-surface deflection as function of $\overline{\theta}$ for different ratios $\frac{t}{a}$ and $\beta = 0.1$, at $\rho =(\beta,\ 0.25,\ 0.40,\ 0.60,\ 0.80)$ - quasi-isotropic lay-up.

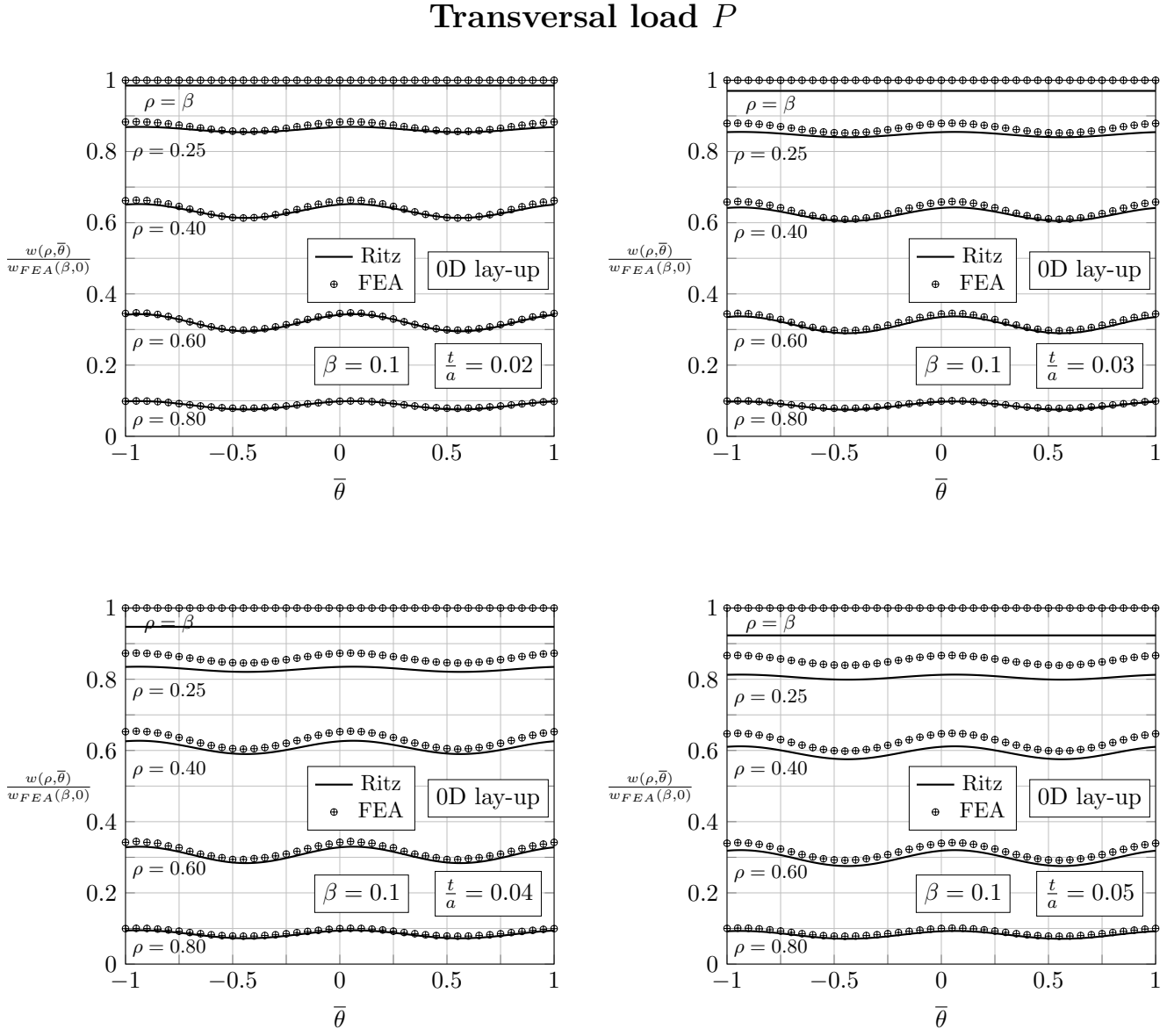

Figure 7.5: Curves of dimensionless mid-surface deflection as function of $\overline{\theta}$ for different ratios $\frac{t}{a}$ and $\beta = 0.1$, at $\rho =(\beta,\ 0.25,\ 0.40,\ 0.60,\ 0.80)$ - zero-dominated lay-up.

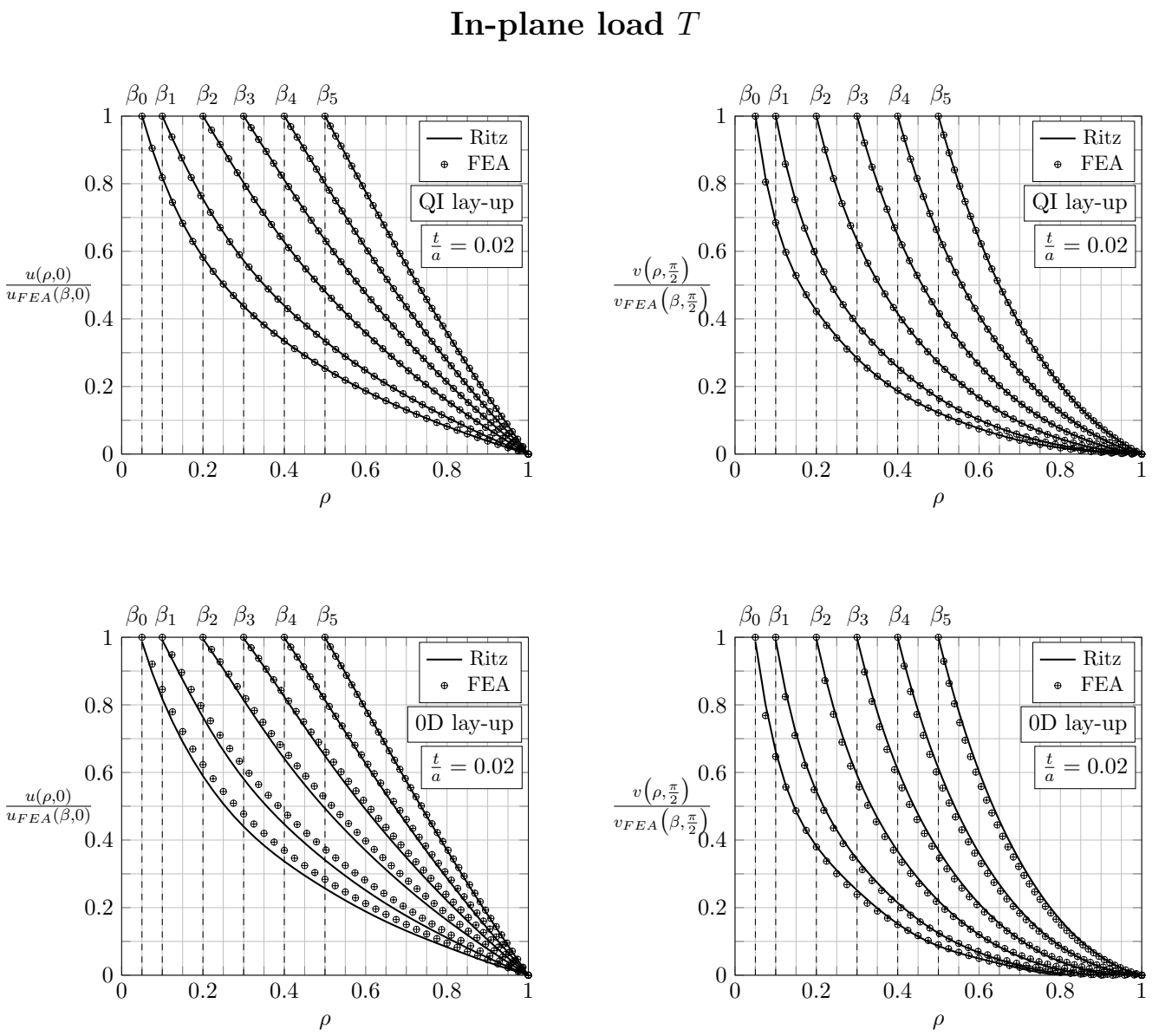

Figure 7.6: Curves of dimensionless mid-surface radial and circumferential displacement components as function of ρ, evaluated at $\theta = 0$, for $\beta_0 = 0.05$, $\beta_1 = 0.1$, $\beta_2 = 0.2$, $\beta_3 = 0.3$, $\beta_4 = 0.4$ and $\beta_5 = 0.5$, with quasi-isotropic (QI) and zero-dominated (0D) lay-ups.

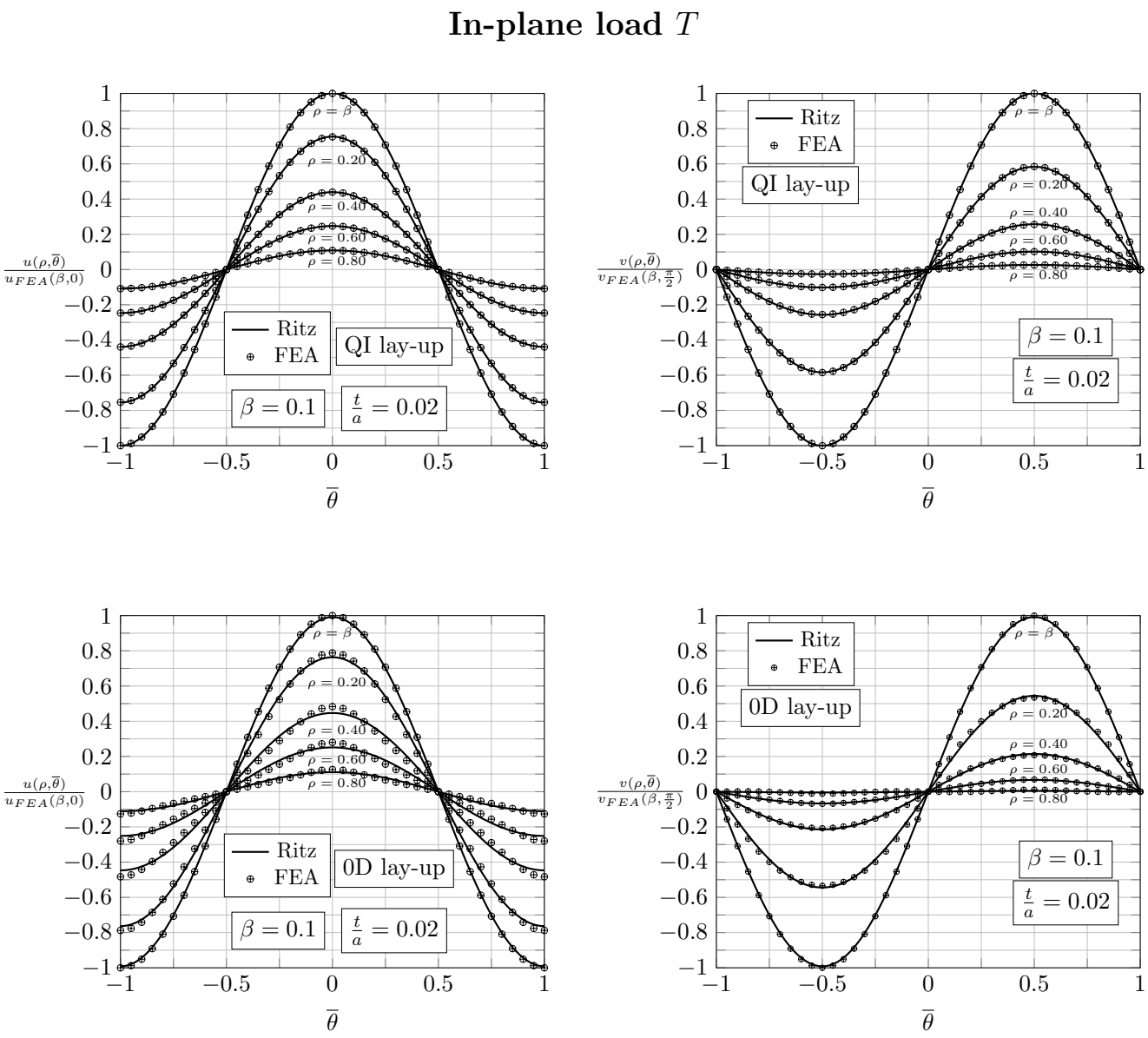

Figure 7.7: Curves of dimensionless mid-surface radial and circumferential displacement components as function of $\overline{\theta}$, for $\beta = 0.1$, at $\rho = (\beta,\ 0.20,\ 0.40,\ 0.60,\ 0.80)$, with quasi-isotropic (QI) and zero-dominated (0D) lay-ups.

7.2.3 Bending moment M

The dimensionless mid-surface deflection is depicted against the dimensionless radius $\rho = \frac{r}{a}$, at the angular coordinate $\theta = \frac{\pi}{2}$ rad, in Figs. 7.8 and 7.9 for the QI and the 0D lay-ups, respectively. The dimensionless deflection is calculated as the ratio between the mid-surface deflection at the angular coordinate $\frac{\pi}{2}$ rad, $w(\rho, \frac{\pi}{2})$, i.e. orthogonally in reference to the direction of the bending moment, and its maximum value, obtained by means of FE analyses, at the same angular coordinate and for the aspect ratio $\beta = 0.1$, i.e. $w_{FEA}^{MAX}(\beta_1)$.

The percentage errors, for both the QI and 0D lay-ups, evaluated at the inner radius $\rho = \beta$ between the results of the presented method and the FE ones are listed in Table 7.3. Overall, the percentage error decreases passing from the β_1 to β_3 or β_4, depending on the specific value of slenderness ratio, and then grows again. As a result, it can be concluded that, for both lay-ups, a greater accuracy of the results is obtainable with medium values of the aspect ratio β.

Furthermore, a validity range of the proposed solution method, that is founded on a theoretical background referred to thin-plates, can be set analyzing the effect of the slenderness ratio on the results accuracy. In fact, an increasing slenderness ratio provokes a bigger deflection at the composite annular plate inner edge because of the higher plate shear deformability that is not taken into account by the Classical Plate Theory; indeed, for a every aspect ratio β, the greater the the slenderness ratio, the greater the percentage error. Anyway, in general, the diagrams showing the mid-surface deflection against the dimensionless radial coordinate exhibit a very good agreement between the the outcomes of Ritz solution method and those of FE analyses.

As regards the influence of the lay-up, it should be noted that the results concerning the 0D lay-up, even maintaining a very acceptable accordance with those of the FE analyses, turn out to be characterized of slightly greater percentage errors with respect to the QI lay-up ones.

The dimensionless mid-surface deflection in function of the dimensionless angle $\overline{\theta} = \frac{\theta}{\pi}$ is shown in Figs. 7.10 and 7.11, for the slenderness ratio $\frac{t}{a} = 0.02$, the aspect ratio $\beta = 0.1$ and for both the QI and 0D lay-ups. The dimensionless form of the mid-surface deflection is evaluated as the ratio of $w(\rho, \overline{\theta})$ and its maximum value obtained with FE analyses. In addition, the diagrams present the circumferential variation of the mid-surface deflection at four values of the dimensionless radius ρ: β, 0.25, 0.40, 0.70. As a result, the Ritz solution method is capable of precisely describe the dependence of the mid-surface deflection on the angular coordinate for both the analyzed lay-ups of composite annular plates.

7.2.4 Torsional moment M_T

The diagrams in Fig. 7.12 report the dimensionless form of the circumferential displacement, for the QI and 0D lay-ups, computed through the ratio of the circumferential displacement at the angular coordinate $\theta = 0$ rad, $v(\rho, 0)$, and the value at the inner edge of the plate computed by finite element analyses $v(\beta, 0)$, against the dimensionless radial coordinate ρ.

Conversely, the dependence on the angular coordinate of the dimensionless circumferential displacement is shown in Fig. 7.13; it is evaluated as the ratio between the circumferential displacement $v(\rho, \overline{\theta})$ and the value at the inner radius $v(\beta, 0)$ obtained with FE analyses. Additionally, the diagrams outline the circumferential variation of the mid-surface deflection at four fixed values of the dimensionless radius ρ: β, 0.50, 0.70, 0.90.

Despite the employment of the $\widetilde{V}_M(r, \theta)$ series, the dependence of the circumferential displacement on the angular coordinate for the composite annular plates featuring QI lay-up is not noticeable. In fact, the diagram on the left side of Fig. 7.13 shows no variation of the circumferential displacement

component with the angular coordinate. Nevertheless, the results demonstrate a high degree of accordance between the proposed method and the FE analyses outcomes for all the values of the aspect ratio β. Moreover, it should be noted that the circumferential displacement is characterized by a high slope in the initial portion of the annular plate which provokes a substantial decrease, indeed its value for $\rho = 0.50$ is close to the half of the maximum value, i.e. the one evaluated at the inner edge.

As regards the results obtained with annular composite plates realized with 0D lay-up, the diagrams on the right side of Fig. 7.13 shows that the plate undergoes an additional displacement in the area surrounding the angular coordinates $\theta = 0$ rad and $\theta = \frac{\pi}{2}$. This effect is clearly visible, e.g., on the the curve with $\rho = 0.5$ on the right side of Fig. 7.13.

Table 7.3: Mid-surface deflection percentage variation $\Delta_{\beta_i}[\%]$, evaluated at $\rho = \beta$ for various values β_i, between analytical method and FEA for both lay-ups.

QI lay-up					
$\frac{t}{a}$	$\Delta_{\beta_1}[\%]$	Δ_{β_2} [%]	Δ_{β_3} [%]	$\Delta_{\beta_4}[\%]$	$\Delta_{\beta_5}[\%]$
0.02	3.78	2.16	1.96	2.18	2.81
0.03	7.71	4.47	4.11	4.64	5.99
0.04	11.76	7.64	6.92	7.85	10.08
0.05	16.34	10.77	9.95	11.61	14.79

0D lay-up					
$\frac{t}{a}$	$\Delta_{\beta_1}[\%]$	Δ_{β_2} [%]	Δ_{β_3} [%]	$\Delta_{\beta_4}[\%]$	$\Delta_{\beta_5}[\%]$
0.02	5.02	3.06	2.55	2.52	2.92
0.03	8.53	5.37	4.61	4.85	5.93
0.04	13.30	8.19	7.30	7.89	9.79
0.05	17.50	11.41	10.46	11.48	14.28

Table 7.4: Circumferential displacement component percentage variation $\Delta_{\beta_i}[\%]$ evaluated at $\rho = \beta$ for various values β_i, $\theta = 0$ rad and $\theta = \frac{\pi}{2}$ rad respectively, between analytical method and FEA for both lay-ups.

Lay-up	$\Delta_{\beta_1}[\%]$	Δ_{β_2} [%]	Δ_{β_3} [%]	$\Delta_{\beta_4}[\%]$	$\Delta_{\beta_5}[\%]$
QI	0.16	0.04	0.04	0.04	0.04
0D	2.93	2.22	1.58	1.12	0.76

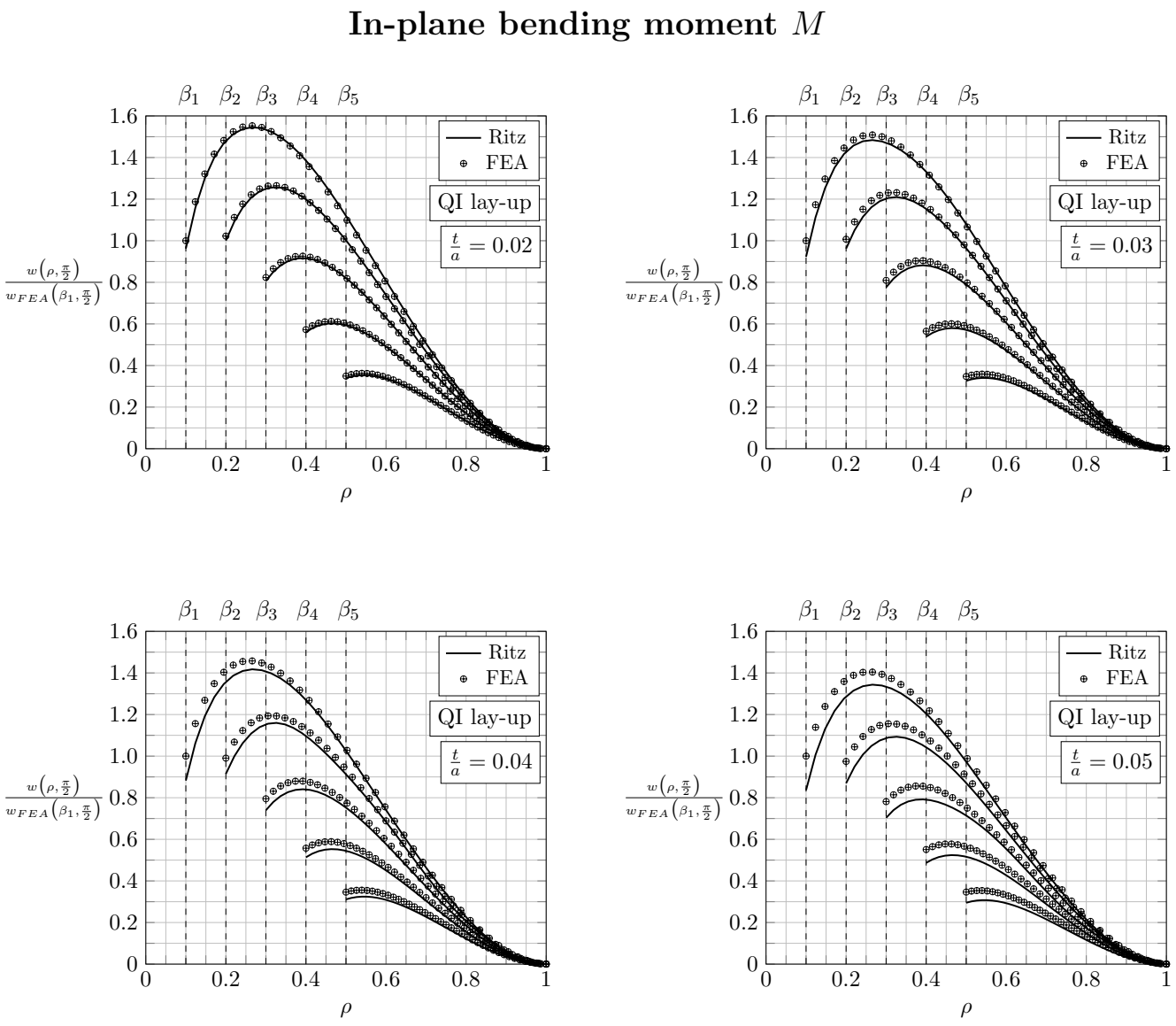

Figure 7.8: Variation of the dimensionless mid-surface deflection along the dimensionless radius ρ, evaluated at $\theta = \frac{\pi}{2}$ rad for different ratios $\frac{t}{a}$ and for $\beta_1 = 0.1$, $\beta_2 = 0.2$, $\beta_3 = 0.3$, $\beta_4 = 0.4$ and $\beta_5 = 0.5$ with quasi-isotropic lay-up.

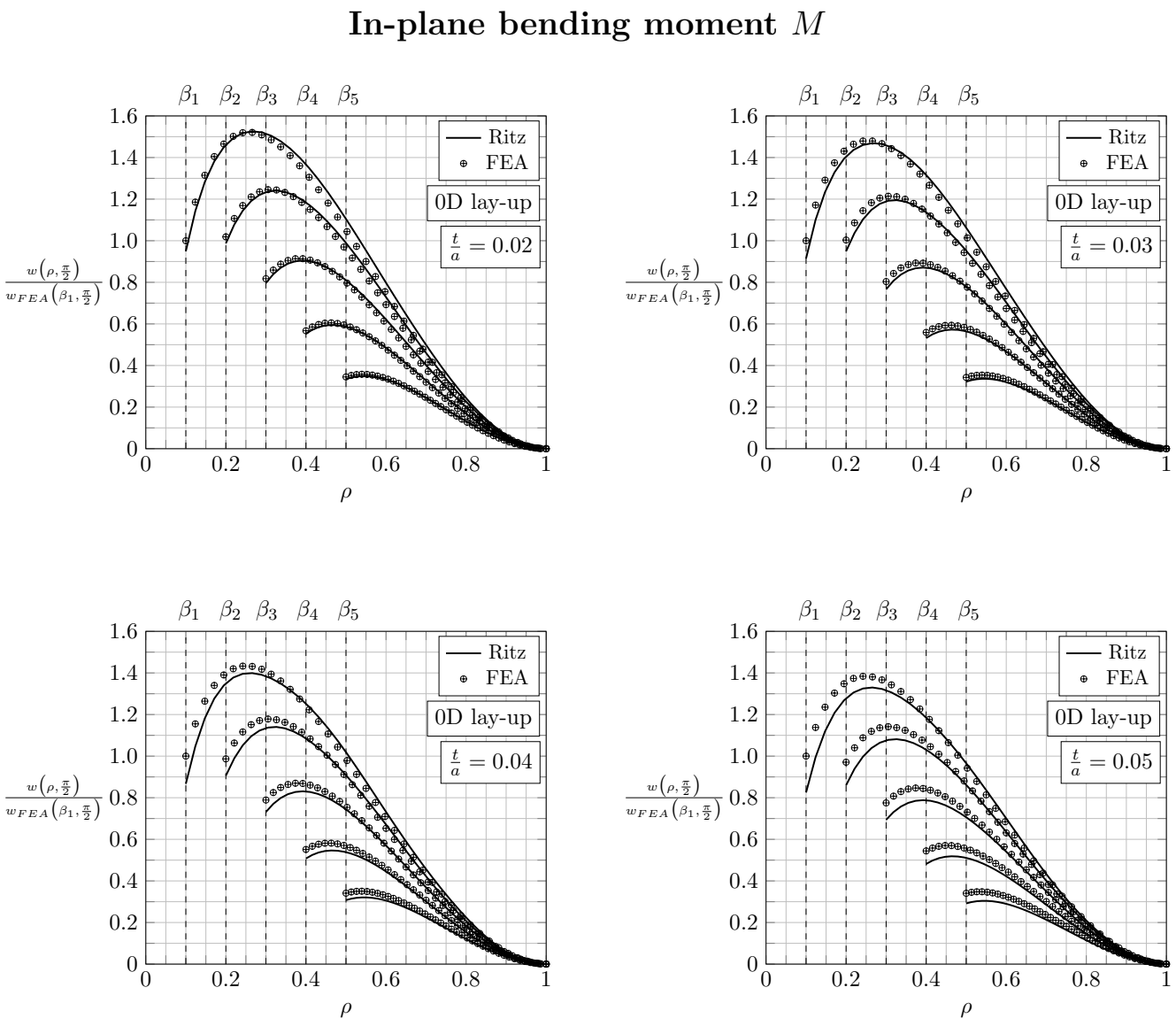

Figure 7.9: Variation of the dimensionless mid-surface deflection along the dimensionless radius ρ, evaluated at $\theta = \frac{\pi}{2}$ rad for different ratios $\frac{t}{a}$ and for $\beta_1 = 0.1$, $\beta_2 = 0.2$, $\beta_3 = 0.3$, $\beta_4 = 0.4$ and $\beta_5 = 0.5$ with zero-dominated lay-up.

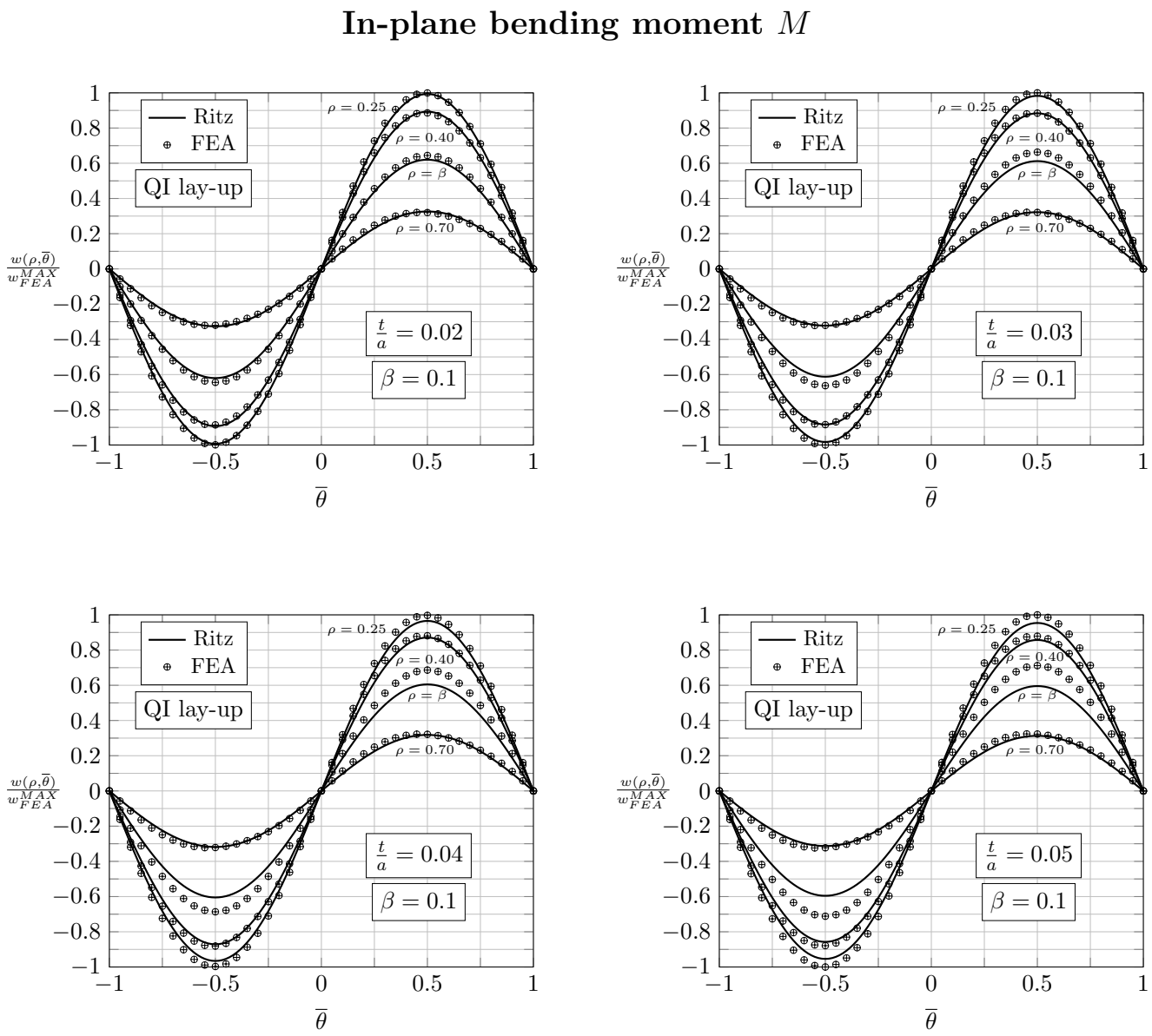

Figure 7.10: Circumferential variation along the dimensionless radial coordinate $\overline{\theta}$ of the dimensionless mid-surface deflection, evaluated for different ratios $\frac{t}{a}$ and for $\beta = 0.1$ at $\rho = \beta$, 0.25, 0.40 and 0.70 with quasi-isotropic lay-up.

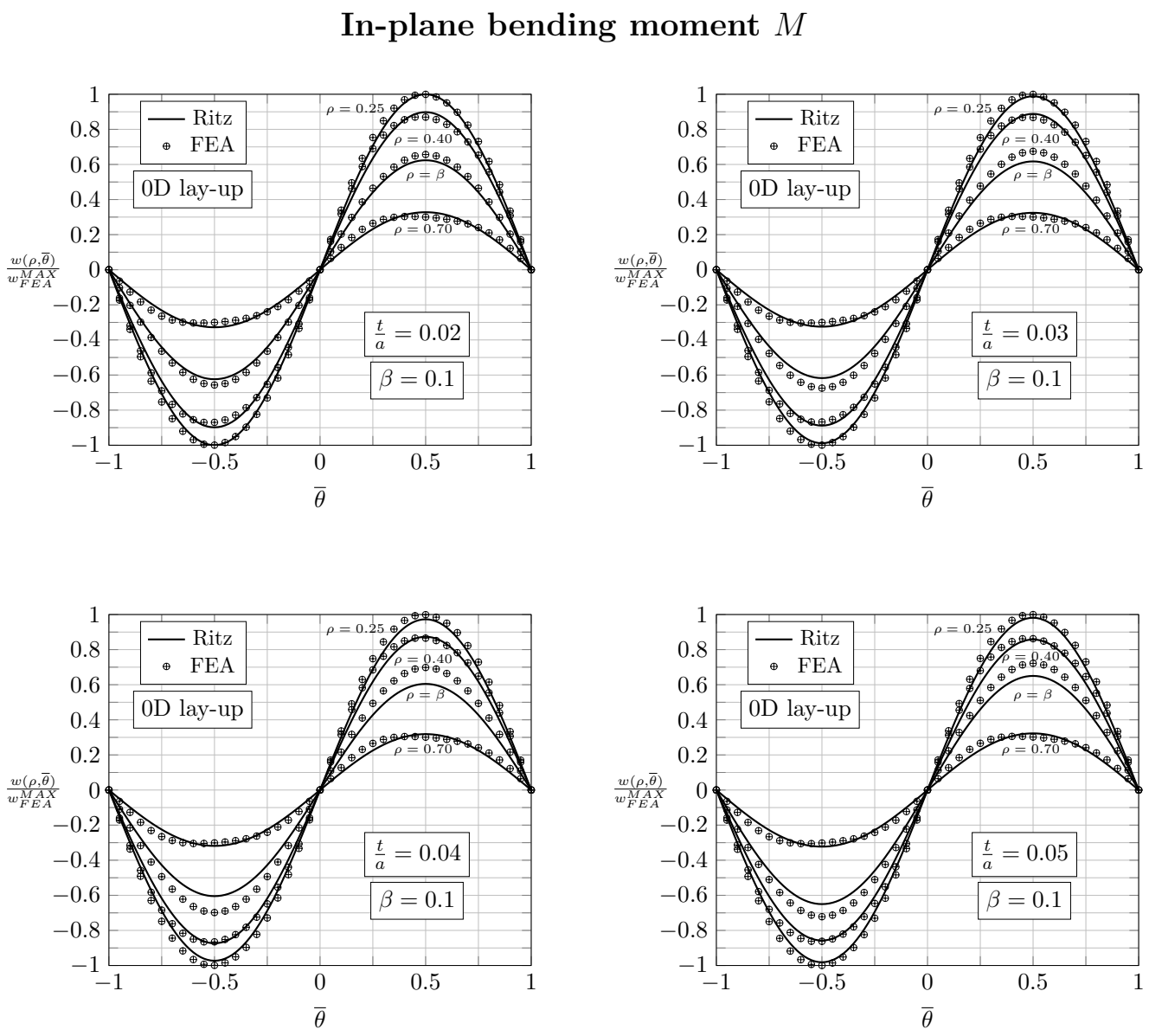

Figure 7.11: Circumferential variation along the dimensionless radial coordinate $\overline{\theta}$ of the dimensionless mid-surface deflection, evaluated for different ratios $\frac{t}{a}$ and for $\beta = 0.1$ at $\rho = \beta$, 0.25, 0.40 and 0.70 with zero-dominated lay-up.

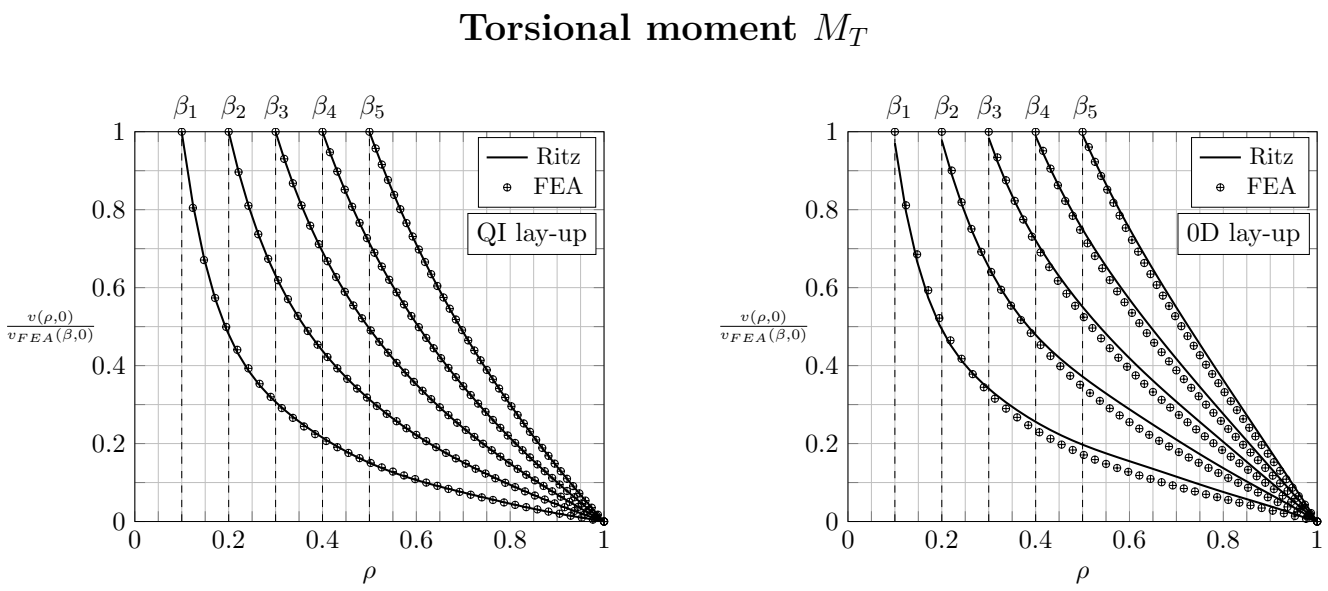

Figure 7.12: The dimensionless mid-surface circumferential displacement against the dimensionless radius ρ, evaluated at $\theta = 0$ rad, for $\beta_1 = 0.1$, $\beta_2 = 0.2$, $\beta_3 = 0.3$, $\beta_4 = 0.4$ and $\beta_5 = 0.5$, with quasi-isotropic (right) and zero-dominated (left) lay-ups.

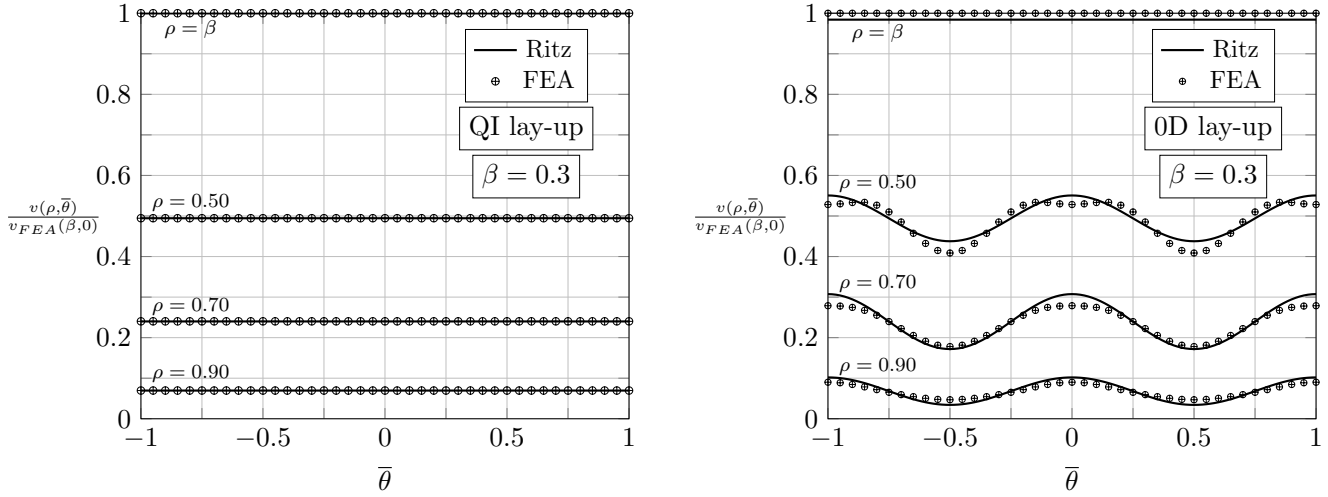

Figure 7.13: The dimensionless mid-surface circumferential displacement against the dimensionless angular coordinate $\overline{\theta}$, for $\beta = 0.3$, at $\rho = \beta$, 0.50, 0.70 and 0.90, with quasi-isotropic (right) and zero-dominated (left) lay-ups.

CHAPTER 8

FIRST-ORDER SHEAR DEFORMATION ANALYSIS OF RECTILINEAR ORTHOTROPIC COMPOSITE CIRCULAR PLATES

The studies presented in previous Chapters allow to completely determine the terms of the new Spot Joint Element stiffness matrix. However, these solutions are obtained in the frame of Classical Plate Theory (CPT) and consequently the displacement field they provide is in accordance with the kinematics hypotheses of Classical Plate Theory which does not account for the effect of transverse shear deformations. This implies that, as shown in Chapter 7, the solution for the transversal and the in-plane bending moment load conditions precisely describe the actual displacement field for low slenderness ratios between thickness and outer radius, whereas the mid-surface deflection turns out be underestimated as long as this parameter is increased. Anyway, slenderness ratios usually employed in constructive practice can be affected by not negligible transverse shear deformations: this requires an improvement of the theoretical framework.

Therefore, this Chapter aims to the definition of an original solution procedure for the transversal load condition based on the First-order Shear Deformation Plate Theory (FSDT) in order to precisely reproduce the mid-surface deflection of annular rectilinear orthotropic circular plates. Thus, the derivation of constitutive equations is outlined in Chapter 5 taking into account the shear deformability to set up a theoretical approach based on the application of Ritz method to solve the principle of virtual works. The general expression of the principle of virtual work is presented for both the transversal and the in-plane bending moment load conditions, as shown in Fig. 8.1; additionally, specific forms of the approximation functions are derived for the mid-surface transversal displacement and the rotations around the circumferential and the radial directions.

Then, results are presented for two symmetrical lay-ups largely employed for industrial applications and in literature regarding composite bolted joints, i.e. the quasi-isotropic (QI) and the zero-dominated (0D) ones [52, 57, 58, 59, 60]. Outcomes of Ritz method showing the dependence of displacement components on both radial and circumferential coordinates are reported and compared with those of FE analyses obtained through a refined reference model. Afterward, the effect of the

aspect ratio of the composite circular plate on the results is further investigated in conjunction with the slenderness ratios one.

In the end, the proposed analytical method results show a very good agreement with the outcomes of reference FE analyses, demonstrating the high reliability and accuracy of the presented method.

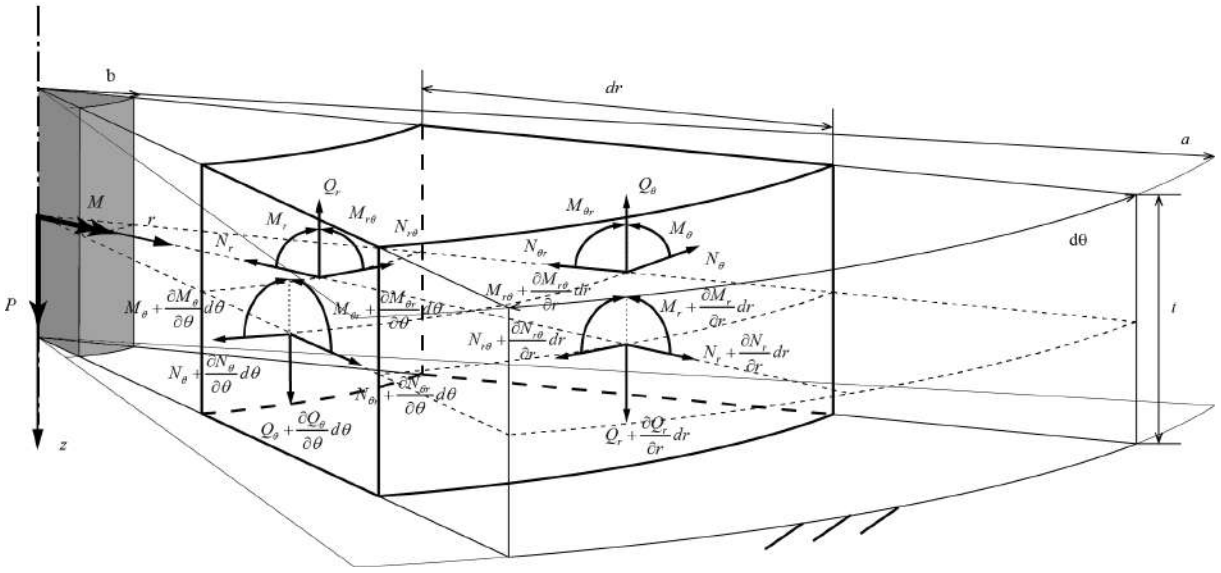

Figure 8.1: Angular sector of the composite bolted joint theoretical reference model undergoing the transversal load P and the in-plane bending moment M.

8.1 Application of Ritz method to the principle of virtual works

The Ritz method must be applied in conjunction with an energy principle that accounts for the natural boundary conditions of the problem [104]. The principle of virtual displacements was chosen to the scope, it states that for a body in equilibrium conditions the work done by all the external applied forces along virtual displacements, i.e. infinitesimal displacements admissible with respect to the geometrical constraints, is zero:

$$\delta W = \delta W_I + \delta W_E = 0 \tag{8.1}$$

where δW_I and δW_E are, respectively, the internal and the external virtual works.

The general expressions of both the internal and the external virtual works for rectilinear orthotropic composite circular plates are:

- Internal virtual work δW_I

$$\begin{aligned}\delta W_I = \int_\Omega \sigma_{ij}\ \delta\varepsilon_{ij}\ d\Omega &= \int_\Omega \Big(\sigma_r\ \delta\varepsilon_r + \sigma_\theta\ \delta\varepsilon_\theta + \tau_{\theta z}\ \delta\gamma_{\theta z} + \tau_{rz}\ \delta\gamma_{rz} + \tau_{r\theta}\ \delta\gamma_{r\theta}\Big)\ d\Omega \\ &= \int_b^a \int_{-\pi}^{\pi} \left[N_r \frac{\partial \delta u}{\partial r} + N_\theta \left(\frac{\delta u}{r} + \frac{1}{r}\frac{\partial \delta v}{\partial \theta} \right) + N_{r\theta} \left(\frac{1}{r}\frac{\partial \delta u}{\partial \theta} + \frac{\partial \delta v}{\partial r} \right) + \right. \\ &+ M_r \frac{\partial \delta \phi_r}{\partial r} + M_\theta \left(\frac{\delta \phi_r}{r} + \frac{1}{r}\frac{\partial \delta \phi_\theta}{\partial \theta} \right) + M_{r\theta} \left(\frac{1}{r}\frac{\partial \delta \phi_r}{\partial \theta} + \frac{\partial \delta \phi_\theta}{\partial r} - \frac{\delta \phi_\theta}{r} \right) + \\ &\left. + Q_r \left(\delta\phi_r + \frac{\partial \delta w}{\partial r} \right) + Q_\theta \left(\delta\phi_\theta + \frac{1}{r}\frac{\partial \delta w}{\partial \theta} \right) \right] d\theta\ r dr\end{aligned} \tag{8.2}$$

- External virtual work δW_E

$$\delta W_E = -\left(\int_\Omega \mathbf{f} \cdot \delta\mathbf{u}\ d\Omega + \int_{\Gamma_\sigma} \mathbf{T} \cdot \delta\mathbf{u}\ d\Gamma \right) \tag{8.3}$$

in which the symbol δ is employed to indicate virtual displacements and strains, Ω is the analytical integration region defining the rectilinear orthotropic composite circular plate, $\mathbf{f}$ denotes the body forces per unit volume, $\mathbf{T}$ the surface tractions per unit area acting on the external boundary portion Γ_σ, whereas $d\Omega$ and $d\Gamma$ are the infinitesimal volume and surface element, respectively.

Furthermore, the Ritz method requires each unknown displacement component s to be written as a finite linear combination of approximation functions:

$$s \approx S_N = \varphi_0 + \sum_{j=1}^{N} c_j\ \varphi_j \tag{8.4}$$

in this expression, c_j are unknown coefficients that serve as weights for the N approximation functions φ_j, φ_0 is the approximation function needed to satisfy the non-homogeneous essential boundary conditions if any is required. The approximation functions are required to be a continuous, linear independent and complete set of functions fulfilling the homogeneous form of the essential boundary conditions.

After the selection of the approximation functions, Ritz method addresses the substitution of the approximate form of the displacement components (8.4) in the energy principle, i.e. the virtual displacement statement outlined in (8.1) in this case. By virtue of this substitution, the principle of virtual displacements depends only on the N unknown coefficients. Then, its validity must be assured for every admissible virtual displacement obtained with the δc_i coefficients, this requirement implies the validity of the principle of virtual displacements independently from these coefficients:

$$\delta W(S_N) = \sum_{i=1}^{N} \frac{\partial W}{\partial c_i} \delta c_i = 0 \quad \forall \delta c_i \quad \Rightarrow \quad \frac{\partial W}{\partial c_i} = 0 \tag{8.5}$$

The validity of Eq. (8.5) requires the solution of a linear system of N algebraic equations to find the N unknown coefficients; each equation is of the type:

$$\sum_{j=1}^{N} R_{ij}\ c_j - F_i = 0, \qquad i = 1, 2, \ldots, N \tag{8.6}$$

in which the coefficient matrix terms R_{ij} are dependent on the approximation functions, material properties and plate geometry, meanwhile the known terms F_i depend on the external loads.

Afterwards, the algebraic equations system (8.6) is specialized for the different load conditions considered in this work. They consist in an annular plate featuring a rigid core at the inner edge and a fully clamped constraint at the outer one, made up of composite material with rectilinear orthotropic properties subject to transversal loads or in-plane bending moments.

According to these specific load conditions, the radial u and the circumferential v displacement components of the composite annular plate are null and the displacement components that must be determined are the mid-surface deflection w in conjunction with the rotations of the normal to the plate mid-surface about the circumferential and radial directions, ϕ_r and ϕ_θ respectively. Indeed, taking into account a symmetrical lay-up with respect to the composite plate mid-surface, the bending-extension coupling stiffness terms $B_{ij}(\theta)$ are all null and subsequently no in-plane displacements are induced by the plate bending. Additionally, the application of a load transversal to the plate mid-surface does not produce any membrane-shell coupling effect since the linear strain-displacement relations have been considered, consequently the are no components of displacement acting in the plate mid-surface.

8.2 Transversal load condition − FSDT

The transversal load condition involves the application of external loads orthogonally with respect to the mid-surface of the plate, such as distributed forces per unit-length acting at the outer or at the inner plate edge, Q_a and Q_b respectively, or a distributed load $q(r,\theta)$; therefore the general expression of the external virtual work for the transversal load condition is:

$$\delta W_E = -\int_{-\pi}^{\pi} \Big(b\ Q_b\ \delta w(b,\theta) - a\ Q_a\ \delta w(a,\theta) \Big)\ d\theta\ - \int_b^a \int_{-\pi}^{\pi} q(r,\theta)\ \delta w(r,\theta)\ d\theta\ r dr \tag{8.7}$$

The boundary conditions deriving from the theoretical reference model of composite bolted joint for a transversally loaded composite annular plate are:

- Outer edge of the plate: $r = a$

$$\begin{gathered} (I)\ w(a,\theta) = 0 \\ (II)\ \phi_r(a,\theta) = 0 \\ (III)\ \phi_\theta(a,\theta) = 0 \end{gathered} \tag{8.8}$$

- Inner edge of the plate: $r = b$

$$\begin{gathered} (IV)\ w(b,\theta) = const\ \ \forall\theta \Rightarrow\ \frac{\partial w(b,\theta)}{\partial\theta} = 0 \\ (V)\ \phi_r(b,\theta) = 0 \\ (VI)\ \phi_\theta(b,\theta) = 0 \end{gathered} \tag{8.9}$$

Null deflection at the outer radius, null rotations about the circumferential and the radial directions at the same radius of the plate are addressed by conditions (I), (II) and (III) respectively. Moreover, condition (IV) imposes constant deflection at the inner radius in reference to the angular coordinate θ, whereas conditions (V) and (VI) state null rotations around the circumferential and the radial directions at the inner edge.

Owing to the circumferentially variable bending stiffnesses, the three unknown displacement components of the rectilinear orthotropic composite circular are not axisymmetric and depend on the angular coordinate θ according to a trigonometric function. As a consequence, the approximate form of the mid-plate transversal displacement and the rotations about the circumferential and radial directions, i.e. $W_N(r,\theta)$, $\Phi_r^N(r,\theta)$ and $\Phi_\theta^N(r,\theta)$ respectively, are expressed as the summation of two contributions: the first one represents the medium contribution of the displacement component, not function of the circumferential coordinate θ; the second one is representative of the angular perturbation induced on the medium component of displacement by the not-axisymmetry of the material properties. Thus, the approximate form of the three displacement components to be determined are expressed as the summation of two contributions:

- Approximate mid-surface deflection

$$w(r,\theta) \approx W_N(r,\theta) = \overline{W}_M(r) + \widetilde{W}_N(r,\theta) = \sum_{j=1}^{M_\alpha} c_j \ \varphi_j(r) \ + \sum_{j=M_\alpha+1}^{N_\alpha} c_j \ \varphi_j(r,\theta) \tag{8.10}$$

- Approximate rotation about the circumferential direction

$$\phi_r(r,\theta) \approx \Phi_r^N(r,\theta) = \bar{\Phi}_r^M(r) + \widetilde{\Phi}_r^N(r,\theta) = \sum_{l=1}^{M_\beta} k_l \ \psi_l(r) \ + \sum_{l=M_\beta+1}^{N_\beta} k_l \ \psi_l(r,\theta) \tag{8.11}$$

- Approximate rotation about the radial direction

$$\phi_\theta(r,\theta) \approx \Phi_\theta^N(r,\theta) = \bar{\Phi}_\theta^M(r) + \widetilde{\Phi}_\theta^N(r,\theta) = \sum_{n=1}^{M_\gamma} h_n \ \lambda_n(r) \ + \sum_{n=M_\gamma+1}^{N_\gamma} h_n \ \lambda_n(r,\theta) \tag{8.12}$$

where c_j, k_l and h_n are the unknown scalar coefficients of the three approximate displacement components. In Eqs. (8.10-8.12), the first series $\overline{W}_M(r)$, $\bar{\Phi}_r^M(r)$ and $\bar{\Phi}_\theta^M(r)$ represent the medium and axisymmetric contribution of displacement component, the second ones $\widetilde{W}_N(r,\theta)$, $\widetilde{\Phi}_r^N(r,\theta)$ and $\widetilde{\Phi}_\theta^N(r,\theta)$ are the contributions for the angular perturbation needed to take into account the variable bending stiffnesses; being all the boundary conditions homogeneous, φ_0 is null. Further, the subscripts α, β and γ are employed because, in general, the number of terms in the series of the approximate displacement components are different.

The approximation functions $\varphi_j(r,\theta)$, $\psi_l(r,\theta)$ and $\lambda_n(r,\theta)$ for the angular perturbation contribution of the mid-surface deflection w and the rotations about the circumferential and the radial directions, ϕ_r and ϕ_θ, are defined as the product of a function that only depends on the radial

coordinate r, and a function which in turn is function of the only angular coordinate θ:

$$\begin{aligned} \varphi_j(r,\theta) &= p_j(r)\ g(\theta) \\ \psi_l(r,\theta) &= p_l(r)\ g(\theta) \\ \lambda_n(r,\theta) &= p_n(r)\ \frac{dg(\theta)}{d\theta} \end{aligned} \tag{8.13}$$

in which the functions $p(r)$ are employed for the angular dependent contribution of all three displacement components because they have to satisfy the same boundary conditions. Moreover, it can be concluded that the functions $p(r)$ can be utilized even for describe the axisymmetric contribution of the rotations ϕ_r and ϕ_θ, i.e.:

$$\begin{aligned} \psi_l(r) &= p_l(r) \\ \lambda_n(r) &= p_n(r) \end{aligned} \tag{8.14}$$

Moreover, according to the mid-plate transversal displacement, the purpose of the functions $p(r)$ is the fulfillment of the boundary conditions (8.8) and (8.9). Consequently, in order to respect the boundary condition (IV) which prescribes a uniform transversal displacement at the inner edge of the annular plate, the series $\widetilde{W}_N(r,\theta)$ must vanish at the inner radius b, even if the actual displacement of the composite annular plate at the inner edge is not null. This characteristic underlines the task carried out by the contribution $\widetilde{W}_N(r,\theta)$: it represents the circumferential fluctuation of the composite annular plate mid-surface deflection own to the θ-dependent bending stiffnesses.

Furthermore, the function $g(\theta)$ is a trigonometric function needed to take into account the circumferential variation of the displacement components in question and it assumes a specific form according to the lay-up of the composite annular plate. The two symmetrical lay-ups analyzed in the subsequent Section feature the following forms of the trigonometric function $g(\theta)$:

- QI lay-up

$$g(\theta) = \sin\left(2\theta + \frac{\pi}{4}\right) \tag{8.15}$$

- 0D lay-up

$$g(\theta) = \cos\left(2\theta - \frac{\pi}{8}\right) \tag{8.16}$$

The case studies hereinafter discussed in §8.4.1 make use of series $W_N(r,\theta)$, $\Phi_r^N(r,\theta)$ and $\Phi_\theta^N(r,\theta)$ composed of 10 terms; in particular, 5 terms series to represent the medium and axisymmetric contribution of displacement component and 5 for the not-axisymmetric ones. Both the functions $p(r)$ and the approximation functions $\varphi_j(r)$ employed in the numerical examples are of polynomial type and cannot be expressed through a general form, so the they are listed in the Appendix A and Appendix B, respectively.

For what concerns the determination of the unknown scalar coefficients c_j, k_l and h_n, the substitution of the approximate form of the displacement components outlined in Eqs. (8.10-8.12) in the principle of virtual displacements (8.5) returns a linear system of the type (8.6):

$$\left[\begin{array}{c|c|c} \boldsymbol{R}_{ij}^{N_\alpha x N_\alpha} & \boldsymbol{R}_{il}^{N_\alpha x N_\beta} & \boldsymbol{R}_{in}^{N_\alpha x N_\gamma} \\ \hline \boldsymbol{R}_{kj}^{N_\beta x N_\alpha} & \boldsymbol{R}_{kl}^{N_\beta x N_\beta} & \boldsymbol{R}_{kn}^{N_\beta x N_\gamma} \\ \hline \boldsymbol{R}_{mj}^{N_\gamma x N_\alpha} & \boldsymbol{R}_{ml}^{N_\gamma x N_\beta} & \boldsymbol{R}_{mn}^{N_\gamma x N_\gamma} \end{array}\right] \left\{\begin{array}{c} \vdots \\ c_j \\ \vdots \\ k_l \\ \vdots \\ h_n \\ \vdots \end{array}\right\} = \left\{\begin{array}{c} \vdots \\ F_i \\ \vdots \\ 0 \\ \vdots \\ 0 \\ \vdots \end{array}\right\} \tag{8.17}$$

Furthermore, in the coefficient matrix of the system of algebraic equations (8.17), different submatrices can be identified whose elements are:

$$R_{ij} = \int_b^a \int_{-\pi}^{\pi} \left\{\Phi_i\right\}^T \left[A(\theta)\right] \left\{\Phi_j\right\} \; d\theta \; r dr \tag{8.18a}$$

$$R_{il} = \int_b^a \int_{-\pi}^{\pi} \left\{\Phi_i\right\}^T \left[A_1(\theta)\right] \psi_l \; d\theta \; r dr \tag{8.18b}$$

$$R_{in} = \int_b^a \int_{-\pi}^{\pi} \left\{\Phi_i\right\}^T \left[A_2(\theta)\right] \lambda_n \; d\theta \; r dr \tag{8.18c}$$

$$R_{kj} = \int_b^a \int_{-\pi}^{\pi} \psi_k \left[A_1(\theta)\right]^T \left\{\Phi_j\right\} \; d\theta \; r dr \tag{8.18d}$$

$$R_{kl} = \int_b^a \int_{-\pi}^{\pi} \left(\left\{\Psi_k\right\}^T \left[D(\theta)\right] \left\{\Psi_l\right\} + A_{55}(\theta) \psi_k \psi_l \right) d\theta \; r dr \tag{8.18e}$$

$$R_{kn} = \int_b^a \int_{-\pi}^{\pi} \left(\left\{\Psi_k\right\}^T \left[D_1(\theta)\right] \left\{\Lambda_n\right\} + A_{45}(\theta) \psi_k \lambda_n \right) d\theta \; r dr \tag{8.18f}$$

$$R_{mj} = \int_b^a \int_{-\pi}^{\pi} \lambda_m \left[A_2(\theta)\right]^T \left\{\Phi_j\right\} \; d\theta \; r dr \tag{8.18g}$$

$$R_{ml} = \int_b^a \int_{-\pi}^{\pi} \left(\left\{\Lambda_m\right\}^T \left[D_1(\theta)\right]^T \left\{\Psi_l\right\} + A_{45}(\theta) \lambda_m \psi_l \right) d\theta \; r dr \tag{8.18h}$$

$$R_{mn} = \int_b^a \int_{-\pi}^{\pi} \left(\left\{\Lambda_m\right\}^T \left[D_2(\theta)\right] \left\{\Lambda_n\right\} + A_{44}(\theta) \lambda_m \lambda_n \right) d\theta \; r dr \tag{8.18i}$$

where:

$$\left\{\Phi_{i,j}\right\} = \left\{\begin{array}{c} \frac{1}{r} \frac{\partial \varphi_{i,j}}{\partial \theta} \\ \frac{\partial \varphi_{i,j}}{\partial r} \end{array}\right\} \qquad \left\{\Psi_{k,l}\right\} = \left\{\begin{array}{c} \frac{\partial \psi_{k,l}}{\partial r} \\ \frac{\psi_{k,l}}{r} \\ \frac{1}{r} \frac{\partial \psi_{k,l}}{\partial \theta} \end{array}\right\} \qquad \left\{\Lambda_{m,n}\right\} = \left\{\begin{array}{c} \frac{1}{r} \frac{\partial \lambda_{m,n}}{\partial \theta} \\ \frac{\partial \lambda_{m,n}}{\partial r} - \frac{\lambda_{m,n}}{r} \end{array}\right\} \tag{8.19}$$

$$\big[A_1(\theta)\big] = \begin{bmatrix} A_{45}(\theta) \\ A_{55}(\theta) \end{bmatrix} \qquad \big[A_2(\theta)\big] = \begin{bmatrix} A_{44}(\theta) \\ A_{45}(\theta) \end{bmatrix} \tag{8.20}$$

$$\big[D_1(\theta)\big] = \begin{bmatrix} D_{12}(\theta) & D_{16}(\theta) \\ D_{22}(\theta) & D_{26}(\theta) \\ D_{26}(\theta) & D_{66}(\theta) \end{bmatrix} \qquad \big[D_2(\theta)\big] = \begin{bmatrix} D_{22}(\theta) & D_{26}(\theta) \\ D_{26}(\theta) & D_{66}(\theta) \end{bmatrix} \tag{8.21}$$

Additionally, according to the expression of the external virtual work in (8.7), the known terms in the general case where different kinds of load act on the annular plate are:

$$F_i = \int_{-\pi}^{\pi} \Big(b\ Q_b\ \varphi_i(b,\theta) - a\ Q_a\ \varphi_i(a,\theta) \Big)\ d\theta\ + \int_b^a \int_{-\pi}^{\pi} q(r,\theta)\ \varphi_i(r,\theta)\ d\theta\ r dr \tag{8.22}$$

In order to solve a load condition aimed to the definition of a custom composite bolted joint finite element stiffness matrix, the transversal load of interest is represented by a force P applied to the annular plate axis, in correspondence of the rigid core, directed as the z-axis of cylindrical coordinate system. Since the rigid core does not belong to the integration domain Ω where the annular plate is defined, a statically equivalent distributed force per unit-length acting at the inner edge of the plate $Q_b = \frac{P}{2\pi b}$ is analyzed instead of the load P.

8.3 In-plane bending moment − FSDT

The load condition hereinafter discussed regards the rectilinear orthotropic composite annular plate undergoing an in-plane bending moment M, applied in correspondence of the symmetry axis, acting on its mid-surface along the x-axis of the global Cartesian coordinate system. As a consequence, the external virtual work is:

$$\delta W_E = -\left(\frac{M}{2} \delta\phi_\theta(b,0) - \frac{M}{2} \delta\phi_\theta(b,\pi) \right) \tag{8.23}$$

It should be noted that the application point of the in-plane bending moment M does not belong to the annular plate integration domain Ω, so the external load was considered halved in two contributions, acting along its direction, and applied at the inner radius b of the composite annular plate and at the angular coordinates $\theta = 0$ and π.

The theoretical reference model of composite bolted joint for a composite annular plate undergoing an in-plane bending moment imposes the following boundary conditions:

- Outer edge of the plate: $r = a$

$$\begin{gathered} (I)\ w(a,\theta) = 0 \\ (II)\ \phi_r(a,\theta) = 0 \\ (III)\ \phi_\theta(a,\theta) = 0 \end{gathered} \tag{8.24}$$

- Inner edge of the plate: $r = b$

$$\begin{aligned} (IV)\ \phi_r(b,\theta) &= \frac{w(b,\theta)}{b} \\ (V)\ \phi_\theta(b,\theta) &= \frac{1}{b}\ w\left(b, \theta + \frac{\pi}{2}\right) \end{aligned} \tag{8.25}$$

The boundary condition (I) states null deflection at the outer edge of the composite annular plate, whereas boundary conditions (II) and (III) impose null rotations about the circumferential and the radial direction, respectively. Then, owing to the rigid core, condition (IV) addresses that the rotation about the circumferential direction evaluated at the inner radius must be equal to the ratio between the deflection, at the same radial coordinate, and the inner radius; moreover, analogously, condition (V) regards the equality between the rotation about the radial direction and the ratio of the deflection, at the inner radius and at a radial coordinate out-of-phase of $\frac{\pi}{2}$ rad, and the inner radius.

The approximate forms of the in-plane displacement components w and ϕ_r and ϕ_θ are:

- Approximate mid-surface deflection

$$w(r,\theta) \approx W_N(r,\theta) = c_0\ \varphi_0(r,\theta) + \sum_{j=1}^{N_\alpha} c_j\ \varphi_j(r,\theta) \tag{8.26}$$

- Approximate rotation about the circumferential direction

$$\phi_r(r,\theta) \approx \Phi_r^N(r,\theta) = k_0\ \psi_0(r,\theta) + \sum_{l=1}^{N_\beta} k_l\ \psi_l(r,\theta) \tag{8.27}$$

- Approximate rotation about the radial direction

$$\phi_\theta(r,\theta) \approx \Phi_\theta^N(r,\theta) = h_0\ \lambda_0(r,\theta) + \sum_{n=1}^{N_\gamma} h_n\ \lambda_n(r,\theta) \tag{8.28}$$

The employment of the φ_0 and ψ_0 approximation functions is related to the fact that at the inner radius the mid-surface deflection and the rotations about the circumferential direction are other than zero but not known a priori.

In addition, the substitution of the approximated displacement components (8.26) and (8.27) in the (IV) boundary condition is helpful to characterize them:

$$c_0\ \varphi_0(b,\theta) + \sum_{j=1}^{N_\alpha} c_j\ \varphi_j(b,\theta) = \ k_0\ \psi_0(b,\theta) + \sum_{l=1}^{N_\beta} k_l\ \psi_l(b,\theta) \tag{8.29}$$

Primarily, the terms of the series featuring the approximation functions φ_j and ψ_l cannot be equal and opposite: in that case the trends of the mid-surface deflection w and the rotation about the circumferential direction ϕ_r would result the same meanwhile they are distinct; therefore, in order to verify Eq. (8.29), they must necessarily vanish at the inner edge of the composite annular plate. Conversely, the terms with the approximation functions φ_0 and ψ_0 must be equal, so it is assumed

that the scalar coefficients $c_0 = k_0$ and that the approximation functions $\varphi_0(b,\theta)$ and $\psi_0(b,\theta)$ are equal.

Similarly, the substitution of the approximated displacement components (8.26) and (8.28) in the (V) boundary condition leads to similar considerations, i.e. even the approximation functions λ_n must vanish at the inner radius, the approximation functions φ_0 and λ_0 must be equal and the scalar coefficients $c_0 = h_0$.

According to the load condition and the material properties, the displacement components of the rectilinear orthotropic composite circular plate turns out to be not-axisymmetric, so the approximation functions present in Eqs. (8.26-8.28) are defined as the product of two functions: the first one only depends on the radial coordinate r, and the second one which in turn is function of the only angular coordinate θ:

$$\begin{aligned} \varphi_{0,j}(r,\theta) &= p_{0,j}(r)\sin(\theta) \\ \psi_{0,l}(r,\theta) &= p_{0,l}(r)\sin(\theta) \\ \lambda_n(r,\theta) &= p_{0,n}(r)\cos(\theta) \end{aligned} \tag{8.30}$$

Moreover, the choice of the sinusoidal function for the approximation functions $\varphi_{0,j}$ and $\psi_{0,l}$ is justified by the necessity of achieving displacement components that are maximum along the direction orthogonal to the in-plane bending moment M and null along its direction of application; analogously, the rotations about the radial direction must result maximum at the angular coordinate $\theta = 0$ and null in amplitude for $\theta = \frac{\pi}{2}$. The functions $p(r)$ cannot be depicted in a general form, subsequently the functions utilized in the numerical case studies are reported in the Appendix A.

A linear system of the type (6.9) to determine the scalar coefficients c_j is defined through the substitution of the approximate form of transversal displacement, expressed in (8.26), in the principle of virtual displacements (7.5). The matrix coefficients features terms of the type: The application of Ritz method to the principle of virtual displacements in (7.5) for the in-plane load condition returns the following system of algebraic equations that must be solved to determine the weight coefficients of the approximation functions:

$$\left[\begin{array}{c|c|c|c} R_{00}^{1x1} & R_{0j}^{1xN_\alpha} & R_{0l}^{0xN_\beta} & R_{0n}^{0xN_\gamma} \\ \hline R_{i0}^{N_\alpha x1} & R_{ij}^{N_\alpha xN_\alpha} & R_{il}^{N_\alpha xN_\beta} & R_{in}^{N_\alpha xN_\gamma} \\ \hline R_{k0}^{N_\beta x1} & R_{kj}^{N_\beta xN_\alpha} & R_{kl}^{N_\beta xN_\beta} & R_{kn}^{N_\beta xN_\gamma} \\ \hline R_{m0}^{N_\gamma x1} & R_{mj}^{N_\gamma xN_\alpha} & R_{ml}^{N_\gamma xN_\beta} & R_{mn}^{N_\gamma xN_\gamma} \end{array}\right] \left\{\begin{array}{c} c_0 \\ \vdots \\ c_j \\ \vdots \\ k_l \\ \vdots \\ h_n \\ \vdots \end{array}\right\} = \left\{\begin{array}{c} 0 \\ \vdots \\ 0 \\ \vdots \\ 0 \\ \vdots \\ F_n \\ \vdots \end{array}\right\} \tag{8.31}$$

Furthermore, in the coefficient matrix of the system of algebraic equations (8.31), different submatrices can be identified whose elements are:

$$R_{00} = \int_b^a \int_{-\pi}^{\pi} \left(\left(\left\{\Psi_0\right\} + \left\{\Lambda_0\right\} \right)^T \left[D(\theta)\right] \left(\left\{\Psi_0\right\} + \left\{\Lambda_0\right\} \right) + \left\{\Upsilon_0\right\}^T \left[A(\theta)\right] \left\{\Upsilon_0\right\} \right) d\theta \; rdr \tag{8.32a}$$

$$R_{0j} = \int_b^a \int_{-\pi}^{\pi} \left\{\Upsilon_0\right\}^T \left[A(\theta)\right] \left\{\Phi_j\right\} \; d\theta \; rdr \tag{8.32b}$$

$$R_{0l} = \int_b^a \int_{-\pi}^{\pi} \left(\left(\left\{\Psi_0\right\} + \left\{\Lambda_0\right\} \right)^T \left[D(\theta)\right] \left\{\Psi_l\right\} + \left\{\Upsilon_0\right\}^T \left[A_1(\theta)\right] \psi_l \right) d\theta \; rdr \tag{8.32c}$$

$$R_{0n} = \int_b^a \int_{-\pi}^{\pi} \left\{\Phi_0\right\}^T \left[A_2(\theta)\right] \lambda_n \; d\theta \; rdr \tag{8.32d}$$

$$R_{i0} = \int_b^a \int_{-\pi}^{\pi} \left\{\Phi_i\right\}^T \left[A(\theta)\right] \left\{\Upsilon_0\right\} \; d\theta \; rdr \tag{8.32e}$$

$$R_{ij} = \int_b^a \int_{-\pi}^{\pi} \left\{\Phi_i\right\}^T \left[A(\theta)\right] \left\{\Phi_j\right\} \; d\theta \; rdr \tag{8.32f}$$

$$R_{il} = \int_b^a \int_{-\pi}^{\pi} \left\{\Phi_i\right\}^T \left[A_1(\theta)\right] \psi_l \; d\theta \; rdr \tag{8.32g}$$

$$R_{in} = \int_b^a \int_{-\pi}^{\pi} \left\{\Phi_i\right\}^T \left[A_2(\theta)\right] \lambda_n \; d\theta \; rdr \tag{8.32h}$$

$$R_{k0} = \int_b^a \int_{-\pi}^{\pi} \left(\left\{\Psi_k\right\}^T \left[D(\theta)\right] \left(\left\{\Psi_0\right\} + \left\{\Lambda_0\right\} \right) + \psi_k \left[A_1(\theta)\right]^T \left\{\Upsilon_0\right\} \right) d\theta \; rdr \tag{8.32i}$$

$$R_{kj} = \int_b^a \int_{-\pi}^{\pi} \psi_k \left[A_1(\theta)\right]^T \left\{\Phi_j\right\} \; d\theta \; rdr \tag{8.32j}$$

$$R_{kl} = \int_b^a \int_{-\pi}^{\pi} \left(\left\{\Psi_k\right\}^T \left[D(\theta)\right] \left\{\Psi_l\right\} + A_{55}(\theta)\psi_k\psi_l \right) d\theta \; rdr \tag{8.32k}$$

$$R_{kn} = \int_b^a \int_{-\pi}^{\pi} \left(\left\{\Psi_k\right\}^T \left[D_1(\theta)\right] \left\{\Lambda_n\right\} + A_{45}(\theta)\psi_k\lambda_n \right) d\theta \; rdr \tag{8.32l}$$

$$R_{m0} = \int_b^a \int_{-\pi}^{\pi} \left(\left\{\Lambda_m\right\}^T \left[D_1(\theta)\right]^T \left(\left\{\Psi_0\right\} + \left\{\Lambda_0\right\} \right) + \lambda_m \left[A_2(\theta)\right]^T \left\{\Upsilon_0\right\} \right) d\theta \; rdr \tag{8.32m}$$

$$R_{mj} = \int_b^a \int_{-\pi}^{\pi} \lambda_m \left[A_2(\theta)\right]^T \left\{\Phi_j\right\} \; d\theta \; rdr \tag{8.32n}$$

$$R_{ml} = \int_b^a \int_{-\pi}^{\pi} \left(\left\{\Lambda_m\right\}^T \left[D_1(\theta)\right]^T \left\{\Psi_l\right\} + A_{45}(\theta)\lambda_m\psi_l \right) d\theta \; rdr \tag{8.32o}$$

$$R_{mn} = \int_b^a \int_{-\pi}^{\pi} \left(\left\{\Lambda_m\right\}^T \left[D_2(\theta)\right] \left\{\Lambda_n\right\} + A_{44}(\theta)\lambda_m\lambda_n \right) d\theta \; rdr \tag{8.32p}$$

in which:

$$\left\{\Phi_{0,i,j}\right\} = \begin{Bmatrix} \frac{1}{r}\frac{\partial \varphi_{0,i,j}}{\partial \theta} \\ \frac{\partial \varphi_{0,i,j}}{\partial r} \end{Bmatrix} \qquad \left\{\Upsilon_0\right\} = \begin{Bmatrix} \lambda_0 + \frac{1}{r}\frac{\partial \varphi_0}{\partial \theta} \\ \psi_0 + \frac{\partial \varphi_0}{\partial r} \end{Bmatrix}$$

$$\left\{\Psi_{0,k,l}\right\} = \begin{Bmatrix} \frac{\partial \psi_{0,k,l}}{\partial r} \\ \frac{\psi_{0,k,l}}{r} \\ \frac{1}{r}\frac{\partial \psi_{0,k,l}}{\partial \theta} \end{Bmatrix} \qquad \left\{\Lambda_{m,n}\right\} = \begin{Bmatrix} \frac{1}{r}\frac{\partial \lambda_{m,n}}{\partial \theta} \\ \frac{\partial \lambda_{m,n}}{\partial r} - \frac{\lambda_{m,n}}{r} \end{Bmatrix} \tag{8.33}$$

$$\left[A_1(\theta)\right] = \begin{bmatrix} A_{45}(\theta) \\ A_{55}(\theta) \end{bmatrix} \qquad \left[A_2(\theta)\right] = \begin{bmatrix} A_{44}(\theta) \\ A_{45}(\theta) \end{bmatrix} \tag{8.34}$$

$$\left[D_1(\theta)\right] = \begin{bmatrix} D_{12}(\theta) & D_{16}(\theta) \\ D_{22}(\theta) & D_{26}(\theta) \\ D_{26}(\theta) & D_{66}(\theta) \end{bmatrix} \qquad \left[D_2(\theta)\right] = \begin{bmatrix} D_{22}(\theta) & D_{26}(\theta) \\ D_{26}(\theta) & D_{66}(\theta) \end{bmatrix} \tag{8.35}$$

Moreover, as can be deduced from the the external virtual work outlined in Eq. (8.23), the known terms of the linear system for the in-plane bending moment load condition are:

$$F_n = \frac{M}{2}\lambda_n(b,0) - \frac{M}{2}\lambda_n(b,\pi) \tag{8.36}$$

where, in order to transfer the in-plane bending moment M on the integration domain Ω of the annular plate, it was split into two bending moments acting at the inner radius and in correspondence of the angular coordinates $\theta = 0$ and $\theta = \pi$, i.e. alongside the direction of the external load M.

8.4 Results

This Section concerns the application of the proposed analytical method to some case studies reproducing the reference model of Spot Joint Element to verify the proposed method reliability. As previously described, they are referred to annular plates clamped on the outer radius and featuring an internal rigid core. The composite annular plates hereinafter analyzed are transversally loaded as regards the outcomes presented in §8.4.1 and in §8.4.2 they undergo an in-plane bending moment.

The external transversal loads acting on the annular plates consist in a unitary force P applied to the plate axis, along the z-axis of the cylindrical coordinate system and with the same verse; whereas, the second load condition prescribes a unitary in-plane bending moment M applied along the x-axis of the global Cartesian coordinate system (see Fig. 8.1).

Results from all proposed case studies are then compared with those obtained by means of refined FE models. The FE models were made using layered shell featuring 4 nodes with 6 DOFs per node.

The application examples are carried out making use of rectilinear orthotropic composite annular plates made up of widely employed lay-ups for applications concerning composite bolted joints, i.e. QI and 0D lay-ups as reported in [52, 57, 58, 59, 60]. Specifically, the employed stacking sequences (Table 6.1) and the unidirectional fiber-reinforced layer stiffness properties (Table 6.2) are reported in [57]; the layer thickness is $t_{lay} = 0.13$ mm.

All the numerical tests were executed with a fixed value of the overall composite annular plate thickness $t = 5.2$ mm. Besides, the impact on results accuracy of composite annular plates geometrical characteristics was investigated. In particular, three different slenderness ratios between the plate thickness t and its outer radius a were examined: 0.05, 0.075 and 0.100. This study is needed to progressively emphasize the plate shear deformability and highlight how it affects the results furnished by the proposed method and that cannot be taken into account by the methods proposed in [64, 65, 66, 67] which are based on the CPT.

Additionally, six different plate aspect ratios $\beta = \frac{b}{a}$ obtained trough the ratio between the inner and the outer radii of the plate were analyzed: $\beta_0 = 0.05$, $\beta_1 = 0.1$, $\beta_2 = 0.2$, $\beta_3 = 0.3$, $\beta_4 = 0.4$ and $\beta_5 = 0.5$.

The comparisons between results of the proposed analytical method (named FSDT in the Figures) and those of FE analyses are presented in the diagrams in dimensionless form, showing the distribution of the displacement components along both radial and circumferential coordinates.

Moreover, for what concerns the composite annular plate configuration characterized by slenderness ratio $\frac{t}{a} = 0.050$, which represents the upper-bound value for the application of the thin-plate theory, results obtained through the analytical method founded on the Classical Plate Theory (named CPT in the Figures) outlined in [66, 67] are further reported in terms of mid-surface deflection and rotations about the circumferential direction; whereas analogous outcomes for the rotations about the radial direction are not reported in the case of transversal load condition since their percentage variation with respect to the FE solution is too considerable.

8.4.1 Transversal load P – FSDT

As regards results for the mid-surface deflection, numerical results in Fig. 8.2 are presented in terms of dimensionless deflection, for both QI and 0D lay-ups and all the considered slenderness ratios, that is the ratio between the mid-surface deflection $w(r, 0)$ and its value at the inner edge $w(\beta, 0)$ obtained with FE analyses. These diagrams show the dimensionless deflection variation along the dimensionless radius $\rho = \frac{r}{a}$, at the angular coordinate $\theta = 0$ rad. Similarly, Fig. 8.3 reports for both QI and 0D lay-ups, for all the considered slenderness ratios $\frac{t}{a}$, and for an aspect ratio $\beta = 0.1$, the variation of the dimensionless mid-surface deflection along the dimensionless angle $\overline{\theta} = \frac{\theta}{\pi}$. Again, dimensionless quantities are based on the mid-surface deflection at the inner edge $w(\beta, 0)$ obtained with FE analyses. Moreover, any of these diagrams outline the circumferential variation of the mid-surface deflection at five values of the dimensionless radius: ρ=(β, 0.25, 0.40, 0.60, 0.80).

Results in Figs. 8.2 and 8.3 demonstrate that the proposed analytical method is capable of describing the composite annular plate mid-surface deflection with an excellent level of fidelity for both the dependences on the radial and the angular coordinates. Further, Table 8.1 reports the percentage variations Δ_β, evaluated at the inner radius $\rho = \beta$, between the results of the analytical method and the FE ones for both QI and 0D lay-ups. It is evidenced that regardless the lay-up, the slenderness and the aspect ratios the percentage variations are contained within the threshold of the numerical error, stating a significant coincidence between the outcomes of the proposed analytical method and the FE ones.

Additionally, as regards the angular variation of the mid-surface deflection (Fig. 8.3), the curves for $\rho = 0.40$ and 0.60 feature a more notable fluctuation with the angular coordinate, meanwhile it is less evident for $\rho = \beta$, 0.25 and 0.80 because the constrains acting on the internal and external radii tend to limit its circumferential variability. It should be noted that the mid-surface deflection for $\rho = \beta$ turns out to be not dependent on the angular coordinate θ: this confirms the capability of

Table 8.1: Mid-surface deflection percentage variation $\Delta_{\beta_i}[\%]$, evaluated at $\rho = \beta$ for various values β_i, between analytical method and FEA for both lay-ups.

QI lay-up							
	$\frac{t}{a}$	$\Delta_{\beta_0}[\%]$	$\Delta_{\beta_1}[\%]$	$\Delta_{\beta_2}[\%]$	$\Delta_{\beta_3}[\%]$	$\Delta_{\beta_4}[\%]$	$\Delta_{\beta_5}[\%]$
CPT	0.050	−8.20	−7.55	−7.71	−8.94	−11.16	−14.83
FSDT	0.050	−0.68	−0.56	−0.31	−0.33	−0.37	−0.38
	0.075	−0.79	−0.66	−0.38	−0.63	−0.77	−0.98
	0.100	−1.11	−0.88	−0.89	−0.99	−1.17	−1.44

0D lay-up							
	$\frac{t}{a}$	$\Delta_{\beta_0}[\%]$	$\Delta_{\beta_1}[\%]$	$\Delta_{\beta_2}[\%]$	$\Delta_{\beta_3}[\%]$	$\Delta_{\beta_4}[\%]$	$\Delta_{\beta_5}[\%]$
CPT	0.050	−8.45	−7.69	−7.95	−9.36	−11.4	−15.19
FSDT	0.050	−0.71	−0.58	−0.34	−0.30	−0.37	−0.51
	0.075	−0.82	−0.61	−0.58	−0.64	−0.75	−1.02
	0.100	−1.15	−0.92	−0.88	−0.97	−1.14	−1.41

Table 8.2: Rotation about the circumferential direction percentage variation $\Delta_{\beta_i}[\%]$, evaluated for the maximum value at $\overline{\theta} = 0.5$, for various values β_i, between analytical method and FEA for both lay-ups.

QI lay-up							
	$\frac{t}{a}$	$\Delta_{\beta_0}[\%]$	$\Delta_{\beta_1}[\%]$	$\Delta_{\beta_2}[\%]$	$\Delta_{\beta_3}[\%]$	$\Delta_{\beta_4}[\%]$	$\Delta_{\beta_5}[\%]$
CPT	0.050	0.57	−0.61	−0.26	−0.02	0.04	0.29
FSDT	0.050	−0.26	0.20	0.06	−0.28	−0.50	0.30
	0.075	−1.00	−0.45	−0.62	−0.57	−0.85	−1.13
	0.100	−1.45	−0.97	−0.75	−1.03	−1.36	−1.73

0D lay-up							
	$\frac{t}{a}$	$\Delta_{\beta_0}[\%]$	$\Delta_{\beta_1}[\%]$	$\Delta_{\beta_2}[\%]$	$\Delta_{\beta_3}[\%]$	$\Delta_{\beta_4}[\%]$	$\Delta_{\beta_5}[\%]$
CPT	0.050	0.11	0.06	−0.45	−0.62	1.21	2.33
FSDT	0.050	−0.13	0.21	0.26	−0.43	−0.04	0.39
	0.075	−0.83	−0.23	0.17	0.38	0.49	0.56
	0.100	−1.27	−0.54	0.08	0.40	0.37	0.76

Table 8.3: Rotation about the radial direction percentage variation $\Delta_{\beta_i}[\%]$, evaluated for the maximum value at $\overline{\theta} = 0.5$, for various values β_i, between analytical method and FEA for both lay-ups.

QI lay-up						
$\frac{t}{a}$	$\Delta_{\beta_0}[\%]$	$\Delta_{\beta_1}[\%]$	$\Delta_{\beta_2}[\%]$	$\Delta_{\beta_3}[\%]$	$\Delta_{\beta_4}[\%]$	$\Delta_{\beta_5}[\%]$
0.050	1.92	0.77	1.13	2.44	−3.30	−11.67
0.075	3.08	1.59	−1.77	−3.07	−10.35	−14.37
0.100	2.11	0.19	−3.39	−8.01	−12.67	−15.34

0D lay-up						
$\frac{t}{a}$	$\Delta_{\beta_0}[\%]$	$\Delta_{\beta_1}[\%]$	$\Delta_{\beta_2}[\%]$	$\Delta_{\beta_3}[\%]$	$\Delta_{\beta_4}[\%]$	$\Delta_{\beta_5}[\%]$
0.050	2.52	5.78	0.90	−10.50	−11.02	−17.23
0.075	0.20	1.52	2.91	−12.86	−12.09	−16.54
0.100	−1.26	−1.66	−1.04	−11.84	−13.84	−16.86

chosen approximation functions of fulfilling the (IV) of boundary conditions (8.9).

Then, according to the lay-up influence, the composite annular plates featuring QI lay-up present a maximum circumferential variation of the mid-surface deflection, for a given value of ρ, of 5%; instead, the laminates with 0D lay-up are characterized by a circumferential variation of mid-surface deflection of the order of 10%. Hence, the composite annular plates with 0D lay-up more strongly depends on the angular coordinate θ.

Furthermore, the comparison between the methods based on the FSDT and on the CPT for the plate configuration with slenderness ratio $\frac{t}{a} = 0.050$ reveals that the percentage variations Δ_β observed in the results derived by means of the analytical method described in [66] can be abated, for all the considered aspect ratios, taking into account the plate shear deformability, i.e. exploiting the proposed analytical method. Thus, the slenderness ratio $\frac{t}{a} = 0.050$ can be considered as an indicative threshold value between the application field of the thin-plate theory and the range where the contribution of the plate shear deformability cannot be neglected.

Besides, Figs. 8.4 and 8.6 summarize, for both lay-ups, results regarding the variation along the dimensionless radial coordinate ρ of the dimensionless forms of the rotations about the circumferential and the radial coordinates, respectively, that are obtained through the ratios between the functions $\phi_r(\rho, 0)$ and $\phi_\theta(\rho, \frac{\pi}{2})$ and their maximum values obtained by means of FE analyses with aspect ratio β_0. In addition, the circumferential variation of the rotation components is shown in dimensionless form in Figs. 8.5 and 8.7, for the shape factor $\beta = 0.1$, against the dimensionless angular coordinate $\overline{\theta}$; dimensionless quantities are based on the maximum value of rotation components obtained with FE analyses. Different specific values of the dimensionless radii are considered: ρ=(β, 0.20, 0.40, 0.60 and 0.80) for the rotation about the circumferential direction and ρ=(0.40, 0.60 and 0.80) for the rotation about the radial direction.

As for the mid-surface deflection, both the radial and the circumferential variations of the rotation ϕ_r (Figs. 8.4 and 8.5) are described with high precision by the proposed analytical method. Observing the curves for this rotation component against the dimensionless radial coordinate ρ (Fig. 8.4), it should be noticed that, for every aspect ratio β_i and both lay-ups, the maximum value of the functions ϕ_r is located at a radial coordinate which is approximately distant 0.3 from the inner edge of the

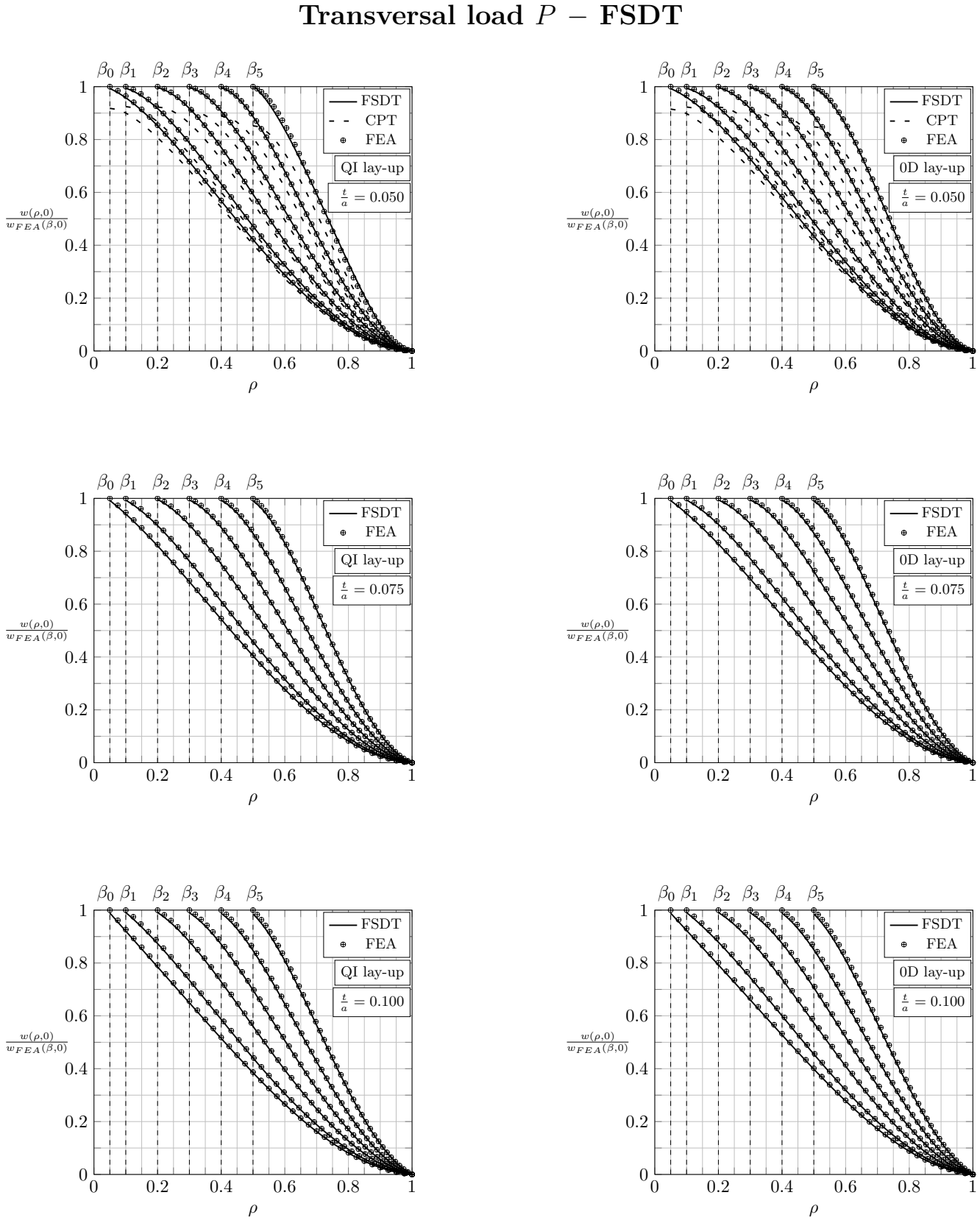

Figure 8.2: Curves of dimensionless mid-surface deflection as function of ρ, evaluated at $\theta = 0$ rad for different ratios $\frac{t}{a}$ and for $\beta_0 = 0.05$, $\beta_1 = 0.1$, $\beta_2 = 0.2$, $\beta_3 = 0.3$, $\beta_4 = 0.4$ and $\beta_5 = 0.5$ with QI and 0D lay-ups.

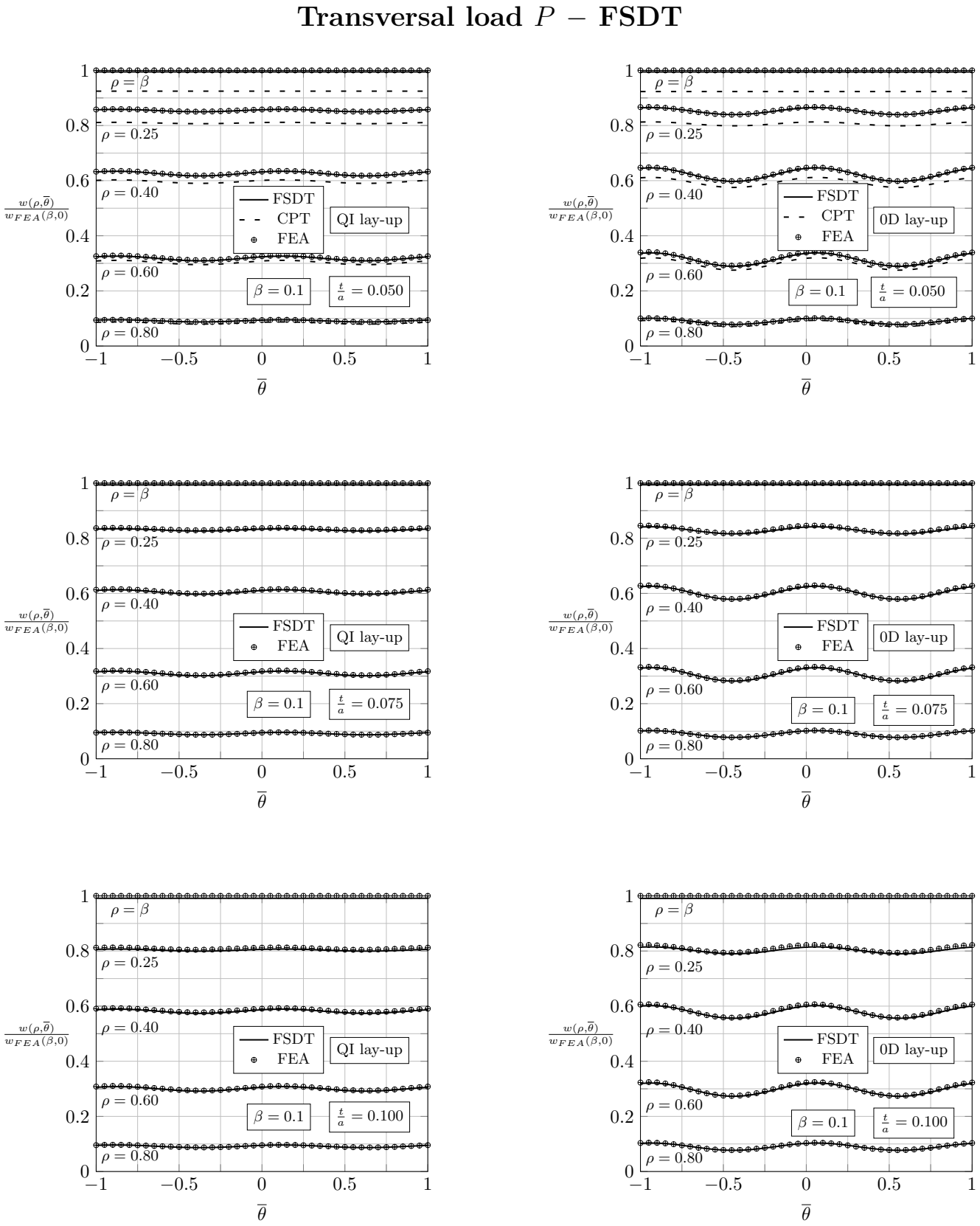

Figure 8.3: Curves of dimensionless mid-surface deflection as function of $\overline{\theta}$ for different ratios $\frac{t}{a}$ and $\beta = 0.1$, at $\rho =(\beta, 0.25, 0.40, 0.60, 0.80)$ with QI and 0D lay-ups.

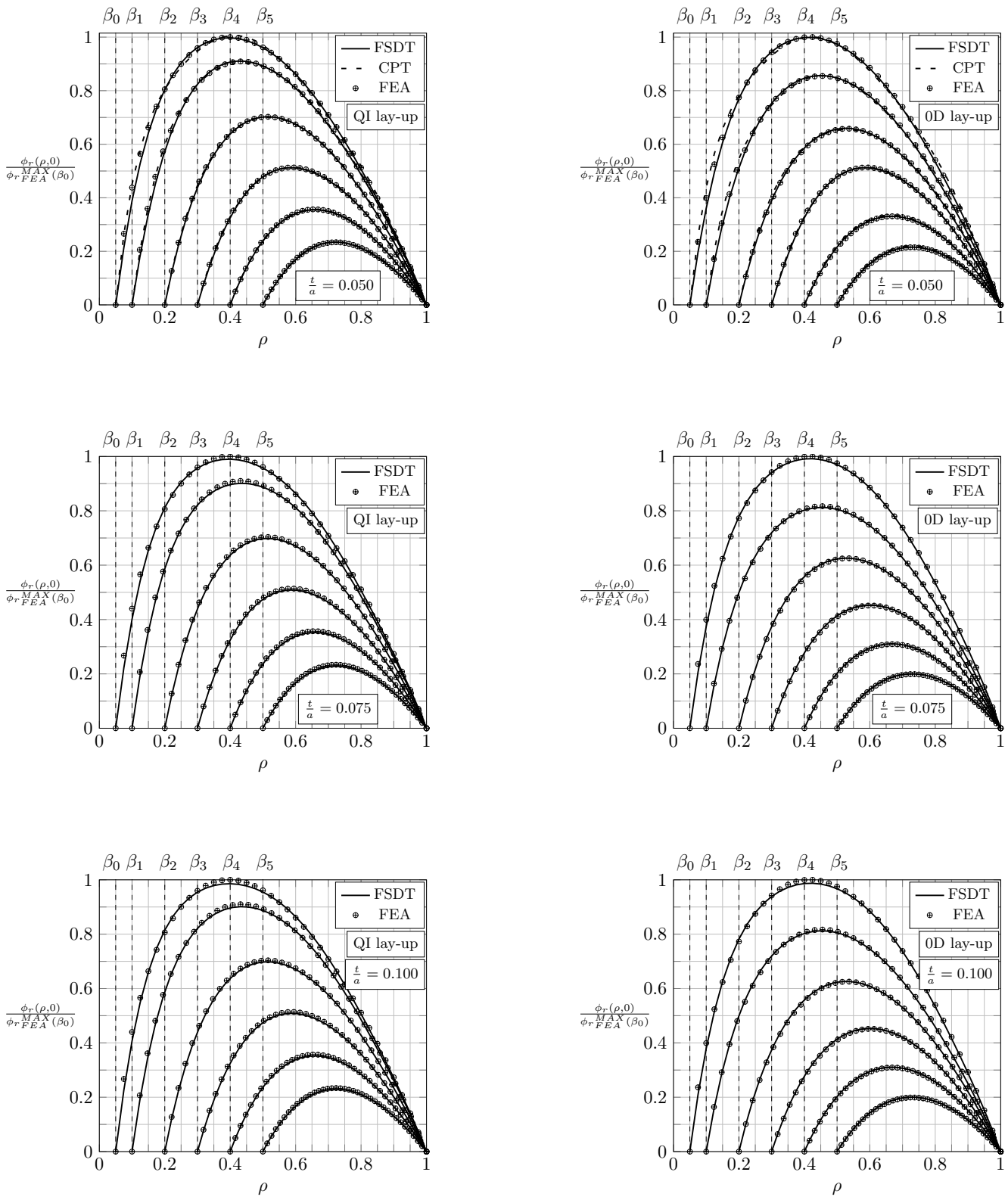

Figure 8.4: Curves of dimensionless rotation about the circumferential direction as function of ρ, evaluated at $\theta = 0$ rad for different ratios $\frac{t}{a}$ and for $\beta_0 = 0.05$, $\beta_1 = 0.1$, $\beta_2 = 0.2$, $\beta_3 = 0.3$, $\beta_4 = 0.4$ and $\beta_5 = 0.5$ with QI and 0D lay-ups.

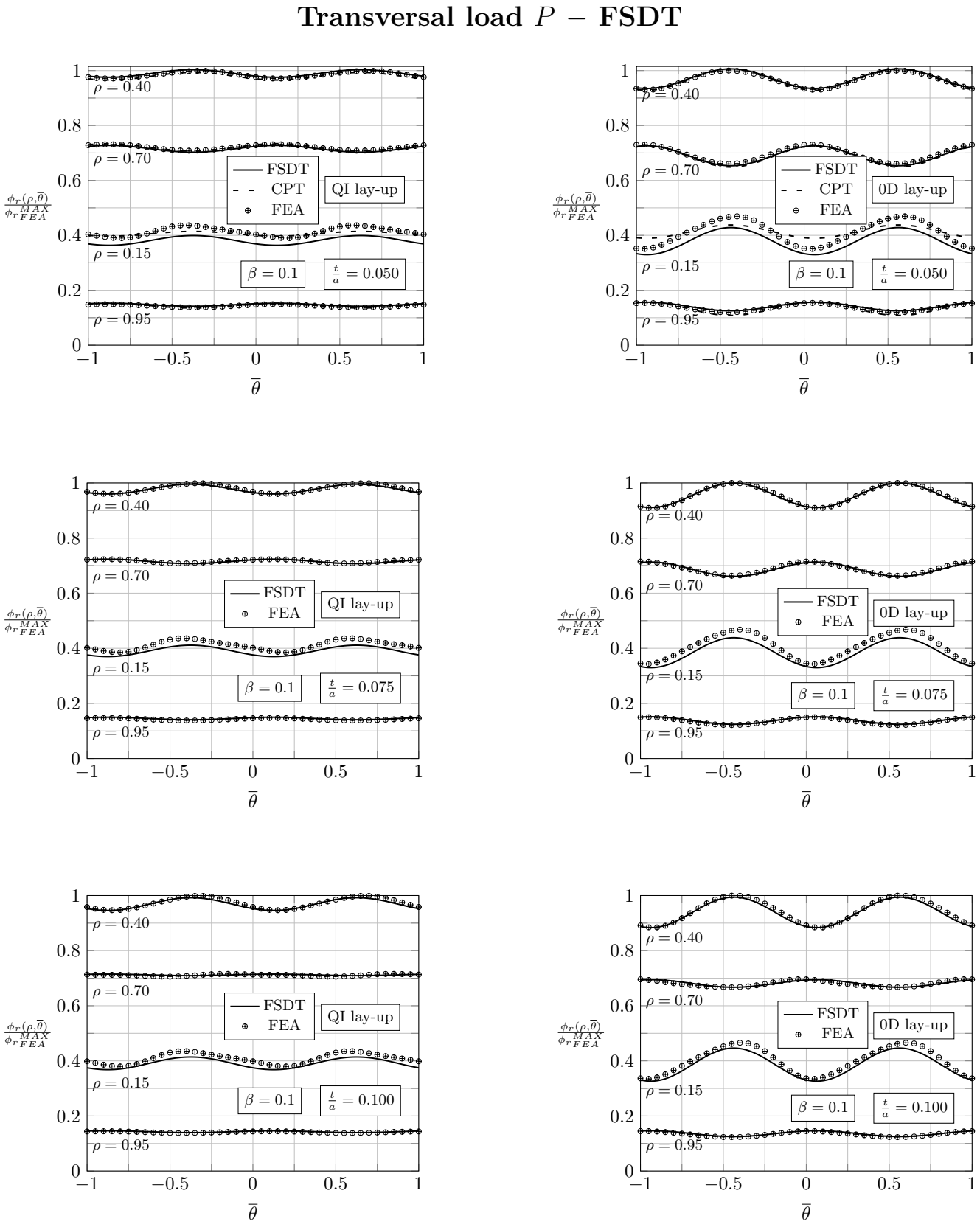

Figure 8.5: Curves of dimensionless rotation about the circumferential direction as function of $\overline{\theta}$ for different ratios $\frac{t}{a}$ and $\beta = 0.1$, at $\rho =(\beta,\ 0.25,\ 0.40,\ 0.60,\ 0.80)$ with QI and 0D lay-ups.

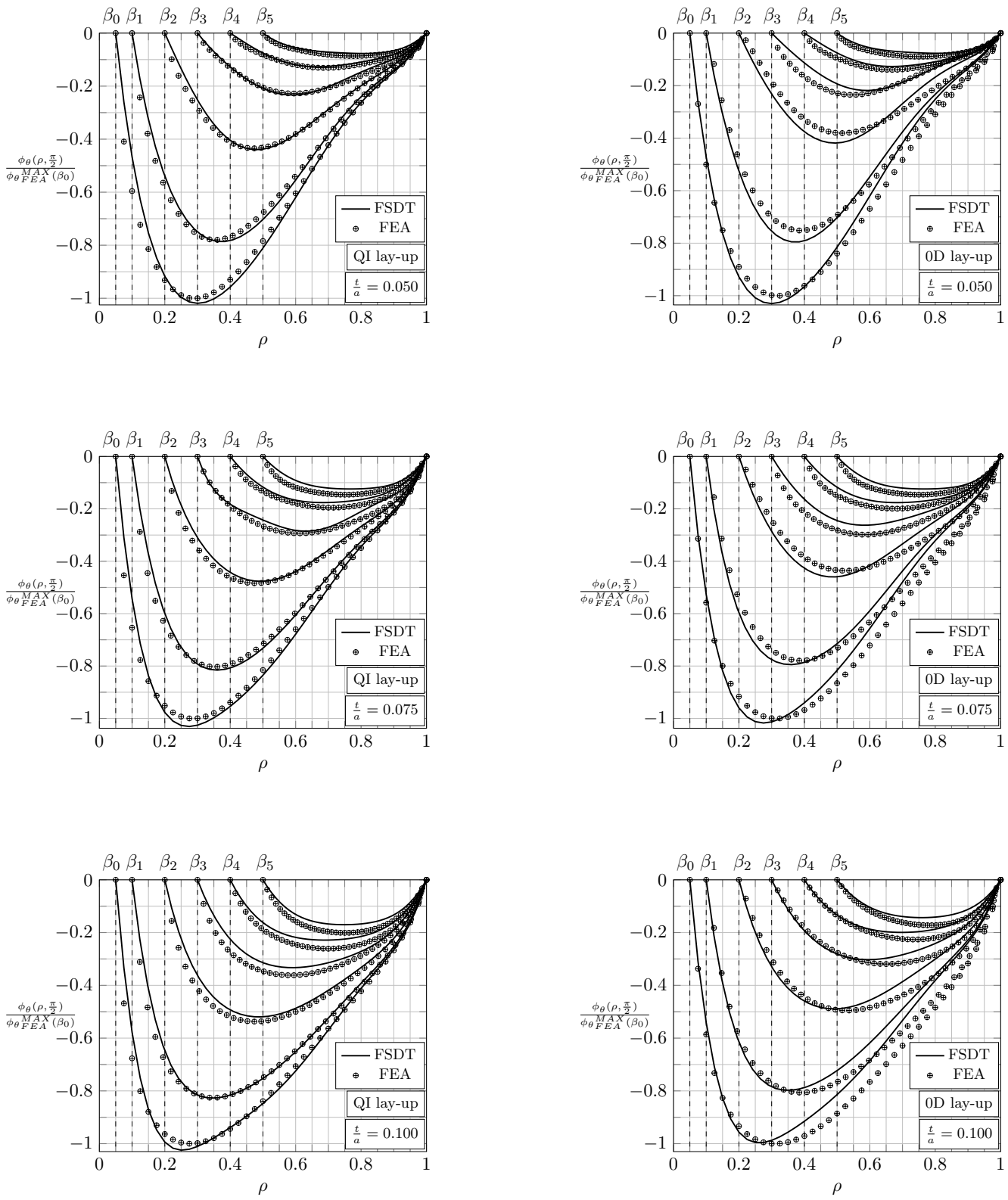

Figure 8.6: Curves of dimensionless rotation about the radial direction as function of ρ, evaluated at $\theta = 0$ rad for different ratios $\frac{t}{a}$ and for $\beta_0 = 0.05$, $\beta_1 = 0.1$, $\beta_2 = 0.2$, $\beta_3 = 0.3$, $\beta_4 = 0.4$ and $\beta_5 = 0.5$ with QI and 0D lay-ups.

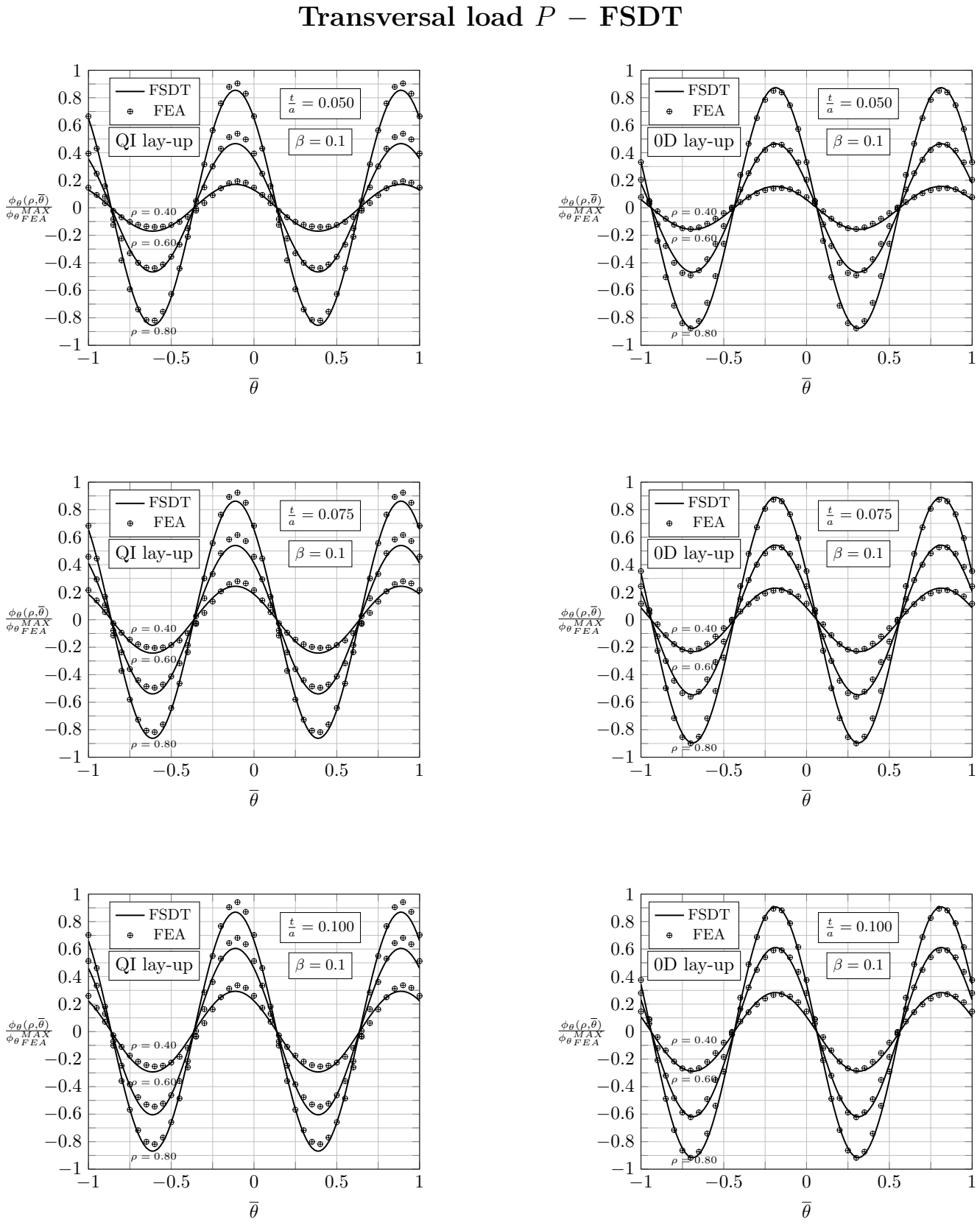

Figure 8.7: Curves of dimensionless rotation about the radial direction as function of $\overline{\theta}$ for different ratios $\frac{t}{a}$ and $\beta = 0.1$, at $\rho =$(β, 0.25, 0.40, 0.60, 0.80) with QI and 0D lay-ups.

composite annular plate.

Moreover, the neglect of the plate shear deformation does not significantly affect the results accuracy as demonstrated by the results obtained making use of the CPT. Table 8.2 outlines the percentage variation Δ_β in correspondence of the radial coordinate where the maximum rotation is measured by the FE analyses. Even in this case the percentage variation is attributable to the numerical approximation and, subsequently, the agreement between the results of the proposed analytical method and those obtained by FE analyses is highly confirmed.

Once again the lay-up has direct influence on the variation of the displacement component with the angular coordinate. Indeed, as reported in Fig. 8.5, the composite annular plates characterized by 0D lay-up show a more evident angular variation of the rotation about the circumferential direction with respect to the plates featuring the QI lay-up. Nevertheless, the influence of the constraints present at the inner and at the outer edges of the annular plate on this displacement component is different from the one experienced by the mid-surface deflection. In this regard, the curves with $\rho =$ 0.15 and 0.40 show a more pronounced dependence on the angular coordinate whereas the effect is more mitigated if the rotation about the circumferential direction is evaluated at $\rho = 0.70$ and 0.90; it can be deduced that the rotation about the circumferential direction is more angularly variable in the plate portion enclosed by the inner radius and the radial coordinate where ϕ_r assumes its maximum value.

According to the rotation about the radial direction, the deviation between the solution of the proposed analytical method and the FE one is more considerable in comparison with those of the other displacement components, even though it is still very acceptable.

In reference to Table 8.3, it can be concluded that the outcomes turn out to be not particularly influenced by the slenderness ratio of the plate, meanwhile the effect of the aspect ratio is more remarkable for both QI and 0D lay-ups. In fact, the percentage variations Δ_β are limited for the aspect ratios β_0 - β_2, whereas they undergo an increase when higher values of the aspect ratio are taken into account.

Overall, as regards the variation along the radius (Fig. 8.6), results for composite annular plates featuring QI lay-up better agree with FE reference solution. In addition, Fig. 8.7, the analytical method appropriately match the circumferential variability of the rotation about the radial direction.

8.4.2 Bending moment M – FSDT

The dimensionless mid-surface deflection is depicted against the dimensionless radius $\rho = \frac{r}{a}$, at the angular coordinate $\theta = \frac{\pi}{2}$ rad, in Fig. 8.8 for the QI and the 0D lay-ups, respectively. The dimensionless deflection is calculated as the ratio between the mid-surface deflection at the angular coordinate $\frac{\pi}{2}$ rad, $w(\rho, \frac{\pi}{2})$, i.e. orthogonally in reference to the direction of the bending moment, and its maximum value, obtained by means of FE analyses, at the same angular coordinate and for the aspect ratio $\beta = 0.1$, i.e. $w_{FEA}^{MAX}(\beta_1)$. These diagrams show the dimensionless deflection variation along the dimensionless radius $\rho = \frac{r}{a}$, at the angular coordinate $\theta = \frac{\pi}{2}$ rad. Similarly, Fig. 8.9 reports for both QI and 0D lay-ups, for all the considered slenderness ratios $\frac{t}{a}$, and for an aspect ratio $\beta = 0.1$, the variation of the dimensionless mid-surface deflection along the dimensionless angle $\overline{\theta} = \frac{\theta}{\pi}$. Again, dimensionless quantities are based on the maximum value of the mid-surface deflection obtained with FE analyses. Moreover, any of these diagrams outline the circumferential variation of the mid-surface deflection at five values of the dimensionless radius: ρ=(β, 0.25, 0.40, 0.60, 0.80).

The curves reported in Figs. 8.8 and 8.9 evidence a substantial agreement in terms of variation with the radial and the circumferential coordinate of the proposed analytical method results and the

ones obtained exploiting FE analyses. In addition, the proposed method is also capable of capturing the sinusoidal variation of the mid-surface deflection imposed by the external load.

Besides, Table 8.4 lists the percentage variations between the outcomes of the proposed methodology and the FE ones concerning the mid-surface deflection, for the two lay-ups considered, estimated at the plate inner edge $\rho = \beta$. Then, the percentage variation becomes lower passing from β_0 to β_2 or β_3, according to the particular value of slenderness ratio, after that it grows again up to β_5; thus, it should be noted that the outcomes accuracy is excellent in all the range of variation of the β parameter. The 0D lay-up feature a general slightly higher percentage variation if compared to the QI lay-up case; nevertheless, in both cases, it is contained within the threshold of the negligible numerical error from the engineering standpoint.

Table 8.4: Displacement components percentage variation $\Delta_{\beta_i}[\%]$, evaluated at $\rho = \beta$ for various values β_i, between analytical method and FEA for both lay-ups.

QI lay-up							
$\frac{t}{a}$		$\Delta_{\beta_0}[\%]$	$\Delta_{\beta_1}[\%]$	$\Delta_{\beta_2}[\%]$	$\Delta_{\beta_3}[\%]$	$\Delta_{\beta_4}[\%]$	$\Delta_{\beta_5}[\%]$
CPT	0.050	27.14	16.34	10.77	9.95	11.61	14.79
FSDT	0.050	2.58	1.22	0.69	0.54	0.65	1.93
	0.075	2.55	1.19	0.83	0.98	1.14	1.40
	0.100	2.94	2.30	1.23	1.14	1.59	1.93

0D lay-up							
$\frac{t}{a}$		$\Delta_{\beta_0}[\%]$	$\Delta_{\beta_1}[\%]$	$\Delta_{\beta_2}[\%]$	$\Delta_{\beta_3}[\%]$	$\Delta_{\beta_4}[\%]$	$\Delta_{\beta_5}[\%]$
CPT	0.050	29.58	17.50	11.41	10.46	11.48	14.28
FSDT	0.050	3.74	1.77	1.75	1.33	1.19	1.26
	0.075	3.22	2.26	1.75	1.71	1.74	1.86
	0.100	2.52	2.26	2.07	2.12	2.27	2.64

Additionally, it can be concluded that the slenderness ratio $\frac{t}{a} = 0.050$ is a possible limit for the utilization of the CPT, founded on the thin-plate assumption, and the FSDT which on the other hand provides an assessment of the plate shear deformability. Indeed, the results referred to the FSDT are much more accurate than those of the analytical methodology exploiting the CPT, outlined in Ref. [67], that underestimates the plate mid-surface deflection; as a matter of fact, the diagrams of annular plates with slenderness ratio $\frac{t}{a} = 0.050$ clearly show that the percentage variation Δ_β is reduced.

Moreover, Figs. 8.10 and 8.12 reports the dimensionless form of the rotations about the circumferential and the radial coordinates, respectively, against the dimensionless radial coordinate ρ that are achieved, for each value of the aspect ratio β, by means of the ratio between the functions $\phi_r(\rho, 0)$ and $\phi_\theta(\rho, 0)$ and their maximum values obtained by means of FE analyses. Further, the analogous diagrams of both the rotations in function of the dimensionless angular coordinate $\overline{\theta}$ are outlined in Figs. 8.11 and 8.13, for annular plates with shape factor $\beta = 0.1$, in this case the dimensionless quantities are based on the maximum value of rotation components obtained with FE analyses. The rotations are reported at particular values of the dimensionless radius: ρ=(β, 0.15, 0.25, 0.40 and

0.70) as regards the rotation about the circumferential direction, whereas ρ=(β, 0.25, 0.40, 0.60 and 0.80) for the rotation about the radial direction.

Once again, both the dependencies of the rotation ϕ_r, Figs. 8.10 and 8.11, obtained through Ritz solution method demonstrate a strong precision in comparison with those of the FE analyses. Table 8.4 clearly shows that the percentage variation Δ_β evaluated at the inner radius can be reduced accounting for the shear deformation of the plate, i.e. analyzing the composite annular plates in the frame of the FSDT instead of the CPT. Analogously, the angular variation of the rotation about the circumferential direction is efficiently reproduced.

With reference to the rotation about the radial direction, the variation with the dimensionless radial coordinate ρ, shown in Fig. 8.12, is reproduced with strong accuracy by the proposed method based on Ritz method. Additionally, the improvement of outcomes for the composite annular plate with aspect ratio $\frac{t}{a} = 0.050$ is evident if compared with those of CPT; these benefits are likewise remarkable even for the dependence on the angular coordinate shown in 8.13.

Bending moment M – FSDT

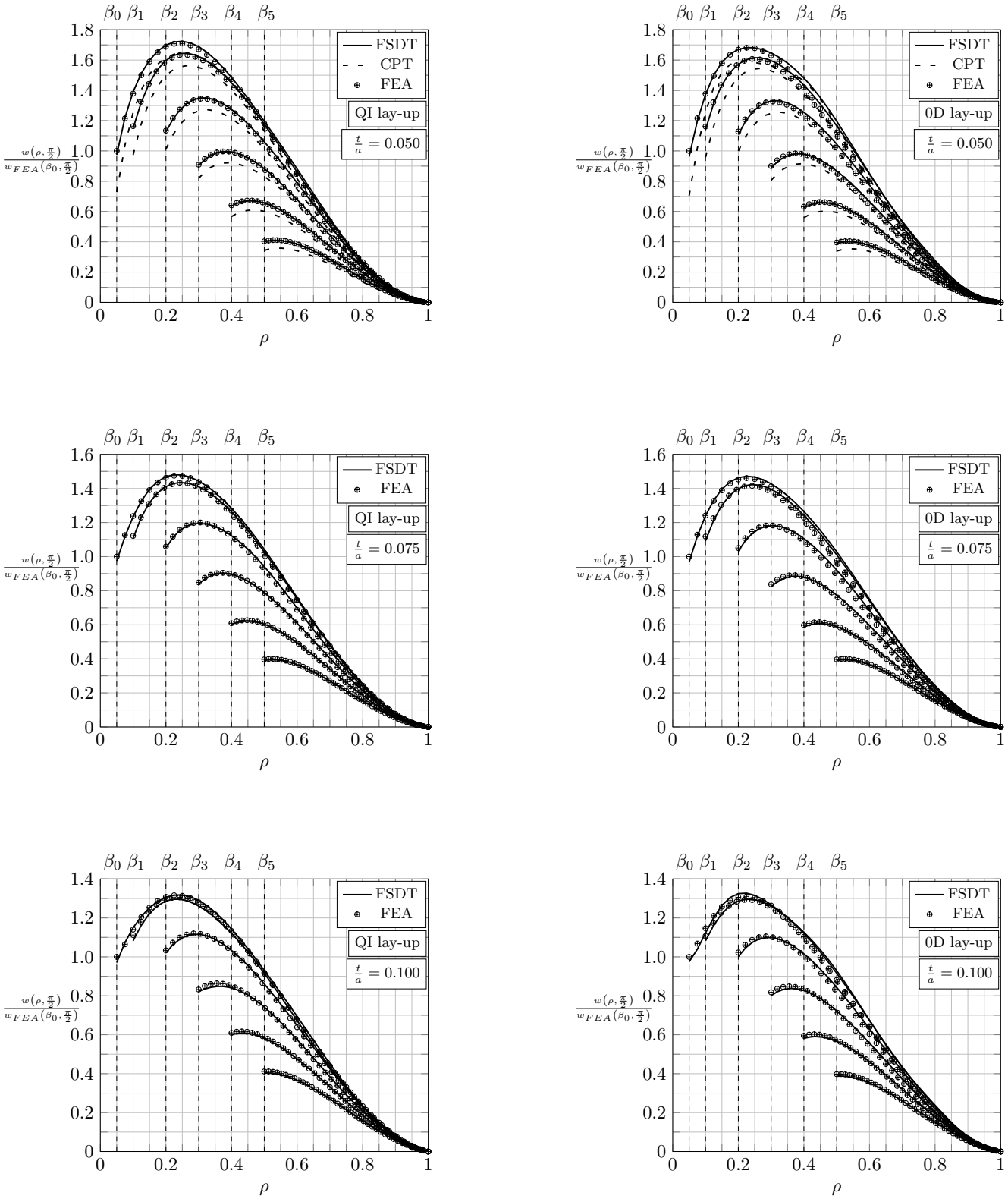

Figure 8.8: Curves of dimensionless mid-surface deflection as function of ρ, evaluated at $\theta = 0$ rad for different ratios $\frac{t}{a}$ and for $\beta_0 = 0.05$, $\beta_1 = 0.1$, $\beta_2 = 0.2$, $\beta_3 = 0.3$, $\beta_4 = 0.4$ and $\beta_5 = 0.5$ with QI and 0D lay-ups.

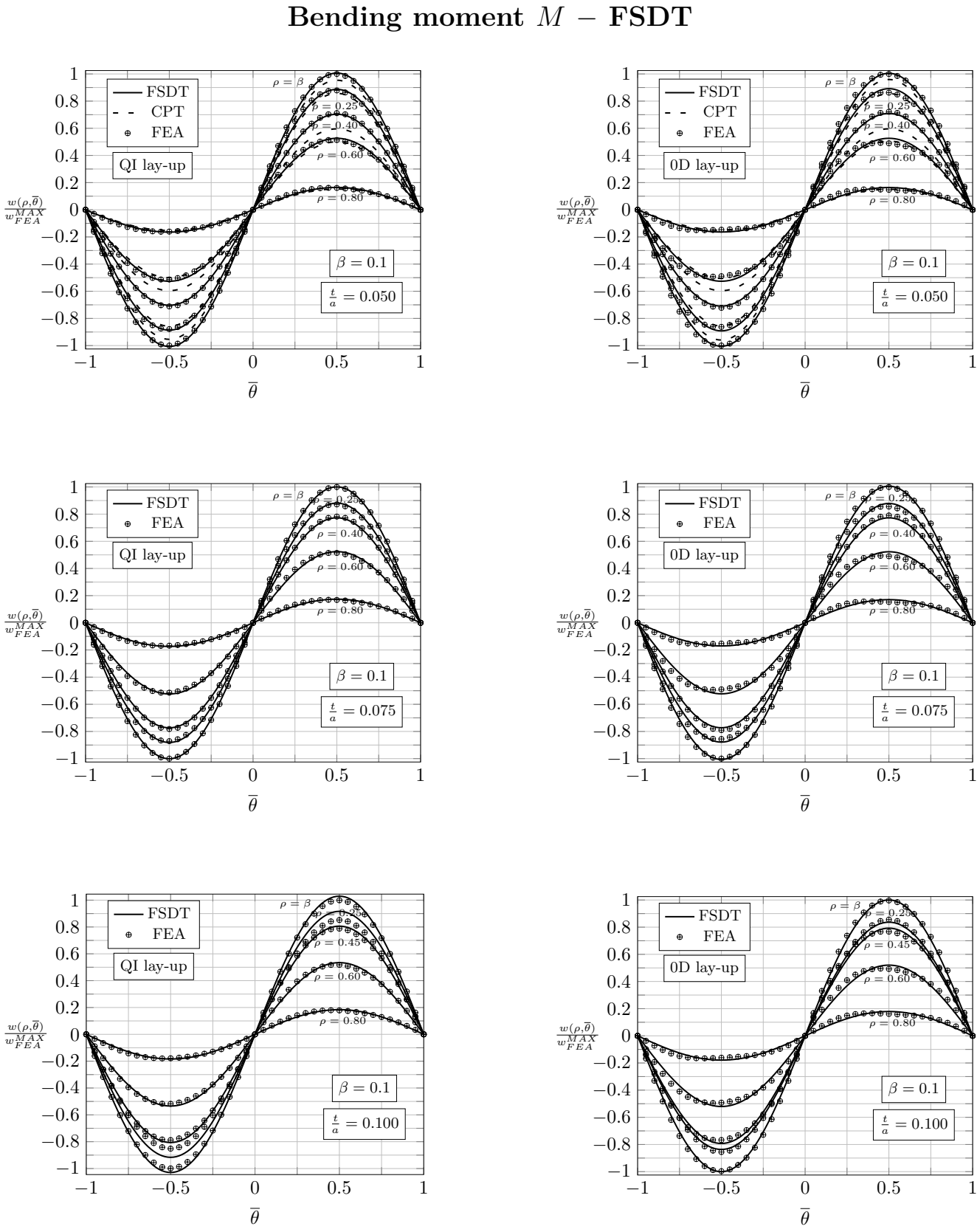

Figure 8.9: Curves of dimensionless mid-surface deflection as function of $\overline{\theta}$ for different ratios $\frac{t}{a}$ and $\beta = 0.1$, at $\rho =(\beta, 0.25, 0.40, 0.60, 0.80)$ with QI and 0D lay-ups.

Bending moment M – FSDT

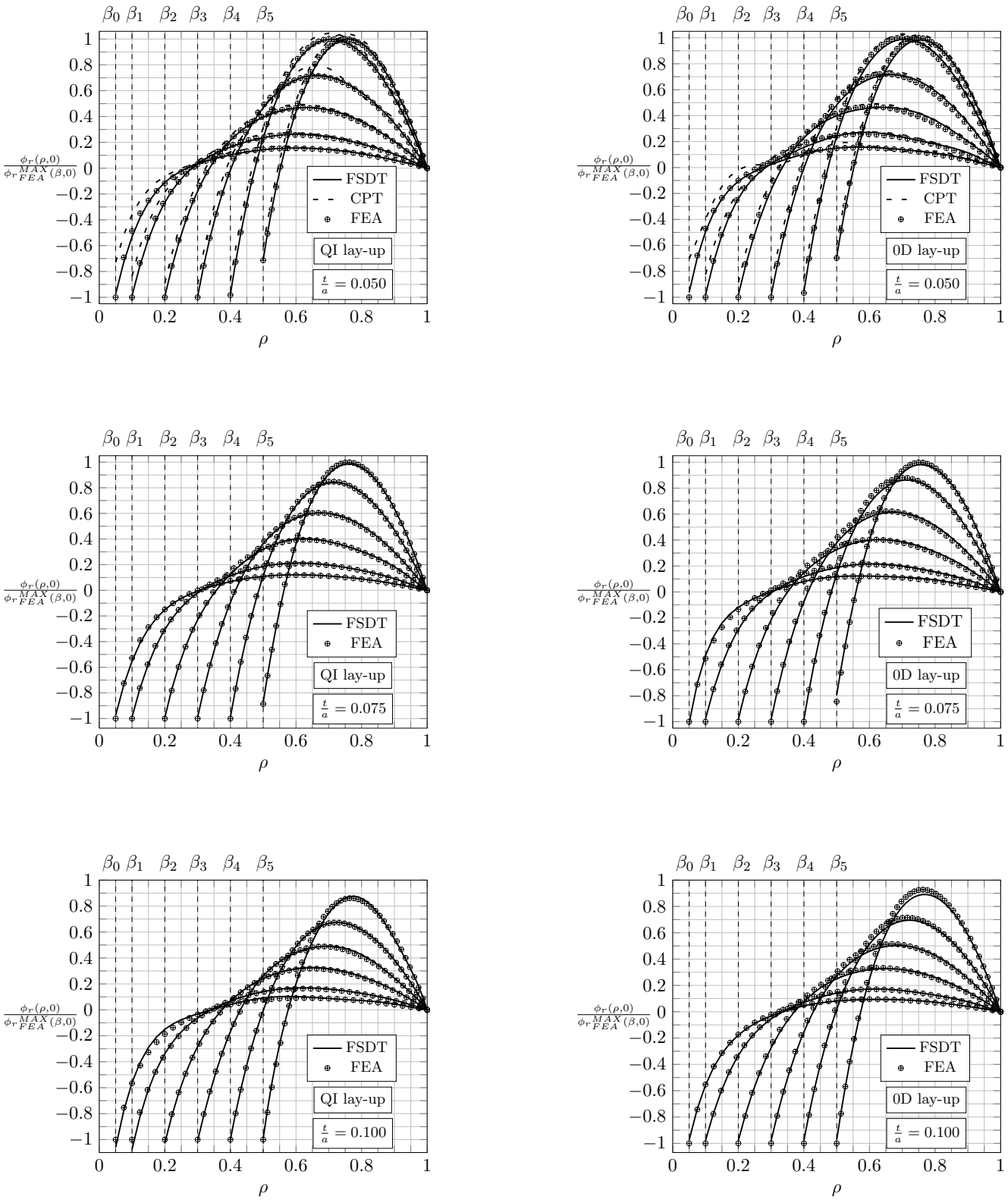

Figure 8.10: Curves of dimensionless rotation about the circumferential direction as function of ρ, evaluated at $\theta = 0$ rad for different ratios $\frac{t}{a}$ and for $\beta_0 = 0.05$, $\beta_1 = 0.1$, $\beta_2 = 0.2$, $\beta_3 = 0.3$, $\beta_4 = 0.4$ and $\beta_5 = 0.5$ with QI and 0D lay-ups.

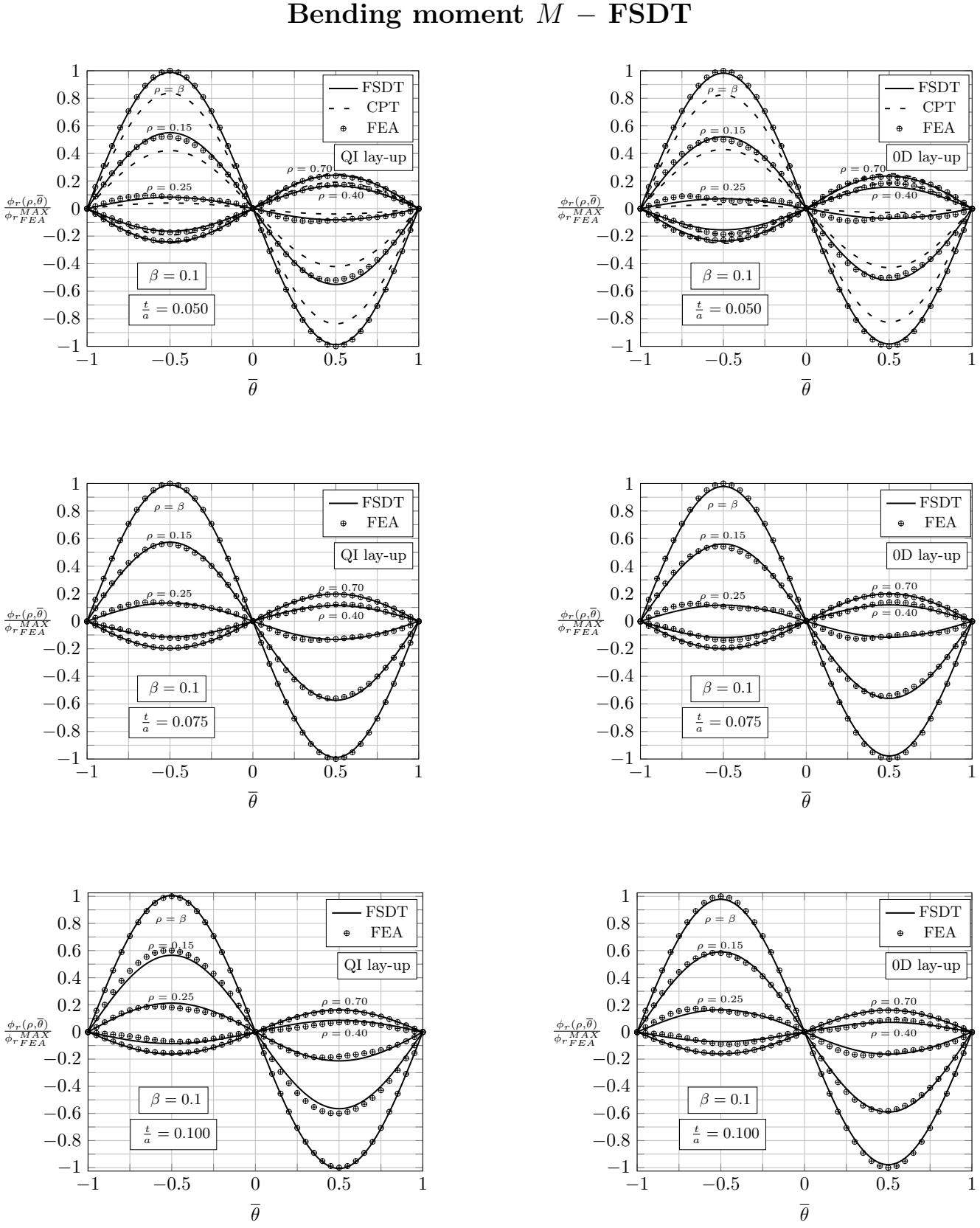

Figure 8.11: Curves of dimensionless rotation about the circumferential direction as function of $\overline{\theta}$ for different ratios $\frac{t}{a}$ and $\beta = 0.1$, at $\rho =(\beta, 0.25, 0.40, 0.60, 0.80)$ with QI and 0D lay-ups.

Bending moment M – FSDT

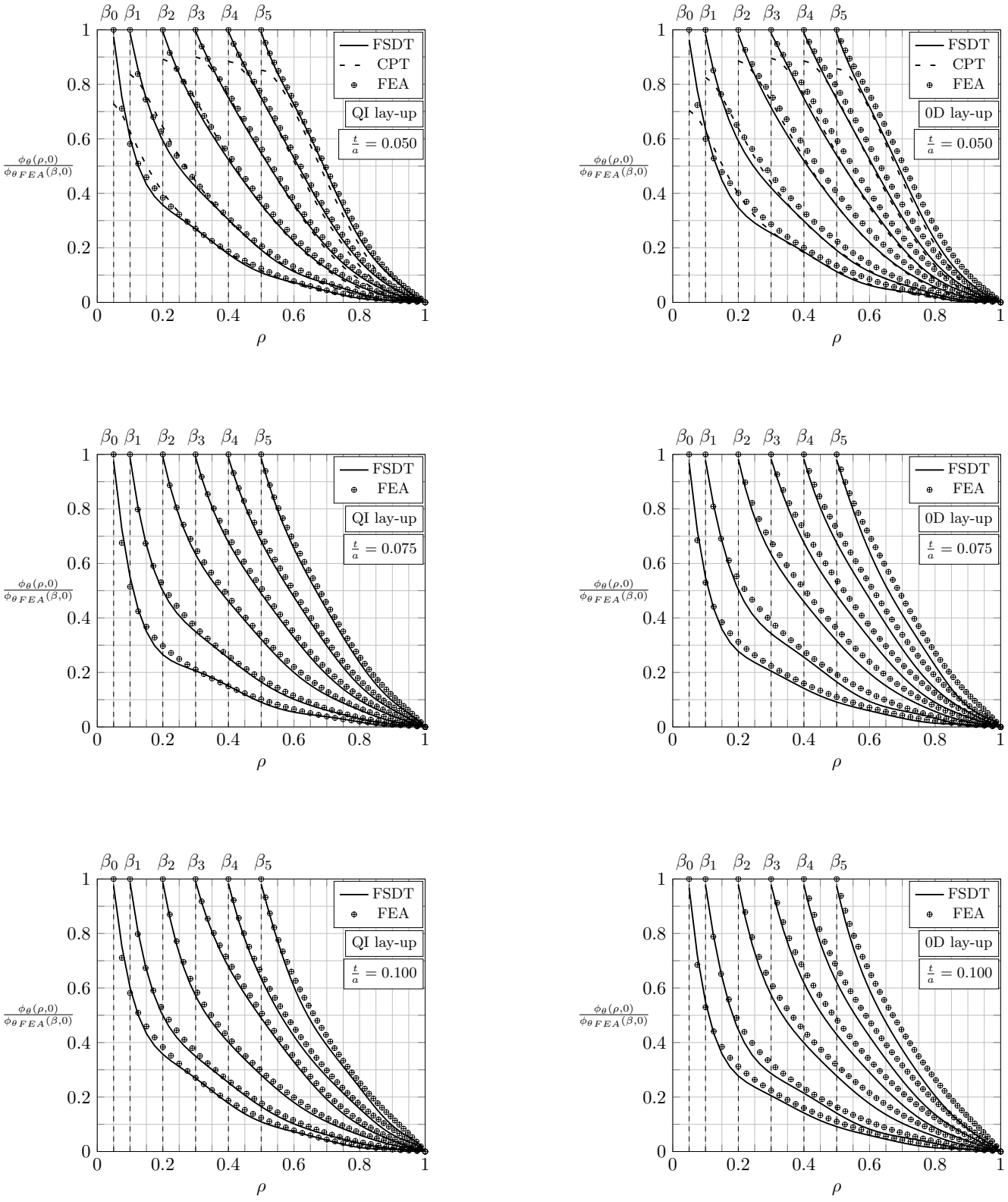

Figure 8.12: Curves of dimensionless rotation about the radial direction as function of ρ, evaluated at $\theta = 0$ rad for different ratios $\frac{t}{a}$ and for $\beta_0 = 0.05$, $\beta_1 = 0.1$, $\beta_2 = 0.2$, $\beta_3 = 0.3$, $\beta_4 = 0.4$ and $\beta_5 = 0.5$ with QI and 0D lay-ups.

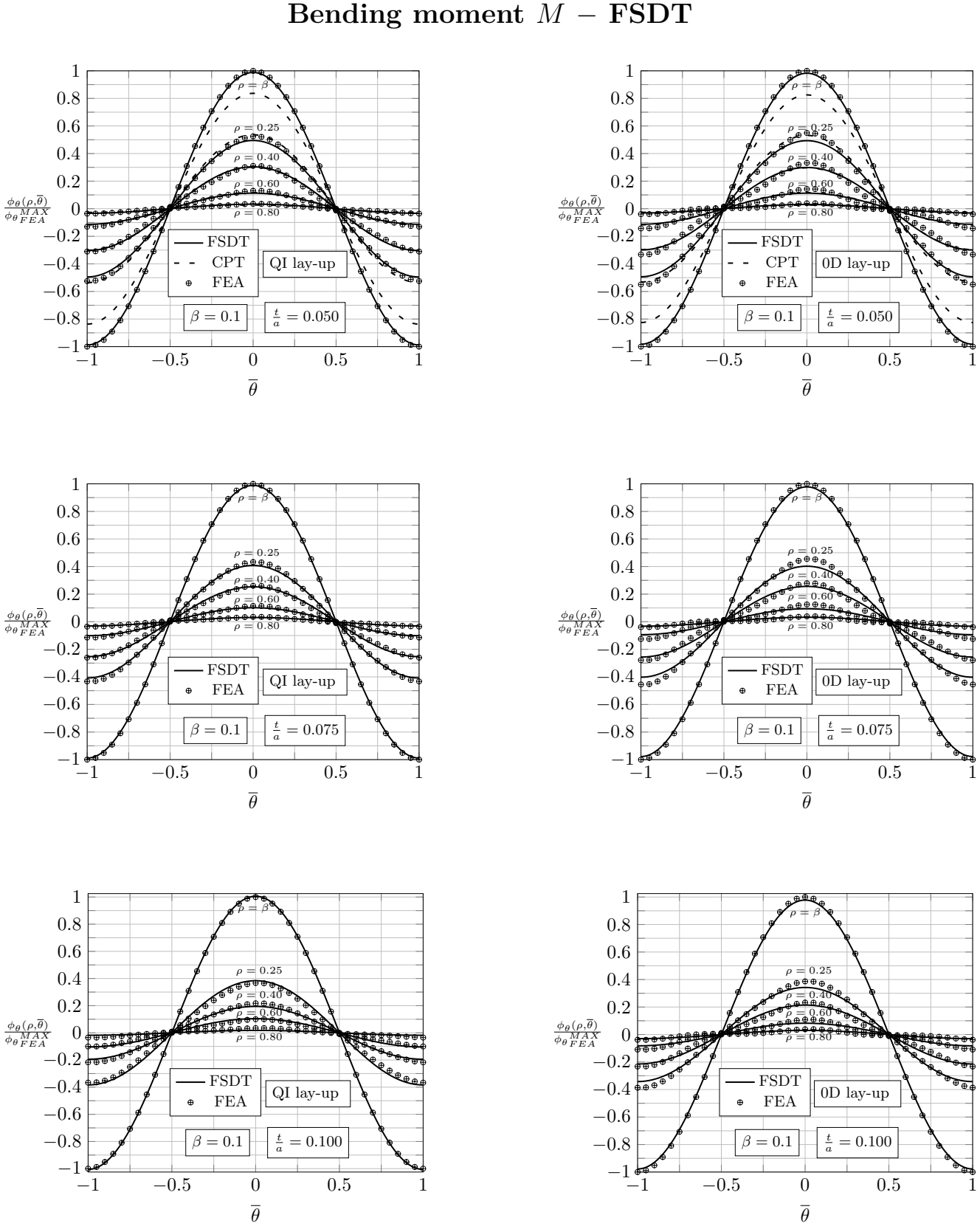

Figure 8.13: Curves of dimensionless rotation about the radial direction as function of $\overline{\theta}$ for different ratios $\frac{t}{a}$ and $\beta = 0.1$, at $\rho =(\beta,\ 0.25,\ 0.40,\ 0.60,\ 0.80)$ with QI and 0D lay-ups.

CHAPTER 9

A NOVEL COMPOSITE BOLTED JOINT ELEMENT: APPLICATION TO IN-PLANE LOAD CONDITION

DEMOUNTABLE joint connections represent a strategic connection method in the overall engineering fields. Moreover, the aeronautic and the aerospace fields are particularly sensible to the proper design of these structural elements and in the evaluation of their influence on the adjacent jointed components stress field, as testified by the published works related to the subject: in [57] a three-dimensional FE model is developed; the work by [59] depicts the definition of a user-defined finite element to describe the load distribution of bolted composite structures; [52, 53] provided specific insights for aircraft structures applications.

Specifically, the necessities of developing efficient design tools for composite bolted joints is particularly relevant in aerospace design. As an example, considering anisogrid composite lattice structures that are progressively replacing metallic shells [35, 51], one of the main issues linked to their utilization is represented by the connection of their composite endings to metallic flanges through demountable joints.

Hereinafter, an original FE modeling technique for composite bolted joints is presented. The methodology is founded on the new definition of a Spot Joint Element, representative of the structural behavior of a region surrounding the spot joint. This joint element is based on the FE architecture of the Spot Joint Element, discussed in [62] and able to simulate spot welded or riveted joint for metal sheets. The enhanced version implements a stiffness matrix whose terms are obtained according to the analytical solution of the composite bolted joint theoretical reference model.

The theoretical model consists in an annular plate, with rectilinear orthotropic material properties, featuring a rigid core at the inner radius and fully clamped conditions at the outer edge undergoing different external loads, it was analyzed in detail in the previous Chapters.

The bolted joint element is realized through a suitable assembly of beam-type elements and it is representative of the structural behavior of a region surrounding the bolted joint, comprising the bolt and a circular portion of the connected plates. Furthermore, even if this FE tool features a reduced number of DOFs with respect to a complex 3D model, it preserves a substantial accuracy in the simulation of the bolted joint connection.

In the present Chapter, the solution of the in-plane load condition of the theoretical reference

model, outlined in Chapter 7 [66] presenting the derivation of both the radial and the circumferential displacement components according to the energy based methodology which exploits Ritz method, is utilized in order to determine the in-plane stiffness properties of the composite bolted joint version of the Spot Joint Element.

Then, the bases of the structural equivalence of the theoretical reference model and the beam assembly that constitutes the Spot Joint Element, which allow to obtain an analogous stiffness between them, are provided as regards the stiffnesses related to the action of external loads acting on the plate mid-surface. In fact, in many technical applications, the more severe load acting on the bolted joint is represented by the shear load undergone by the connection. As an example, it could be taken into account one of the most extensively employed bolted joint configuration: the double lap shear joint, where the mutual interaction of the flanges makes negligible the bending load effects, especially on the central plate, with respect to the action of the in-plane shear load.

Moreover, the analogy concerning the in-plane stiffness terms is established by means of the proper definition of the beams cross-section properties.

The quasi-isotropic lay-up of the composite plates is considered in the work because of its wide employment in applications concerning composite bolted joints, as confirmed in [57, 58, 59, 52, 60].

The Results Section depict a comparison between FE models of rectilinear orthotropic composite plates realized with traditional shell elements, featuring 4 nodes with 6 DOFs per node, that are employed as reference and models presenting the novel composite bolted joint. The effect of the aspect ratio of the novel composite bolted joint is investigated as long as the the bolt diameter one. The outcomes present a high degree of matching indicating an elevated accuracy of the proposed FE tool which can advantageously be utilized as an efficient design solution for the simulation of multi-jointed composite structures.

Furthermore, in §9.2.2 a comparative analysis between a full 3D FE model of a double-lap hybrid bolted joint and a shell FE model implementing the new Spot Joint Element is reported; the great benefits deriving from the employment of this novel FE modeling technique are shown.

9.1 Composite bolted joint finite element − in-plane stiffness matrix terms definition

This Chapter is focused on the definition of the stiffness matrix terms of the novel composite bolted joint element related to the in-plane load condition, i.e. on the identification of the stiffnesses along the radial r and the circumferential θ directions.

The novel composite bolted joint element is made up of a set of radial beams, featuring 6 DOFs per node, which replace a portion of preexisting shell elements mesh present in the overall FE model, as shown in Fig. 9.2. The set of radial beams lies on the composite plate mid-surface and it is equivalent from a structural point of view to the correspondent theoretical model, Fig. 9.3. In addition, a single beam element exhibits the same stiffnesses of a circular sector of the theoretical model having $\alpha_1 + \alpha_2$ angular extension with high degree of fidelity. The composite bolted joint element presents a very limited amount of DOFs, if compared to complex 3D models or even to shell models, and it is capable of improving the results accuracy with respect to approximate simulation techniques.

The stiffness equivalence between the theoretical reference model and the novel composite bolted joint element is obtained through the solution of a system of linear equations that is needed to determine the geometrical properties of the radial beams that must assure the structural equivalence

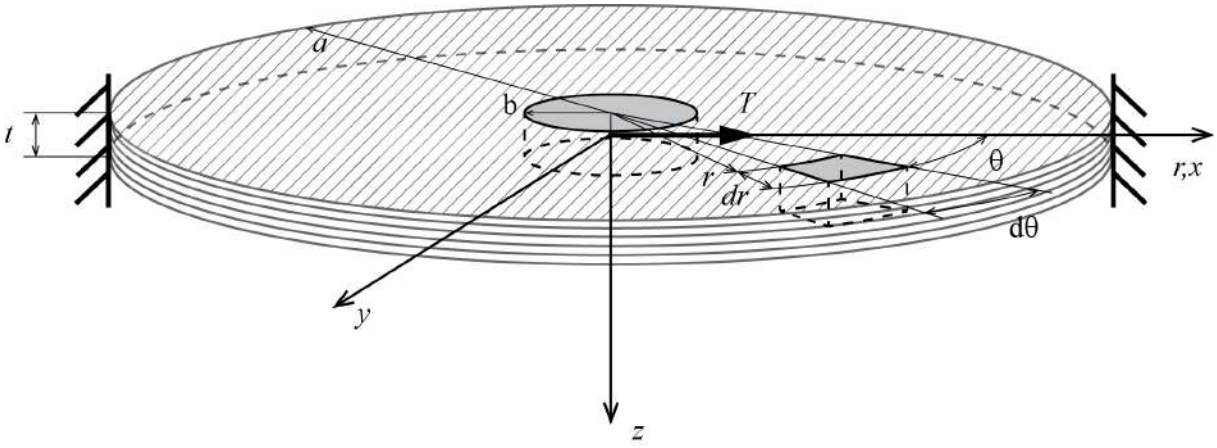

Figure 9.1: Rectilinear orthotropic composite circular plate undergoing in-plane load T.

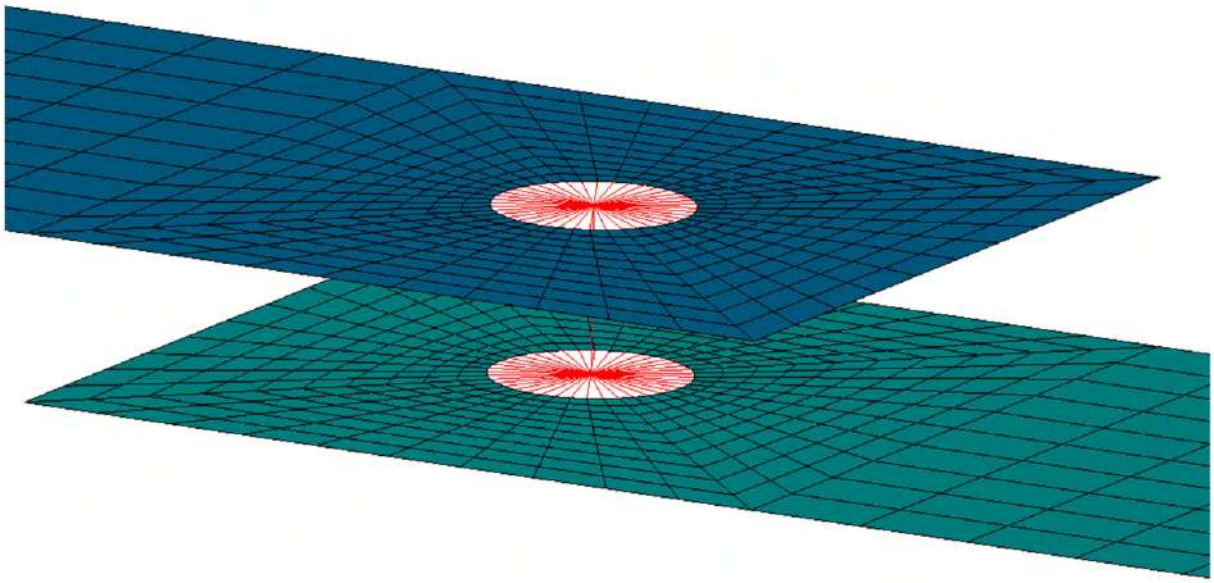

Figure 9.2: Example of Spot Joint Element.

which is established adjusting the beam cross-section properties in terms of inertia moment J_y and area A.

Consequently, the stiffnesses equivalence is obtained through the solution of the following system of algebraic equations that poses the equalities between the theoretical stiffness terms, defined as the ratio of a resulting generic force at the peripheral node and the displacement evaluated at the axis of the rigid nugget, and those related to the beam elements:

$$\begin{cases} K^{th}_{Fn_u} = K^{beam}_{Fn_u}\Big(J_y\Big) \\ \\ K^{th}_{Ft_v} = K^{beam}_{Ft_v}\Big(A\Big) \end{cases} \tag{9.1}$$

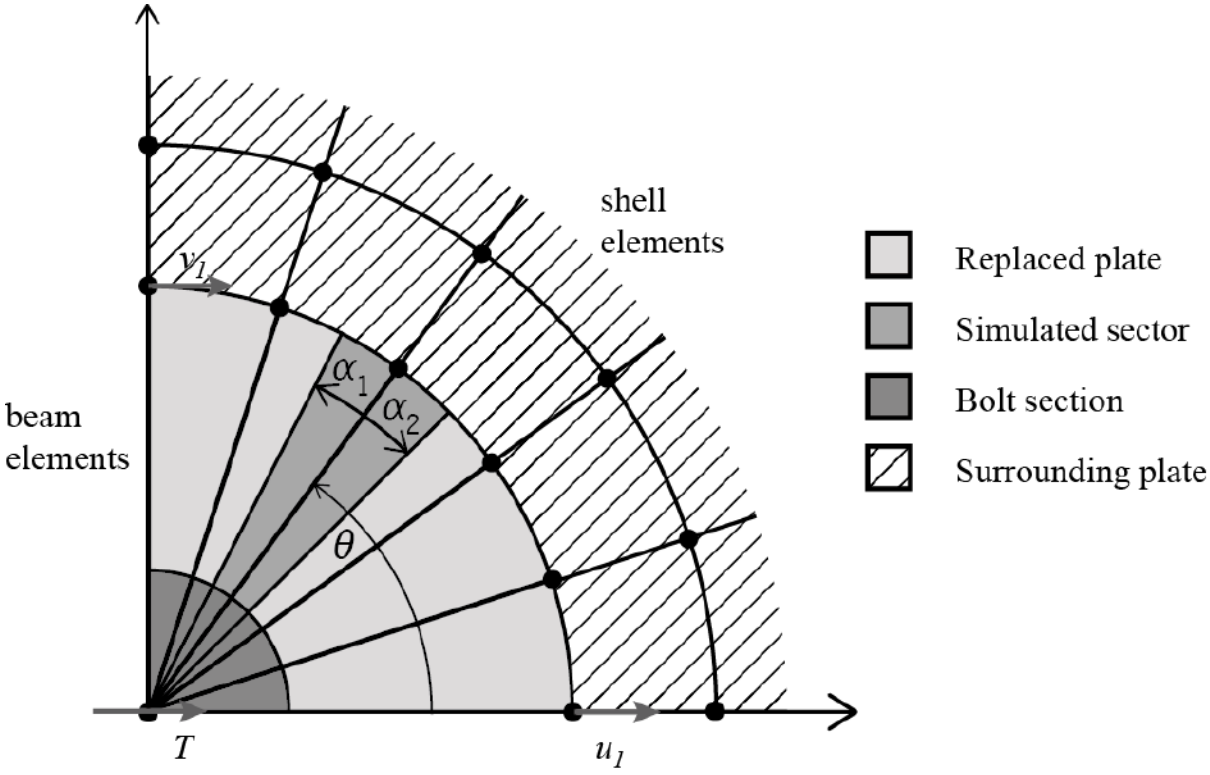

Figure 9.3: Composite bolted joint element.

Besides, $K^{th}_{Fn_u}$ and $K^{th}_{Ft_v}$ are evaluated as:

$$\begin{cases} K^{th}_{Fn_u} = \dfrac{Fn_2}{u_1} = \dfrac{a\int_{\alpha_1}^{\alpha_2} N_r(a,0)}{u(b,0)} \\ \\ K^{th}_{Ft_v} = \dfrac{Ft_2}{v_1} = \dfrac{a\int_{\alpha_1}^{\alpha_2} N_{r\theta}\left(a,\frac{\pi}{2}\right)}{v\left(b,\frac{\pi}{2}\right)} \end{cases} \tag{9.2}$$

being the theoretical stiffness terms defined as:

- $K^{th}_{Fn_u}$ the ratio of the resultant radial in-plane loads Fn_2 on the outer border of the circular sector having extension $\alpha_1 + \alpha_2$ and centered on $\theta = 0$ − which is the maximum radial nodal loads − and the radial displacement at the nugget edge u_1.

- $K^{th}_{Ft_v}$ the ratio between the resulting tangential in-plane loads Ft_2 on the outer border of the circular sector having extension $\alpha_1 + \alpha_2$ and centered on $\theta = \frac{\pi}{2}$ − which is the maximum tangential nodal loads − and the tangential displacement at the rigid nugget edge v_1 for $\theta = \frac{\pi}{2}$ (v_1=u_1).

Moreover, as regards the lay-up considered in the Results Section, i.e. the quasi-isotropic one (details can be found in §9.2), even though the plate is made up of composite material, the in-plane stiffness terms $A_{ij}(\theta)$ do not depend on the angular coordinate. Indeed, Fig. 9.4 outlines the dependence of the in-plane stiffness terms on the dimensionless angular coordinate $\overline{\theta}$, which shows a

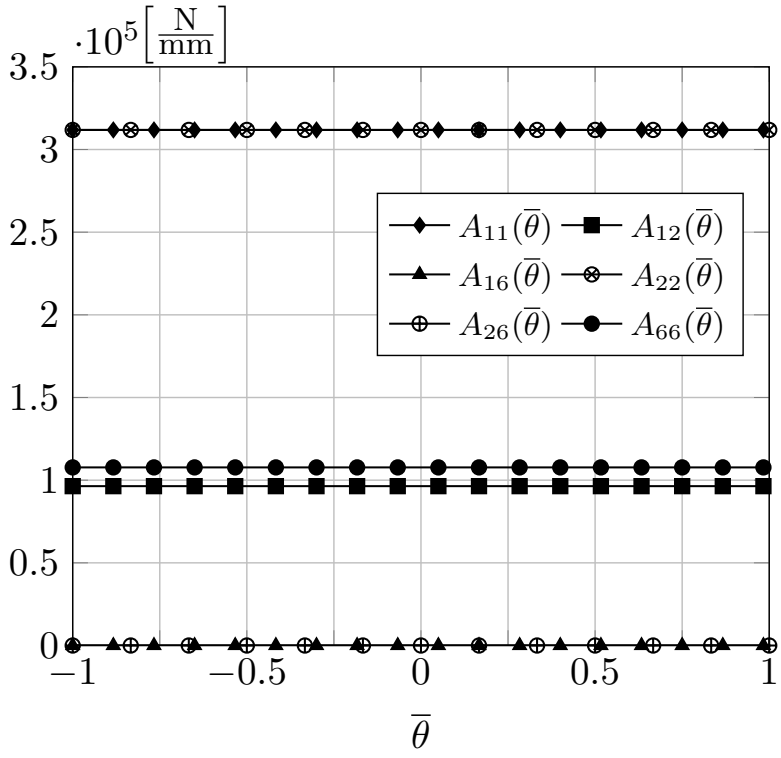

Figure 9.4: Circumferential variation along the dimensionless angular coordinate $\overline{\theta}$ of the $A_{ij}(\theta)$ terms of the extensional stiffnesses matrix.

not appreciable circular variation. This aspect justifies the considerations regarding the employment of the maximum values of Fn_2 and Ft_2 in order to define the stiffness functions $K^{th}_{Fn_u}$ and $K^{th}_{Ft_v}$ which, as a consequence (see Eq. (9.2)), do not depend on the angular coordinate θ.

Likewise, the FE stiffness terms proper of the beam elements can be obtained considering the following relations deriving from the beam theory:

$$\begin{cases} K^{beam}_{Fn_u}\Big(J_y\Big) = \frac{EA}{a} \\ \\ K^{beam}_{Ft_v}\Big(A\Big) = 12\frac{EJ_y}{a^3} \end{cases} \tag{9.3}$$

where E is the Young Modulus of the beam elements material.

9.2 Results

9.2.1 Benchmark tests

The results shown in this Section report the comparison between two variants of FE models of rectilinear orthotropic composite circular plates, featuring an internal rigid core: the first one realized with traditional FE modeling techniques and the second one with the novel composite bolted joint

element. The load condition analyzed consists in an in-plane load T, of unitary intensity, acting on rigid nugget and along the x-axis of the global Cartesian coordinate system.

The plates thickness is $t = 5.2$ mm and they are characterized by quasi-isotropic lay-up: $[45/0/-45/90]_{5s}$; each layer has a thickness $t_{lay} = 0.13$ mm and mechanical properties listed are in Table 6.2.

The refined FE reference model is realized with layered shell elements featuring 4 nodes with 6 DOFs per node, whereas the internal rigid core is obtained by means of a material much more rigid than the composite one. Moreover, the FE reference model features an external radius $r_e = 24$ mm and two values of the bolt radius r_{bolt} were employed: 4 and 5 mm.

The FE models with the novel composite bolted joint are obtained through the replacement of a portion of the FE reference model that is substituted by the radial set of beams that composes the novel composite bolted joint, with cross-section properties obtained through Eq. (9.1).

In order to investigate the influence of the geometrical parameters on the results accuracy, different aspect ratios β between the internal and the external radii, b and a respectively, of the theoretical reference model (Fig. 9.1) were considered, i.e. $\beta_1 = 0.3$, $\beta_2 = 0.4$ and $\beta_3 = 0.5$.

Table 9.1: Radial displacement component evaluated at $\rho = 0$ with FE reference model u_{REF} and with FE model featuring the novel composite bolted joint element for various values β_i, between FE reference method and FE model with the novel composite bolted joint element.

r_{bolt} [mm]	$u_{REF} \cdot 10^5$ [mm]	$u_{\beta_1} \cdot 10^5$ [mm]	$u_{\beta_2} \cdot 10^5$ [mm]	$u_{\beta_3} \cdot 10^5$ [mm]
4	1.553	1.548	1.511	1.487
5	1.340	1.393	1.390	1.388

Table 9.2: Radial displacement component percentage variation $\Delta_{\beta_i}[\%]$ evaluated at $\rho = 0$ for various values β_i, between FE reference method and FE model featuring the novel composite bolted joint element.

r_{bolt} [mm]	$\Delta_{\beta_1}[\%]$	$\Delta_{\beta_2}[\%]$	$\Delta_{\beta_3}[\%]$
4	-0.32	-2.70	-4.25
5	3.96	3.73	3.58

Table 9.3: Node and element numbers of FE reference method and FE model featuring the novel composite bolted joint element with different aspect ratios β.

	REF	β_1	$\Delta_{\beta_1}[\%]$	β_2	$\Delta_{\beta_2}[\%]$	β_3	$\Delta_{\beta_3}[\%]$
Nodes	5041	1922	-61.9	2882	-42.8	3482	-30.9
Elements	5040	1920	-61.9	2880	-42.9	3480	-31.0

Table 9.1 outlines the radial displacements u evaluated alongside the external load T direction by means of the FE reference models and the ones featuring the novel composite bolted joint element, meanwhile the percentage errors between these values are depicted in Table 9.2.

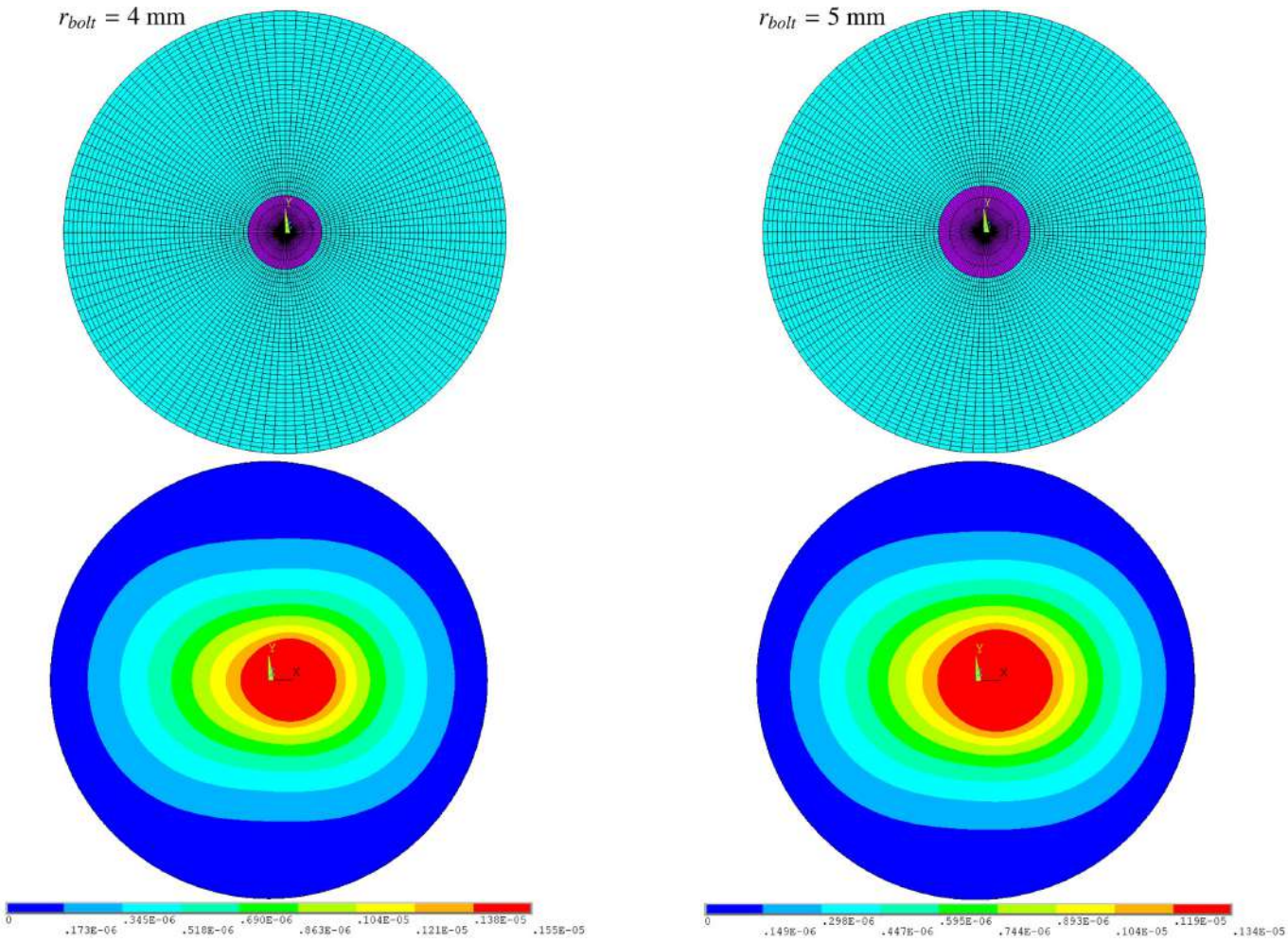

Figure 9.5: FE reference models and contour of the displacement along the x-direction of the rectilinear orthotropic composite circular plates featuring $r_{bolt} = 4$ mm (left) and $r_{bolt} = 5$ mm (right).

Besides, it can be concluded that, regardless of the specific geometrical configurations, the application of the novel composite bolted joint is capable of satisfactorily describing the structural behavior of the joint model as testified by the modest percentage errors.

Furthermore, it should be noted that such a remarkable level of results matching is realized through the adoption of meshes featuring a limited number of nodes and elements, with respect to the FE reference models, for all the aspect ratios considered, as listed in Table 9.3. Additionally, irrespective of the value of r_{bolt}, the two FE reference models and the FE models with the same aspect ratio β were realized by means of the same amount of nodes and finite elements.

Fig. 9.5 reports the FE reference models for the two values of r_{bolt} presenting the internal core made of rigid material properties and the contours relative to the displacement along the x-direction of the Global Cartesian coordinate system provoked by the external load T. Analogous contours are reported in Fig. 9.6 for the three FE models featuring the novel composite bolted joint element with different aspect ratios; the comparison of these result maps demonstrate that the overall stiffness of the models is equivalent to the reference one since the displacement distribution on the circular

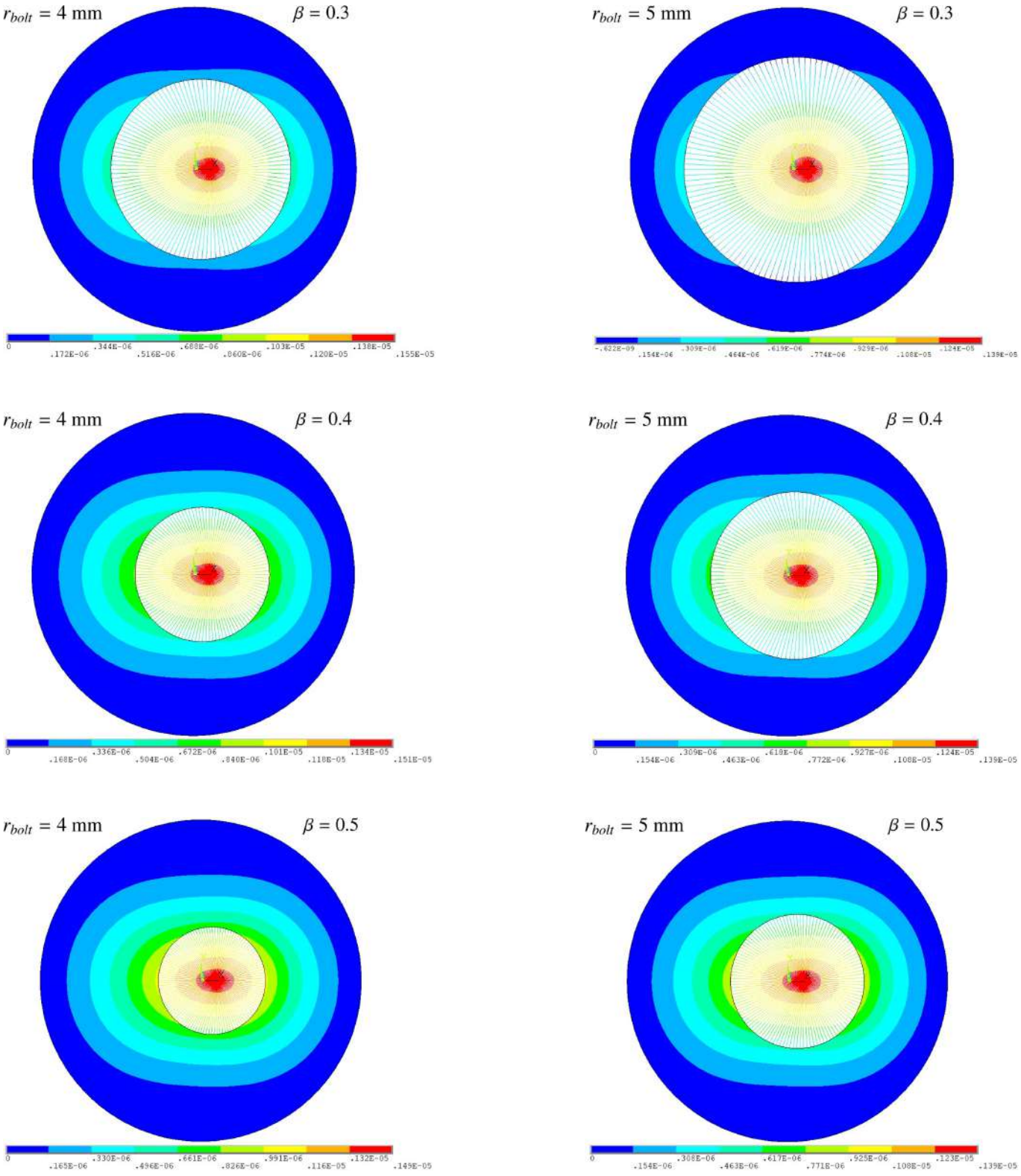

Figure 9.6: FE models with the novel composite bolted joint element and contour of the displacement along the x-direction of the rectilinear orthotropic composite circular plates featuring $r_{bolt} = 4$ mm (left) and $r_{bolt} = 5$ mm (right).

plates models can be superimposed to those in Fig. 9.5.

9.2.2 Double-lap hybrid bolted joint: comparison between conventional and novel FE simulation techniques

This Section concerns a preliminary study, by means of FE simulation, of the bolted joints between the anisogrid interstage and the aluminum flanges necessary to connect the interstage to the rocket engines of the launcher. The bolted connections in question are double-lap joints as the anisogrid end-rings are delimited by the flanges on both sides, i.e. the flanges are overlapped to the end-rings on both the inner and the outer side of the interstage. Moreover, being the anisogrid lattice structure made up of composite material and the flanges of aluminum alloy, these joints can be defined hybrid joints by virtue of the different material of components.

In order to approach the analysis of the bolted joints between the anisogrid lattice structures composite endings and the metallic flanges, a sample of double-lap hybrid bolted joint depicted in Fig. 9.7 is investigated. It is composed of an inner composite plate realized with a quasi-isotropic lay-up, reported in Table 6.1 with a thickness $t = 5.2$ mm, and a two lateral aluminum plates, featuring a thickness $t_{al} = 3$ mm, jointed by a steel bolt; mechanical properties of aluminum and steel are listed in Table 9.4. The bolt features a diameter $d_{bolt} = 8$ mm and it is preloaded with a tensile stress $\sigma_{pre} = 250$ MPa. Additionally, the three rectangular plates feature the same width and height (Fig. 9.7), meanwhile the external plates are thinner than the inner one. Finally, the double-lap hybrid joint is loaded with a traction force $F = 20$ kN on the right edge of the composite plate.

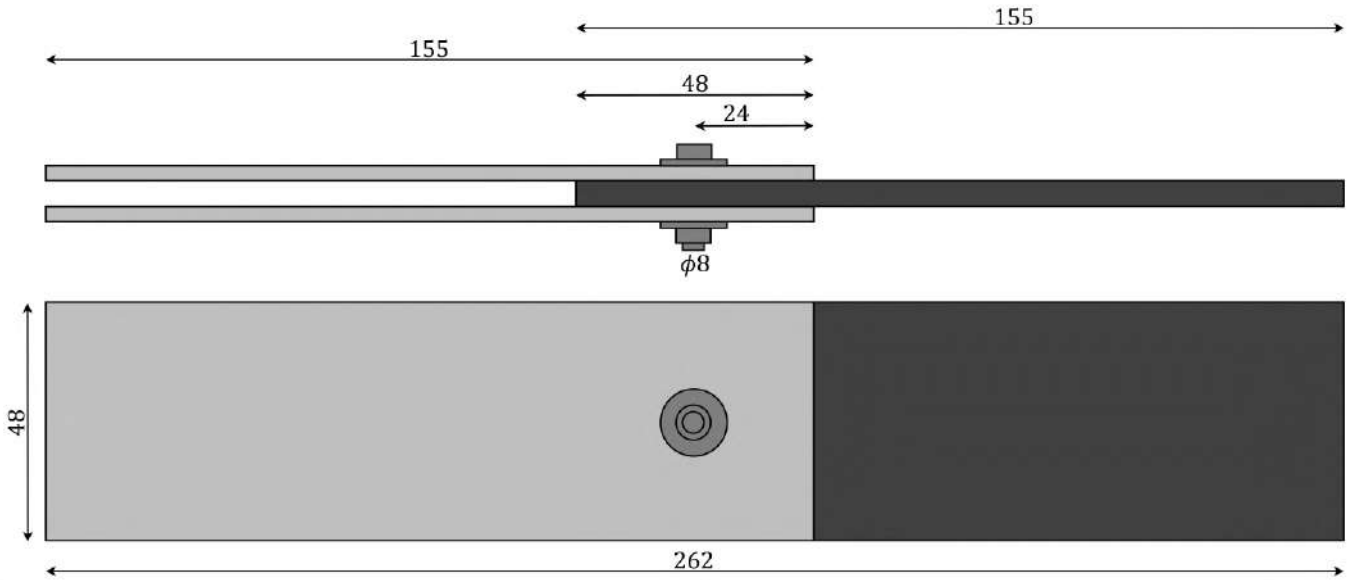

Figure 9.7: Double-lap hybrid joint analyzed by means of different FE techniques.

Keeping in mind a double-lap bolted joint, the predominant displacements undergone by the plates act in their mid-surface since the geometrical symmetry of the joint limits the plates bending that is circumscribed to a portion of the external ones surrounding the bolt. Consequently, the first assessment of the double-lap joint behavior was realized, as discussed in §9.1, establishing the stiffness equivalence for what regards the in-plane stiffness properties between the composite bolted

joint theoretical reference model and the Spot Joint Element. Then, this enhanced FE simulation technique is exploited for the central plate of the double-lap joint, i.e. the composite material one, whereas the classical version is utilized for the modeling of the outer aluminum plates.

Table 9.4: Mechanical properties of aluminum plates and steel bolt.

	Young Modulus [GPa]	Poisson's Ratio [ν]
Aluminum	69	0.33
Steel	210	0.30

As shown in Fig. 9.8, two FE models of the double-lap hybrid bolted joint were realized and compared: the first one is a full detailed 3D model comprehensive of contact elements between components and bolt preload; the latter is a simplified shell model including the novel composite bolted joint element. The two modeling techniques strongly differ from a computational standpoint, in fact the simplified model that makes use of the novel composite bolted joint demands a considerably reduced quantitative of nodes and elements, Table 9.5. As a consequence, the computational savings that its employment involves are strongly remarkable, especially if considered together with the obtainable accuracy. In fact, the principle advantage in the employment of the novel composite bolted joint element is the possibility of combining important and relevant reduction in the simulation time, because of the reduced quantity of DOFs in the overall model, along with a substantial reliability of the outcomes.

Furthermore, Fig. 9.9 reports the displacement measured along the direction of the external load T (x-axis of the Cartesian coordinate system of the FE model), obtained by both the FE analyses. Again, it should be noted that despite the consistent reduction of the FE analysis burden, the contour of the simulation executed with the simplified model is characterized by an excellent degree of matching with the the one of the full 3D model.

Table 9.5: Node and element numbers of 3D FE Model and FE model featuring the novel composite bolted joint element.

	3D FE Model	FE simplified model	Δ[%]
Nodes	51,166	1,819	−96.44
Elements	53,233	1,772	−96.67

The diagram in Fig. 9.10 represent the curves of the joint force F against the displacement u_x along the load direction related to different FE modeling techniques, i.e. the full 3D one and that exploiting the novel composite bolted joint previously described; in addition it is also reported the curve deduced from the FE shell-beam model that, among the simplified modeling techniques, is the most widespread. The curve of the FE model with the novel composite bolted joint element adequately match the full 3D curve, in particular in the initial and final portions of the curve; in the central one the gap is slightly ampler but still really acceptable. Besides, the light difference in the central zone of the curve is own to the friction effect: the distance keeps growing until the plates start mutually moving in consequence of the fact that the static friction force is overcame by the tensile force applied to the joint; then, after the plates sliding starts, the full 3D model becomes less stiff and the difference between the curves progressively decreases.

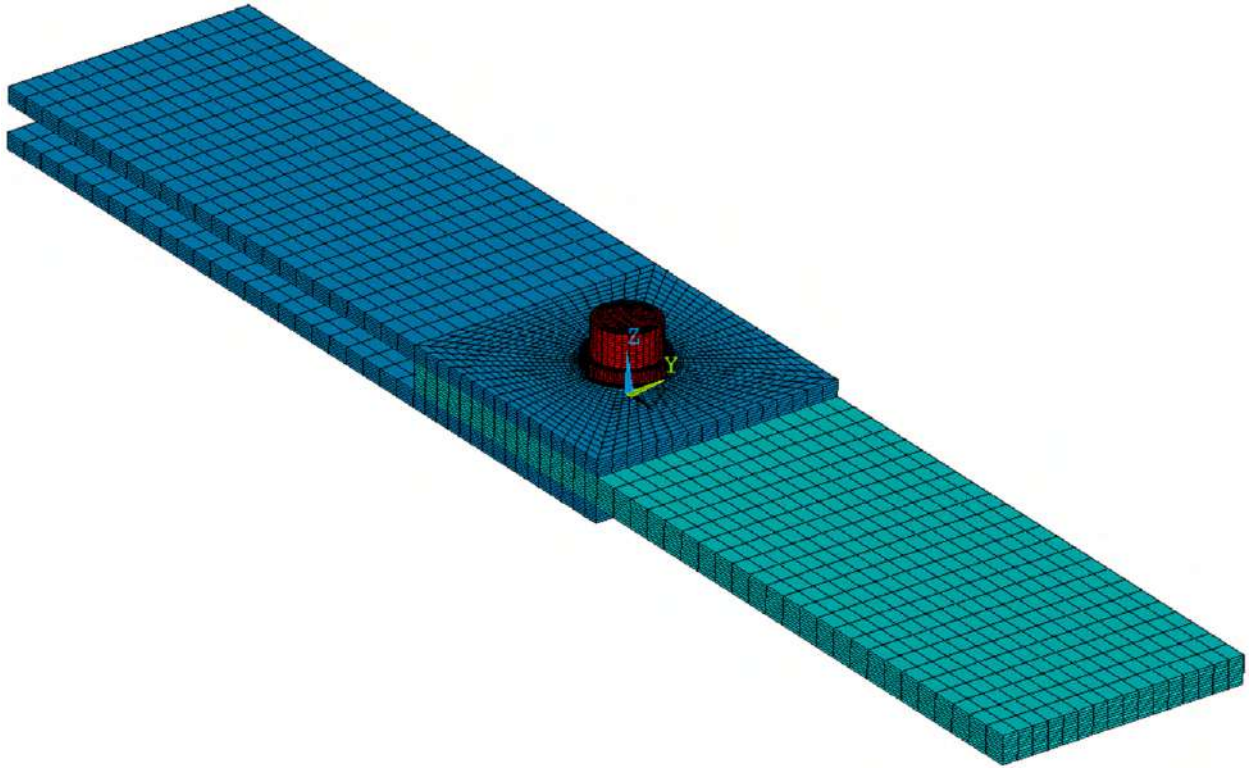

(a)

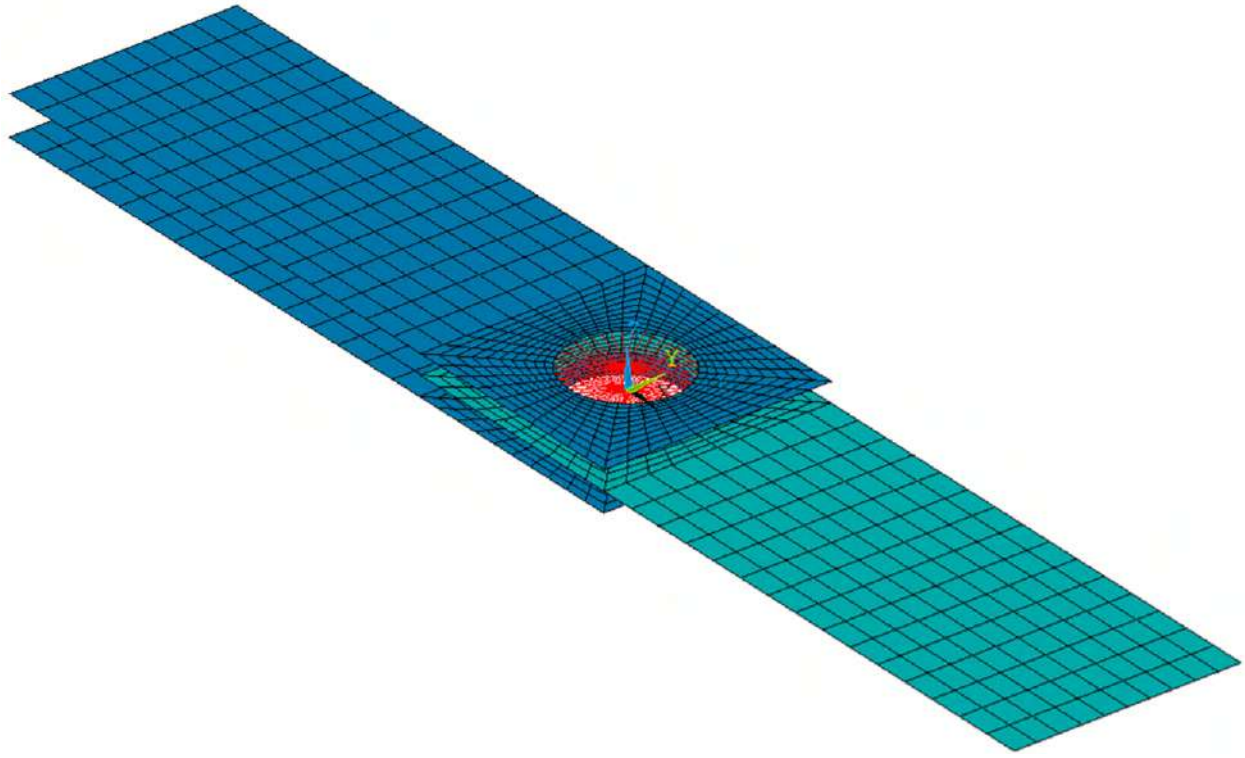

(b)

Figure 9.8: (a) Conventional 3D FE Model; (b) FE Model featuring novel composite bolted joint.

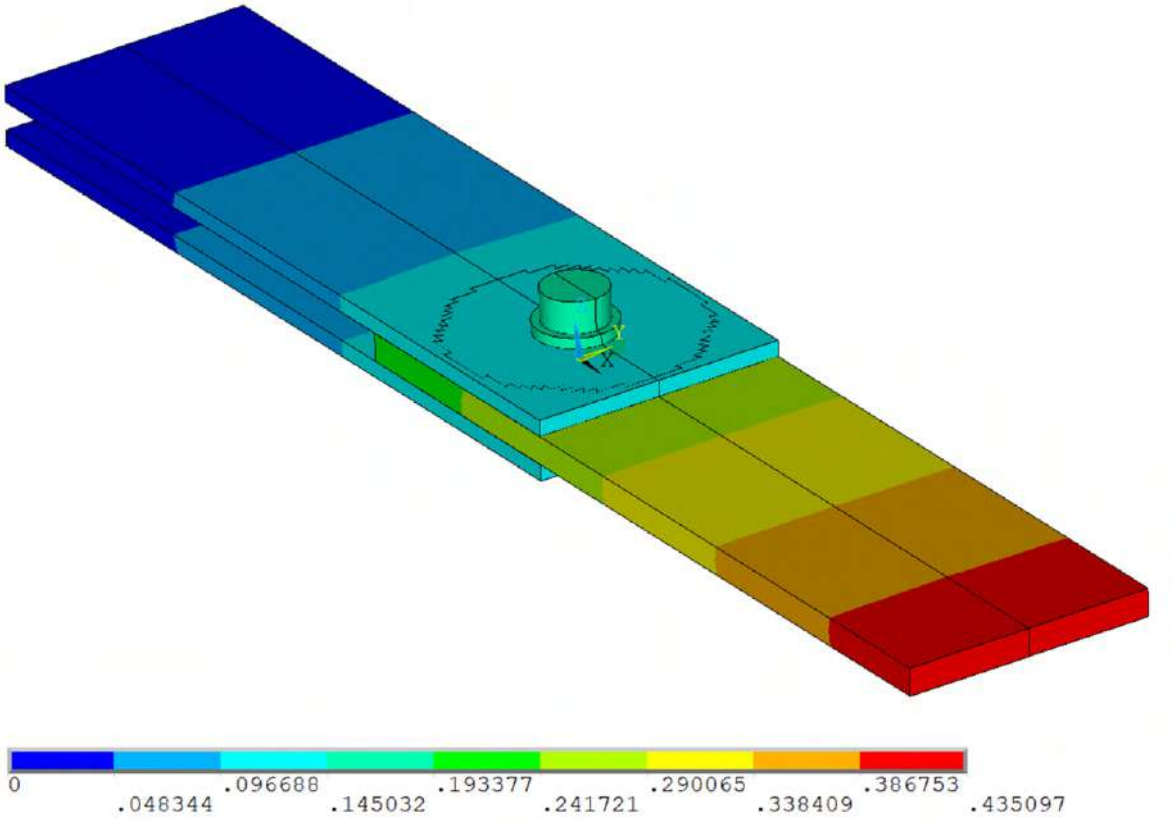

(a)

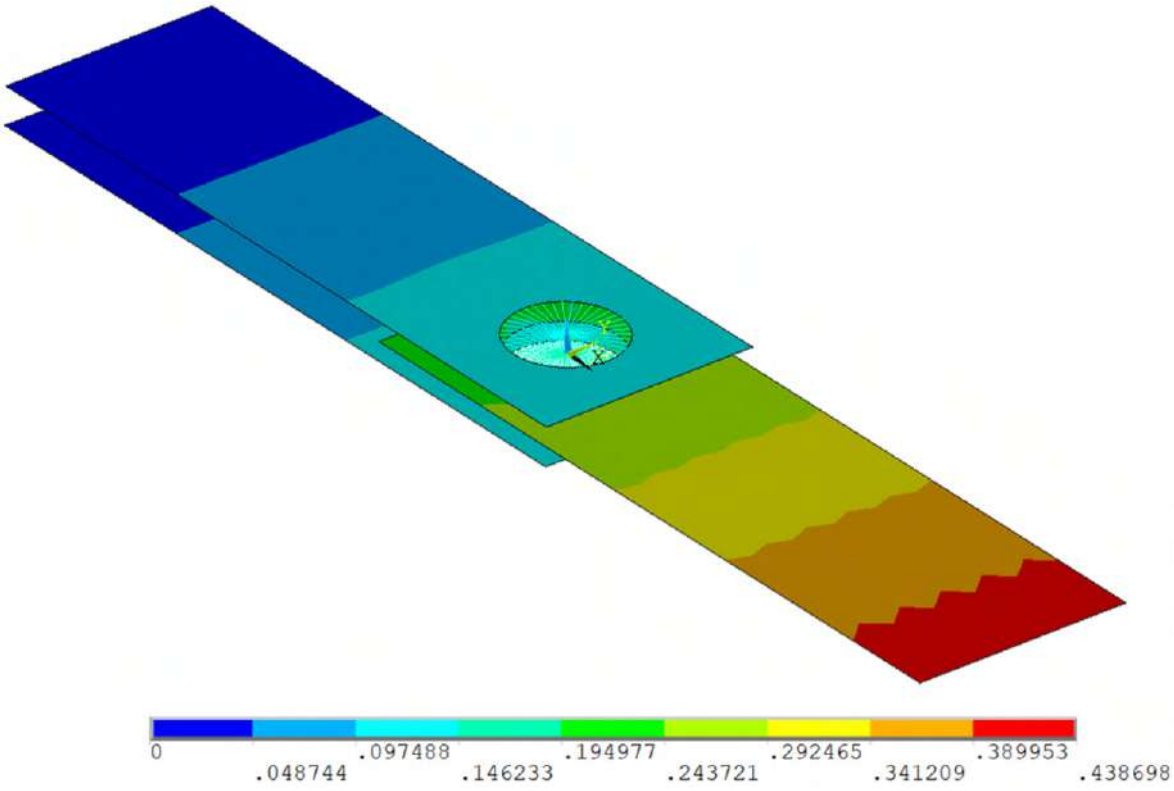

(b)

Figure 9.9: Displacement along the long direction obtained with: (a) 3D FE Model and (b) FE Model featuring novel composite bolted joint.

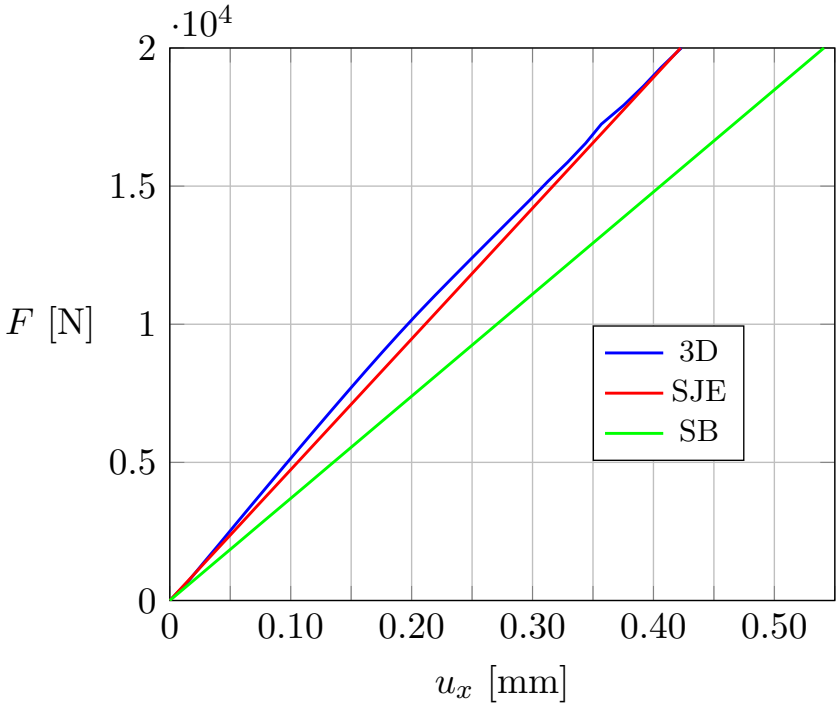

Figure 9.10: Force-displacement curve of the hybrid bolted joint obtained by means of 3D model, FE model with novel composite bolted joint element and shell-beam modeling.

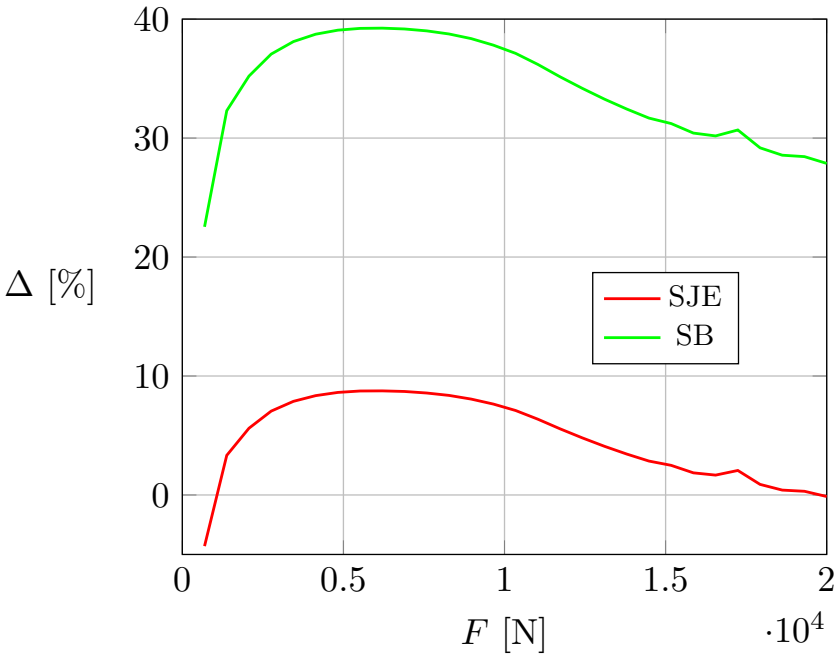

Figure 9.11: Percentage error of force-displacement curve evaluated by means of FE model with novel composite bolted joint element and shell-beam modeling.

On the other hand, the curve of the FE shell-beam model is not adequate to reproduce the structural behavior of the double-lap hybrid bolted joint, indeed the associated force-displacement curve overestimates the displacement of the joint for any given value of external tensile force, and the misfit constantly grows with the tensile force value.

A further comparison between the two simplified modeling approaches can be carried out taking into account the curves in Fig. 9.11 regarding the percentage error Δ versus the external tensile force F, with respect to the full 3D model, introduced by these modeling approaches. It should be noted that the employment of the FE model featuring the novel composite bolted joint element markedly reduces the FE analysis percentage error in reference to the FE shell-beam model that is the most common modeling approach.

Once again, the novel composite bolted joint element demonstrate strong capabilities in terms of accuracy and reliability, being able of providing results in very good matching with those of complete and computationally heavy 3D models, which is a technique that can unlikely be utilized for the modeling of real complex and multi-jointed structures; meanwhile the novel composite bolted joint element is suitable for this kind of simulation problems. Additionally, the proposed FE modeling technique turns out be more effective than other simplified modeling techniques such as the FE shell-beam one.

CHAPTER 10

CONCLUSIONS

In this Thesis an original methodology for the design and the optimization for both anisogrid lattice cylindrical and conical structures is presented. The procedure allows to deduce the minimum mass configuration of the lattice shell undergoing multiple external loads concurrently applied and required to satisfy any kind of stiffness requirements. This optimization technique enhances the buckling prediction capabilities with respect to analytical approaches for the design of anisogrid structures which take into account a restricted number of buckling failure modes and the consequent possibility of not satisfying the structural requirements. Furthermore, the possibilities of optimization are expanded to include loading conditions typical of the real operative conditions.

A versatile parametric FE modeling technique was developed, making use of continuous variables to describe the cross-section dimensions of the unidirectional composite ribs and discrete variables to modify the numbers of helical ribs and of elementary lattice cells alongside the meridian curve of the lattice shell. Five geometrical quantities are utilized as input variables: three of them are continuous variables needed to characterize the cross-section dimensions of the unidirectional composite ribs and two represents the numbers of helical and hoop ribs. The proposed method exploits the capabilities of the genetic algorithm NSGA-II which, according to the results of the finite element analysis, manages the input variables of the parametric model to identify the design solution fulfilling all the constraints with the minimum request of mass, i.e. the optimal one.

The design method enlarges the possibilities of optimization of the anisogrid lattice structures encompassing load cases characteristic of the real operative conditions, more complex than the axial compression.

The practical usefulness and applicability to industrial cases was demonstrated through numerical examples featuring different typologies of external loads and stiffness constraints, demonstrating the accuracy of the presented method and the applicability to industrial cases such as launcher interstages, payload adapters or spacecraft bodies.

Furthermore, as regards the analysis of composite bolted joints with the finality of defining a simplified and accurate FE modeling technique, the theoretical background necessary to the derivation of the stiffness matrix of the enhanced version of the Spot Joint Element was defined. It is founded on the definition of a custom finite element able of simulating the structural behavior of composite bolted joints, on the basis of the Spot Joint Element architecture defined in [62] for metal sheet connections.

The employment of the Spot Joint Element tool to simulate the behavior of a composite bolted

joint connection can lead to relevant simplifications both in the realization of the overall FE model of a multi-connected structure and in substantial savings in the computational efforts of FE analyses. The advantages related to the flexible use of a theoretical model solved analytically are in fact always evident, compared to the rigid use of complex FE models.

Based on this framework, the theoretical reference model of composite bolted joints was considered as a rectilinear orthotropic composite annular plate with a rigid central core and clamped at the outer radius undergoing different external loads.

In this order ideas, the Classical plate theory was employed to derive the stress resultants, in-plane forces and bending and torque moments, in cylindrical coordinates in conjunction with the global equilibrium equation to obtain the governing equation for this class of plates, i.e. a third order partial differential equation in terms of mid-surface deflection. Then, the constitutive equations are further derived according to First-order Shear Deformation Plate Theory.

Afterward, an original solution to the problem of transversally loaded linear elastic rectilinear orthotropic composite annular plate was presented, considering a solution approach based on Galerkin method. This solution is needed to evaluate the corresponding terms of the Spot Element stiffness matrix.

As required by Galerkin method, approximation functions compliant with both essential and natural boundary conditions were derived, considering that all the boundary conditions introduced by the theoretical reference model are essential. The approximated form of the mid-surface deflection was split into a contribution not-dependent on the angular coordinate θ and into a contribution of the circumferential variation of the mid-surface deflection, due to the not-axisymmetry of the material properties.

Results of the original proposed method were compared to those obtained by means of FEA performed with a refined reference model, obtaining a good agreement. A quasi-isotropic and a zero-dominated symmetrical lay-ups were considered in the numerical examples because of their widespread employment in the realization of composite materials components to be connected with bolted joints, considering different slenderness ratios in order to define the limit of validity of the plate theory introduced.

Following, a novel analytical method for linear elastic analysis of rectilinear orthotropic composite circular plates was presented. Solutions were provided making use of Ritz method, the general expression of the principle of virtual works was defined and particularized for the four load conditions acting in the composite bolted joint theoretical reference model. The unknown displacement components were written in discretized form through the formulations of original approximation functions compliant with both essential and natural boundary conditions of the problem.

The generalized form of the systems of linear equations for the load conditions are reported and solved for some case studies. As regards the transversal the in-plane bending moment load conditions, in order to assess the limit of validity of the thin-plates theory employed in theoretical definition of solution method, the influence of the slenderness ratio variation on the results was investigated. Furthermore, the effect of the plate aspect ratio was also analyzed.

The results of the original proposed method were presented in comparison with the FE analyses ones, considering a refined reference model, demonstrating a very good agreement.

Moreover, stemming from the influence of shear deformability on results accuracy for a not-negligible range of slenderness ratios, the linear elastic analysis of rectilinear orthotropic composite annular plate for the transversal and in-plane bending moment load conditions was further conducted considering a solution approach based on Ritz method in the framework of the First-order Shear Deformation Plate Theory.

Even in this case, the general expression of the principle of virtual works was defined and particularized for the load conditions considered. The unknown displacement components were written in discretized form through the formulations of original approximation functions compliant with both essential and natural boundary conditions of the problem. The approximated form of the mid-surface deflection and of the rotations about the circumferential and the radial directions were split into a contribution not-dependent on the angular coordinate θ and into a contribution needed to account for their circumferential variation, due to the not-axisymmetry of the material properties. The generalized form of the system of linear equations for the transversal load condition is reported and solved for some case studies.

Results of the original proposed method were compared to those obtained by means of FEA performed with a refined reference model, obtaining a good agreement.

In the final Chapter of the Thesis the first transfer from analytical solution to FE application is reported: the in-plane behavior of the Spot Joint Element stiffness matrix is tuned according to the related Ritz method solution.

The sensibility of this simulation methodology against geometrical parameters was tested revealing a limited influence of these characteristics on the outcomes fidelity in the range of common applicability of the novel composite bolted joint element.

The presented model is capable of reproducing both the local displacement occurring on the bolt and the global displacement field of the plates in the area surrounding the bolted connection according to the proper definition of its stiffness matrix.

In the end, the proposed novel composite bolted joint element can be profitably exploited in the simulation of elaborate and computationally heavy FE simulations in order to reduce the model magnitude with no introduction of elevated and unacceptable approximations.

Future works about the topics discussed in the present Thesis regard the full implementation of the new version of the Spot Joint Element, including the bending behavior determined by the solution of the transversal and in-plane bending moment load conditions so as to obtain a complete design instrument.

The theoretical background of the new Spot Joint Element could be further improved acting on the shear correction factor introduced with the First-order Shear Deformation Plate Theory solution approach. The utilization of a not constant value for the shear coefficient may produce improvements in the solution accuracy and this aspect could be investigated.

As regards the validation of the presented methodology, a proper experimental campaign can be defined in order to compare the numerically obtained Force-displacement curve with its experimental counterpart for different joint types such as the single-lap and the double-lap in both the composite and the hybrid configurations.

From the modeling standpoint, the Spot Joint Element could be improved defining a procedure capable of reproducing the effect of static friction forces between plate interfaces and their release when the slipping force value is reached. After that the plates start slipping reciprocally, if the bolt holes present a radial gap, this aspect produces a plateau in the Force-displacement curve which should be taken into account in the joint modeling.

APPENDIX A

As described in §7.1.2, the numerical examples were realized making use of 7 terms for both the radial and circumferential approximated displacement components, U_N and V_M respectively.

The functions of the radial coordinate $p(r)$ which are part of the approximation functions $\varphi_{0,j}$ and $\psi_{0,l}$ revealed to possess no general and repetitive expression; thus, the polynomial functions from $p_0(r)$ to $p_6(r)$, ranging from a first degree polynomial function in the variable r until a seventh degree one, employed for the realization of the case studies are hereinafter reported:

$$p_0(r) = r - a$$

$$p_1(r) = \Big(r - a\Big)\Big(r - b\Big)$$

$$p_2(r) = \Big(r - a\Big)\Big(r - b\Big)\Big(a + b + 1 + r\Big)$$

$$p_3(r) = \Big(r - a\Big)\Big(r - b\Big)\Big(r^2 + (a + b + 1)r + a^2 + ab + b^2 + a + b + 1\Big)$$

$$p_4(r) = \Big(r - a\Big)\Big(r - b\Big)\Big(r^3 + (a + b + 1)r^2 + (a^2 + ab + b^2 + a + b + 1)r + a^3 + a^2b + ab^2 + b^3 + a^2 + \\ + ab + b^2 + a + b + 1\Big)$$

$$p_5(r) = \Big(r-a\Big)\Big(r-b\Big)\Big(r^4+(a+b+1)r^3+(a^2+ab+b^2+a+b+1)r^2+(a^3+a^2b+ab^2+b^3+a^2+ \\ +ab+b^2+a+b+1)r+a^4+a^3b+a^2b^2+ab^3+b^4+a^3+a^2b+ab^2+b^3+a^2+ab+b^2+a+b+1\Big)$$

$$p_6(r) = \Big(r-a\Big)\Big(r-b\Big)\Big(r^5+(a+b+1)r^4+(a^2+ab+b^2+a+b+1)r^3+(a^3+a^2b+ab^2+b^3+a^2b+ \\ +ab^2+b^3+a^2+ab+a^2+ab+b^2+a+b+1)r^2+(a^4+a^3b+a^2b^2+ab^3+b^4+a^3+b^2+a+ \\ +b+1)r+a^5+b^5+a^4b+a^3b^2+a^2b^3+ab^4+a^4+b^4+ab^3+a^3b+a^2b^2+a^2b+ab^2+a^2+b^2+ \\ +a^3+b^3+a+b+ab+1\Big)$$

APPENDIX B

The results outlined in §7.2 are obtained with 10 terms of the series $W_N(r,\theta)$ representing the discretized form of the mid-surface transversal displacement. The functions $f(r)$ cannot be depicted in a general form, so the functions from $f_1(r)$ to $f_{10}(r)$ employed in the numerical examples are shown below:

$$f_1(r) = \frac{(r-a)^2}{a+b}\Big((a+b)r - 2b^2\Big)$$

$$f_2(r) = \frac{(r-a)^2}{a+b}\Big((a+b)r^2 + (2a^2+2ab+a+b)r - 3ab^2 - 3b^3 - 2b^2\Big)$$

$$f_3(r) = \frac{(r-a)^2}{a+b}\Big(r^3(a+b) + (2a^2+2ab+a+b)r^2 + (3a^3+3a^2b+2a^2+2ab+a+b)r - 4a^2b^2 + \\ - 4ab^3 - 4b^4 - 3ab^2 - 3b^3 - 2b^2\Big)$$

$$f_4(r) = \frac{(r-a)^2}{a+b}\Big(r^4(a+b) + (2a^2+2ab+a+b)r^3 + 3a^3 + 3a^2b + 2a^2 + 2ab + a + b)r + (3a^3 + \\ + 3a^2b + 2a^2 + 2ab + a + b)r^2 + (4a^4 + 3a^3 + 3a^2b + 2a^2 + 2ab + a + b)r - 5a^3b^2 - 5a^2b^3 + \\ - 5ab^4 - 5b^5 - 4a^2b^2 - 4ab^3 - 4b^4 - 3ab^2 - 3b^3 - 2b^2\Big)$$

$$f_5(r) = \frac{(r-a)^2}{a+b}\Big(r^5(a+b) + (2a^2+2ab+a+b)r^4 + (3a^3+3a^2b+2a^2+2ab+a+b)r^3 + (4a^4 + \\ + 4a^3b + 3a^3 + 3a^2b + 2a^2 + 2ab + a + b)r^2 + (5a^5 + 5a^4b + 4a^4 + 4a^3b + 3a^3 + 3a^2b + 2a^2 + \\ + 2ab + a + b)r - 6a^4b^2 - 6a^3b^3 - 6a^2b^4 - 6ab^5 + -6b^6 - 5a^3b^2 - 5a^2b^3 - 5ab^4 - 5b^5 - 4a^2b^2 + \\ - 4ab^3 - 4b^4 - 3ab^2 - 3b^3 - 2b^2\Big)$$

$$f_6(r) = \frac{(r-a)^2}{a+b}\Big((a+b)r^6 + (2a^2+2ab+a+b)r^5 + (3a^3+3a^2b+2a^2+2ab+a+b)r^4 + (4a^4 +$$

$$+ 4a^3b + 3a^3 + 3a^2b + 2a^2 + 2ab + a + b)r^3 + (5a^5 + 5a^4b + 4a^4 + 4a^3b + 3a^3 + 3a^2b + 2a^2 +$$
$$+ 2ab + a + b)r^2 + (6a^6 + 6a^5b + 5a^5 + 5a^4b + 4a^4 + 4a^3b + 3a^3 + 3a^2b + 2a^2 + 2ab + a + b)r +$$
$$- 7a^5b^2 - 7a^4b^3 - 7a^3b^4 - 2b^2 - 3ab^2 - 4b^4 - 3b^3 - 5b^5 - 6a^4b^2 - 6a^3b^3 - 6a^2b^4 - 6ab^5 - 4a^2b^2 +$$
$$- 4ab^3 - 7b^7 - 6b^6 - 5a^3b^2 - 5a^2b^3 - 5ab^4\Big)$$

$$f_7(r) = \frac{(r-a)^2}{a+b}\Big((a+b)r^7 + (2a^2 + 2ab + a + b)r^6 + (3a^3 + 3a^2b + 2a^2 + 2ab + a + b)r^5 + (4a^4 + 4a^3b +$$
$$+ 3a^3 + 3a^2b + 2a^2 + 2ab + a + b)r^4 + (5a^5 + 5a^4b + 4a^4 + 4a^3b + 3a^3 + 3a^2b + 2a^2 + 2ab + a +$$
$$+ b)r^3 + (6a^6 + 6a^5b + 5a^5 + 5a^4b + 4a^4 + 4a^3b + 3a^3 + 3a^2b + 2a^2 + 2ab + a + b)r^2 + (7a^7 + 7a^6b +$$
$$+ 6a^6 + 6a^5b + 5a^5 + 5a^4 + b4a^4 + 4a^3b + 3a^3 + 3a^2b + 2a^2 + 2ab + a + b)r - 7b^7 - 6b^6 - 8a^6b^2 +$$
$$- 8a^5b^3 - 8a^4b^4 - 8a^3b^5 - 8a^2b^6 - 8ab^7 - 5a^3b^2 - 5a^2b^3 - 5ab^4 - 8b^8 - 7a^5b^2 - 7a^4b^3 - 7a^3b^4 +$$
$$- 7a^2b^5 - 7ab^6 - 2b^2 - 3ab^2 - 4b^4 - 3b^3 - 5b^5 - 6a^4b^2 - 6a^3b^3 - 6a^2b^4 - 6ab^5 - 4a^2b^2 - 4ab^3\Big)$$

$$f_8(r) = \frac{(r-a)^2}{a+b}\Big((a+b)r^8 + (2a^2 + 2ab + a + b)r^7 + (3a^3 + 3a^2b + 2a^2 + 2ab + a + b)r^6 + (4a^4 +$$
$$+ 4a^3b + 3a^3 + 3a^2b + 2a^2 + 2ab + a + b)r^5 + (5a^5 + 5a^4b + 4a^4 + 4a^3b + 3a^3 + 3a^2b + 2a^2 +$$
$$+ 2ab + a + b)r^4 + (6a^6 + 6a^5b + 5a^5 + 5a^4b + 4a^4 + 4a^3b + 3a^3 + 3a^2b + 2a^2 + 2ab + a + b)r^3 +$$
$$+ (7a^7 + 7a^6b + 6a^6 + 6a^5b + 5a^5 + 5a^4b + 4a^4 + 4a^3b + 3a^3 + 3a^2b + 2a^2 + 2ab + a + b)r^2 +$$
$$+ (8a^8 + 8a^7b + 7a^7 + 7a^6b + 6a^6 + 6a^5b + 5a^5 + 5a^4b + 4a^4 + 4a^3b + 3a^3 + 3a^2b + 2a^2 + 2ab +$$
$$+ a + b)r - 6a^4b^2 - 6a^3b^3 - 6a^2b^4 - 6ab^5 - 9a^7b^2 - 9a^6b^3 - 9a^5b^4 - 9a^4b^5 - 9a^3b^6 - 9a^2b^7 - 9ab^8 +$$
$$- 4a^2b^2 - 4ab^3 - 7b^7 - 6b^6 - 8a^6b^2 - 8a^5b^3 - 8a^4b^4 - 8a^3b^5 - 8a^2b^6 - 8ab^7 - 5a^3b^2 - 5a^2b^3 +$$
$$- 5ab^4 - 8b^8 - 7a^5b^2 - 7a^4b^3 - 7a^3b^4 - 7a^2b^5 - 7ab^6 - 2b^2 - 3ab^2 - 4b^4 - 3b^3 - 5b^5 - 9b^9\Big)$$

$$f_9(r) = \frac{(r-a)^2}{a+b}\Big((a+b)r^9 + (2a^2 + 2ab + a + b)r^8 + (3a^3 + 3a^2b + 2a^2 + 2ab + a + b)r^7 + (4a^4 + 4a^3b +$$
$$+ 3a^3 + 3a^2b + 2a^2 + 2ab + a + b)r^6 + (5a^5 + 5a^4b + 4a^4 + 4a^3b + 3a^3 + 3a^2b + 2a^2 + 2ab +$$
$$+ a + b)r^5 + (6a^6 + +6a^5b + 5a^5 + 5a^4b + 4a^4 + 4a^3b + 3a^3 + 3a^2b + 2a^2 + (7a^7 + 7a^6b + 6a^6 +$$
$$+ 6a^5b + 5a^5 + 5a^4b + 4a^4 + 4a^3b + 3a^3 + 2ab + a + b)r^4 + 3a^2b + 2a^2 + 2ab + a + b)r^3 + (8a^8 +$$
$$+ 8a^7b + 7a^7 + 7a^6b + 6a^6 + 6a^5b + +5a^5 + 5a^4b + 4a^4 + 4a^3b + 3a^3 + 3a^2b2a^2 + 2ab + a +$$
$$+ b)r^2 + (9a^9 + 9a^8b + 8a^8 + 8a^7b + 7a^7 + 7a^6b + 6a^6 + b + 6a^5b + 5a^5 + 5a^4b + 4a^4 + 4a^3 + 3a^3 +$$
$$+ 3a^2b + 2a^2 + 2ab + a + b)r - 10b^{10} - 2b^2 - 3ab^2 - 4b^4 - 3b^3 - 5b^5 - 9b^9 - 6a^4b^2 - 6a^3b^3 - 6a^2b^4 +$$
$$- 6ab^5 - 9a^7b^2 - 9a^6b^3 - 9a^5b^4 - 9a^4b^5 - 9a^3b^6 - 9a^2b^7 - 9ab^8 - 4a^2b^2 - 4ab^3 - 7b^7 - 6b^6 +$$
$$- 8a^6b^2 - 8a^5b^3 - 8a^4b^4 - 8a^3b^5 - 8a^2b^6 - 8ab^7 - 5a^3b^2 - 5a^2b^3 - 5ab^4 - 10a^8b^2 - 10a^4b^6 - 8b^8 +$$
$$- 10a^7b^3 - 10a^6b^4 - 10a^5b^5 - 10a^3b^7 - 10a^2b^8 - 10ab^9 - 7a^5b^2 - 7a^4b^3 - 7a^3b^4 - 7a^2b^5 - 7ab^6\Big)$$

$$f_{10}(r) = \frac{(r-a)^2}{a+b}\Big((a+b)r^{10} + (2a^2 + 2ab + a + b)r^9 + (3a^3 + 3a^2b + 2a^2 + 2ab + a + b)r^8 + (4a^4 +$$

$$+ 4a^3b + 3a^3 + 3a^2b + 2a^2 + 2ab + a + b)r^7 + (5a^5 + 5a^4b + 4a^4 + 4a^3b + 3a^3 + 3a^2b + 2a^2 +$$
$$+ 2ab + a + b)r^6 + (6a^6 + +6a^5b + 5a^5 + 5a^4b + 4a^4 + 4a^3b + 3a^3 + 3a^2b + 2a^2 + 2ab + a + b)r^5 +$$
$$+ (7a^7 + 7a^6b + 6a^6 + 6a^5b + 5a^5 + 5a^4b + 4a^4 + 4a^3b + 3a^3 + 3a^2b + 2a^2 + 2ab + a + b)r^4 +$$
$$+ (8a^8 + 8a^7b + 7a^7 + 7a^6b + 6a^6 + 6a^5b + 5a^5 + 5a^4b + 4a^4 + 4a^3b + 3a^3 + 3a^2b + 2a^2 + 2ab + a +$$
$$+ b)r^3 + (9a^9 + 9a^8b + 8a^8 + 8a^7b + 7a^7 + 7a^6b + 6a^6 + 6a^5b + 5a^5 + 5a^4b + 4a^4 + 4a^3b + 3a^3 +$$
$$+ 3a^2b + 2a^2 + 2ab + a + b)r^2 + (10a^{10} + 10a^9b + 9a^9 + 9a^8b^8 + 8a^8 + 8a^7b + 7a^7 + 7a^6b + 6a^6 +$$
$$+ 6a^5b + 5a^5 + 5a^4b + 4a^4 + 4a^3b + 3a^3 + 3a^2b + 2a^2 + 2ab + a + b)r - 3b^3 - 5b^5 - 9b^9 - 6a^4b^2 +$$
$$- 6a^3b^3 - 6a^2b^4 - 6ab^5 - 9a^7b^2 - 9a^6b^3 - 9a^5b^4 - 9a^4b^5 - 9a^3b^6 - 9a^2b^7 - 9ab^8 - 11a^9b^2 - 11a^8b^3 +$$
$$- 11a^7b^4 - 11a^6b^5 - 11a^5b^6 - 11a^4b^7 - 11a^3b^8 - 11a^2b^9 - 11ab^{10} - 4a^2b^2 - 4ab^3 - 7b^7 - 6b^6 +$$
$$- 8a^4b^4 - 8a^3b^5 - 8a^2b^6 - 8ab^7 - 5a^3b^2 - 5a^2b^3 - 5ab^4 - 10a^8b^2 - 8a^6b^2 - 8a^5b^3 + 10a^4b^6 - 8b^8 +$$
$$- 10a^7b^3 - 10a^6b^4 - 10a^5b^5 - 10a^3b^7 - 10a^2b^8 - 10ab^9 - 7a^5b^2 - 7a^4b^3 - 7a^3b^4 - 7a^2b^5 - 7ab^6 +$$
$$- 11b^{11} - 10b^{10} - 2b^2 - 3ab^2 - 4b^4\Big)$$

APPENDIX C

As described in §7.2.4, the numerical examples are realized making use of a 10 terms series $V_N(r,\theta)$ for the approximated circumferential displacement component, 9 of them belong to the series for the medium and axisymmetric component of the circumferential displacement $\overline{V}_N(r)$. Approximation functions $\psi_l(r)$ of polynomial type ranging from a first degree polynomial function in the variable r until a ninth degree one are employed for the realization of the case studies. These functions revealed to possess no general and repetitive expression and they are hereafter reported.

Moreover, with referring to §8.2, the numerical examples were realized making use of series $W_N(r,\theta)$, $\Phi_r^N(r,\theta)$ and $\Phi_\theta^N(r,\theta)$ composed of 10 terms; in particular, 5 terms series to represent the medium and axisymmetric contribution of displacement component and 5 for the not-axisymmetric ones. The approximation functions $\varphi_j(r)$ employed in the numerical examples are of polynomial type revealed to possess no general and repetitive expression and they are listed in this Appendix.

It should be noted that the approximation functions $\psi_l(r)$ and $\varphi_j(r)$ are coicident polynomial functions:

$$\varphi_1(r) = \psi_1(r) = r - a$$

$$\varphi_2(r) = \psi_2(r) = \Big(r - a\Big)\Big(a + 1 + r\Big)$$

$$\varphi_3(r) = \psi_3(r) = \Big(r - a\Big)\Big(r^2 + (a+1)r + a^2 + a + 1\Big)$$

$$\varphi_4(r) = \psi_4(r) = \Big(r - a\Big)\Big(r^3 + (a+1)r^2 + (a^2 + a + 1)r + a^3 + a^2 + a + 1\Big)$$

$$\varphi_5(r) = \psi_5(r) = \Big(r - a\Big)\Big(r^4 + (a+1)r^3 + (a^2 + a + 1)r^2 + (a^3 + a^2 + a + 1)r + a^4 + a^3 + a^2 + a + 1\Big)$$

$$\psi_6(r) = \Big(r - a\Big)\Big(r^5 + (a+1)r^4 + (a^2 + a + 1)r^3 + (a^3 + a^2 + a + 1)r^2 + (a^4 + a^3 + a^2 + a + \\ + 1)r + a^5 + a^4 + a^3 + a^2 + a + 1\Big)$$

$$\psi_7(r) = \Big(r-a\Big)\Big(r^6+(a+1)r^5+(a^2+a+1)r^4+(a^3+a^2+a+1)r^3+(a^4+a^3+a^2+a+\\ +1)r^2+(a^5+a^4+a^3+a^2+a+1)r+a^6+a^5+a^4+a^3+a^2+a+1\Big)$$

$$\psi_8(r) = \Big(r-a\Big)\Big(r^7+(a+1)r^6+(a^2+a+1)r^5+(a^3+a^2+a+1)r^4+(a^4+a^3+a^2+a+\\ +1)r^3+(a^5+a^4+a^3+a^2+a+1)r^2+(a^6+a^5+a^4+a^3+a^2+a+1)r+a^7+a^6+\\ +a^5+a^4+a^3+a^2+a+1\Big)$$

$$\psi_9(r) = \Big(r-a\Big)\Big(r^8+(a+1)r^7+(a^2+a+1)r^6+(a^3+a^2+a+1)r^5+(a^4+a^3+a^2+a+\\ +1)r^4+(a^5+a^4+a^3+a^2+a+1)r^3+(a^6+a^5+a^4+a^3+a^2+a+1)r^2+(a^7+a^6+\\ +a^5+a^4+a^3+a^2+a+1)r+a^8+a^7+a^6+a^5+a^4+a^3+a^2+a+1\Big)$$

LIST OF PUBLICATIONS

V.G. Belardi, P. Fanelli, F. Vivio, P. Perugini, A. Zallo. Modellazione parametrica ed ottimizzazione strutturale di strutture anisogrid a guscio in composito. AIAS – Associazione Italiana per l'Analisi delle Sollecitazioni 45° Convegno Nazionale, 7-10 settembre 2016 − Università degli Studi di Trieste.

V. G. Belardi, P. Fanelli, and F. Vivio. Structural analysis and optimization of anisogrid composite lattice cylindrical shells. Composites Part B: Engineering 139 (2018) 203−215.

V. G. Belardi, P. Fanelli, and F. Vivio. Bending analysis with Galerkin method of rectilinear orthotropic composite circular plates subject to transversal load. Composites Part B: Engineering, 140 (2018) 250−259.

V. G. Belardi, P. Fanelli, and F. Vivio. Structural analysis of transversally loaded quasi-isotropic rectilinear orthotropic composite circular plates with Galerkin method. Procedia Structural Integrity, 8 (2018) 368−378.

V. G. Belardi, P. Fanelli, and F. Vivio. Elastic analysis of rectilinear orthotropic composite circular plates subject to transversal and in-plane load conditions using Ritz method. Composite Structures, 199 (2018) 63−75.

V. G. Belardi, P. Fanelli, and F. Vivio. Design, analysis and optimization of anisogrid composite lattice conical shells. Composites Part B: Engineering, 150 (2018) 184−195.

V. G. Belardi, P. Fanelli, and F. Vivio. A novel composite bolted joint element: application to a single-bolted joint. Procedia Structural Integrity, Procedia Structural Integrity, 12 (2018) 281−295

V. G. Belardi, P. Fanelli, and F. Vivio. Ritz method analysis of rectilinear orthotropic composite circular plates undergoing in-plane bending and torsional moments. Under Review.

V. G. Belardi, P. Fanelli, and F. Vivio. First-order shear deformation analysis of rectilinear orthotropic composite circular plates undergoing transversal loads. Under Review.

BIBLIOGRAPHY

[1] V. V. Vasiliev, V. Barynin, A. F. Razin, Anisogrid lattice structures – survey of development and application, Composite Structure 54 (2001) 361–70.

[2] V. V. Vasiliev, A. F. Razin, Anisogrid composite structures for spacecraft and aircraft applications, Composite Structure 76 (2006) 182–9.

[3] V. V. Vasiliev, V. Barynin, A. F. Razin, Anisogrid composite lattice structures - development and aerospace applications, Composite Structure 94 (2012) 1117–27.

[4] G. Totaro, F. De Nicola, Recent advance on design and manufacturing of composite anisogrid structures for space launchers, Acta Astronautica 81 (2012) 570–7.

[5] S. Huybrechts, S. W. Tsai, Analysis and behavior of grid structures, Composites Science and Technology 56 (9) (1996) 1001–1015.

[6] S. M. Huybrechts, T. E. Meink, P. M. Wegner, J. M. Ganley, Manufacturing theory for advanced grid stiffened structures, Composites Part A: Applied Science and Manufacturing 33 (2) (2002) 155–161.

[7] K. Terashima, T. Kamita, T. Aoki, T. Yokozeki, G. Kimura, T. Uzawa, Experimental study of buckling properties of composite lattice structures for launcher, in: Proc. of 16th European Conf. on Composite Materials, Sevilla, Spain, 2014.

[8] T. Aoki, T. Yokozeki, K. Terashima, T. Kamita, Mechanical Behavior of Composite Lattice Cylinders, in: 55th AIAA/ASME/ASCE/AHS/ASC Structures, Structural Dynamics, and Materials Conference, 2014.

[9] D. Liu, H. Lohse-Busch, V. Toropov, C. Hühne, U. Armani, Detailed design of a lattice composite fuselage structure by a mixed optimization method, Engineering Optimization 48 (2016) 1707–1720.

[10] T. Yokozeki, Y. Shimizu, M. Ishii, K. Kimizuka, S. Suzuki, Y. Yamasaki, K. Terashima, T. Kamita, T. Aoki, Mechanical behavior in compression of skin-added X-lattice composite panel with corrugated ribs, Composite Structures 168 (2017) 863–871.

[11] V. V. Vasiliev, E. V. Morozov, Advanced mechanics of composite materials and structural elements, 3rd Edition, Amsterdam: Elsevier, 2013.

[12] Z. Totaro, Z. Gürdal, Optimal design of composite lattice shell structures for aerospace applications, Aerospace Science Technology 13 (2009) 157–64.

[13] D. Slinchenko, V. E. Verijenko, Structural analysis of composite lattice shells of revolution on the basis of smearing stiffness, Composite Structures 54 (2001) 341–8.

[14] Q. Zheng, D. Jiang, C. Huang, X. Shang, S. Ju, Analysis of failure loads and optimal design of composite lattice cylinder under axial compression, Composite Structure 131 (2015) 885–94.

[15] E. V. Morozov, A. V. Lopatin, V. A. Nesterov, Finite-element modelling and buckling analysis of anisogrid composite lattice cylindrical shells, Composite Structure 93 (2011) 308–23.

[16] C. Lai, J. Wang, C. Liu, Parameterized finite element modeling and buckling analysis of six typical composite grid cylindrical shells, Applied Composite Materials 21(5) (2014) 739–58.

[17] A. F. Rasin, V. V. Vasiliev, Development of composite anisogrid spacecraft attach fitting, in: Procedia of the 11th European Conference on Composite Materials, Rhodos, Greece (May 31 - June 3, 2004) CD–ROM, 9 p.

[18] G. Totaro, Local buckling modelling of isogrid and anisogrid lattice cylindrical shells with triangular cells, Composite Structure 94 (2012) 446–52.

[19] G. Totaro, Local buckling modelling of isogrid and anisogrid lattice cylindrical shells with hexagonal cells, Composite Structure 95 (2012) 403–10.

[20] V. V. Vasiliev, A. Razin, G. Totaro, F. De Nicola, Anisogrid conical adapters for commercial space application, in: AIAA/CIRA 13th International Space Planes and Hypersonics Systems and Technologies Conference, 2005.

[21] S. Kidane, L. G., J. Helms, S. S. Pang, E. Woldesenbet, Buckling load analysis of grid stiffened composite cylinders, Composites Part B 34 (2003) 1–9.

[22] M. Buragohain, R. Velmurugan, Buckling analysis of composite hexagonal lattice cylindrical shell using smeared stiffener model, Defence Sci J 59(3) (2009) 230–8.

[23] M. Buragohain, R. Velmurugan, Optimal design of lament wound grid-stiffened composite cylindrical structures, Defence Science Journal 61(1) (2011) 88–94.

[24] S. Shi, Z. Sun, M. Ren, H. Chen, X. Hu, Buckling resistance of grid-stiffened carbon-fiber thin-shell structures, Composites Part B: Engineering 45 (2013) 888–896.

[25] A. H. Sofiyev, Buckling of heterogeneous orthotropic composite conical shells under external pressures within the shear deformation theory, Composites Part B: Engineering 84 (2016) 175–187.

[26] A. H. Sofiyev, Z. Zerin, N. Kuruoglu, Thermoelastic buckling of fgm conical shells under nonlinear temperature rise in the framework of the shear deformation theory, Composites Part B: Engineering 108 (2017) 279–290.

[27] J. Sun, C. W. Lim, X. Xu, H. Mao, Accurate buckling solutions of grid-stiffened functionally graded cylindrical shells under compressive and thermal loads, Composites Part B: Engineering 89 (2016) 96–107.

[28] B. Sobhaniaragh, M. Nejati, W. J. Mansur, Buckling modelling of ring and stringer stiffened cylindrical shells aggregated by graded CNTs, Composites Part B: Engineering 124 (2017) 120–133.

[29] F. Mehralian, Y. T. Beni, Size-dependent torsional buckling analysis of functionally graded cylindrical shell, Composites Part B: Engineering 94 (2016) 11–25.

[30] A. V. Lopatin, E. V. Morozov, A. V. Shatov, Buckling of uniaxially compressed composite anisogrid lattice plate with clamped edges, Composite Structures 157 (2016) 187–196.

[31] A. V. Lopatin, E. V. Morozov, A. V. Shatov, Buckling of uniaxially compressed composite anisogrid lattice cylindrical panel with clamped edges, Composite Structures 160 (2017) 765–772.

[32] G. Totaro, Optimal design concepts for flat isogrid and anisogrid lattice panels longitudinally compressed, Composite Structures 129 (2015) 101–110.

[33] A. V. Lopatin, E. V. Morozov, A. V. Shatov, Axial deformability of the composite lattice cylindrical shell under compressive loading: Application to a load-carrying spacecraft tubular body, Composite Structures 146 (2016) 201–206.

[34] G. Totaro, Flexural, torsional, and axial global stiffness properties of anisogrid lattice conical shells in composite material, Composite Structures 153 (2016) 738–745.

[35] V. G. Belardi, P. Fanelli, F. Vivio, Structural analysis and optimization of anisogrid composite lattice cylindrical shells, Composites Part B: Engineering 139 (2018) 203–215.

[36] M. Buragohain, R. Velmurugan, Study of filament wound grid-stiffened composite cylindrical structures, Composite Structure 93 (2011) 1031–38.

[37] L. Sorrentino, M. Marchetti, C. Bellini, A. Delfini, M. Albano, Design and manufacturing of an isogrid structure in composite material: Numerical and experimental results, Composite Structure 143 (2016) 189–201.

[38] E. V. Morozov, A. V. Lopatin, V. A. Nesterov, Buckling analysis and design of anisogrid composite lattice conical shells, Composite Structure 93 (2011) 3150–62.

[39] V. K. Maes, L. Pavlov, S. M. Simonian, An efficient semi-automated optimisation approach for (grid-stiffened) composite structures: Application to ariane 6 interstage, Composite Structure.

[40] S. Shi, Z. Sun, M. Ren, H. Chen, X. Hu, Buckling response of advanced grid stiffened carbon-fiber composite cylindrical shells with reinforced cutouts, Composites Part B: Engineering 44 (2013) 26–33.

[41] A. Fascetti, L. Feo, N. Nisticò, R. Penna, Web-flange behavior of pultruded GFRP I-beams: A lattice model for the interpretation of experimental results, Composites Part B: Engineering 100 (2016) 257–269.

[42] R. Ansari, J. Torabi, Numerical study on the buckling and vibration of functionally graded carbon nanotube-reinforced composite conical shells under axial loading, Composites Part B: Engineering 95 (2016) 196–208.

[43] H. T. Hu, H. C. Chen, Buckling optimization of laminated truncated conical shells subjected to external hydrostatic compression, Composites Part B: Engineering 135 (2018) 95–109.

[44] R. Barretta, M. Čanadija, L. Feo, R. Luciano, F. Marotti de Sciarra, R. Penna, Exact solutions of inflected functionally graded nano-beams in integral elasticity, Composites Part B: Engineering 142 (2018) 273–286.

[45] G. Romano, R. Luciano, R. Barretta, M. Diaco, Nonlocal integral elasticity in nanostructures, mixtures, boundary effects and limit behaviours, Continuum Mechanics and Thermodynamics 30 (3) (2018) 641–655.

[46] A. Apuzzo, R. Barretta, M. Canadija, L. Feo, R. Luciano, F. Marotti de Sciarra, A closed-form model for torsion of nanobeams with an enhanced nonlocal formulation, Composites Part B: Engineering 108 (2017) 315–324.

[47] R. Barretta, S. Ali Faghidian, R. Luciano, C. Medaglia, R. Penna, Stress-driven two-phase integral elasticity for torsion of nano-beams, Composites Part B: Engineering 145 (2018) 62–69.

[48] R. Barretta, M. Diaco, L. Feo, R. Luciano, F. Marotti de Sciarra, R. Penna, Stress-driven integral elastic theory for torsion of nano-beams, Mechanics Research Communications 87 (2018) 35–41.

[49] R. Barretta, M. Čanađija, R. Luciano, F. Marotti de Sciarra, Stress-driven modeling of nonlocal thermoelastic behavior of nanobeams, International Journal of Engineering Science 126 (2018) 53–67.

[50] R. Barretta, S. Faghidian, R. Luciano, Longitudinal vibrations of nano-rods by stress-driven integral elasticity, Mechanics of Advanced Materials and Structures (2018) 1–9.

[51] V. G. Belardi, P. Fanelli, F. Vivio, Design, analysis and optimization of anisogrid composite lattice conical shells, Composites Part B: Engineering 150 (2018) 184–195.

[52] Z. Kapidžić, L. Nilsson, H. Ansell, Finite element modeling of mechanically fastened composite-aluminum joints in aircraft structures, Composite Structures 109 (2014) 198–210.

[53] N. M. Chowdhury, W. K. Chiu, J. Wang, P. Chang, Experimental and finite element studies of bolted, bonded and hybrid step lap joints of thick carbon fibre/epoxy panels used in aircraft structures, Composites Part B: Engineering 100 (2016) 68–77.

[54] Q. Zhang, X. Cheng, J. Zhang, S. Wang, Y. Cheng, T. Zhang, Experimental and numerical investigation of composite box joint under tensile load, Composites Part B: Engineering 107 (2016) 75–83.

[55] X. Cheng, S. Wang, J. Zhang, W. Huang, Y. Cheng, J. Zhang, Effect of damage on failure mode of multi-bolt composite joints using failure envelope method, Composite Structures 160 (2017) 8–15.

[56] M. A. McCarthy, C. T. McCarthy, V. P. Lawlor, W. F. Stanley, Three-dimensional finite element analysis of single-bolt, single-lap composite bolted joints: part I —- model development and validation, Composite Structures 71 (2005) 140–158.

[57] C. T. McCarthy, M. A. McCarthy, Three-dimensional finite element analysis of single-bolt, single-lap composite bolted joints: Part II — effects of bolt-hole clearance, Composite Structures 71 (2) (2005) 159–175.

[58] P. J. Gray, C. T. McCarthy, A global bolted joint model for finite element analysis of load distributions in multi-bolt composite joints, Composites Part B: Engineering 41 (4) (2010) 317–325.

[59] P. J. Gray, C. T. Mccarthy, A highly efficient user-defined finite element for load distribution analysis of large-scale bolted composite structures, Composites Science and Technology 71 (2011) 1517–1527.

[60] Y. Zhou, H. Yazdani Nezhad, C. Hou, X. Wan, C. T. McCarthy, M. A. McCarthy, A three dimensional implicit finite element damage model and its application to single-lap multi-bolt composite joints with variable clearance, Composite Structures 131 (2015) 1060–1072.

[61] S. Y. Yoo, C. H. Kim, J. H. Kweon, J. H. Choi, The structural analysis and strength evaluation of the rivet nut joint for composite repair, Composite Structures 136 (2016) 662–668.

[62] F. Vivio, A new theoretical approach for structural modelling of riveted and spot welded multi-spot structures, International Journal of Solids and Structures 46 (2009) 4006–4024.

[63] F. Di Cicco, P. Fanelli, F. Vivio, Fatigue reliability evaluation of riveted lap joints using a new rivet element and DFR, International Journal of Fatigue 101 (2017) 430–438.

[64] V. G. Belardi, P. Fanelli, F. Vivio, Structural analysis of transversally loaded quasi-isotropic rectilinear orthotropic composite circular plates with Galerkin method, Procedia Structural Integrity 8 (2018) 368–378.

[65] V. G. Belardi, P. Fanelli, F. Vivio, Bending analysis with Galerkin method of rectilinear orthotropic composite circular plates subject to transversal load, Composites Part B: Engineering 140 (2018) 250–259.

[66] V. G. Belardi, P. Fanelli, F. Vivio, Elastic analysis of rectilinear orthotropic composite circular plates subject to transversal and in-plane load conditions using Ritz method, Composite Structures 199 (2018) 63–75.

[67] V. G. Belardi, P. Fanelli, F. Vivio, Ritz method analysis of rectilinear orthotropic composite circular plates undergoing in-plane bending and torsional moments (2019) Under Review.

[68] V. G. Belardi, P. Fanelli, F. Vivio, First-order shear deformation analysis of rectilinear orthotropic composite circular plates undergoing transversal loads (2019) Under Review.

[69] V. G. Belardi, P. Fanelli, F. Vivio, A novel composite bolted joint element: application to a single-bolted joint, Procedia Structural Integrity 12 (2018) 281–295.

[70] S. Timoshenko, S. Woinowsky-Krieger, Theory of plates and shells, 2nd Edition, McGraw-Hill, New York, 1959.

[71] S. G. Lekhnitskii, S. W. Tsai, T. Cheron, Anisotropic Plates, Translated from the second Russian edition by S.W. Tsai and T. Cheron, Gordon and Breach, Gordon and Breach, Science Publishers, Inc., New York, 1968.

[72] S. Tang, Stability of a laminated anisotropic circular plate, Journal of Spacecraft and Rockets 9 (1972) 123–124.

[73] C. Chang-Jun, D. Wei, D. F. Parker, Elastic instability of polar orthotropic annular plates, International Journal of Engineering Science 27 (1989) 109–121.

[74] L. Fu, A. M. Waas, Buckling of polar and rectilinearly orthotropic annuli under uniform internal or external pressure loading, Composite Structures 22 (1992) 47–57.

[75] R. Seifi, N. Khoda-yari, H. Hosseini, Study of critical buckling loads and modes of cross-ply laminated annular plates, Composites Part B: Engineering 43 (2) (2012) 422–430.

[76] R. Lal, N. Ahlawat, Buckling and vibrations of two-directional FGM Mindlin circular plates under hydrostatic peripheral loading, Mechanics of Advanced Materials and Structures 6 (2017) 1–16.

[77] N. R. Rajappa, Free vibration of rectangular and circular orthotropic plates, AIAA Journal 5 (1963) 1194–1195.

[78] S. B. Dong, A. E. Lopez, Natural vibrations of a clamped circular plate with rectilinear orthotropy by least-squares collocation, International Journal of Solids and Structures 21 (5) (1985) 515–526.

[79] T. Prakash, M. Ganapathi, Asymmetric flexural vibration and thermoelastic stability of fgm circular plates using finite element method, Composites Part B: Engineering 37 (2006) 642–649.

[80] L. G. Nallim, R. O. Grossi, Natural frequencies of symmetrically laminated elliptical and circular plates, International Journal of Mechanical Sciences 50 (2008) 1153–1167.

[81] S. Hosseini-Hashemi, M. Azimzadeh-Monfared, H. Rokni Damavandi Taher, A 3-D Ritz solution for free vibration of circular/annular functionally graded plates integrated with piezoelectric layers, International Journal of Engineering Science 48 (2010) 1971–1984.

[82] G. Jin, . Su, T. Ye, S. Gao, Three-dimensional free vibration analysis of functionally graded annular sector plates with general boundary conditions, Composites Part B: Engineering 83 (2015) 352–366.

[83] Q. Wang, D. Shi, Q. Liang, X. Shi, A unified solution for vibration analysis of functionally graded circular, annular and sector plates with general boundary conditions, Composites Part B: Engineering 88 (2016) 264–294.

[84] M. Salehi, A. R. Sobhani, Elastic linear and non-linear analysis of fiber-reinforced symmetrically laminated sector Mindlin plate, Composite Structures 65 (1) (2004) 65–79.

[85] A. Andakhshideh, S. Maleki, M. M. Aghdam, Non-linear bending analysis of laminated sector plates using generalized differential quadrature, Composite Structures 92 (9) (2010) 2258–2264.

[86] M. Kadkhodayan, A. Erfani Moghadam, G. J. Turvey, J. Alamatian, A DXDR large deflection analysis of uniformly loaded square, circular and elliptical orthotropic plates using non-uniform rectangular finite-differences, Journal of Mechanical Science and Technology 26 (10) (2012) 3231–3242.

[87] S. Maleki, M. Tahani, Bending analysis of laminated sector plates with polar and rectilinear orthotropy, European Journal of Mechanics - A/Solids 40 (2013) 84–96.

[88] M. E. Golmakani, M. Kadkhodayan, Large deflection thermoelastic analysis of functionally graded stiffened annular sector plates, International Journal of Mechanical Sciences 69 (2013) 94–106.

[89] M. E. Golmakani, Nonlinear bending analysis of ring-stiffened functionally graded circular plates under mechanical and thermal loadings, International Journal of Mechanical Sciences 79 (2014) 130–142.

[90] M. Jabbari, E. Shahryari, H. Haghighat, M. R. Eslami, An analytical solution for steady state three dimensional thermoelasticity of functionally graded circular plates due to axisymmetric loads, European Journal of Mechanics - A/Solids 47 (2014) 124–142.

[91] N. P. Patel, D. S. Sharma, Bending of composite plate weakened by square hole, International Journal of Mechanical Sciences 94-95 (2015) 131–139.

[92] F. Alinaghizadeh, M. Shariati, Geometrically non-linear bending analysis of thick two-directional functionally graded annular sector and rectangular plates with variable thickness resting on non-linear elastic foundation, Composites Part B: Engineering 86 (2016) 61–83.

[93] P. Li, X. Li, T. Wang, Three-Dimensional Thermo-Electro-Elastic Field in a Circular Plate of Functional Graded Materials with Transverse Isotropy, Mechanics of Advanced Materials and Structures 22 (2015) 537–547.

[94] A. Alibeigloo, Thermo elasticity solution of functionally graded, solid, circular, and annular plates integrated with piezoelectric layers using the differential quadrature method, Mechanics of Advanced Materials and Structures 25 (2018) 766–784.

[95] M. M. Alipour, A novel economical analytical method for bending and stress analysis of functionally graded sandwich circular plates with general elastic edge conditions, subjected to various loads, Composites Part B: Engineering 95 (2016) 48–63.

[96] K. Deb, A. Pratap, S. Agarwal, T. Meyarivan, A fast and elitist multiobjective genetic algorithm: NSGA-II, IEEE Transactions on Evolutionary Computation 6(2) (2002) 182–197.

[97] M. D. Mckay, R. J. Beckman, W. J. Conover, Comparison of Three Methods for Selecting Values of Input Variables in the Analysis of Output from a Computer Code, Technometrics 21(2) (1979) 239–245.

[98] A. F. Rasin, V. V. Vasiliev, Development of composite anisogrid spacecraft attach fitting, in: Proc. of the 11th European Conf. on Composite Materials, Rhodos, Greece, 2004.

[99] K. Deb, A. Pratap, S. Agarwal, T. Meyarivan, A fast and elitist multiobjective genetic algorithm: NSGA-II, IEEE Transactions on Evolutionary Computation 6(2) (2002) 182–197.

[100] R. M. Jones, Mechanics of composite materials, Scripta Book Company Washington DC, 1975.

[101] C. M. Wang, J. N. Reddy, K. H. Lee, Shear deformable beams and plates: relationships with classical solutions, Elsevier, 2000.

[102] F. Nerilli, G. Vairo, Progressive damage in composite bolted joints via a computational micromechanical approach, Composites Part B: Engineering 111 (2017) 357–371.

[103] J. Xiang, S. Zhao, D. Li, Y. Wu, An improved spring method for calculating the load distribution in multi-bolt composite joints, Composites Part B: Engineering 117 (2017) 1–8.

[104] J. N. Reddy, Theory and analysis of elastic plates and shells, CRC press, 2006.